TRANSPORT AND QUANTUM ANOMALIES IN TOPOLOGICAL SEMIMETALS

Dissertation
zur Erlangung des akademischen Grades
Doctor rerum naturalium
(Dr. rer. nat.)

vorgelegt von
Jan Behrends
geboren am 30.05.1987 in Jever
Max-Planck-Institut für Physik komplexer Systeme, Dresden

Wissenschaftlicher Betreuer:
Prof. Dr. Jens H. Bardarson

Fakultät Physik
Bereich Mathematik und Naturwissenschaften
Technische Universität Dresden
2018

Eingereicht am 13. Juli 2018

1. Gutachter:	Prof. Dr. Roderich Moessner
2. Gutachter:	Prof. Dr. Carsten Timm
3. Gutachter:	Prof. Dr. Jens H. Bardarson

Verteidigt am 15. November 2018

Abstract

Weyl semimetals have remarkable properties. Their resistance grows linearly and unsaturated with an applied transversal magnetic field, and they are expected to show a disorder-induced metal-insulator transition. Their charge carriers exhibit the chiral anomaly, i.e., the nonconservation of chiral charge. These properties emerge from their low-energy physics, which are dominated by Weyl nodes: zero-dimensional band crossings at the Fermi energy with a linear dispersion. The band crossings are topologically protected, i.e., they cannot be lifted by small perturbations. Thus, Weyl semimetals are examples of topological semimetals, materials with protected lower-dimensional band crossing close to the Fermi surface.

In this work, we show how the properties of Weyl semimetals are affected by disorder, magnetic fields, and strain. We further provide a link between Weyl semimetals and nodal line semimetals, topological semimetals with a one-dimensional Fermi surface. By using both lattice and low-energy continuum models, we present ways to understand the results from a condensed-matter and a quantum-field-theory perspective.

In particular, we identify an experimental signature of the chiral anomaly: the blue note, a characteristic note-shaped pattern that can be measured in photoemission spectroscopy. Another important signature is the magnetoresistance. In Weyl semimetals, its behavior depends on the angle between the magnetic field and the transport direction. For parallel transport, a negative longitudinal magnetoresistance as a manifestation of the chiral anomaly is observed; for orthogonal transport, the transversal magnetoresistance shows a linear and unsaturated growth. In this thesis, we investigate both regimes analytically and numerically. Inspired by experiments that show a sharply peaked magnetoresistance for parallel fields, we show that the longitudinal magnetoresistance depends on the angle between applied fields and the Weyl node separation, and that it is sharply peaked for fields parallel to the node separation. This effect is especially strong in the limit where only the lowest Landau level contributes to the magnetoresistance, but it survives at higher chemical potentials. For transversal magnetotransport, we numerically investigate the strong-disorder regime that is beyond the reach of perturbation theory and observe a positive magnetoresistance, qualitatively similar to recent experiments.

Strain in Weyl semimetals creates so-called axial fields that result in phenomena similar to the ones driven by electric and magnetic fields, but with some yet unknown consequences. We investigate strain from two perspectives: first, we show how two different predictions from quantum field theory, the consistent and covariant anomalies, manifest on a lattice. Second, we investigate transport in the presence of axial magnetic fields and show that counterpropagating modes are spatially separated, resulting in an unusual scaling of the conductance with the system's width.

We further show how a nodal line semimetal can emerge from a Weyl semimetal on a superlattice. We interpret the presence of surface states in terms of the intercellular Zak phase and show two distinct mechanisms that protect the spectrum from opening a gap. To complete our discussion, transport in nodal line semimetals is briefly discussed, as well as the quantum field theory that describes the low-energy features of these materials. Finally, we conclude this work by showing manifestations of the different symmetry classes that can be realized in the Sachdev-Ye-Kitaev model—a model of randomly interacting particles whose topology is deeply connected to the number of particles.

Zusammenfassung

Weyl-Semimetalle haben bemerkenswerte Eigenschaften. Ihr elektrischer Widerstand steigt linear und unsaturiert mit einem angelegten Magnetfeld, diverse Ergebnisse deuten darauf hin, dass sie einen unordnungsinduzierten Metall-Isolator-Phasenübergang aufweisen und ihre Ladungsträger zeigen die chirale Anomalie, d.h., die Nichtkonservierung der chiralen Ladung. Diese Eigenschaften haben ihren Ursprung in der Niedrigenergiephysik der Weyl-Semimetalle, die von Weyl-Punkten, Berührungspunkten zwischen Leitungs- und Valenzband an der Fermi-Energie mit einer linearen Dispersionsrelation, dominiert wird. Diese Berührungspunkte sind topologisch geschützt, d.h., kleine Störung können ihnen nichts anhaben. Weyl-Semimetalle sind daher Beispiele für topologische Semimetalle, Materialien mit geschützten niedrigdimensionalen Berührungenspunkten, -linien, oder -oberflächen an der Fermi-Energie.

In dieser Arbeit zeigen wir, wie die Eigenschaften von Weyl-Semimetallen durch Unordnung, Magnetfelder und Deformationen beeinflusst werden. Wir zeigen außerdem eine Querverbindung zwischen Weyl-Semimetallen und *nodal line*-Semimetallen, topologisch geschützten Semimetallen mit einer eindimensionalen Fermi-Fläche. Durch die Nutzung von Gitter- und Niedrigenergiekontinuumsmodellen können wir Wege aufzeigen, wie man unsere Ergebnisse sowohl aus einer Festkörperphysik- als auch aus einer Hochenergiephysikperspektive verstehen kann.

Insbesondere identifizieren wir eine experimentelle Signatur der chiralen Anomalie: die blaue Note, ein charakteristisches Muster in Form einer Note, das mit Hilfe von winkelaufgelöster Photoelektronenspektroskopie gemessen werden kann. Ein weiteres wichtiges Charakteristikum ist der Magnetwiderstand, der in Weyl-Semimetallen vom Winkel zwischen einem angelegten Magnetfeld und der Transportrichtung abhängt. Durch den Einfluss der chiralen Anomalie ist der longitudinale Magnetwiderstand negativ, der transversale Widerstand hingegen wächst linear und grenzenlos mit dem angelegten Magnetfeld. In dieser Dissertation untersuchen wir beide Charakteristiken analytisch und numerisch. Inspiriert durch Experimente, in denen ein scharfes Leitfähigkeitsmaximum für paralle elektrische und Magnetfelder observiert wurde, zeigen wir, dass die Leitfähigkeit vom Winkel zwischen den angelegten Feldern und dem Abstandsvektor der Weyl-Punkte abhängt und dass sie insbesondere für Felder parallel zum Abstandsvektor ein scharfes Maximum aufweist. Dieser Effekt ist besonders ausgeprägt, wenn nur das niedrigste Landau-Niveau zur Leitfähigkeit beiträgt, er bleibt aber auch bei höheren Energien beobachtbar. Für parallelen Magnettransport untersuchen wir starke Unordnung, die außerhalb des von der Störungstheorie abgedeckten Bereichs liegt, numerisch und beobachten einen positiven Magnetwiderstand, qualitativ ähnlich zu experimentellen Daten.

Aus Deformationen in Weyl-Semimetallen entstehen sogenannte chirale oder auch axiale Felder, die ähnliche Konsequenzen wie externe elektromagnetische Felder haben, wobei noch viele Details im Verborgenen liegen. Wir untersuchen Deformationen aus zwei verschiedenen Perspektiven: zunächst zeigen wir, wie zwei widersprüchliche Vorhersagen aus der Quantenfeldtheorie, die konsistenten und kovarianten Anomalien, in einem Gittermodell beoachtbar sind. Dann untersuchen wir elektrischen Transport unter Einfluss von axialen Magnetfeldern und zeigen, dass Moden, die sich in unterschiedliche Richtungen bewegen, räumlich getrennt sind. Diese räumliche Trennung hat eine unübliches Wachstums des elektrischen Leitwerts mit der transversalen Systembreite zur Folge.

Des weiteren zeigen wir, wie ein *nodal line*-Semimetall aus einem Weyl-Semimetall entstehen kann, das einer Supergitterstruktur ausgesetzt ist. Wir interpretieren die Oberflächenzustände mit Hilfe der interzellulären Zak-Phase und zeigen zwei verschiedene Mechanismen, die die Bandstruktur vor der Öffnung einer Bandlücke schützen, auf. Um unsere Diskussion abzuschließen, untersuchen wir Transport in *nodal line*-Semimetallen in Kürze und stellen ihre Quantenfeldtheorie vor. Schließlich wenden wir uns wechselwirkenden Phasen zu und zeigen, welche Konsequenzen die Symmetrieklassifizierung des Sachdev-Ye-Kitaev-Modells hat – ein Modell von Teilchen mit zufälligen Wechselwirkungsstärken, dessen Topologie von der Anzahl der enthaltenen Teilchen bestimmt wird.

Contents

1 Introduction **1**

2 Topological Band Theory **5**
- 2.1 Geometric Phase and Berry Phase 6
  - 2.1.1 The Adiabatic Theorem 6
  - 2.1.2 The Zak Phase 7
- 2.2 Tenfold Classification of Topological Insulators and Superconductors 9
- 2.3 Topological Semimetals 13
  - 2.3.1 Weyl Semimetals 15
  - 2.3.2 Nodal Line Semimetals 18
- 2.4 Bulk-boundary Correspondence from the Intercellular Zak Phase 20
  - 2.4.1 Intra- and Intercellular Zak Phase 21
  - 2.4.2 Bulk-boundary Correspondence 24
  - 2.4.3 Conclusion 26

3 Field Theory Perspective on Topological Phases **27**
- 3.1 Topological Insulators 27
- 3.2 Weyl Fermions and the Chiral Anomaly 31
- 3.3 Visualizing the Chiral Anomaly with Photoemission Spectroscopy 32
  - 3.3.1 The Chiral Anomaly in Condensed Matter Systems 32
  - 3.3.2 Model and Methods 36
  - 3.3.3 ARPES Spectra for Weyl and Dirac Semimetals 37
  - 3.3.4 Experimental Details 38
  - 3.3.5 Summary and Conclusion 39
- 3.4 The Consistent and Covariant Anomalies 40
- 3.5 Consistent and Covariant Anomalies on a Lattice 44
  - 3.5.1 Model and Methods 45
  - 3.5.2 Lattice Results for Consistent and Covariant Anomalies 47
  - 3.5.3 Influence of the Mass Term 49
  - 3.5.4 The Quest for One Third 53
- 3.6 The Action of Nodal Line Semimetals 54

4 Transport in Topological Semimetals **57**
- 4.1 Longitudinal Magnetoresistance in Weyl Semimetals 57
- 4.2 Transversal Magnetoresistance in Weyl Semimetals 64
  - 4.2.1 Model 66
  - 4.2.2 Mesoscopic Transport in Clean Samples 66
  - 4.2.3 Numerical Magnetotransport in the Presence of Disorder 68

4.2.4 Born-Kubo Analytical Bulk Conductivity 70
4.2.5 Numerical Results in Disordered Samples 70
4.2.6 Conclusion 72
4.3 Transport in the Presence of Axial Magnetic Fields 72
4.3.1 Model and Methods 73
4.3.2 Longitudinal Magnetotransport for Axial Fields 75
4.3.3 Conclusion 79
4.4 Transport in Nodal Line Semimetals 80

5 Nodal Line Semimetals from Weyl Superlattices **85**
5.1 Weyl Semimetal on a Superlattice 86
5.2 Emergent Nodal Phases 88
5.3 Symmetry Classification of the Nodal Line 90
5.4 Surface States 91
5.5 Stability against Wave Vector Mismatch 94
5.6 Time-reversal Symmetric Weyl Semimetal 95
5.7 Conclusion 97

6 Symmetry Classification of the SYK Model **99**
6.1 Model and Topological Classification 99
6.2 Overlap of Time-reversed Partners 104
6.2.1 Even Number of Majoranas 104
6.2.2 Odd Number of Majoranas 105
6.3 Spectral Function 105
6.3.1 Zero Temperature 106
6.3.2 Infinite Temperature 106
6.4 Symmetry-breaking Terms 108
6.5 Lattice Model 109
6.6 Conclusion 110

7 Conclusion and Outlook **113**

Appendix A Zak Phase and Extra Charge Accumulation **115**

Appendix B Material-specific Details for ARPES **117**
B.1 Relaxation Rates 117
B.2 ARPES in Finite Magnetic Fields 117
B.3 Estimates of the Chiral Chemical Potential Difference 119

Appendix C Weyl Nodes in a Magnetic Field **121**
C.1 Scattering between Different Landau Levels 122
C.2 Analytical Born-Kubo Calculation of Transversal Magnetoconductivity .. 124
C.2.1 Disorder Scattering in Born Approximation 125
C.2.2 Transversal Magnetoconductivity from Kubo Formula 125

Appendix D Transfer Matrix Method **127**
D.1 Longitudinal Magnetic Field 129
D.2 Transversal Magnetic Field 129

Bibliography **133**

Acknowledgments **149**

List of Publications **151**

Versicherung **153**

1 Introduction

The properties of any kind of macroscopic matter are largely determined by its phase, rather than by its constituents. Characterizing different phases of matter has always been a major goal in physics. Landau put the distinction between different phases on a solid ground by formulating that different phases are characterized in terms of spontaneous symmetry breaking.[1] Many examples of spontaneous symmetry breaking occur in our everyday experience: the continuous translational symmetry that is present in liquids and gases is broken upon crystallization to a solid phase that is only symmetric upon discrete translations by a lattice spacing; similarly, the rotational freedom of spins in a paramagnet is broken upon the transition to a ferromagnet where one magnetization direction is chosen. Such phases that are characterized by a broken symmetry are described by a local order parameter, e.g., the density's Fourier transform of a solid or the magnetization of a ferromagnet.

This tradional view was challenged by Kosterlitz and Thouless who realized that some phases cannot be described by such a local order parameter.[2;3] Instead, a global topological invariant characterizes the long-range order of these phases. These rather abstract findings were reinvestigated after the discovery of the quantum Hall effect in two-dimensional electron gases.[4] At low temperatures and large magnetic fields, the Hall conductance is quantized, independent of small variations in the electron density, the magnetic field, or disorder. Experimentally, the quantization is so exact that it led to a new standard definition of the electrical resistance.[5] From a theoretical perspective, the quantized conductance is a manifestation of an integer-valued topological invariant[6] that does not depend on the details of the Hamiltonian and cannot be measured by a local probe.

Haldane soon after proposed a lattice model with a quantized Hall conductance that does not require an external magnetic field.[7] Similar to the quantum Hall effect, this model breaks time-reversal symmetry and its topological invariant is the same as for the quantum Hall effect: the so-called first Chern number.[8] With the advent of two-dimensional materials,[9] Kane and Mele investigated the effect of spin-orbit coupling in graphene.[10] They found that spin-orbit coupling opens up a gap in the bulk spectrum that is accompanied by gapless edge states. Effectively, the phase realized constitutes two time-reversed copies of Haldane's model.[7] Each spin species carries a quantum Hall effect characterized by a topological invariant of opposite sign for opposite spins,[11] so Kane and Mele coined the term quantum spin Hall effect—a so-called topological insulator that respects time-reversal symmetry and is characterized by a $\mathbb{Z}_2$ invariant that distinguishes between two topologically different insulators.[11] However, the gap due to spin-orbit coupling in graphene is very small, making the topological phase inaccessible.[12]

The first time-reversal symmetric topological insulator was realized in mercury telluride-cadmium telluride semiconductor quantum wells.[13;14] Depending on the thickness of a quantum well made of mercury telluride sandwiched between cadmium telluride, the bands in the quantum well get inverted, realizing two copies of a Chern insulator, i.e., a lattice realization of the quantum Hall effect.[13] The underlying mechanism was soon generalized to three dimensions,[15;16] leading to material predictions,[17] and experimental evidence for topological surface states of three-dimensional $\mathbb{Z}_2$ topological insulators.[18] A systematic classification of gapped topological phases according to their antiunitary symmetries[19;20] opened the door to a zoo of topological insulators, ranging from superconductors that host Majorana fermions[21–24] to the reinterpretation of already known phenomena, e.g., the appearance of edge states in the Su-Schrieffer-Heeger model.[25]

Topological phases are not limited to gapped systems. Weyl semimetals are the most prominent manifestation of a topologically nontrivial gapless system. The investigation of their peculiar properties forms the main ingredient of this work; these properties include a large unsaturated transversal magnetoresistance,[26] a disorder-driven metal-insulator transition,[27] and the chiral anomaly, the nonconservation of chiral charge.[28–30] Weyl semimetals are three-dimensional systems with zero-dimensional band crossings, so-called Weyl nodes, which can only be gapped out by annihilating two Weyl nodes of opposite chirality, a property related to the momentum-space structure of their eigenfunctions.[31] Weyl nodes are an example of crossings in the band structure that cannot be lifted by small perturbations.[32] Another example is a one-dimensional band crossing, a so-called nodal line, that needs to be transformed to a point to open up a gap without breaking the symmetry protecting the band crossing.[33] When these band crossings are close to the Fermi energy, the low-temperature behavior of the material is dominated by the crossing, and the material is classified as a topological semimetal. In condensed-matter systems, Weyl nodes were first investigated in superfluid ^{3}He,[34] before the advent of topological insulators inspired proposals to realize Weyl semimetals in solids.[35] These first proposals were soon followed by the theoretical and experimental identification of the first materials.[36–39]

Transport experiments are indispensable tools for revealing the topological nature of gapped and gapless phases. Indeed, the first experiment that measured a topological invariant[6] was a transport experiment, the measurement of the quantized Hall conductance;[4] similarly, the theoretically predicted[13] quantum spin Hall effect in mercury telluride was experimentally confirmed by a conductance measurement.[14] Although no quantized conductance signature has been identified for Weyl semimetals, these materials nevertheless have unique transport properties. Especially magnetotransport is widely regarded as a key signature of Weyl semimetals by being crucial for the experimental identification of the chiral anomaly.[30;40] However, despite a huge progress in magnetotransport measurements, not all experimental results are fully understood.[41] In this work, we deal with one of the experimental issues by carefully examining scattering processes in Weyl semimetals in the presence of magentic fields.[42]

Transversal magnetotransport in Weyl semimetals is fundamentally different from conventional metals.[26] The magnetoresistance shows a linear and unsaturated growth,[43] which can be explained by charged impurities.[26] The perturbative analysis of scalar white-noise disorder, on the other hand, results in a completely different behavior, the growth of the conductivity with the applied magnetic field.[44] To extend these previous findings, we perform a numerical analysis of strong disorder that is beyond the reach of perturbation theory. We show that the conductivity decreases with magnetic field in the strong-disorder regime, in qualitative agreement with experiments.[45] Although strong evidence suggests that charged impurities are in fact responsible for the linear growth, we provide a toolbox to access the strong-disorder regime that can be used in future studies of transport in strongly disordered topological semimetals in the presence of a magnetic field.

Besides these studies focusing on Weyl semimetals, we present preliminary results for transport in another topological semimetal, namely a nodal line semimetal. We show the breakdown of the Kubo formula at zero disorder for transport in the plane of the nodal line, and present ways to investigate transport in disordered systems, connecting to previous work on graphene.[46] Transport as a key property may also reveal anomalies in nodal line semimetals.[47;48]

Apart from the condensed-matter approach that relies on lattice models, quantum field theory can provide useful models to obtain predictions about the behavior of topological phases of matter. For decades, quantum field theory has proven to be a powerful tool to describe broad ranges of physics, from superconductors[49] to high-energy physics.[50] By capturing the collective behavior of the low-energy degrees of freedom, an effective description in terms of fluctuating quantum fields arises, instead of a full (often microscopic) model that is in general too complicated to solve. For example, the standard model of particle physics is preseumably an effective description of the low-energy behavior of a yet unknown full model of the universe.[51] Similarly, the Ginzburg-Landau theory of superconductivity captures macroscopic phenomena sufficiently well by describing it with a fluctuating order parameter.[52]

The electromagnetic response of topological insulators can be obtained from a low-energy description of their electronic structure.[53] More importantly for this thesis, the band crossings in Weyl semimetals are well-captured by a quantum field theory.[54;55] These band crossings have been studied extensively in the context of high-energy physics, as possible extensions to quantum electrodynamics that break Lorentz invariance.[56;57] As massless particles, Weyl fermions exhibit a chiral anomaly: the nonconservation of the classically conserved chiral charge due to quantum fluctuations.[28;29] The chiral anomaly is directly linked to magnetotransport in these materials.[30;40] In this thesis, we identify another experimental signature that is visible in photoemission spectroscopy: the blue note.[58] We argue that this note-shaped pattern is within the reach of current experimental setups, using available Weyl (and Dirac) semimetals.

Since all quantum field theories are effective theories,[59] it is not always clear if all their predictions can be observed in condensed matter systems. All condensed matter models are necessarily defined on a lattice that works as a regulator for the field theory.[60] Not all results derived from the field theory, i.e., the low-energy degrees of freedom, survive upon this regularization at higher energies.[61] For example, the chiral magnetic effect, a dissipationless equilibrium current driven by a magnetic field, cannot be observed in Weyl semimetals,[62] despite contrary results from quantum field theory.[63] Furthermore, some formal derivations have ambiguous results;[64] in high-energy physics, this ambiguity can often be fixed by requiring certain symmetries, e.g., Lorentz-invariance.[65] However, in condensed matter, only a few symmetries need to be satisfied—Weyl fermions, for example, require no symmetries at all.[31] How can these ambiguities be fixed? In this work, we provide one particular example of the ambiguity-fixing for the current in Weyl semimetals, supplementing previous work on the anomalous Hall current.[66] We show how response functions derived from lattice calculations can be interpreted using the so-called consistent and covariant anomalies,[67] quantum anomalies that comprise the chiral anomaly.

The concept of topology in quantum physics is not limited to noninteracting phases. For example, (intrinsic) topological order describes the order of interacting phases that are characterized by a macroscopic ground-state degeneracy, long-range entanglement, and anyonic excitations.[68;69] Different from this intrinsic order, symmetries in interacting systems can also give rise to topologically distinct phases,[70–72] which gives a scheme that is a direct extension of the classification of noninteracting phases. In this work, we describe how the symmetries in the Sachdev-Ye-Kitaev model[73;74] that is known for its AdS/CFT correspondence[74] gives rise to eight distinct topological phases.[71] We show how this classification is directly linked to features in the density of states that should be experimentally observable.

2 Topological Band Theory

The classification of gapped phases of noninteracting fermions, topological band theory, is a building block of this work. It has been proven an essential tool to understand various topological phases of matter, from the quantum Hall effect[4;75] to $\mathbb{Z}_2$ topological insulators.[10;13–16] Although topological band theory provides a well-established toolbox to distinguish different topological phases of matter, the classification is far from being complete: various extensions that take into account, e.g., crystal symmetries[76–79] and interactions[70–72] have been made in the previous years.

In this chapter, we concentrate on the so-called tenfold way, the classification of noninteracting phases based on antiunitary symmetries in the limit of a large number of bands. The tenfold way originates from random matrix theory[80–83] and its importance for topological phases was realized with the advent of the first topological insulators.[19;20] Reviews on topological band theory include Refs. 84–87.

After introducing the tenfold way for gapless systems of arbitrary dimension, we briefly discuss crystal systems where momentum space is defined on a torus before shifting to the topology of gapless systems, i.e., Weyl, Dirac, and nodal line semimetals, the systems in the main focus of this work. The discussion of the tenfold way and its application to gapless topological phases paves the path for two extensions that are made in the course of the thesis, outside this chapter. First, in Chapter 5, we study the combination of antiunitary symmetries with unitary symmetries that allows us to classify a realization of a nodal line semimetal. Second, in Chapter 6, we discuss the Sachdev-Ye-Kitaev (SYK) model and identify experimental signatures of its topology.

Three different approaches have been developed for the classification of noninteracting phases, all resulting in the tenfold way:

1. K-Theory[20]
2. Anderson localization[19;88;89]
3. Quantum anomalies[90]

In this chapter, we review the first approach by introducing the Berry phase and considering simple models. Afterwards, in Chapter 3, we discuss the third approach, which naturally extends to Weyl semimetals and other gapless phases of matter. The second approach uses a nonlinear σ-model, an effective field theory for the disordered surface, to determine the absence or presence of localization at the surface.[19;91] Its discussion is beyond the scope of this thesis.

2.1 Geometric Phase and Berry Phase

A key concept to understand the topological nature of matter is the Berry phase.[92] The Berry phase gives the polarization of solids,[93;94] governs adiabatic transport in one-dimensional systems,[95] and defines a topological invariant, the first Chern number, ultimately helping to explain the quantized conductance plateaus in the quantum Hall effect.[6] The relevance of the phase was not realized until the seminal work by Berry:[92] in fact, some of its consequences, e.g., on semiclassical transport[96] are not taken into account in standard textbooks such as Ref. 97.

2.1.1 The Adiabatic Theorem

The adiabatic theorem[98] plays a central role in quantum mechanics and is essential to the Berry phase:[92] it states that a system prepared in an instantaneous eigenstate with an energy that is separated from all other eigenenergies by Δ stays in that eigenstate when the Hamiltonian is varied sufficiently slowly. This can be understood by considering the Fourier transform $H(\omega)$ of the time-dependent Hamiltonian $H(t)$. If $H(t)$ varies slowly, $H(\omega)$ will only have finite matrix elements for $\omega \ll \Delta$.

We consider a Hamiltonian $H(\mathbf{R}(t))$ that depends on a set of parameters $\mathbf{R}(t) = (R_1(t), R_2(t), \ldots)$ that in turn depend on the time t. The instantaneous eigenstates of H are $|n(\mathbf{R}(t))\rangle$ with energies $\varepsilon_n(\mathbf{R}(t))$. Consider the time evolution of the superposition

$$|\psi(\mathbf{R}(t))\rangle = \sum_n c_n(t)|n(\mathbf{R}(t))\rangle \tag{2.1}$$

that is governed by the Schrödinger equation and gives[87]

$$\dot{c}_n = -\left(\frac{i}{\hbar}\varepsilon_n + \langle n|\frac{d}{dt}|n\rangle\right) c_n - \sum_{m\neq n} c_m \frac{\langle n|\left(\frac{dH}{dt}\right)|m\rangle}{\varepsilon_m - \varepsilon_n}. \tag{2.2}$$

In the adiabatic limit, the last sum is zero since $|\varepsilon_m - \varepsilon_n| \geq \Delta$ stays finite while the matrix elements of dH/dt become arbitrarily small—a detailed proof is given in Ref. 98. In the adiabatic limit, we obtain the time evolution

$$c_n(t) = c_n(t_0)e^{-i\phi_D(t)+i\gamma_n(t)} \tag{2.3}$$

with the dynamical phase $\phi_D(t)$ and the geometric phase $\gamma_n(t)$. The dynamical phase is the integral over energy,

$$\phi_D(t) = \frac{1}{\hbar}\int_{t_0}^{t} dt'\varepsilon_n(\mathbf{R}(t')), \tag{2.4}$$

and it is of no further interest in this work since it is very sensitive to the detailed time-evolution. The geometric phase can be rewritten such that it solely depends on a geometrical property, the path in parameter space $\mathcal{C}$,

$$\gamma_n(t) = i\int_{t_0}^{t} dt'\langle n(\mathbf{R}(t'))|\frac{d}{dt'}|n(\mathbf{R}(t'))\rangle = i\int_{\mathcal{C}} d\mathbf{R}\cdot\langle n(\mathbf{R})|\frac{d}{d\mathbf{R}}|n(\mathbf{R})\rangle, \tag{2.5}$$

hence the name. It turns out to be useful to define the Berry connection[*]

$$\mathcal{A}_n(\mathbf{R}) = i\langle n(\mathbf{R})|\frac{d}{d\mathbf{R}}|n(\mathbf{R}\rangle, \tag{2.6}$$

a real-valued vector function. The Berry connection is gauge-dependent: under the transformation $|n(\mathbf{R})\rangle \to e^{i\zeta(\mathbf{R})}|n(\mathbf{R})\rangle$ with the smooth, single-valued function $\zeta(\mathbf{R})$,[99] the Berry connection changes

$$\mathcal{A}_n(\mathbf{R}) \to \mathcal{A}_n(\mathbf{R}) - \frac{d}{d\mathbf{R}}\zeta(\mathbf{R}), \tag{2.7}$$

changing the geometric phase

$$\gamma_n(t) \to \gamma_n(t) + \zeta(\mathbf{R}(t_0)) - \zeta(\mathbf{R}(t)). \tag{2.8}$$

While Born and Fock argued that it is always possible to chose a gauge $\zeta(\mathbf{R})$ such that $\gamma_n = 0$,[98] Berry realized the importance of the geometric phase by considering closed loops in parameter space,[92] such that the set of parameters returns to its initial state after some time T, $\mathbf{R}(t_0+T) = \mathbf{R}(t_0)$. This imposes the restriction that the instantaneous eigenstates need to return to their initial state $|n(\mathbf{R}(t_0+T))\rangle = |n(\mathbf{R}(t_0))\rangle$, further restricting the gauge choice $\zeta(\mathbf{R}(t_0)) - \zeta(\mathbf{R}(t_0+T)) = 2\pi\nu$ with $\nu \in \mathbb{Z}$. The geometric phase for a closed path thus cannot be canceled by a certain choice of $\zeta(\mathbf{R})$, but just changed by $2\pi\nu$.

For a closed path in parameter space, we can apply Stokes theorem, with the closed path $\mathcal{C} = \partial S$ being the boundary of two-dimensional manifold S, giving

$$\gamma_n = i\oint_{\partial S} d\mathbf{R}\cdot\mathcal{A}_n(\mathbf{R}) = i\int_S \mathcal{F}^n_{\mu\nu} dR^\mu \wedge dR^\nu \tag{2.9}$$

with the Berry curvature

$$\mathcal{F}^n_{\mu\nu} = \langle\partial_\mu n(\mathbf{R})|\partial_\nu n(\mathbf{R})\rangle - \langle\partial_\nu n(\mathbf{R})|\partial_\mu n(\mathbf{R})\rangle. \tag{2.10}$$

In three dimensions, the above expression simplifies to

$$\gamma_n = i\int_S d\mathbf{S}\cdot\Omega_n(\mathbf{R}) \tag{2.11}$$

with the Berry curvature $\Omega_n(\mathbf{R}) = \nabla\times\mathcal{A}_n(\mathbf{R})$. In the following sections, we discuss the physical consequences of the Berry phase and its application in crystals, most notably the Zak phase.

2.1.2 The Zak Phase

It was realized by Zak that the Berry phase naturally has consequences for wave functions in a crystal.[100] To introduce the Berry phase in crystals, it is instructive to quickly review the properties of Bloch waves, a successful ansatz for wave functions in periodic systems. Here, we perform a slight modification of the usual approach that is presented in standard condensed-matter textbooks, e.g., in Ref. 97, skipping some details about the conditions on the crystal momentum imposed by boundary conditions. Following Zak, we introduce a time-dependent vector potential $\mathbf{A}(t)$ by performing a gauge transformation of the single-particle Hamiltonian H that describes the electronic structure of the crystal

---

[*] In mathematical terms, the notation chosen here is a little bit sloppy. The Berry connection is in fact $\mathcal{A}^B = \mathcal{A}_\mu dR^\mu$ and the Berry curvature, defined below $\mathcal{F}^B = \mathcal{F}_{\mu\nu} dR^\mu \wedge dR^\nu$. Following the common notation in physics, we omit some mathematical precision for a more intuitive picture.

$$H \to H'(t) = e^{-i\mathbf{A}(t)\cdot\mathbf{r}} H e^{i\mathbf{A}(t)\cdot\mathbf{r}}. \tag{2.12}$$

This gauge transformation leaves the potential invariant but changes the kinetic part of H by shifting the momentum operator $-i\partial_{\mathbf{r}} \to -i\partial_{\mathbf{r}} + \mathbf{A}$ (in this section: $\hbar = e = 1$). Due to the periodicity of the underlying lattice, both H and H' are invariant under a translation by a multiple of a lattice vector, i.e., the Hamiltonian commutes with the operator $\mathcal{T}(\mathbf{R})$ that generates such a translation by $\mathbf{R}$, $[H, \mathcal{T}(\mathbf{R})] = 0$. Thus, the eigenfunctions of the Hamiltonian are simultaneously eigenfunctions of the operator $\mathcal{T}$, with eigenvalues of the form $e^{i\theta_q}$ since $\mathcal{T}$ is a unitary operator.[97] Instantaneous eigenfunctions at every time t are labeled by (n, q), denoting their eigenvalue of H', $\varepsilon_n(t)$, and their time-independent eigenvalues[100] of $\mathcal{T}$, $e^{i\theta_q}$,

$$H'(t)\psi_{t,n,q}(\mathbf{r}) = \varepsilon_n(t)\psi_{t,n,q}(\mathbf{r}),\ \mathcal{T}\psi_{t,n,q}(\mathbf{r}) = e^{i\theta_q}\psi_{t,n,q}(\mathbf{r}). \tag{2.13}$$

A convenient choice to satisfy this are Bloch waves

$$\psi_{t,n,\mathbf{k}}(\mathbf{r}) = e^{i\mathbf{k}\cdot\mathbf{r}} u_{n,\mathbf{k}'(t)}(\mathbf{r}),\ u_{n,\mathbf{k}'(t)}(\mathbf{r}+\mathbf{R}) = u_{n,\mathbf{k}'(t)}(\mathbf{r}), \tag{2.14}$$

with the lattice-periodic function $u_{n,\mathbf{k}'(t)}(\mathbf{r})$ and $\mathbf{k}'(t) = \mathbf{k} + \mathbf{A}(t)$, the momentum shifted by the time-dependent vector potential. As in the previously discussed case of a general time-dependent Hamiltonian, the time evolution of a state ϕ that was prepared as an instantaneous eigenstate ψ at time t_0 requires an additional phase,

$$\phi_{n,\mathbf{k}}(\mathbf{r}) = e^{-i\phi_D + i\gamma_n}\psi_{t,n,\mathbf{k}}(\mathbf{r}), \tag{2.15}$$

cf. Eq (2.3). While the dynamical phase ϕ_D is entirely given by integral over the state's energy $\varepsilon_{n,\mathbf{k}}(t)$, the contribution by the geometric phase is given by the lattice-periodic part of the wave function that contains the explicit time dependence,[100]

$$\gamma_n = i\int_{t_0}^{t} dt' \langle u_{n,\mathbf{k}'(t')}|\frac{d}{dt'}|u_{n,\mathbf{k}'(t')}\rangle = i\int_{\mathcal{C}} d\mathbf{k}\langle u_{n,\mathbf{k}}|\frac{d}{d\mathbf{k}}|u_{n,\mathbf{k}}\rangle. \tag{2.16}$$

In this form, it is immediately evident that the crystal momentum $\mathbf{k}$ in this setup has the role previously played by the set of parameters $\mathbf{R}$, cf. Eq. (2.5). There are two ways to generate closed paths in momentum space:[101] either by introducing a magnetic field that enforces cyclotron motion on a closed loops, or by introducing an electrical field that enforces linear motion in momentum space, sweeping through the whole Brillouin zone and eventually returning to the initial momentum.

For one-dimensional systems, Zak made the connection between the band center q_n of the nth band and the Berry phase that sweeps through the Brillouin zone, the Zak phase. The band center is defined as

$$q_n \equiv \int dx\, x|W_n(x)|^2 \tag{2.17}$$

with the Wannier functions[102]

$$W_n(x - ma) \equiv W_{n,m}(x) = \frac{1}{\sqrt{N}}\sum_{k\in\mathrm{BZ}} u_{n,k}(x)e^{ik(x-ma)} \tag{2.18}$$

that are exponentially localized around a position in the m-th unit cell for one-dimensional systems.[103–105] Eq. (2.16) can be rewritten in terms of the Wannier functions $W_n(x)$, giving[100]

$$\gamma_n = \frac{2\pi}{a} \int dx x |W_n(x)|^2 = \frac{2\pi}{a} q_n. \tag{2.19}$$

with the lattice constant a. This relationship was endowed with a physical meaning by further connecting this integral to the electronic part of the polarization by Vanderbilt and King-Smith, resolving a longstanding ambiguity in the definition of the polarization.[93;94;106;107]

Since then, Berry-phase effects on solids have been extensively studied to gain insights into a huge variety of electronic phenomena.[101] The Zak phase is an example of a one-dimensional topological invariant.[108;109] Its higher-dimensional analogues give rise to more topological invariants, most notably, the first Chern number.[6]

In fact, it is not Zak phase itself but the difference of the Zak phase between two topologically distinct sectors that gives a topological invariant. In one-dimensional systems, the Zak phase can be changed by a different choice of the bulk unit cell, while differences between two sectors stay invariant.[110–112] This property is discussed in more detail in Sec. 2.4, where we split the Zak phase into two parts and provide an interpretation of the two parts for tight-binding systems.[113]

2.2 Tenfold Classification of Topological Insulators and Superconductors

A physical system is characterized by a set of symmetries. Unitary symmetries, such as invariance under translation, reflection, and rotation, are represented by unitary matrices that commute with the Hamiltonian H. If the Hamiltonian is invariant under a group of symmetries G, the vector space $\mathcal{V}$ spanned by the single-particle states decomposes into a direct sum of vector spaces $\mathcal{V}_\lambda$ associated with certain irreducible representation of G. Thus, the Hamiltonian obtains a block-diagonal form with blocks $H^{(\lambda)}$ defined by the irreducible representation λ. Antiunitary symmetries, such as time-reversal symmetry, however, do not allow for the decomposition of $\mathcal{V}$ into a direct sum of vector spaces, giving a different classification scheme.

Time-reversal symmetry is represented by an antiunitary operator that commutes with the Hamiltonian. An antiunitary operator is a combination of a unitary operator and complex conjugation $\mathcal{K}$, i.e., time-reversal symmetry is represented by

$$T = U_T \mathcal{K}, \ [T, H] = 0 \tag{2.20}$$

with $U_T^\dagger U_T = 1$. The product $T^2 = U_T U_T^* = \pm 1$ classifies two distinct realizations of time-reversal symmetry.[†] Particle-hole symmetry is represented by an antiunitary operator that anticommutes with the Hamiltonian,

$$C = U_C \mathcal{K}, \ \{C, H\} = 0 \tag{2.21}$$

with $U_C^\dagger U_C = 1$ and $C^2 = U_C U_C^* = \pm 1$. Since there exist three distinct choices for time-reversal and particle-hole symmetry (absence of the symmetry, and presence with

---

[†] Applying T twice on the Hamiltonian gives $(U_T U_T^*) H (U_T U_T^*)^\dagger = H$ with the unitary matrix $U_T U_T^*$. According to Schur's lemma, $U_T U_T^* = e^{i\phi}$ since H runs over an irreducible representation space.[114] Together with $U_T^\dagger U_T = 1$, this gives $U_T U_T^* = \pm 1$. For particle-hole symmetry, the argument is analogue.

	A	AIII	AI	BDI	D	DIII	AII	CII	C	CI
T	0	0	$+1$	$+1$	0	-1	-1	-1	0	$+1$
C	0	0	0	$+1$	$+1$	$+1$	0	-1	-1	-1
S	0	1	0	1	0	1	0	1	0	0

TABLE 2.1: Tenfold symmetry classification of noninteracting Hamiltonians based on time-reversal T, particle-hole C, and chiral symmetry $S = TC$. The upper row denotes the Cartan label of the symmetry class that is characterized by the presence (denoted by ±1 and 1) or absence (denoted by 0) of the three symmetries. In presence of time-reversal or particle-hole symmetry, the label denotes the square of the operators $T^2 = \pm 1$, $C^2 = \pm 1$.[19;83]

$U_{T,C}U^*_{T,C} = \pm 1$), there are nine different possibilities for the behavior of a Hamiltonian under these symmetries. To complete this classification, another symmetry is necessary: in presence of both time-reversal and particle-hole symmetry, their product $S = TC$ is automatically present; whenever one of T or C is broken, S is broken as well. However, if both T and C are broken, their combination may still be present. This introduces the tenth possibility, the presence of chiral symmetry S in absence of both T and C. As T and C are both represented by antiunitary operators that commute or anticommute with H, $S = U_T U^*_C$ is necessarily a unitary operator that anticommutes with the Hamiltonian, $\{S, H\} = 0$. The ten different possibilities are given in Tab. 2.1, together with their so-called Cartan labels.[83]

What properties follow from these symmetries? To identify topologically inequivalent insulators, we need to classify the homotopically inequivalent maps $\mathbf{k} \to H(\mathbf{k})$ from momentum space to the Hamiltonian. For now, we restrict ourselves to gapped noninteracting Hamiltonians. A gap is necessary to have a clear distinction between occupied and unoccupied states. Details of the Hamiltonian's spectrum are not of interest for such a classification, since the spectrum can be adiabatically transformed without closing the gap. Thus, instead of classifying $H(\mathbf{k})$ directly, we rather investigate the flat-band Hamiltonian $Q(\mathbf{k})$ with eigenvalues $\varepsilon_- = -1$ for all occupied states and $\varepsilon_+ = 1$ for all empty states. To contruct $Q(\mathbf{k})$, we introduce the projection onto the occupied states

$$P(\mathbf{k}) = \sum_{j \in \text{occ.}} |u_{j,\mathbf{k}}\rangle\langle u_{j,\mathbf{k}}| \tag{2.22}$$

that gives the flat-band Hamiltonian[19;53;87]

$$Q(\mathbf{k}) = \varepsilon_- P(\mathbf{k}) + \varepsilon_+ [1 - P(\mathbf{k})] = 1 - 2P(\mathbf{k}), \tag{2.23}$$

which is unitary $Q^2 = 1$, and has a dimension of $n + m$, the sum of the number of empty (m) and occupied bands (n). Its trace is the difference between the number of empty and occupied bands, $\mathrm{tr}\,[Q] = m - n$. Since occupied and unoccupied eigenstates are only defined up to a basis transformation of dimension n and m, respectively, Q has a $U(n) \times U(m)$ gauge degree of freedom. This implies that Q is in the symmetric space

$$G_{n+m,m}(\mathbb{C}) = G_{n+m,n}(\mathbb{C}) = U(n+m)/(U(n) \times U(m)) \tag{2.24}$$

with the complex Grassmanian $G_{i,j}(\mathbb{C})$. When no symmetries are imposed on Q, the Grassmanian $G_{n+m,n}(\mathbb{C})$ is the classifying space of Q. Then, the group g of inequivalent maps

Class	Constraint	Classifying space
A	None	$C_0 = U(n+m)/(U(n) \times U(m))$
AIII	None	$C_1 = U(n)$
AI	$Q^T(\mathbf{k}) = Q(-\mathbf{k})$	$R_0 = O(n+m)/(O(n) \times O(m))$
BDI	$q^*(\mathbf{k}) = q(-\mathbf{k})$	$R_1 = O(n)$
D	$\tau_x Q^T(\mathbf{k})\tau_x = -Q(-\mathbf{k}), m = n$	$R_2 = U(2n)/U(n)$
DIII	$q^T(\mathbf{k}) = -q(-\mathbf{k}), m = n$ even	$R_3 = U(2n)/Sp(2n)$
AII	$\sigma_y Q^T(\mathbf{k})\sigma_y = Q(-\mathbf{k}), m, n$ even	$R_4 = Sp(n+m)/(Sp(n) \times Sp(m)$
CII	$\sigma_y q^*(\mathbf{k})\sigma_y = q(-\mathbf{k}), m = n$ even	$R_5 = Sp(n)$
C	$\tau_y Q^T(\mathbf{k})\tau_y = -Q(-\mathbf{k}), m = n$	$R_6 = Sp(2n)/U(n)$
CI	$q^T(\mathbf{k}) = q(-\mathbf{k}), m = n$	$R_7 = U(n)/O(n)$

Table 2.2: Constraints on the matrices Q (in absence of chiral symmetry) and q (in presence of chiral symmetry) imposed by antiunitary symmetries for all Altland-Zirnbauer classes.[20;83;87] Without loss of generality, time-reversal symmetry is represented by $T = \mathcal{K}$ for $T^2 = +1$ and $T = \sigma_y\mathcal{K}$ for $T^2 = -1$. Similarly, particle-hole symmetry is represented by $C = \tau_x\mathcal{K}$ for $C^2 = +1$ and by $C = \tau_y\mathcal{K}$ for $C^2 = -1$. The symmetry classes are separated into two groups, complex classes (A,AII) and real classes (all other classes), depending on the presence of a reality condition, i.e., time-reversal or particle-hole symmetry. Due to the conditions imposed on q and Q, the space of q and Q is restricted to the classifying spaces C_q and R_q shown in the third column. In a d-dimensional system, the group of inequivalent maps from momentum space to q and Q is given by the d-th homotopy group $\pi_d(C_q)$ for complex classes and $\pi_d(R_q)$ for real classes. These are given in Tab. 2.3

$\mathbf{k} \to Q(\mathbf{k})$ from d-dimensional momentum space $\bar{S}^d$ (a d-dimensional sphere S^d with the involution $\mathbf{k} \to -\mathbf{k}$[20;87]) to the flat-band Hamiltonian is the d-th homotopy group π_d

$$g = \pi_d(G_{n+m,m}(\mathbb{C})). \tag{2.25}$$

Note that we use the momentum space $\bar{S}^d$, a sphere rather than a torus $\bar{T}^d$ that constitutes the d-dimensional Brillouin zone of a crystal. As briefly discussed in Sec. 2.3, the classification of a torus offers a richer classification than a sphere, giving rise to topological phenomena that just exist on a lattice, but not in continuum models.

Eq. (2.25) is the first example of a topological classification of a gapped system that we encounter in this thesis; in particular, it gives the classification of a gapped system without any further symmetries. While the computation of $\pi_d(V)$ is generally a complicated task, we can make use of an existing mathematical framework, K-theory, that allows to obtain all relevant d-th homotopy groups that are used in this work.[‡] For example, $\pi_{2j}(G_{n+m,m}(\mathbb{C})) = \mathbb{Z}$ and $\pi_{2j+1}(G_{n+m,m}(\mathbb{C})) = 0$ with $j = 0, 1, \ldots$. Thus, for a system without any antiunitary symmetries, in $d = 2j$ dimensions, different topological sectors are characterized by an integer invariant; in $d = 2j + 1$ dimensions, however, just one (trivial) sector exists.

[‡] In fact, it does not require K-theory to compute $\pi_d(G_{n+m,n}(\mathbb{C}))$—however, K-theory is handy to compute more homotopy groups and to relate the d-th group with homotopy groups in other dimensions.[20]

Symmetries restrict the classifying space. In presence of chiral symmetry, the Hamiltonian obeys $SHS^{-1} = -H$ and Q can be brought to the off-diagonal form[19]

$$Q = \begin{pmatrix} & q \\ q^\dagger & \end{pmatrix} \tag{2.26}$$

with $q^\dagger q = 1$. There are no further restrictions on q, i.e., the target space is $U(n)$. In even dimensions d, the $d = 2j$-th homotopy group of $U(n)$ is $\pi_{2j}(U(n)) = 0$, and in odd dimensions, the $d = (2j+1)$-th group $\pi_{2j+1}(U(n)) = \mathbb{Z}$, provided $n \geq (d+1)/2$.[87]

Similarly, time-reversal symmetry and particle-hole symmetry restrict the group of Q (in absence of chiral symmetry) and q (in presence of chiral symmetry) further. Without going into details, we present the restrictions on Q and q in Tab. 2.2 for a certain basis choice of the operators T and C. These restrictions shrink the group of Q and q to a subgroup, the classifying space[20] that is given in the third column of Tab. 2.2.

More general than Eq. (2.25), we denote the group of inequivalent maps from Λ to the classifying spaces C_q, R_q by the restricted real and complex K-groups

$$\tilde{K}_{\mathbb{R}}^{-q}(\Lambda) = \pi(\Lambda, R_q), \qquad \tilde{K}_{\mathbb{C}}^{-q}(\Lambda) = \pi(\Lambda, C_q), \tag{2.27}$$

which simplifies to the homotopy group $\pi_d(R_q)$, $\pi_d(C_q)$ for $\Lambda = \bar{S}^d$. The notion of a restricted K-group originates from K-theory; without touching the subject of K-theory in this thesis, we just borrow its notation and main results: the determination of the group of inequivalent maps from Λ to R_q, as already discussed above for $\Lambda = \bar{S}^d$ and C_0, C_1. The use of the restricted K-group is necessary to fix the spectrum at $k = \infty$, in contrast to the absolute K-group $K_{\mathbb{R}/\mathbb{C}}^{-q}(\Lambda)$ that is used in crystal system where momentum space is defined on a torus.[20]

Two insights from K-theory are important in particular: first, the classification has a periodicity, the Bott periodicity, with

$$\tilde{K}_k^{-q-p_k}(\Lambda) = \tilde{K}_k^{-q}(\Lambda), \;\; k = \mathbb{R}, \mathbb{C} \tag{2.28}$$

and $p_{\mathbb{C}} = 2$, $p_{\mathbb{R}} = 8$. Second, the map from the d-dimensional momentum-space sphere can be simplified to a map from a point,

$$\tilde{K}_{\mathbb{R}}^{-q}(\bar{S}^d) = \pi_d(R_q) = \pi_0(R_{q-d}). \tag{2.29}$$

These two insights are visible in Tab. 2.3, where the group of inequivalent maps, i.e., the classification of the different topological sectors of the quantum ground state, is shown for all ten symmetry classes. For the complex symmetry classes, the results for $\pi_{2j}(C_q)$ and $\pi_{2j+1}(C_q)$ that respect the Bott periodicity with $p_{\mathbb{C}} = 2$ are shown in the first two rows of Tab. 2.2. We do not discuss the detailed results for the real symmetry classes and $\pi_d(R_q)$, but point out that the Bott periodicity is reflected in the fact that only dimensions $d = 0, \ldots, 7$ are shown. For higher-dimensional systems, the classification is given by $d \mod 8$. Eq. (2.29) is reflected in the repetition of the pattern for different classifying spaces R_q.

A large number of systems is known whose properties are captured by an topological invariant, filling the different entries in Tab. 2.3 with life. Certainly, one of the most famous examples of a topological phenomenon is the quantum Hall effect that occurs in a two-dimensional system where time-reversal symmetry is explicitly broken by a magnetic field (class A), allowing for a $\mathbb{Z}$ classification in $d = 2$ dimensions. The topological index $\nu \in \mathbb{Z}$

Class	T	C	S	$d=0$	$d=1$	$d=2$	$d=3$	$d=4$	$d=5$	$d=6$	$d=7$
A	0	0	0	$\mathbb{Z}$	0	$\mathbb{Z}$	0	$\mathbb{Z}$	0	$\mathbb{Z}$	0
AIII	0	0	1	0	$\mathbb{Z}$	0	$\mathbb{Z}$	0	$\mathbb{Z}$	0	$\mathbb{Z}$
AI	$+1$	0	0	$\mathbb{Z}$	0	0	0	$2\mathbb{Z}$	0	$\mathbb{Z}_2$	$\mathbb{Z}_2$
BDI	$+1$	$+1$	1	$\mathbb{Z}_2$	$\mathbb{Z}$	0	0	0	$2\mathbb{Z}$	0	$\mathbb{Z}_2$
D	0	$+1$	0	$\mathbb{Z}_2$	$\mathbb{Z}_2$	$\mathbb{Z}$	0	0	0	$2\mathbb{Z}$	0
DIII	-1	$+1$	1	0	$\mathbb{Z}_2$	$\mathbb{Z}_2$	$\mathbb{Z}$	0	0	0	$2\mathbb{Z}$
AII	-1	0	0	$2\mathbb{Z}$	0	$\mathbb{Z}_2$	$\mathbb{Z}_2$	$\mathbb{Z}$	0	0	0
CII	-1	-1	1	0	$2\mathbb{Z}$	0	$\mathbb{Z}_2$	$\mathbb{Z}_2$	$\mathbb{Z}$	0	0
C	0	-1	0	0	0	$2\mathbb{Z}$	0	$\mathbb{Z}_2$	$\mathbb{Z}_2$	$\mathbb{Z}$	0
CI	$+1$	-1	0	0	0	0	$2\mathbb{Z}$	0	$\mathbb{Z}_2$	$\mathbb{Z}_2$	$\mathbb{Z}$

TABLE 2.3: Periodic table of topological insulators and superconductors. The left columns denote the Cartan label and the presence or absence of time-reversal (T), particle-hole (C), and chiral symmetry (S), cf. Tab. 2.1. Depending on the dimension d of the gapped fermionic Hamiltonian that is characterized, the space of quantum ground states is partitioned into different topological sectors labeled by an integer or a $\mathbb{Z}_2$ invariant; the label 0 indicates that just one (trivial) sector exists and $2\mathbb{Z}$ denotes that an even-integer invariant exists.

is the first Chern number that gives the quantized Hall conductance, $\sigma_{xy} = \nu e^2/h$. Other examples include $\mathbb{Z}_2$ topological insulators in $d = 2$ and $d = 3$ (symmetry class AII), one-dimensional p-wave superconductors with Majorana end states (class D, $\mathbb{Z}_2$ classification), and many more.

Since this classification exclusively refers to gapped systems, some modifications are necessary such that it can be applied to gapless systems. Before turning in that direction, we quickly discuss a richer classification that is possible in a crystal, where momentum space is defined on a torus.

2.3 Topological Semimetals

While continuous free-fermion Hamiltonians that fulfill a reality condition are classified by $\tilde{K}_{\mathbb{R}}^{-q}(\bar{S}^d) = \pi_0(R_{q-d})$, the momentum space in a crystal is actually a torus $\bar{T}^d$, hence the classification is given by[20][§]

$$K_{\mathbb{R}}^{-q}(\bar{T}^d) \cong \pi_0(R_{q-d}) \oplus \tilde{K}_{\mathbb{R}}^{d-q}(T^d), \tag{2.30}$$

i.e., it includes the result for continuous Hamiltonian $\pi_0(R_{q-d})$ as a direct summand. The other term, $\tilde{K}_{\mathbb{R}}^{d-q}(T^d)$, gives rise to another set of topological invariants, *weak topological indices.*[15;16;115] The most prominent example where weak topological indices are important is a three-dimensional topological insulator in symmetry class AII with time-reversal symmetry $T^2 = -1$, i.e., $d = 3$ and $q = 4$. While the classification of a continuum model with momentum space defined on a sphere gives a $\pi_0(R_{4-3}) \cong \mathbb{Z}_2$-invariant, considering a

---

[§] For a torus, we do not have to take special care of the point at $k \to \infty$, the reason why the classification on a sphere is given by the restricted K-group rather than $K_{\mathbb{R}}^{-q}(\bar{S}^d)$.

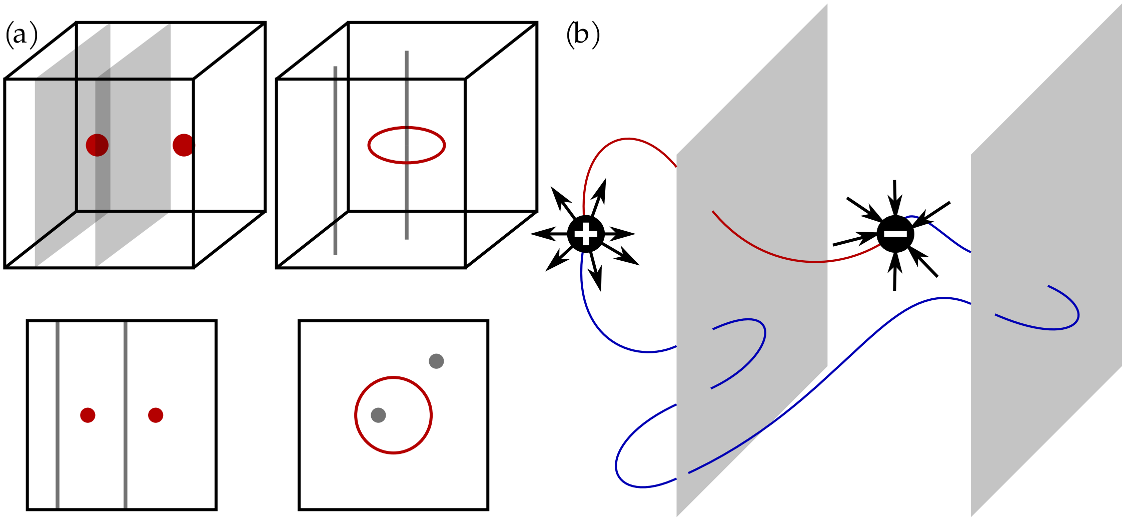

FIGURE 2.1: (a) The classification of d_{FS}-dimensional Fermi surfaces embedded in d-dimensional systems ("ambient space") is possible by classifying $p-1$-dimensional hyperplanes,[32;116] with the codimension of the Fermi surface $p = d - d_{\mathrm{FS}}$. Here, the red points and lines show the Fermi surfaces in two- and three-dimensional systems, respectively. Topological invariants are defined on the gray planes, lines, and points, with the Fermi surface being topologically protected if the invariants differ for hyperplanes separated by a gap closing. (b) The Fermi arcs of a Weyl semimetal can be seen as a manifestation of a Dirac string created by the monopoles of the Berry flux. Since the Dirac string is not gauge-invariant, different paths are possible (red and blue). When a plane in momentum space is crossed an odd number of times, surface states emerge at these planes in momentum space.

crystal with momentum space on a torus gives rise to another set of invariants,

$$\tilde{K}_{\mathbb{R}}^{-1}(T^3) \cong \mathbb{Z} \oplus 3\mathbb{Z}_2. \tag{2.31}$$

The number $\mathbb{Z}$ counts the number of Kramers-degenerate valence bands, and $3\mathbb{Z}_2$ gives three additional weak topological invariants. The strong $\mathbb{Z}_2$ invariant and the three weak invariants are commonly noted as a pair $(\nu_0; \nu_1\nu_2\nu_3)$. The weak topological invariants are computed by considering mirror-invariant planes and by calculating the topological index of these two-dimensional planes.

This approach can be used to classify topological semimetals: although the full system is gapless, lower-dimensional planes, lines or points in momentum space remain gapped, cf. Fig. 2.1 (a). The topological index of these lower-dimensional manifolds can only change when the gap in the band structure closes, i.e., at certain points or lines in the Brillouin zone. We call gapless phases *topological* when different topological indices are realized in the gapped planes of the same material. This implies that the gap closing points are protected: without breaking the symmetry necessary for the topology of the lower-dimensional planes, there needs to be a gap closing in between them. The only way to open a gap is by annihilating gap closings with each other, i.e., by shrinking the momentum space region realizing a certain lower-dimensional phase to zero. For example, the nodal points in Fig. 2.1 (a) can be annihilated by merging them with each other.

2.3.1 Weyl Semimetals

Among the first experimentally realized[36–39] topological semimetals are Weyl semimetals, materials that host Weyl nodes close to their Fermi level.[35] Weyl nodes are band crossings in three-dimensional system that do not require the presence of any symmetries.[¶] Generic band crossings of two bands at the momentum $\mathbf{b}$ can be expanded for small momenta $\mathbf{k}-\mathbf{b}$ around the crossing, giving the Hamiltonian

$$\mathcal{H} = \varepsilon_0(k) + \sum_{ij}(k_i - b_i)A_{ij}\sigma_j + \sum_{ijk}(k_i - b_i)(k_j - b_j)B_{ijk}\sigma_k + \mathcal{O}((\mathbf{k}-\mathbf{b})^3) \tag{2.32}$$

with the zero-point energy $\varepsilon_0(k)$, the Pauli matrices σ_μ, and generic tensors A_{ij}, B_{ijk}. When $\det A \neq 0$, the lowest-order contribution is linear in momentum and we can neglect the quadratic terms. The linear-order terms generally comes with anisotropic velocities v_i. Upon rescaling of momenta $k_i - b_i \to k_i/(\hbar v_i)$ and subtracting the constant energy ε_0, the linearized Hamiltonian reads

$$\mathcal{H}^{(\chi)}_{\mathbf{k}} = \chi \mathbf{k}\cdot\boldsymbol{\sigma}, \tag{2.33}$$

a Weyl Hamiltonian of chirality $\chi = \operatorname{sgn}(\det A)$. The term “Weyl fermion” used for the low-energy degrees of freedom close to such a band crossing originates from high-energy field theory; a massless Dirac fermion can be split up into two Weyl fermions with chirality χ, $\psi_\chi = \left(1 + \chi\gamma^5\right)\psi$ where γ^5 is the chiral matrix that distinguishes the two chiralities.[117]

As shown by Nielsen and Ninomiya in a series of seminal papers,[118–120] noninteracting Weyl nodes realized on a lattice need to come in pairs of left-handed ($\chi = -1$) and right-handed ($\chi = +1$) chirality. Any condensed-matter realization of noninteracting Weyl fermions thus requires an even number of Weyl nodes. While we focus on the symmetry and topology of these Weyl nodes in the following, a field-theory perspective is provided in Sec. 3.2, introducing the chiral anomaly, the nonconservation of chiral charge.

Weyl nodes require the absence of certain symmetries on a lattice. In presence of inversion symmetry, a Weyl node of chirality χ at momentum $\mathbf{b}$ requires another Weyl node of opposite chirality $-\chi$ at $-\mathbf{b}$, since

$$\left.\mathcal{H}^{(\chi)}_{\mathbf{k}-\mathbf{b}}\right|_{\mathbf{k}\to-\mathbf{k}} = -\chi\,(\mathbf{k}+\mathbf{b})\cdot\boldsymbol{\sigma} = \mathcal{H}^{(-\chi)}_{\mathbf{k}+\mathbf{b}}. \tag{2.34}$$

In presence of time-reversal symmetry represented by $T = \sigma_y\mathcal{K}$, however, a Weyl node of chirality χ at $\mathbf{b}$ requires another Weyl node of the same chirality χ at $-\mathbf{b}$, since

$$\sigma_y \left.\left(\mathcal{H}^{(\chi)}_{\mathbf{k}-\mathbf{b}}\right)^*\right|_{\mathbf{k}\to-\mathbf{k}} \sigma_y = \chi\,(\mathbf{k}+\mathbf{b})\cdot\boldsymbol{\sigma} = \mathcal{H}^{(\chi)}_{\mathbf{k}+\mathbf{b}}. \tag{2.35}$$

This implies that, in presence of both symmetries, at least four Weyl nodes at the same energy are present in the system: two Weyl nodes of opposite chiralities at $\mathbf{b}$ and two Weyl nodes at $-\mathbf{b}$. If no additional symmetry protects them from mixing, they will annihilate, leading to a gapped system. If an additional symmetry, e.g., C_4 rotational symmetry,[121] prevents those Weyl nodes from annihilating, a fourfold degenerate band crossing will be present; this is commonly referred to as a Dirac node, since a three-dimensional 4×4 massless Dirac Hamiltonian constitutes the low-energy physics of this band crossing.

The term “Weyl node” exclusively refers to zero-dimensional crossings of two bands in three-dimensional system with a linear dispersion. Zero-dimensional crossings in two-dimensional systems, e.g., in graphene, are called Dirac nodes: in fact, they realize a massless Dirac Hamiltonian in $2+1$ dimensions that requires a 2×2 basis. The low-energy behavior of graphene is not discussed in this thesis. A comprehensive review of the electronic structure of graphene is given, e.g., in Ref. 12.

[¶] In fact, as shown later, Weyl nodes require the *absence* of certain symmetries.

Weyl nodes are monopoles of Berry curvature in momentum space. The eigenfunctions of the Weyl Hamiltonian (2.33) with eigenvalues $\varepsilon_\pm = \pm\chi k$ carry a Berry curvature $\Omega_\pm = \mp\chi/(2k^2)\hat{k}$ with $\hat{k}$ the unit vector in the radial direction, analogue to the magnetic field of a magnetic monopole. Integrating the Berry curvature of the occupied band (with energy $\varepsilon = -k$) over a surface enclosing the Weyl node gives the quantized Berry flux

$$\Phi^B_\chi = \oint_{\partial V} d\mathbf{S} \cdot \Omega_{-\chi} = 2\pi\chi, \tag{2.36}$$

with a topological $\mathbb{Z}$ invariant[32] $\nu = \Phi^B_\chi/(2\pi)$. While realizations with $\nu = \pm 1$ come without symmetry restrictions, higher-order Weyl nodes with $|\nu| > 1$ require additional point group symmetries.[122]

In analogy to magnetic monopoles, a Dirac string necessarily emanates from the monopoles of Berry flux, thereby connecting a pair of Weyl nodes of opposite chirality.[123] A Dirac string is a one-dimensional curve in space whose path is gauge-dependent, but whose presence is not. For isolated monopoles, it goes to infinity; when two monopoles of opposite charge are present, the Dirac string connects those monopoles. In a Weyl semimetal, this string crosses planes in momentum space an even or an odd number of times, cf. Fig. 2.1 (b). For an odd number of crossings, a surface state is required at this plane. This implies that the surface state exists for a limited range of momenta. The separator between occupied and unoccupied states forms an arc—the Fermi arc.

Another way to understand surface states is by performing a topological classification of lower-dimensional planes in momentum space. To enrich the discussion by considering a concrete example, we introduce the time-reversal symmetry breaking Hamiltonian that is realized on a cubic lattice[124]

$$\mathcal{H}(\mathbf{k}) = v\,(\sin k_x\sigma_x + \sin k_y\sigma_y) + M_\mathbf{k}\sigma_z, \tag{2.37}$$

where $M_\mathbf{k} = t(2 - \cos k_x - \cos k_y) + v(\cos k_z - m)$ and the lattice constant is set to $a = 1$. For certain values of m, e.g., $-1 < m < 5$ at $v = t$, the model describes a Weyl semimetal[125] with the Weyl nodes separated along z with the separation controlled by m. For simplicity, we first discuss $m = 0$ before coming back to more general cases in the course of this work. The two-dimensional system parametrized by k_z is a simple lattice model for a Chern insulator:[126] a two-dimensional lattice realization of gapped system that breaks time-reversal symmetry and allows for a topological $\mathbb{Z}$ classification.[7]

Using the previously introduced techniques, we can compute the topological invariant assigned to the Chern insulator as a function of k_z. Writing the Hamiltonian as $\mathcal{H}(\mathbf{k}) = \boldsymbol{\sigma}\cdot\mathbf{d}(\mathbf{k})$, we recognize its similarity to a Weyl Hamiltonian (2.33) where we replaced $\chi\mathbf{k}$ by the more general vector $\mathbf{d}(\mathbf{k})$. The topological $\mathbb{Z}$ invariant is now simply given by the integral of over the Berry curvature of the occupied band[6] with energy $\varepsilon_- = -d$ that we denote by $|u_-\rangle$

$$\nu = \int_{\mathrm{BZ}} \frac{d\mathbf{S}_k}{2\pi} \cdot (\nabla_\mathbf{k} \times \langle u_-|\nabla_\mathbf{k}|u_-\rangle) = \int_{\mathrm{BZ}} \frac{dk_x dk_y}{2\pi} \left(\langle\partial_{k_x}u_-|\partial_{k_y}u_-\rangle - \langle\partial_{k_y}u_-|\partial_{k_x}u_-\rangle\right). \tag{2.38}$$

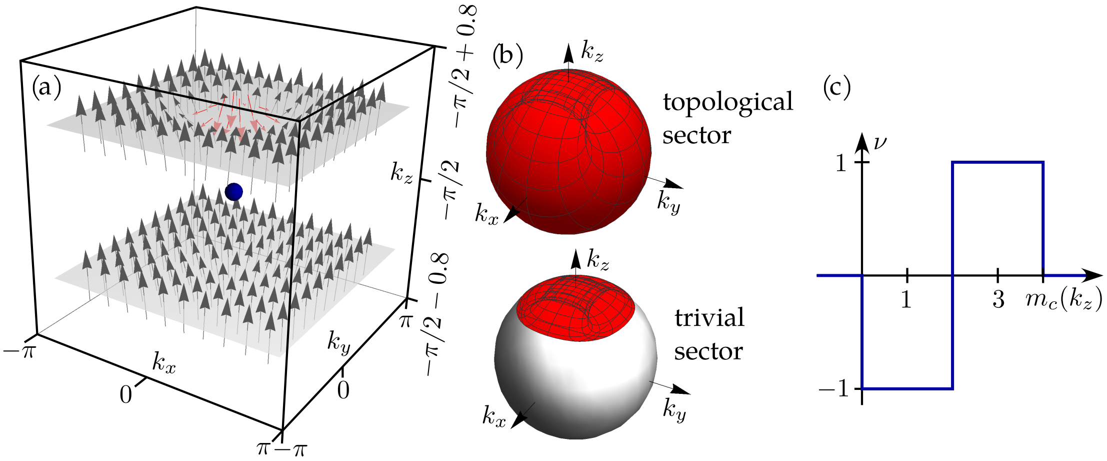

FIGURE 2.2: (a) Configuration of $\hat{d}(\mathbf{k})$ in the two-dimensional Brillouin zone defined by k_x, k_y for two different values of k_z for the Hamiltonian (2.37) with $v = t$ and $m = 0$. The Weyl points are located at $\mathbf{b} = (0, 0, \pm\pi/2)$ (blue sphere), i.e., the system is gapped in planes defined by constant $k_z \neq \pm\pi/2$. For $|k_z| < \pi/2$, $\hat{d}$ has a topologically nontrivial Skyrmion configuration, for $|k_z| > \pi/2$, the configuration is trivial. (b) For a nontrivial Skyrmion configuration, $\hat{d}$ covers the whole Bloch sphere when integrating over the Brillouin zone. For a trivial configuration, only parts of the upper semisphere are covered. (c) First Chern number ν as a function of the Chern mass $m_c(k_z) = \cos k_z - m$. Eq. (2.37) is a Weyl semimetal when different Chern numbers ν are obtained for different k_z.

We rewrite derivatives in terms of $\mathbf{d}(\mathbf{k})$, $\partial_{k_i} = (\partial_{k_i} d_j)\partial_{d_j}$ (summation over repeating indices is implied) to obtain a simpler form of the invariant

$$\nu = \int_{\mathrm{BZ}} \frac{dk_x dk_y}{2\pi} (\partial_{k_x} d_i)(\partial_{k_y} d_j) \underbrace{\left(\langle \partial_{d_i} u_- | \partial_{d_j} u_- \rangle - \langle \partial_{d_j} u_- | \partial_{d_i} u_- \rangle\right)}_{=F^{\mathbf{d}}_{ij}} \tag{2.39}$$

with the general form of the Berry curvature $F^{\mathbf{d}}_{ij} = \Omega^{\mathbf{d}}_k \epsilon^{kij}$. From the previous discussion of the Weyl Hamiltonian (2.33) we know that $\Omega^{\mathbf{d}} = 1/(2d^2)\hat{d}$ with $\hat{d} = \mathbf{d}/d$ being the unit vector pointing in the direction of $\mathbf{d}$. This gives the general form of the invariant for two-dimensional systems on a lattice, the first Chern number[126]

$$\nu = \frac{1}{4\pi} \int dk_x dk_y \, \hat{d} \cdot \left(\partial_x \hat{d} \times \partial_y \hat{d} \right). \tag{2.40}$$

In Fig. 2.2 (a), we show the configuration of $\hat{d}$ over the two-dimensional Brillouin zone for two different values of $k_z = -\pi/2 \pm 0.8$. In the topologically nontrivial sector, the vector $\hat{d}$ has a Skyrmion configuration: it covers the whole Bloch sphere as a function of k_x and k_y (Fig. 2.2 (b)) while only parts of the upper semisphere are covered for the topologically trivial sector. The resulting Chern number ν is shown in Fig. 2.2 (c) as a function of the momentum-dependent Chern mass term $m_c(k_z) = \cos k_z - m$.

Certainly, not all materials with Weyl nodes in their band structure are Weyl semimetals; in fact, many metallic materials such as iron have Weyl nodes at higher energies.[127] In principle, the term semimetal exclusively refers to materials where the density of states is

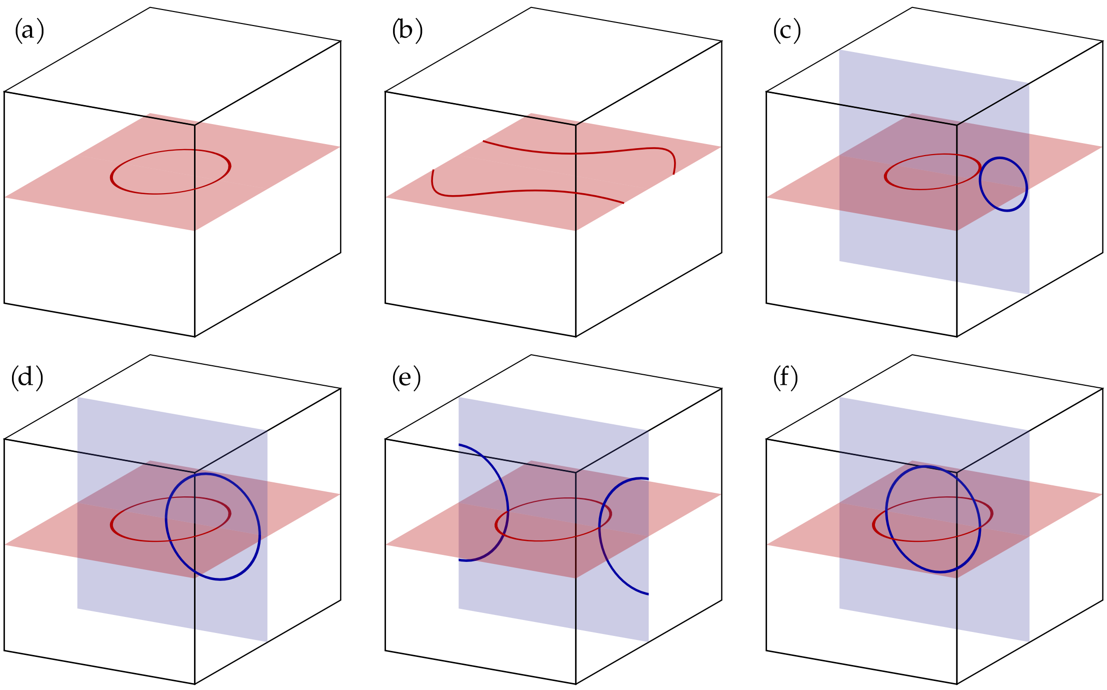

Figure 2.3: Nodal lines in a three-dimensional Brillouin zone. (a) A ring-shaped nodal line, described by the low-energy Hamiltonian (2.41), is often fixed to a certain plane in momentum space by symmetries, such as mirror symmetry or a nonsymmorphic symmetry. (b) On a lattice, the ring can be distorted such that it opens to two nodal lines that pierce through the whole Brillouin zone. (c) Additional symmetries may allow nodal lines restricted to other planes in momentum space. (d) When these nodal line pass through each other, a topologically nontrivial structure forms, a so-called Hopf link.[128] When two nodal lines touch at a point, they form a chain. Two distinct realizations are possible on a lattice, an outer chain (e) or an inner chain (f).

zero directly at the Fermi level,[‖] but increases immediately as soon as the energy is varied, i.e., the Fermi level is directly at the gap closing point. Here, we use less strict definition and refer to materials as Weyl semimetals when the Fermi level is in the vicinity of the gap closing point, such that the low-energy behavior is dominated by the Weyl Hamiltonian. The same applies for other topological semimetals that are discussed in this work.

In the course of this work, we encounter several other lattice models of Weyl semimetals, including models that preserve time-reversal symmetry (such that a different invariant needs to be found) and a four-band Hamiltonian that has an analogue in field theory. The continuum version of the aforementioned four-band Hamiltonian is discussed in the following section, together with other terms that perturb the Hamiltonian and generate more, interesting gap closings.

2.3.2 Nodal Line Semimetals

Another example of gapless topological phases is a nodal line semimetal, with a one-dimensional Fermi surface embodied in a three-dimensional system. In lattice systems,

---

[‖] No commonly accepted definition of a semimetals exists, e.g., materials with equal number of electrons and holes are sometimes called semimetals. To avoid confusion, we use the definition above.

these nodal lines may occur in various momentum-space shapes, e.g., rings, or lines that pierce through the full Brillouin zone, cf. Fig. 2.3. In this work, we exclusively discuss ring-shaped nodal lines, leaving the properties of more exotic shapes for future studies.

In contrast to Weyl nodes, nodal lines require additional symmetries that prevent them from gapping out. This can be understood by investigating the properties of the low-energy Hamiltonian[33]

$$\mathcal{H}_{\mathbf{k}} = \mathbf{k}\cdot\boldsymbol{\sigma}\tau_z + m\tau_x + b_0\tau_z + \mathbf{b}\cdot\boldsymbol{\sigma} + \mathbf{b}'\cdot\boldsymbol{\sigma}\tau_x + \mathbf{p}\cdot\boldsymbol{\sigma}\tau_y \tag{2.41}$$

with the four-vector $b_\mu = (b_0, \mathbf{b})$ and the three-dimensional vectors $\mathbf{b}'$ and $\mathbf{p}$. Both vectors $\mathbf{b}$ and $\mathbf{b}'$ break time-reversal symmetry $T = \sigma_y\mathcal{K}$. The terms b_0 and $\mathbf{p}$ break inversion symmetry given by $\tau_x\mathcal{H}_{-\mathbf{k}}\tau_x = \mathcal{H}_{\mathbf{k}}$. A physical realization of this low-energy Hamiltonian is presented in Sec. 5.

The four-vector b_μ effectively acts as a Weyl node separation in energy and momentum space. We encounter a deeper connection between the effective action of Weyl fermions and the Hamiltonian (2.41) in Sec. 3.3. For a nodal line described by Eq. (2.41), the term b_μ is just relevant in terms of stability.

For $b_\mu = \mathbf{p} = m = 0$, the vector $\mathbf{b}'$ creates a nodal line with radius b' in a plane orthogonal to $\mathbf{b}'$. The radius shrinks to $\sqrt{b'^2 - m^2}$ for $m \neq 0$, but remains stable until it eventually gaps out at $m = b'$. When further introducing a term $\mathbf{b}||\mathbf{b}'$, the nodal line band crossing remains stable, but moves to different energies.[**] Also, the nodal line is stable towards terms $\mathbf{p} \perp \mathbf{b}'$, although $\mathbf{p}$ shifts it to nonzero energies.

The stability is due to the presence of mirror symmetry. Since Eq. (2.41) is isotropic for $\mathbf{b}' = \mathbf{b} = \mathbf{p} = 0$, we can choose without loss of generality $\mathbf{b}' = b'\hat{z}$ and gradually introduce more terms to the Hamiltonian. Then, Eq. (2.41) is mirror-symmetric with respect to the z-plane, especially

$$\sigma_z\tau_x\,\mathcal{H}_{\mathbf{k}}|_{k_z\to -k_z}\,\sigma_z\tau_x = \mathcal{H}_{\mathbf{k}}. \tag{2.42}$$

Terms $\mathbf{p} \perp \mathbf{b}'$ and $\mathbf{b} \parallel \mathbf{b}'$ preserve this symmetry, while all others break it and open up a gap in the spectrum.

Similarly, at $b_\mu = \mathbf{b}' = m = 0$, $\mathbf{p}$ introduces a nodal line of radius p in the plane orthogonal to $\mathbf{p}$. However, any nonzero mass immediately opens up a gap, since it breaks another mirror symmetry given by the operator $M_j = \sigma_j\tau_y$ (for $\mathbf{p} = p\hat{j}$).

As realized by Fang *et al.*, it is possible to calculate two different invariants for the nodal line.[129] First, integrating the Berry connection along a loop surrounding the nodal line gives the Zak phase; if this invariant equals π, symmetry-preserving terms cannot open a gap in the line. Second, the monopole charge of the line can be calculated by evaluating the integral of the Berry curvature over a sphere surrounding the nodal line, analogue to the monopole charge of a Weyl semimetal, Eq. (2.36). If the monopole charge is nonzero, the nodal line cannot be annihilated by shrinking it to zero.[129] For the model defined in Eq. 2.41 with $m = \mathbf{b} = \mathbf{p} = 0$, it can be easily seen that both invariants must be nonzero: when mirror symmetry is preserved, the nodal line remains gapless; by tuning $\mathbf{b}'$, we can only change the diameter of the nodal line to zero at $\mathbf{b}' = 0$, but not annihilate the nodal line.

[**] In other words, the Fermi surface evolves into a nodal torus, as argued by Burkov *et al.* in Ref. 33.

2.4 Bulk-boundary Correspondence from the Intercellular Zak Phase

As seen in the previous section, topological invariants of lower-dimensional systems play a relevant role in classifying weak topological insulators and gapless topological phases. An important example for such a topological invariant was introduced in Sec. 2.1.2: the Zak phase for one-dimensional systems. In the study of topological aspects of materials, the Zak phase has been utilized as a topological number to classify various genuine one-dimensional topological insulators,[108;109] as well as effective ones, such as those obtained by fixing one or two momenta of two- or three-dimensional Hamiltonians;[110–112;130–143] it was naturally extended to the concept of nonabelian Wilson loops in the multi-band case and used for classifications of topological insulators with inversion or nonsymmorphic symmetries and topological crystalline insulators.[144–149] Furthermore, the Zak phase has been widely used for the $\mathbb{Z}_2$ classification of inversion symmetric 1D systems where it is quantized to 0 or π (mod 2π).[100] In this case, the conventional bulk-boundary correspondence states that there are boundary modes if the Zak phase is nontrivial, $\gamma = \pi$, while $\gamma = 0$ is considered a trivial insulator without surface modes.[109;130–134]

Recent work, however, pointed out that the Zak phase depends on the gauge choice of choosing the origin of the real space, and how one defines boundaries of the unit cell, although it is invariant under gauge transformations of the form $u_{n,k} \rightarrow e^{i\phi_k} u_{n,k}$.[110–112] This means that the Zak phase itself is not a well-defined topological number since it cannot characterize the bulk uniquely. In an attempt to resolve this ambiguity, Atala *et al.* suggested that the difference of the Zak phase between different states could be a proper topological number,[110] and De Juan *et al.* revised the Zak phase by adding a unit-cell dependent term such that the resultant $\mathbb{Z}_2$ number plays the role of a gauge-invariant topological number.[111] In spite of these issues, the conventional bulk-boundary correspondence using the Zak phase has been successfully applied in many cases.[109;130–134] Furthermore, additional conditions for the applicability of the correspondence to finite systems have been given, such as that terminated edges should not break the inversion symmetry of the bulk[129;150] or that the finite system should be commensurate with the bulk's unit cell.[111] However, the necessity of those assumptions has not been demonstrated in general one-dimensional systems, and we in fact find that the conventional bulk-boundary correspondence using γ can fail, even in the presence of inversion symmetry both in the bulk and terminated system.[113]

In this section, following Ref. 113, we resolve these issues by providing a more detailed analysis of the Zak phase, dealing with general one-dimensional tight-binding systems. To this end, we split the Zak phase into two terms, the *intracellular* and *intercellular* Zak phase[151] (this splitting was earlier introduced by Kudin *et al.*) and provide them with their proper physical interpretations. The intracellular Zak phase γ^{intra} describes the electronic part of the classical polarization of the bulk's unit cell, and the intercellular Zak phase γ^{inter} represents the difference between the net weight of the Wannier functions in the left and right sides of the one-dimensional system with respect to a unit cell boundary, with their centers belonging to opposite sides as illustrated in Fig. 2.4 (a). We then show that, in a terminated system, this interpretation of the intercellular Zak phase leads to an accurate prediction of the extra charge accumulation (total charge including ionic contributions) in the surface regions. This is the essential new result of Ref. 113, applicable to any translationally invariant insulator, that provides a new bulk-boundary correspondence: there are $n_s = \gamma^{\text{inter}}/\pi$ (mod 2) surface modes below the Fermi level in a finite system

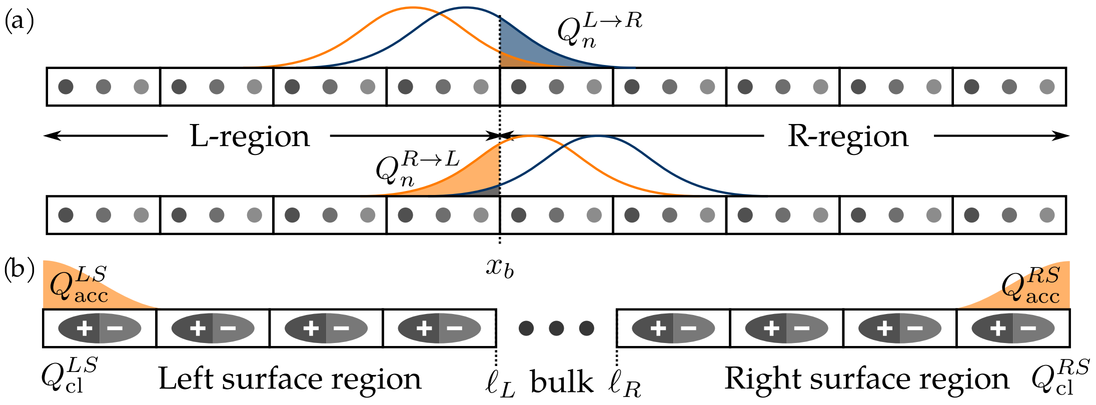

FIGURE 2.4: (a) A general one-dimensional system with an arbitrary number of atomic sites (gray circles, here: three sites) per unit cell (black boxes) is split into two regions (L and R regions) at the position x_b (dotted line). Its Wannier functions have their maximum either in the left or the right region. The charge $Q_n^{R\to L}$ represents the weight of the right sides's Wannier function that is on the left right of the system, and vice versa for $Q_n^{L\to R}$. (b) A finite one-dimensional system is split up into three regions: bulk, left, and right surfaces. Classical bound surface charges ($Q_{\rm cl}^{LS(RS)} = \mathbf{P}_{\rm cl}\cdot\hat{n}$) and extra charge accumulations ($Q_{\rm acc}^{LS(RS)}$) in two surface regions are also illustrated schematically. In each bulk unit cell, the dipole moment ($\mathbf{P}_{\rm cl}$) of the bulk unit cell is drawn symbolically.

if it is commensurate with an inversion symmetric unit cell and $\gamma^{\rm inter}$ is evaluated from this commensurate unit cell. Our new bulk-boundary correspondence resolves the above-mentioned subtle issues of the conventional bulk-boundary correspondence because $\gamma^{\rm inter}$ is independent of the choice of the real-space origin while its unit-cell dependence is included in the commensurability condition.

One example for this bulk-boundary correspondence is given in Sec. 5, where it is shown how the surface states of are nodal line semimetal are tied to the intercellular Zak phase.[152] More examples are given in Ref. 113, where the bulk-boundary correspondence is shown in more detail.

2.4.1 Intra- and Intercellular Zak Phase

Let us consider a general translationally-invariant one-dimensional system described within the tight-binding approximation. Using periodic boundary condition, the Bloch eigenfunctions satisfy $\psi_{n,k}(x+Na) = \psi_{n,k}(x)$ with the lattice constant a and the number of unit cells N. The Zak phase, following Kudin *et al.*, can be split into two terms. Using an explicit real-space basis[††] for the lattice-periodic part of the wave function, the one-dimensional

---

[††] The normalization chosen for $\psi_{n,k}(x)$ is different from Ref. 113 to be consistent with the rest of this work. We use $\int_\Omega dx\, u^*_{n,k}(x)u_{n',k'}(x) = \int_\Omega dx\, \psi^*_{n,k}(x)\psi_{n',k'}(x) = \delta_{k,k'}\delta_{n,n'}$ with the integral taken over one unit cell Ω.

Zak phase (2.16) can be written in terms of Bloch waves (2.14),

$$\begin{aligned}\gamma_n =& i\int_0^{2\pi/a} dk\langle u_{n,k}|\partial u_{n,k}\rangle = i\int_0^{2\pi/a} dk\int_\Omega dx\, u^*_{n,k}(x)\partial_k u_{n,k}(x) && (2.43)\\ =& \underbrace{i\int_0^{2\pi/a} dk\langle\psi_{n,k}|\partial_k\psi_{n,k}\rangle}_{\gamma_n^{\text{inter}}} + \underbrace{\int_\Omega dx\,(x+m_\Omega a)\int_0^{2\pi/a} dk|\psi_{n,k}(x)|^2}_{\gamma_n^{\text{intra}}} && (2.44)\end{aligned}$$

with the real-space integration going over one unit cell Ω at the position $x = m_\Omega a$. The intracellular part is just defined up to a factor of $2\pi m_\Omega$ with the integer m_Ω, as we realize from rewriting

$$\begin{aligned}\gamma_n^{\text{intra}} &= \int_\Omega dx\, x\int_0^{2\pi/a} dk|\psi_{n,k}(x)|^2 + m_\Omega a\int_0^{2\pi/a} dk\int_\Omega dx|\psi_{n,k}(x)|^2 && (2.45)\\ &= \int_\Omega dx\, x\int_0^{2\pi/a} dk|\psi_{n,k}(x)|^2 + 2\pi m_\Omega, && (2.46)\end{aligned}$$

where we used $\int_\Omega dx|\psi_{n,k}(x)|^2 = 1$ from the normalization condition. The same is true for the intercellular Zak phase, as it can be shown by a gauge transformation of $\psi_{n,k}(x)$.

The separation of the Zak phase into inter- and intracellular parts is not unique—it depends on the origin of the unit cell. Nevertheless, the separation is meaningful: the intracellular Zak amounts to the classical polarization of the unit cell,

$$P_n^{\text{cl}} = \frac{1}{a}\int_\Omega dx\, x\rho_n(x) = \frac{e}{a}\int_\Omega dx\, x\sum_k |\psi_{n,k}(x)|^2 = \frac{e}{2\pi}\gamma_n^{\text{intra}} - m_\Omega e, \tag{2.47}$$

where $\rho_n(x)$ is the electronic density corresponding to the n-th band. That is, P_n^{cl} can be evaluated from the intracellular Zak phase up to mod e. Note that γ_n^{intra} depends on the real-space origin while γ_n^{inter} does not.

The physical interpretation of the intercellular Zak phase can be given in terms of Wannier functions, Eq. (2.18), which satisfy the orthonormality condition $\langle W_{n,m}|W_{n',m'}\rangle = \delta_{n,n'}\delta_{m,m'}$. Note that in one dimensions, the Wannier function $W_{n,m}(x)$ is in general guaranteed to be exponentially localized around a position in the m-th unit cell[103–105] while, in 2D and 3D, this is true if and only if the Chern number of the band vanishes.[153;154] By fixing a point x_b at the boundary between neighbouring unit cells, which we assume for concreteness to be between the $(m = -1)$-th and $(m = 0)$-th unit cell, the system is split into the left (L) and right (R) regions as depicted in Fig. 2.4 (a). In Appendix A, we explicitly show how the intercellular Zak phase naturally splits up into two parts[113]

$$\gamma_n^{\text{inter}} = \gamma_n^{L\to R} - \gamma_n^{R\to L} \tag{2.48}$$

that are related to the weight of the Wannier functions centered at different sides of the cut x_b. More explicitly, $\gamma_n^{R\to L}$ is proportional to the weight on the left side of the system $(x < x_b)$ of those Wannier functions centered on the right side $(m \geq 0)$, while $\gamma_n^{L\to R}$ is proportional to the weight on the right side $(x > x_b)$ of the Wannier functions centered on the right side $(m < 0)$, i.e.,

$$\gamma_n^{R\to L} = 2\pi\sum_{m=0}^{\infty}\int_{-\infty}^{x_b} dx\,|W_{n,m}(x)|^2\,, \quad \gamma_n^{L\to R} = 2\pi\sum_{m=-\infty}^{-1}\int_{x_b}^{\infty} dx\,|W_{n,m}(x)|^2\,. \tag{2.49}$$

The right-hand sides of Eqs. (2.49) are visualized in Fig. 2.4 (a). Summing over all occupied bands, the weight of the Wannier functions corresponds to a charge transfer from the left to right and vice versa. The difference between these charge transfers is the intercellular Zak phase, summed over all occupied bands,[113]

$$\Delta Q = Q^{R\to L} - Q^{L\to R} = \frac{e}{2\pi}\sum_{n\in \text{occ.}} \gamma_n^{\text{inter}} \tag{2.50}$$

with the charge transfers defined by $Q^{R\to L} \equiv e\sum_{n\in\text{occ.}}\sum_{m=0}^{\infty}\int_{-\infty}^{x_b} dx\,|W_{n,m}(x)|^2$ and $Q^{L\to R} \equiv e\sum_n\sum_{m=-\infty}^{-1}\int_{x_b}^{\infty} dx\,|W_{n,m}(x)|^2$. Due to the translational symmetry of the system, this result is valid for any unit-cell boundary. Also, this quantity does not depend on the position of the origin since the intercellular Zak phase does not, as mentioned previously. Note that, from the point of view of the electronic density of the infinite system without boundaries, every unit cell is neutral and there is no extra charge in the L and R regions of the bulk illustrated in Fig. 2.4 (a).

However, we want to eventually obtain the extra charge accumulation around the surfaces when the system is terminated as shown in Fig. 2.4 (b). Consider such a terminated system that is divided into three regions as illustrated in Fig. 2.4 (b): two surface regions separated by the bulk at the unit cells ℓ_L and ℓ_R. We choose the boundaries of the surface regions large enough so that there are no boundary effects in the bulk. All regions are commensurate with the bulk's unit cell, namely, they do not contain any partial unit cells. While the extra charge accumulation in the surface region is defined as the additional charge over the bulk's charge distribution, it is equivalent to the total charge including ions in this region, because of the commensurability condition and the neutrality of the bulk's unit cell. Further, the finite system must be insulating because otherwise partially filled degenerate states at the Fermi level would yield ambiguity in evaluating physical quantities depending on which states we choose to be occupied. If the surface region is commensurate with the bulk's unit cell, the extra charge accumulation $Q_{\text{acc}}^{LS(RS)}$ in the left (right) surface region of a neutral 1D insulator is given by

$$Q_{\text{acc}}^{LS(RS)} = +(-)\frac{e}{2\pi}\gamma^{\text{inter}} \pmod{e} \tag{2.51}$$

as shown explicitly in Ref. 113. The intercellular Zak phase γ_n^{inter} is evaluated based on the commensurate unit cell. We define $\gamma^{\text{inter}} = \sum_{n\in\text{occ.}}\gamma_n^{\text{inter}}$ for convenience (γ^{intra} analogue). Thus, the intercellular Zak phase predicts the extra charge accumulation in the surface region modulo e.

Before continuing, it is important to point out the difference between the bound surface charge and the extra charge accumulation. The bound surface charge σ is a quantity measured in a capacitance measurement and is related to the modern definition of the polarization by $\sigma = \mathbf{P}\cdot\hat{n}$, where $\hat{n}$ is the surface orientation ($\hat{n} = -(+)\hat{x}$ for the left (right) edge in the 1D case).[93] The bound surface charge of the total charge density $\rho(x)$ of the finite system is evaluated explicitly as[93;155;156]

$$\sigma^{LS} = \frac{1}{a}\int_{-\infty}^{x_c} dx \int_{x-\frac{a}{2}}^{x+\frac{a}{2}} dx'\rho(x'), \qquad \sigma^{RS} = \frac{1}{a}\int_{x_d}^{\infty} dx \int_{x-\frac{a}{2}}^{x+\frac{a}{2}} dx'\rho(x') \tag{2.52}$$

at the left (LS) and right surfaces (RS), where x_c and x_d are arbitrary positions[‡‡] in the middle of the finite system far away from the surfaces. Similar to the Zak phase, the bound surface charge can be split up into two parts. In particular, if we choose $x_c = x_{\ell_L} + a/2$ and $x_d = x_{N-\ell_R} - a/2$, the left and right bound surface charge can be rewritten

---

[‡‡] In fact, the results are independent from x_c and x_d, since the surfaces are located at infinity.[113]

$$\sigma^{LS} = -\frac{1}{a}\int_{x_{\ell_L}}^{x_{\ell_L}+a} dx\, x\rho(x) + \int_0^{x_{\ell_L}} dx \rho(x) \tag{2.53a}$$

$$\sigma^{RS} = \frac{1}{a}\int_{x_{N-\ell_R}-a}^{x_{N-\ell_R}} dx\, x\rho(x) + \int_{x_{N-\ell_R}}^{x_N} dx \rho(x). \tag{2.53b}$$

The first terms of Eqs. (2.53) are exactly $\mathbf{P}_{\text{cl}} \cdot \hat{n}$ because x_{ℓ_L} and $x_{N-\ell_R}$ are far enough from the edges so that $\rho(x)$ can be considered a bulk charge density. We call them the *classical bound surface charges* $Q_{\text{cl}}^{LS(RS)}$, because in classical electrodynamics, they are the bound surface charges in a dielectric material with a uniform dipole distribution through the whole finite system. The second terms of Eqs. (2.53) are just the total charges in the left and right surface regions, which are equal to the extra charge accumulations in those regions in the neutral systems. This is consistent with the splitting of the Zak phase into the intra- and intercellular Zak phase. Thus, the modern definition of polarization is actually composed of two kinds of polarization: the classical from the bulk's dipole moment, and the polarization from the extra charge accumulations at opposite edges.

2.4.2 Bulk-boundary Correspondence

The relationship between the extra charge accumulation at the surfaces and the intercellular Zak phase enables us to reformulate the bulk-boundary correspondence in the following way: there are $n = \gamma^{\text{inter}}/\pi \pmod 2$ surface modes below the Fermi level if there is inversion symmetry both before and after termination, and the finite system is commensurate with the bulk unit cell used for the calculation of γ^{inter}. It is the intercellular Zak phase and not the total Zak phase that determines the number of surface modes; while the intercellular Zak phase gives the amount of the extra charge accumulation around the surfaces, which is closely related to the surface modes, the intracellular Zak phase, the bulk dipole moment, has nothing to do with the surface modes.

Before considering the more general case, we note that, if the bulk respects inversion symmetry, γ^{inter} is quantized to integer multiples π.[100] When the real-space origin is at one of the inversion centers, the total Zak phase γ is quantized to π while its intracellular part vanishes because the dipole moment of the bulk unit cell is zero in this case. Therefore, $\gamma^{\text{inter}} = \gamma$ is also quantized to π, and it is independent of the choice of the origin as mentioned in Sec. 2.4.1. The surface modes are the eigenstates generated in the bulk gaps as a result of the edge termination, exponentially localized at one of the edges.[113] For any surface state localized at the left edge, inversion symmetry requires a counterpart localized at the right edge with the same energy. The degeneracy might increase if the system preserves additional symmetries such as the time-reversal symmetry.

The general statement about the bulk-boundary correspondence can be justified by distinguishing between two different cases: the finite system can be either an insulator, i.e., the surface modes do not cross the Fermi level, or a metal with surface modes crossing the Fermi level.

First, let us consider the case when the finite system is insulating. Then, the only allowed value of the total charge accumulations is $Q_{\text{acc}}^{LS} = Q_{\text{acc}}^{RS} = 0$ due to charge neutrality and inversion symmetry. According to (2.51), the intercellular Zak phase should be 0 (mod 2π) in this case. Since every surface mode has an inversion partner with the same energy, there should be an even number of surface states below the Fermi level. This means the general statement holds for insulating phases with inversion symmetry.

Second, we consider the case when the Fermi level is located at the surface modes. In this case, we cannot use the results of the previous section since there, we assume the finite system is insulating. However, we can resolve this obstacle by opening tiny gaps between degenerate surface modes without changing the total number of surface modes in the bulk gap. We assume that this can be done by applying local perturbative potentials on both edges that break symmetries corresponding to those degeneracies. For instance, different on-site potentials at opposite edges break the degeneracy responsible for inversion symmetry. Similarly, a local Zeeman field could be used to break spin degeneracy.

Let us investigate the dependence of the surface modes on the tiny inversion symmetry breaking, which is relevant for the quantization of the extra charge accumulations on the edges as explained below. This is achieved by applying an on-site potential δ to the first unit cell and $-\delta$ to the N-th unit cell of the finite system where δ is nonzero but small compared to the bulk gap. Then, the eigenstates at opposite edges have different energies, and it is impossible to construct surface modes localized at both edges simultaneously from them. As a result, the eigenstate of each lifted surface mode is localized to only one of the left and right edges. This implies that each surface mode yields an integer charge $Q^{LS}_{S_i,\text{acc}} = -e$ or $Q^{RS}_{S_i,\text{acc}} = -e$, where $Q^{LS(RS)}_{S_i,\text{acc}}$ is the contribution of the i-th surface mode to the extra charge accumulation in the left (right) surface region. After taking into account the inversion symmetry breaking, we assume that other perturbative potentials would not affect this property of the lifted surface modes.

On the other hand, the charge distribution calculated from the bulk band continuum is insensitive against this kind of local perturbation due to its bulk character.[157] So, the charge distribution of the bulk band continuum maintains almost the same form as the unperturbed inversion symmetric system. In the unperturbed inversion symmetric system, the extra charge accumulation from the bulk band continuum can only take values of $Q^{LS}_{B,\text{acc}} = Q^{RS}_{B,\text{acc}} = (p + 1/2)e$ or pe where p is an integer, because the total charge of the finite system is an integer multiple of e, and the system has inversion symmetry. Here, $Q^{LS(RS)}_{B,\text{acc}}$ is the contribution of the bulk band continuum to the extra charge accumulation in the left (right) surface region. Note that although we slightly break the inversion symmetry to make the system insulating, its presence in the unperturbed system is essential for the constraint on $Q^{LS(RS)}_{B,\text{acc}}$.

If $Q^{LS(RS)}_{B,\text{acc}} = (p+1/2)e$, the total charge accumulations originating from surface modes on both sides are $\sum_{E_i<E_F}(Q^{LS}_{S_i,\text{acc}} + Q^{RS}_{S_i,\text{acc}}) = -(2p + 1)e$ to maintain neutrality. This means that there is an odd number of surface modes below the Fermi level in the gap because there was an even number of occupied surface modes in other gaps before breaking inversion symmetry, and we have assumed that this number is unchanged by the symmetry breaking perturbations. Also, due to the same reason, this implies that we have an odd number of surface modes below the Fermi energy in the main gap before breaking those symmetries. In the perspective of the intercellular Zak phase, the fact that the extra charge accumulation $Q^{LS(RS)}_{B,\text{acc}} + \sum_{E_i<E_F} Q^{LS(RS)}_{S_i,\text{acc}}$ is a half-integer multiple of e implies that the intercellular Zak phase is a half-integer multiple of 2π according to (2.51). In conclusion, the number of surface modes equals $\gamma^{\text{inter}}/\pi \mod 2$ in this case.

In similar fashion, when $Q^{LS(RS)}_{B,\text{acc}} = pe$, the surface modes' extra charge accumulations on both edges are $\sum_{E_i<E_F}(Q^{LS}_{S_i,\text{acc}} + Q^{RS}_{S_i,\text{acc}}) = -2pe$ to maintain charge neutrality, implying that there is an even number of surface modes in the main gap and that the

intercellular Zak phase is even. Thus, the number of surface modes equals $\gamma^{\text{inter}}/\pi \mod 2$ also in this case.

Finally, we note that this bulk-boundary correspondence can be restated by using the Zak phase when the real-space origin is at the inversion center. This is because the intracellular Zak phase becomes zero ($\mod 2\pi$) according to (2.46), so that the Zak phase is identical to the intercellular Zak phase in this case.

2.4.3 Conclusion

In this section, we have demonstrated that the intercellular Zak phase γ^{inter} predicts whether the number of surface modes below the Fermi level in one-dimensional insulators is even or odd, when the commensurate bulk unit cell respects inversion symmetry. While the Zak phase itself cannot give such a prediction due to its arbitrariness depending on the choice of the real-space origin and the unit cell, we have shown that γ^{inter}, as an origin-independent quantity, can be exploited for this bulk-boundary correspondence. Although γ^{inter} also depends on the unit cell choice it is not arbitrary once we select a unit cell that is commensurate with the finite system. Our bulk-boundary correspondence using γ^{inter} was justified with a microscopic interpretation of γ^{intra} and γ^{inter}. We explicitly showed that γ^{intra} is the electronic part of the bulk dipole moment of the unit cell, and γ^{inter} represents how much weight of the Wannier functions is exchanged with respect to a unit cell boundary. When the system is terminated, γ^{intra} is interpreted as the classical bound surface charge, while γ^{inter} is understood as the extra charge accumulation around surfaces. Since the number of surface modes is closely related to the extra charge accumulation, we argue how it is related to γ^{inter} when the commensurate unit cell preserves inversion symmetry. If the origin is at the inversion center, γ^{inter} becomes identical to the Zak phase, and our bulk-boundary correspondence reduces to the conventional one. Thereby, our work also clarifies the conditions under which the conventional bulk-boundary correspondence using the Zak phase works.

We expect that the extra charge accumulation can be measured by scanning quantum dot microscopy (SQDM).[158] SQDM offers three-dimensional images of electrostatic potentials down to the subnanometer level from which one could infer the total amount of its source charge. Since the electric field caused by extra charge accumulations at opposite edges of a long enough 1D chain can be considered independent, the extra charge accumulation at one edge can be obtained from the local electrostatic potential profile. Therefore, SQDM could be the characterizing experiment for the intercellular Zak phase like the capacitance measurement for the Zak phase.

3 Field Theory Perspective on Topological Phases

How do the consequences of topologically nontrivial band structures manifest themselves in a field theory that describes the effective low-energy degrees of freedom? A formulation of topological phases in terms of a quantum field theory boils down the full microscopic model to a small number of fluctuating fields. Instead of looking at a complicated model, the quantum field theory allows for a simple computation of response functions, e.g., to external fields. In many cases, the computation of response functions is possible by using standard textbook methods—in fact, many results for topological semimetals have been computed before in the context of high-energy physics. As we see in the course of this chapter, the field theory description additionally allows for a reinterpretation of phenomena known from band theory, such as surface states, in terms of topological contributions to the action.

Based on an axion contribution to the action, a framework originally intended to explain the absence of the so-called charge-parity violation in quantum chromodynamics,[159;160] we introduce a topological θ-term that does not depend on details of the system.[53] This topological term changes Maxwell's equations,[160] giving rise to an unusual response to external electric and magnetic fields, as shown in Sec. 3.1. The topological contribution easily extends to Weyl semimetals,[63;161;162] where the θ-term results in an anomalous Hall effect and the chiral anomaly, Sec. 3.2. One experimental signature of the chiral anomaly is the blue note,[58] an unusual pattern with a terminated Fermi arc that is visible in angle-resolved photoemission spectroscopy, Sec. 3.3.

However, nothing comes for free and there is one major drawback: results from field theory are often ambiguous. In high-energy physics, this problem can usually be circumvented by requiring certain symmetries to be fulfilled, e.g., Lorentz-invariance, which fixes the result. In condensed matter, however, virtually all symmetries can be broken, for example in Weyl semimetals that do not require any symmetries, as shown in Sec. 2.3.1, Thus, ambiguities that occur in the theory need to be solved differently. One example is given in Sec. 3.5, where an interpretation of two different outcomes from quantum field theory is discussed.

3.1 Topological Insulators

To get an idea of the origin of the θ-term, we discuss the action of massive Dirac fermions in $3+1$ dimensions. This action serves well to describe the low-energy degrees of freedom of three-dimensional band insulators, although more general mass terms are possible.[163]

Coupled to a vector field A_μ, the action reads[*]

$$\mathcal{S} = \int d^4x \bar{\psi} \left(i \left(\partial_\mu + iA_\mu\right) \gamma^\mu - m\right) \psi \tag{3.1}$$

with $\mu = (0, 1, 2, 3)$, the contravariant gamma matrices $\gamma^{0\cdots3}$ and their product $\gamma^5 = i\gamma^0\gamma^1\gamma^2\gamma^3$. The gamma matrices generate a Clifford algebra by fulfilling the anticommutation relation

$$\{\gamma^\mu, \gamma^\nu\} = 2g^{\mu\nu} \tag{3.2}$$

with the Minkowski metric $g^{\mu\nu}$ with signature $(+---)$. Further, we employ the notation $\bar{\psi} = \psi^\dagger\gamma^0$. In the subsequent discussion, we use the chiral basis $\gamma^0 = \tau_x$ and $\gamma^j = -i\sigma_j\tau_y$ with the Pauli matrices σ_μ and τ_ν, resulting in the product $\gamma^5 = \tau_z$.

This action corresponds to the Lagrange density

$$\mathcal{L} = \psi^\dagger \left(i\partial_t - A_0 - \mathcal{H}\right) \psi = \psi^\dagger \left(i \left(\partial_\mu + iA_\mu\right) \gamma^0\gamma^\mu - m\gamma^0\right) \psi \tag{3.3}$$

and, thus, to the Hamiltonian $\mathcal{H} = -i\partial_j\sigma_j\tau_z + m\tau_x$ that is gapped for $m \neq 0$ and is subjected to the gauge field A_j. The Hamiltonian respects time-reversal symmetry with $T = \sigma_y\mathcal{K}$ and $T^2 = -1$, as well as particle-hole symmetry $\Xi = \sigma_y\tau_y\mathcal{K}$, $\Xi^2 = +1$. In a $\mathbb{Z}_2$ topological insulator, particle-hole symmetry (and thus, chiral symmetry) is explicitly broken by a momentum-dependent term proportional to the identify matrix. Since it does not affect the main message of this section, we ignore the presence of particle-hole and chiral symmetry that is investigated in detail, e.g., in Ref. 163.

Two different topological sectors are possible, depending on the sign of the mass term;[163] this is quite counterintuitive since the actions having mass terms of opposite sign can be continuously transformed into each other. Following Ref. 164, we see that a topological term arises due to changes in the measure of the path integral. To explicitly derive the topological contribution, we first perform a Wick rotation into Euclidean space time

$$ix^0 = x^4,\ \partial_0 = i\partial_4, \tag{3.4a}$$
$$i\gamma^0 = \gamma^4,\ A_0 = iA_4, \tag{3.4b}$$

with the metric $g^{\mu\nu} = -\delta^{\mu\nu}$ and antihermitian Euclidean gamma matrices $\gamma^{\mu\dagger} = -\gamma^\mu$ with $\mu = (1, 2, 3, 4)$ (note that $\gamma^5 = -\gamma^1\gamma^2\gamma^3\gamma^4$ remains hermitian). Due to the antihermicity of the gamma matrices, the Dirac operator $\not{D} = \gamma^\mu \left(\partial_\mu + iA_\mu\right)$ is hermitian in this basis. We now perform a global chiral rotation on the action[163;165]

$$\psi \to \psi = e^{is\theta\gamma^5/2}\psi_s \tag{3.5a}$$
$$\bar{\psi} \to \bar{\psi} = \bar{\psi}_s e^{is\theta\gamma^5/2} \tag{3.5b}$$

that changes the Lagrange density

$$\mathcal{L} \to \bar{\psi}_s \left(i\not{D} - me^{is\theta\gamma^5}\right) \psi_s. \tag{3.6}$$

---

[*] We use conventions commonly used in high energy physics, e.g., in Ref. 65. This includes working in natural units, setting $e = \hbar = c = 1$, such that energy and momentum have the same units. Summation over repeated indices is implied, with Greek letters labeling $3+1$ dimensional space-time and Latin letters labeling 3 spatial dimensions.

Here, we chose a constant term $\theta = \pi$, making the chiral rotation global, and a free parameter s. For $s = 1$, the sign of the mass term changes, tempting us to naively argue that the sign of the mass does not change the partition function—however, this is not the case. The reason for that originates in the chiral anomaly: the measure of the path integral $\mathcal{D}(\bar{\psi}, \psi)$ changes upon performing the above rotation.

To determine the change of the path integral measure, we expand the Grassmann field $\bar{\psi}, \psi$ in terms of the eigenfunctions $\phi_n(x)$ of the hermitian Dirac operator $\not{D}$ with eigenvalues λ_n,

$$\psi_s = \sum_n c_n(s)\phi_n(x), \;\; \bar{\psi}_s = \sum_n \phi_n^*(x)\bar{c}_n(s) \tag{3.7}$$

with the transformed Grassmann fields $c_n(s), \bar{c}_n(s)$. Upon an infinitesimal rotation by ds, the fields change

$$\psi_{s+ds} = e^{-ids\theta\gamma^5/2}\psi_s = \sum_n (1 - ids\gamma^5/2)c_n(s)\phi_n(x) = \sum_n c_n(s+ds)\phi_n(x) \tag{3.8}$$

$$\bar{\psi}_{s+ds} = \bar{\psi}_s e^{-ids\theta\gamma^5/2} = \sum_n \phi_n^*(x)\bar{c}_n(s)(1 - ids\gamma^5/2) = \sum_n \phi_n^*(x)\bar{c}_n(s+ds) \tag{3.9}$$

where we identify the transformed Grassmann fields at $s + ds$

$$c_n(s+ds) = \sum_m U_{nm} c_n(s), \qquad \bar{c}_n(s+ds) = \sum_m U_{nm}\bar{c}_n(s) \tag{3.10}$$

with the infinitesimal chiral transformation operator

$$U_{nm} = \delta_{nm} - ds\frac{i}{2}\int d^4x\, \theta\phi_n^*(x)\gamma^5\phi_m(x). \tag{3.11}$$

This operator determines the change of the Jacobian in the path integral by

$$\prod_n dc_n(s+ds) = (\det U)^{-1}\prod_n c_n(s), \;\; \prod_n d\bar{c}_n(s+ds) = (\det U)^{-1}\prod_n \bar{c}_n(s) \tag{3.12}$$

so that $\mathcal{D}(\bar{\psi}_{s+ds}, \psi_{s+ds}) = (\det U)^{-2}\mathcal{D}(\bar{\psi}_s, \psi_s) \equiv \mathcal{J}(s, s+ds)\mathcal{D}(\bar{\psi}_s, \psi_s)$ with the Jacobian

$$\mathcal{J}(s, s+ds) = \exp\left[-2\mathrm{tr}\ln U\right] = \exp\left[-ids\int d^4x\theta\sum_n \phi_n^*(x)\gamma^5\phi_n(x)\right]. \tag{3.13}$$

To determine the Jacobian $\mathcal{J}$, we need to evaluate the function $I(x) = \sum_n \phi_n^*(x)\gamma^5\phi_n(x)$. Since γ^5 anticommutes with $\not{D}$, the function $\gamma^5\phi_n(x)$ is an eigenfunction of $\not{D}$ with eigenvalue $-\lambda_n$. Due to the orthogonality of the functions $\phi_n(x)$, this implies that only zero eigenvalues of $\not{D}$ contribute to the integral

$$\int d^4x I(x) = n_+ - n_- = \mathrm{ind}\left(\not{D}\right) \tag{3.14}$$

where $n_+(n_-)$ is the number of ($\lambda_n = 0$)-eigenstates with positive (negative) eigenvalue of γ^5, i.e., a positive or negative chirality. The notation $\mathrm{ind}\left(\not{D}\right)$ corresponds to the analytical index of $\not{D}$.[63] To evaluate $I(x)$, we use a heat-kernel regularization that is required since the finite result of the integral (3.14) is obtained due to mutual cancellation of divergent contributions. Heat-kernel regularization means that we introduce factors of $1 = \lim_{M\to\infty} \exp(-\lambda_n^2/M^2)$ before evaluating the integral. The function $I(x)$ reads

$$I(x) = \lim_{M\to\infty} \sum_n \phi_n^*(x)\gamma^5 e^{-\lambda_n^2/M^2}\phi_n(x) = \lim_{M\to\infty} \sum_n \phi_n^*(x)\gamma^5 e^{-\not{D}^2/M^2}\phi_n(x) \tag{3.15}$$

with the square of the Dirac operator

$$\not{D}^2 = -D_\mu D_\mu + \frac{i}{4}\left[\gamma^\mu, \gamma^\nu\right] F_{\mu\nu} \tag{3.16}$$

and the definition $D_\mu \equiv \partial_\mu + iA_\mu$. Switching to the Fourier transform of $\phi_n(x)$, $\phi_n^*(x)$ and inserting their completeness relation gives

$$I(x) = \lim_{M\to\infty} \int \frac{d^4k}{(2\pi)^4} \mathrm{tr}\left[\gamma^5 \exp\left[\frac{(ik_\mu + D_\mu)^2}{M^2} - \frac{i}{4M^2}\left[\gamma^\mu, \gamma^\nu\right] F_{\mu\nu}\right]\right] = \frac{1}{32\pi^2}\epsilon^{\mu\nu\sigma\rho}F_{\mu\nu}F_{\sigma\rho} \tag{3.17}$$

where we took the limit $M \to \infty$. After substituting the expression for $I(x)$ back into the Jacobian and performing the integral over s, the Jacobian of the global chiral transformation reads

$$\mathcal{J}(0,1) = \exp\left[-\int d^4x \frac{\theta}{32\pi^2}\epsilon^{\mu\nu\sigma\rho}F_{\mu\nu}F_{\sigma\rho}\right] \equiv \exp\left[-\mathcal{S}_\theta\right]. \tag{3.18}$$

The action $\mathcal{S}_\theta$ in as an example of a so-called θ-term; here, we have $\theta = \pi$ for a topological insulator. In presence of time-reversal symmetry, θ is restricted to two quantized values $\theta = 0, \pi$.[53]

The topological term in the action S_θ becomes relevant at those surfaces where a transition from $\theta = \pi$ to $\theta = 0$ is necessary, i.e., at transitions from a topological insulator ($\theta = \pi$) to a trivial insulator ($\theta = 0$), for example to the vacuum. We model the surface of a topological insulator by $\theta(z) = \pi\Theta(-z)$ with the Heaviside step function $\Theta(z)$, which gives a sharp transition between the topological and the trivial insulator. To rewrite the action in a Chern-Simons form, we use the derivative $\partial_z\theta(z) = -\pi\delta(z)$, which gives[53]

$$\mathcal{S}_\theta = -\frac{1}{8\pi^2}\int d^4x \epsilon^{\mu\nu\sigma\rho}A_\nu(\partial_\mu\theta)\partial_\sigma A_\rho = \frac{1}{8\pi}\int d^3x \epsilon^{z\nu\sigma\rho}A_\nu\partial_\sigma A_\rho, \tag{3.19}$$

giving the current $j_\nu = \varepsilon^{z\nu\sigma\rho}\partial_\sigma A_\rho/(4\pi)$ by the variation of $\mathcal{S}_\theta$ with respect to A_ν. This current amounts to a half quantum Hall effect on the surface[†]

$$\rho = \frac{1}{4\pi}B_z,\ \mathbf{j} = \frac{1}{4\pi}\mathbf{e}_z \times \mathbf{E}, \tag{3.20}$$

a special property of massless Dirac fermions,[53] the surface states of the $\mathbb{Z}_2$ topological insulator. The half-integer quantum Hall effect cannot be measured in a transport experiment, since transport experiments do not probe the local characteristics of a topological insulator surface.[166;167] However, local probes of the half-integer quantum Hall effects can give experimentally measurable signatures.[167]

[†] Keep in mind that that $\hbar = e = 1$, such that the conductivity below amounts to $\sigma_{xy} = e^2/(2h)$ when restoring $\hbar$ and e, thus, the expression *half* a quantum Hall effect.

3.2 Weyl Fermions and the Chiral Anomaly

A more general form of the chiral rotation (3.5) allows for a local function $\theta \to \theta(x)$ instead of a global constant. The consequences of such a local transformation are particularly rich for massless Dirac fermions, i.e., particles described by the action (3.1) with the mass set to zero. After performing a chiral rotation with $s = 1$, the action changes[164]

$$\mathcal{S} \to \mathcal{S}' = \mathcal{S} - \frac{1}{2}\int d^4x(\partial^\mu\theta)\bar{\psi}\gamma^\mu\gamma^5\psi = \mathcal{S} + \frac{1}{2}\int d^4x\theta\,\partial^\mu j^5_\mu \tag{3.21}$$

with the chiral current $j^5_\mu \equiv \bar{\psi}\gamma^\mu\gamma^5\psi$. Classically, as a manifestation of Noether's theorem, the action must remain invariant under the chiral transformation.[164] This implies that, since $\theta(x)$ can be an arbitrary function, the chiral current needs to be conserved, $\partial^\mu j^5_\mu = 0$. As we saw in the previous section, this is not true for a quantum field theory: the change in the path integral measure generates an additional contribution to the action,

$$\mathcal{S}_\theta = \frac{1}{32\pi^2}\int d^4x\theta(x)\epsilon^{\mu\nu\sigma\rho}F_{\mu\nu}F_{\sigma\rho}, \tag{3.22}$$

resulting in

$$\partial^\mu j^5_\mu = -\frac{1}{16\pi^2}\epsilon^{\mu\nu\sigma\rho}F_{\mu\nu}F_{\sigma\rho} = \frac{1}{2\pi^2}\mathbf{E}\cdot\mathbf{B}. \tag{3.23}$$

For massless Dirac fermions, the chiral charge is therefore not conserved. This is the chiral anomaly: a classically preserved symmetry, i.e., chiral charge conservation, is broken by quantum fluctuations.[28;29]

How does the chiral anomaly manifest itself in Weyl semimetals? We explore a more general form of the action with the two chiralities separated in momentum and energy, aiming to understand the importance of the chiral anomaly in condensed-matter physics. Separating the different chiralities in momentum and energy by the four-vector $b_\mu = (b_0, \mathbf{b})$ gives a Lorentz-violating extension of the previously considered massless Dirac action[51;57;161]

$$\mathcal{S} = \int d^4x\bar{\psi}\gamma^\mu(i\partial_\mu - A_\mu - b_\mu\gamma^5)\psi. \tag{3.24}$$

A chiral rotation with $\theta(x) = 2x^\mu b_\mu$ eliminates the Lorentz-violating term b_μ for $s = 1$, giving rise to a peculiar form of the action. In Chern-Simons forms, cf. Eq. (3.19), it reads[63]

$$\mathcal{S}_\theta = -\frac{1}{8\pi^2}\int d^4x\epsilon^{\mu\nu\alpha\beta}(\partial_\mu\theta)A_\nu\partial_\alpha A_\beta = -\frac{1}{4\pi^2}\int d^4x\epsilon^{\mu\nu\alpha\beta}b_\mu A_\nu\partial_\alpha A_\beta. \tag{3.25}$$

Varying the action with respect to b_μ gives the chiral current $j^{5,\mu} = \delta\mathcal{S}_\theta/\delta b_\mu$, which shows the chiral anomaly, Eq. (3.23). Varying the action with respect to A_ν gives the following contributions to current and charge (we restore e and $\hbar$ to connect with condensed-matter literature)

$$\rho = \frac{e^2}{2\pi^2\hbar}\mathbf{b}\cdot\mathbf{B},\ \mathbf{j} = \frac{e^2}{2\pi^2\hbar}(\mathbf{b}\times\mathbf{E} - b_0\mathbf{B}) \tag{3.26}$$

where the node separation in momentum space $\mathbf{b}$ is given in units of inverse length and the separation in energy b_0 in unit of inverse time. The current contribution is comprised of two parts: the anomalous Hall effect, a current orthogonal to the applied electric field, and the chiral magnetic effect, a dissipationless equilibrium current proportional to **B**. While there is no doubt about the presence of the anomalous Hall effect,[62;168] the chiral magnetic effect is odd—completely filled bands cannot contribute to the electrical current[97]. In fact, calculations using tight-binding models that take into account the regularization imposed by the underlying lattice show that the chiral magnetic effect does not occur in Weyl semimetals in equilibrium,[62;169] although this may be circumvented in superconductors that allow for dissipationless currents.[170] This tells us that one has to be careful with predictions from quantum field theories that serve to describe the effective low-energy physics. Another example of an ambiguous result from quantum field theory is discussed in Sec. 3.5.

3.3 Visualizing the Chiral Anomaly with Photoemission Spectroscopy

From a condensed-matter perspective, it is most pressing to ask for experimental consequences of the chiral anomaly. The chiral anomaly is theoretically predicted to result in negative magnetoresistance[30;40] (consistent with recent magneto-transport experiments,[41;171–179] cf. Sec. 4.1 for a more detailed discussion), local[55;180] and non-local[181] transport phenomena, and rotation induced cooling.[182]

A clean diagnostic tool for the chiral anomaly is still lacking, since transport signatures, such as negative magnetoresistance, are not as unequivocal as initially believed.[44;183] In this section, following Ref. 58, we explore the feasibility of angle-resolved photoemission spectroscopy (ARPES) that has been previously overlooked in this regard despite its importance in observing topological semimetals. A possible reason for this is that the finite magnetic field required to observe the chiral anomaly may complicate the disentangling of electron trajectories needed for angular resolution. Setting aside this obstacle (we return to it at the end of this section where we argue that it can be overcome), we identify the main spectral signatures of the chiral anomaly and its observable effect on the Fermi arcs. First, the bulk spectrum is determined by the differently occupied Weyl nodes distinguished by their chiralities; second, the bulk chiral imbalance tilts the Fermi arcs, which then appear at fixed energy as finite segments stemming from the bulk Fermi surface. Together, these two features form a distinguishing note-shaped photoemission pattern that we argue is within reach of current experimental state of the art. We further calculate angle-integrated photoemission spectroscopy (PES), which does not suffer from the magnetic field complications of its angle-resolved relative, and show that distinct signatures of the chiral anomaly survive. Overall, these results supply essential theoretical input that render photoemission spectroscopy a viable probe to visualize the chiral anomaly in Dirac and Weyl semimetals.

3.3.1 The Chiral Anomaly in Condensed Matter Systems

To support our conclusions, we start by discussing the main features of the band structure of Weyl semimetals, shown in Fig. 3.1 (a). Their low-energy bulk spectrum consists of an even number of band touching points of left and right handed chirality that are separated in energy and momentum by breaking inversion or time-reversal symmetry. Close to the Weyl points the energy dispersion is approximately linear and described by a Weyl Hamiltonian of chirality χ, cf. Eq. (2.33),

$$\mathcal{H}_{\mathbf{k}}^{(\chi)} = \chi\hbar v\mathbf{k}\cdot\boldsymbol{\sigma}, \tag{3.27}$$

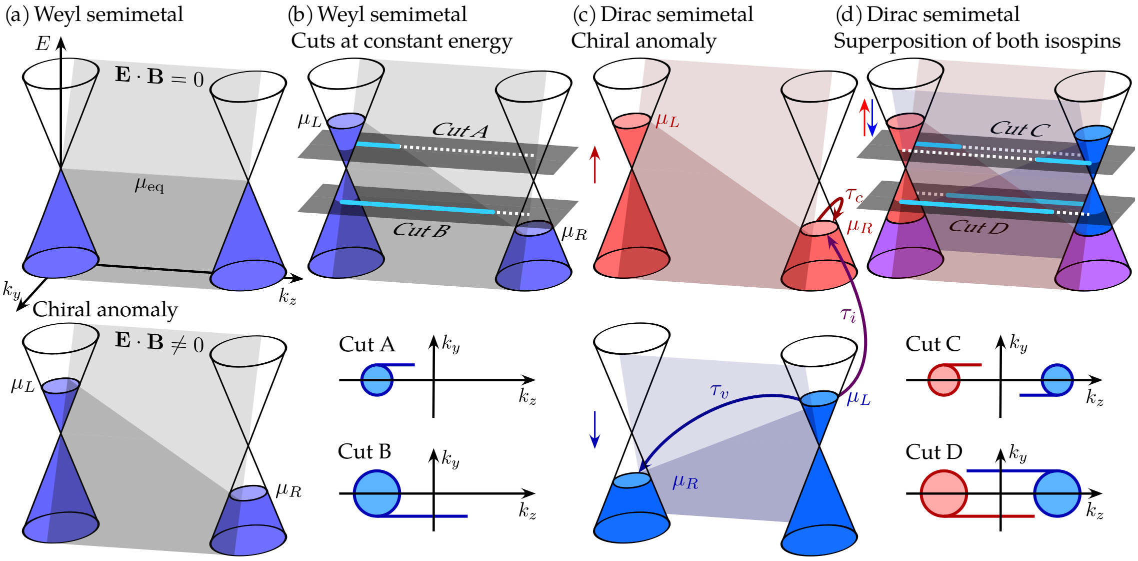
(a) Weyl semimetal
E
$\mathbf{E}\cdot\mathbf{B}=0$
μ_{eq}
k_y
k_z
Chiral anomaly
$\mathbf{E}\cdot\mathbf{B}\neq 0$
μ_L
μ_R
(b) Weyl semimetal
Cuts at constant energy
μ_L
Cut A
Cut B
μ_R
Cut A
k_y
k_z
Cut B
k_y
k_z
(c) Dirac semimetal
Chiral anomaly
μ_L
τ_c
μ_R
τ_i
τ_v
μ_L
μ_R
(d) Dirac semimetal
Superposition of both isospins
Cut C
Cut D
Cut C
k_y
k_z
Cut D
k_y
k_z

FIGURE 3.1: Visualization of the chiral anomaly in Dirac and Weyl semimetals. (a) Low-energy spectrum of a Weyl semimetal film with two bulk Weyl nodes of different chirality separated in momentum space. The grey plane represents the surface state at the film's top surface, occupied up to the equilibrium chemical potential μ_{eq}. Applying external magnetic and electric fields that satisfy $\mathbf{E}\cdot\mathbf{B}\neq 0$ results in a steady state with left and right cone chemical potentials $\mu_L \neq \mu_R$, linearly interpolated by a tilted Fermi arc. (b) Two constant energy cuts (A and B) through the band structure, with occupied and empty surface states depicted by solid light blue and white dashed lines respectively. The occupation at these cuts shows a characteristic blue note-shaped pattern depicted in the lower panel. (c) Dirac semimetals host pairs of Weyl cones, each pair with fixed isospin ($\uparrow$ or $\downarrow$) and both left and right chiralities, that respond to the chiral anomaly in the opposite way. Two edge states with opposite velocities (light red and light blue planes), appear at each boundary of the Dirac semimetal. Scattering processes within and between cones with scattering times τ_c, τ_v and τ_i are depicted by arrows. (d) The two pairs of Weyl nodes in (c) together comprise a pair of Dirac nodes. At a fixed energy cuts (C and D) between μ_L and μ_R, both bulk nodes are occupied while the surface states are only partially occupied. The total occupation in these planes describes two facing note-shaped patterns, illustrated in the bottom panel.

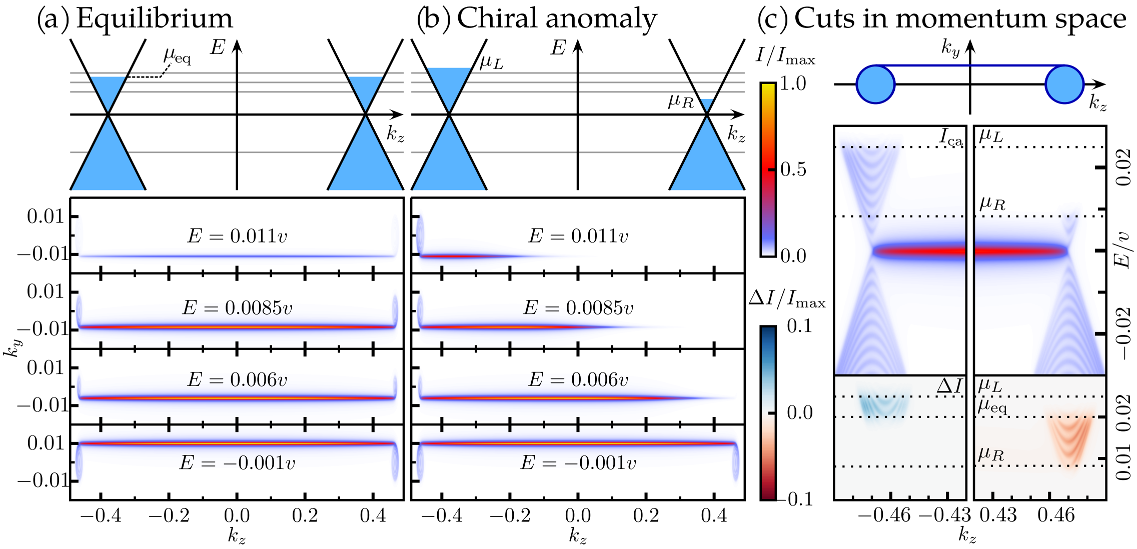

FIGURE 3.2: ARPES signatures of the chiral anomaly in Weyl semimetals. Numerically computed ARPES spectra for a doped Weyl semimetal film with $L = 2000$ layers in (a) equilibrium and (b) and (c) the chiral anomaly induced steady state. The parameters are such that the equilibrium chemical potential is $\mu_{\rm eq} = 0.02\,v$ while in non-equilibrium the left and right cones are filled up to $\mu_L = 0.025\,v$ and $\mu_R = 0.008\,v$ respectively. The lower panels in (a) and (b) show the momentum resolved spectra at a fixed energy, located as schematically shown with grey lines in the upper panels. In equilibrium (a), bulk cones and the surface state are observed, while the chiral anomaly (b) results in the disappearance of one cone and the emerging of the characteristic note-shaped pattern between μ_L and μ_R. The panel (c) shows the ARPES spectrum in non-equilibrium at a fixed $k_y = 0$, depicted in the top panel. The upper plot in the lower panel shows the total ARPES spectra, demonstrating the cone-like structure from the bulk and the flat surface state; the lower plot displays the intensity difference $\Delta I = I_{\rm ca} - I_{\rm eq}$ between the out-of-equilibrium and the equilibrium states. The dashed lines mark the chemical potentials μ_L, μ_R and $\mu_{\rm eq}$. These plots were obtained for $v = v_z$, $t = 0.5\,v$, $\epsilon = 6\,t$ and $b_z = 0.9\,v$ with the temperature set to $T = 0.001v$, which corresponds to $T \approx 5$ K for a typical Fermi velocity of $v = 0.45\,$eV (see Sec. 3.3.2 and Appendix B for details).

where we reintroduced the Fermi velocity v. As argued in Sec. 2.3.1, each Weyl node is a monopole of Berry curvature, and thus, acts as the origin of a Dirac string.[123] On a lattice, the Dirac string connects pairs of Weyl nodes of opposite chirality, resulting in surface states for a restricted range of momenta.

In the presence of non-orthogonal external electric and magnetic fields, the chiral anomaly leads to a non-conservation of the left and right handed electron densities.[28;29] This is expressed by the two coupled continuity equations

$$e\,\partial_t n_\chi + \nabla \cdot \mathbf{j}_\chi = \chi \frac{e^3}{4\pi^2\hbar^2}\mathbf{E}\cdot\mathbf{B} - \chi\frac{e}{2\,\tau_v}(n_R - n_L), \tag{3.28}$$

where n_χ is the density of left and right handed fermions measured from the Weyl point and $\mathbf{j}_\chi$ their current density. The first term on the right hand side is the anomaly contribution, Eq. (3.23), which has a different sign for the two chiralities; the second term represents the inter-valley scattering with rate τ_v^{-1}. At long times, a steady state with occupation

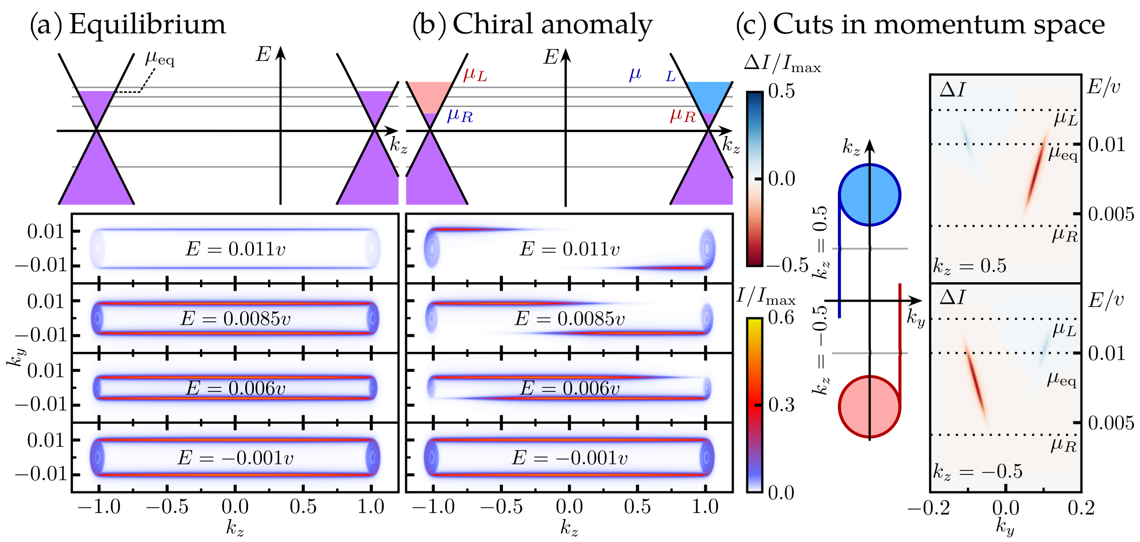

FIGURE 3.3: ARPES signatures of the chiral anomaly in Dirac semimetals. Numerically computed ARPES spectra for a doped Dirac semimetal film of $L = 2000$ layers in (a) equilibrium and (b) and (c) the presence of $\mathbf{E}\cdot\mathbf{B} \neq 0$. The spectra in (a) and (b) are the momentum resolved spectra at the fixed energies schematically shown at the top as gray lines. The equilibrium chemical potential is set to $\mu_{\text{eq}} = 0.020\,v$ while the left and right out of equilibrium chemical potentials are chosen to be $\mu_L = 0.025\,v$ and $\mu_R = 0.008\,v$. While there is a slight bulk Dirac cone intensity reduction from the equilibrium to the non-equilibrium situation, a stark qualitative difference is observed in the surface states that leads to the characteristic double note-shaped pattern. In (c) we plot the intensity difference $\Delta I = I_{\text{ca}} - I_{\text{eq}}$ for a fixed momentum $k_z = \pm 0.5$, which reveals the linear dispersion of the edge state. These plots were obtained for $M_0 = -0.2\,v$, $M_1 = -0.25\,v$, $M_2 = -0.75\,v$ and a temperature of $T = 0.001\,v$. With $v = 0.45\,\text{eV}$ for Na_3Bi, the temperature corresponds to $T \approx 5\,\text{K}$ and the induced chemical potential difference to $\delta\mu \approx 8\,\text{meV}$.

difference between the two chiralities is obtained. The continuity equations (3.28) and particle conservation then define the left and right handed chemical potentials

$$\mu_\chi = \left[\mu_{\text{eq}}^3 - \chi\frac{3}{2}\hbar v^3 e^2 \tau_v \mathbf{E}\cdot\mathbf{B}\right]^{1/3}, \tag{3.29}$$

where μ_{eq} is the equilibrium chemical potential and we have used that $n^{(\chi)} = \mu_\chi^3/(6\pi^2\hbar^3 v^3)$ for three dimensional Weyl fermions. In defining μ_χ we assume that the equilibration[‡] within a node with intra-valley relaxation time τ_c is much shorter than the inter-valley equilibration time τ_v [181] (both relaxation times τ_c and τ_v are calculated in Sec. 4.1). This similarly suggests that relaxation along the surfaces is dominated by small momentum scattering such that the Fermi arc linearly interpolates in momentum space between μ_L and μ_R, analogous to the voltage drop along an ohmic wire, leading to the steady-state occupation shown in the bottom of Fig. 3.1 (a). At a fixed energy between μ_R and μ_L, this results in the characteristic note-shaped occupation schematically shown in Fig. 3.1 (b) for the two constant energy planes denoted cut A and cut B.

[‡] The definition of the relaxation times includes energy relaxation processes at small momenta, which we assume happen on a timescale shorter than any elastic scattering.

Dirac semimetals can be understood as two copies of Weyl semimetals, with each Dirac node composed of two Weyl fermions of opposite chirality. The two copies are distinguished by their different total angular momentum,[184] which can be captured by an isospin quantum number that we denote with ↑ and ↓. As long as the crystal symmetry is not broken, the isospin remains a good quantum number. This has two important consequences: one, the two chiral fermions comprising a Dirac node are decoupled and therefore a gap does not open; two, the Weyl nodes still act as monopoles in momentum space and their Dirac string connects monopoles with opposite chirality but the *same* isospin. Dirac semimetals therefore have two Fermi arcs with opposite velocity on each surface.

The two pairs of Weyl fermions in the Dirac semimetal are oppositely affected by the chiral anomaly. External and non-orthogonal **E** and **B** fields shift the occupation in one Dirac cone to higher energies for one isospin and to lower for the other, and oppositely in the other Dirac cone, as schematically shown in Fig. 3.1 (c). For this steady state to be realized, intra-valley relaxation at fixed chirality must be larger than both the inter-valley relaxation, $\tau_c^{-1} \gg \tau_v^{-1}$, and the intra-valley relaxation between isospins, $\tau_c^{-1} \gg \tau_i^{-1}$ (the different relaxation processes are depicted with arrows in Fig. 3.1 (c)). Both conditions are estimated to be satisfied in Dirac semimetals.[181] Moreover, high mobility materials such as graphene satisfy the condition $\tau_c^{-1} \gg \tau_v^{-1}$, which allows for the experimental observation of a chemical potential imbalance[185] and suggests that it is also met in $\mathrm{Cd_3As_2}$.

The total occupation of a given Dirac cone is a superposition of both isospins, and therefore the bulk occupation in the chiral anomaly induced steady state is qualitatively the same as in its absence: two circular disks. In contrast, the tilt of the Fermi arcs and the resulting partial occupation at a fixed energy, see Fig. 3.1 (d), leads to a qualitatively new signature in the form of two facing note-shaped patterns (familiar from the Weyl semimetal case). This key property, which allows photoemission of Dirac semimetals to show evidence of the chiral anomaly, is a central result of this section.

3.3.2 Model and Methods

We establish by a numerical computation that these note-shaped patterns are indeed directly manifested in photoemission spectra. Our simulated data is obtained with exact diagonalization of tight binding models of Weyl and Dirac semimetals. For a Weyl semimetal, we take a Wilson lattice regularization[60] of the previously considered action describing Weyl fermions (3.24),[62]

$$\mathcal{H}^{\mathrm{W}}_{\mathbf{k}} = v(\sin k_y \sigma_x - \sin k_y \sigma_y)\tau_z + v_z \sin k_z \tau_y + M_{\mathbf{k}} \tau_x + \sum_{\mu} u^{\mu} b_{\mu} \tag{3.30}$$

with $M_{\mathbf{k}} = m + t\sum_i (1 - \cos k_i)$ breaking chiral symmetry[60] and the matrices $u^{\mu} = (\sigma_z\tau_y, -\sigma_x\tau_x, -\sigma_y\tau_x, \sigma_z)$. The velocity v in the x- and y-directions differs from that in the z-direction (v_z) consistent with experimentally relevant materials. For $b_\mu = 0$ and $m < 0$, the Hamiltonian models a three-dimensional topological insulator[84] with a phase transition to a trivial insulator at $m = 0$. At the phase transition, a degenerate three-dimensional Dirac node is obtained at $\mathbf{k} = 0$ that is split up into two separate Weyl nodes for $b_\mu \neq 0$. The inversion-symmetry breaking component b_0 separates the Weyl nodes in energy and the time-reversal-symmetry breaking vector **b** splits them in momentum space.[62] In our simulation we take $b_0 = 0$, $m = 0$ and fix the direction of $\mathbf{b} = b_z\hat{z}$ such that the Dirac cone is split into two Weyl cones at $k_z \approx \pm b_z/v_z$.

The low-energy spectrum of both Dirac semimetals Na_3Bi[121] and Cd_3As_2[184] is modeled by the Hamiltonian

$$\mathcal{H}^{\mathrm{D}}_{\mathbf{k}} = v(\sin k_x \sigma_x \tau_z - \sin k_y \sigma_y) + M_{\mathbf{k}} \sigma_z, \tag{3.31}$$

which can be understood as two time-reversed copies of a modified version of the two-band lattice model for Weyl semimetals, Eq. (2.37). The mass term $M_{\mathbf{k}} = M_0 + 2M_1(\cos k_z - 1) + 2M_2(\cos k_x + \cos k_y - 2)$ sets the velocity in k_z direction to $v_z = 2\sqrt{M_0 M_1}$ and the Dirac cones to be at $k_z^c = \pm\sqrt{M_0/M_1}$.

To model a film we take the system finite in the direction orthogonal to the separation of the cones in momentum space, which is the surface where the edge states are maximally visible. The ARPES spectrum is given by an integral over the local density of states

$$I(\mathbf{k}_\parallel, \omega) = \int dx \sum_n |\psi_{n,\mathbf{k}_\parallel}(x)|^2 \, \delta(\varepsilon_{n,\mathbf{k}_\parallel} - \omega) w(x) n_F(\omega - \mu_{\mathbf{k}_\parallel}), \tag{3.32}$$

where x is the coordinate in the finite direction of the film, $w(x) = \exp(-x/\xi)$ is a weight function modelling the incoming light's intensity decay with depth into the sample with decay length ξ, and n_F is the Fermi-Dirac distribution. The wavefunctions $\psi_{n,\mathbf{k}_\parallel}$ are the eigenfunctions of the Hamiltonians and $\varepsilon_{n,\mathbf{k}_\parallel}$ the corresponding eigenvalues, which depend on the momentum $\mathbf{k}_\parallel$ parallel to the surface. To model the chiral anomaly induced steady state, the chemical potential $\mu_{\mathbf{k}_\parallel}$ is taken to be $\mathbf{k}_\parallel$- and isospin-dependent. For the surface states, $\mu_{\mathbf{k}_\parallel}$ depends linearly on k_z.

3.3.3 ARPES Spectra for Weyl and Dirac Semimetals

In Fig. 3.2 (a), we plot the momentum resolved ARPES spectra at various fixed energies for a doped Weyl semimetal in equilibrium. Two bulk cones and one surface state at the probed surface are clearly seen; the surface state localized at the opposite surface is not visible due to the finite penetration depth of the incoming photon. In the presence of external fields $\mathbf{E}\cdot\mathbf{B} \neq 0$, the note-shaped pattern of the occupied states is seen in Fig. 3.2 (b) for energies between μ_L and μ_R. An alternative way to illustrate the steady state occupation with $\mu_R \neq \mu_L$ is through a cut in momentum space at a fixed $k_y = 0$ as provided in Fig. 3.2 (c). The pumping of charge between the different chiralities is clearly revealed in the intensity difference between the equilibrium I_{eq} and chiral anomaly induced steady state I_{ca}, shown in the lower panel of Fig. 3.2 (c).

The numerically computed ARPES spectra for a Dirac semimetal, shown in Fig. 3.3, similarly reveal the essential features discussed in Fig. 3.1. In equilibrium two bulk cones and two counter-propagating edge states at the same surface are seen in Fig. 3.3 (a), similar to the experimental observations for Na_3Bi.[186] The non-equilibrium spectra in the presence of electric and magnetic fields are qualitatively different; two copies of the note-shaped pattern clearly reveal the chiral anomaly in Dirac semimetals. To further highlight this feature, we plot, as for the Weyl semimetal, the intensity difference between the equilibrium and non-equilibrium in Fig. 3.3 (c) for fixed $k_z = \pm 0.5$. The qualitatively most notable feature is the partial occupation of the surface state that results in the stem of the note. The bulk, though, is not entirely insensitive to the chiral anomaly: first, states are occupied up to an energy $\max(\mu_L, \mu_R)$ that is higher than in the equilibrium situation; second, only one isospin band is filled between μ_L and μ_R resulting in a decreased intensity.

Note that the surface states survive in the strong field limit when Landau levels emerge,[187] but the shape of the Fermi arc may change. A drop in the occupation along the surface states, however, remains.

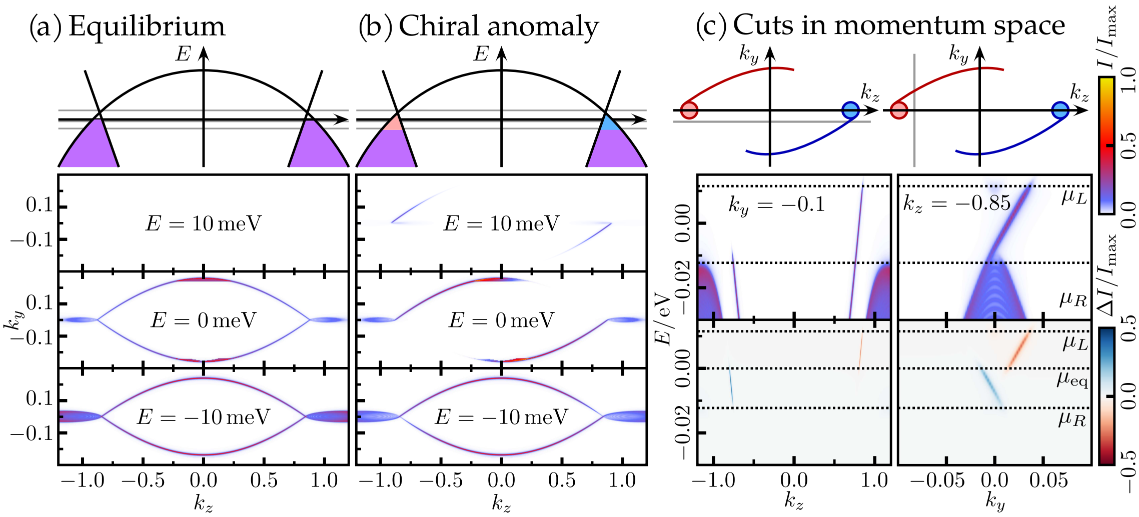

FIGURE 3.4: Visualization of the chiral anomaly in Na_3Bi (a) Numerically computed equilibrium ARPES spectra for a doped Dirac semimetal film Na_3Bi with $\mu_{\mathrm{eq}} = 0$. The pair of Fermi arcs are well within experimental energy and momentum resolution, confirmed by the recent experiment Ref. 186. (b) Chiral anomaly induced ARPES spectra for the same material and an estimate of the chiral chemical potential difference $\delta\mu \approx 20\,\mathrm{meV}$ derived in Appendix B. The Fermi arcs show evidence of partial occupation within experimental resolution. The upper panels in (a) and (b) show a schematic representation of the bulk band structure with two Dirac nodes connected at higher energies. (c) The lower panel shows two cuts through momentum space at $k_y = -0.1$ and $k_z = -0.85$ in units of the lattice constants and represented schematically by the horizontal and vertical light grey lines in the upper panel. The parameters of the low energy model used to obtain these figures are extracted from first principles in Ref. 121 and take the values $v = 0.45\,\mathrm{eV}$, $M_0 = -0.087\,\mathrm{eV}$, $M_1 = -0.11\,\mathrm{eV}$, $M_2 = -0.35\,\mathrm{eV}$ and $C_0 = -0.064\,\mathrm{eV}$, $C_1 = 0.094\,\mathrm{eV}$, $C_2 = -0.28\,\mathrm{eV}$. All calculations were performed at a temperature of $T = 1\,\mathrm{meV} = 11.6\,\mathrm{K}$ and for a film thickness of $L = 1000$ layers.

3.3.4 Experimental Details

From the chiral anomaly equation (3.29) we estimate the induced chiral chemical potential difference $\delta\mu = \mu_L - \mu_R$ to be within experimental state of the art. For the doping levels of Na_3Bi, an electric field strength of $10^4\,\mathrm{V\,m^{-1}}$ and a magnetic field of $1\,\mathrm{mT}$ gives $\delta\mu$ of the order of 10 meV, which is well within ARPES resolution. Remarkably, magnetic fields as small as $6\,\mu\mathrm{T}$ can still achieve observable $\delta\mu \approx 2.7\,\mathrm{meV}$ for Na_3Bi and can reach $\delta\mu \approx 5.4\,\mathrm{meV}$ in Cd_3As_2 (details of the experimental values used to compute these estimates for different materials are given in Tab. B.1). The fact that experimental observation of Fermi arcs in equilibrium have already been reported also bodes well.[38;39;186] To achieve momentum resolution in ARPES it is necessary to correlate the angle at which an electron is detected to its initial momentum. In free space, electrons move in straight lines making this task straightforward, and a constant electric field does not overly complicate it. A magnetic field turns the electron trajectories into spirals and may, depending on the distance to the detector and size of the magnetic field, make momentum resolution difficult. However, since the magnetic field strength needed for an observable effect is rather small, correcting induced deviations is plausible.[188] Alternatively, a larger uniform magnetic field finite within the sample could in principle be engineered with a ferromagnetic material in the picture frame geometry: a closed magnetic circuit that minimizes stray fields outside the sample that has been used to experimentally study ferromagnetic metals via ARPES[189] (see Appendix B.2).

Similarly, if either field can be turned off fast enough (faster than the inter-valley relaxation) a pump-probe setup could observe the non-equilibrium steady state and its equilibration, which would allow for a direct measurement of the inter-valley relaxation time in addition to visualizing the chiral anomaly. While none of these are simple tasks, we believe that the rewards are significant enough that the experimental challenge will be met.

In order to make definite contact with current experimental state of the art, we discuss the features of the chiral anomaly for Na_3Bi. To this extent, we combine the experimental constants given in Tab. B.1 with parameters obtained from *ab initio* calculations for this material that define the realistic low energy model described in Ref. 121. Such a model is a low energy expansion of Eq. (3.31) that accounts for a Fermi arc curvature via anisotropic coefficients and a topologically trivial function $\varepsilon_0(\mathbf{k})$ that is even in $\mathbf{k}$ and proportional to the identity. The equilibrium ARPES spectra computed for such model is shown in Fig. 3.4 (a). The figure shows a clear pair of curved Fermi arcs that connect two Dirac nodes. Distinguishing clearly these pair of arcs is well within experimental resolution, as confirmed by recent experiments [cf. Fig. 2A of Ref. 186]. Upon applying external fields that satisfy $\mathbf{E} \cdot \mathbf{B} \neq 0$, the chiral anomaly induces a chiral chemical potential difference of the order $\delta\mu \sim 10\,\text{meV}$, as estimated in Appendix B.3. In Fig. 3.4 (b), we show the chiral anomaly induced ARPES spectrum for Na_3Bi corresponding to such value of $\delta\mu$. The surface states at a constant energy are partially occupied and thus end before reaching the bulk Fermi surface, the latter not visible within this resolution. The observation of such features would directly visualize the chiral anomaly and confirm its effect on the surface electronic spectrum as predicted before.

In absence of momentum resolution, the angular averaged but energy resolved photoemission spectroscopy likewise contains direct signatures of the chiral anomaly. In Fig. 3.5 we plot the numerically computed PES spectra as a function of energy for both Weyl and Dirac semimetals. In equilibrium it has a single step that is smeared by temperature. In the non-equilibrium steady state, the occupation is shifted from lower energies to higher, such that the bulk spectra would have a double step profile, with one step at μ_L and the other at μ_R. In the total spectra the two steps are hard to see since the surface states contribute significantly to smoothen the profile. The intensity difference $\Delta I = I_{\text{eq}} - I_{\text{ca}}$ instead shows a characteristic peak-dip structure for low temperatures, which reflects the chiral anomaly pumping of fermions of one chirality into the other, evolving into a single peak as temperature is increased.

3.3.5 Summary and Conclusion

In conclusion, we have promoted photoemission as a tool to experimentally visualize the chiral anomaly in the solid state. The main effect that allows this is the tilt of the Fermi arc in the presence of non-orthogonal electric and magnetic fields that, through the chiral anomaly, pump electrons from one chirality to the other. As a consequence, the surface state occupation at a fixed energy no longer connects bulk nodes but rather terminates in between, resulting in a qualitatively distinct note-shaped photoemission pattern identifying the chiral anomaly. We argued, by estimating from experimentally available parameters the relevant chiral chemical potential difference to be about 10 meV, that a direct visualization

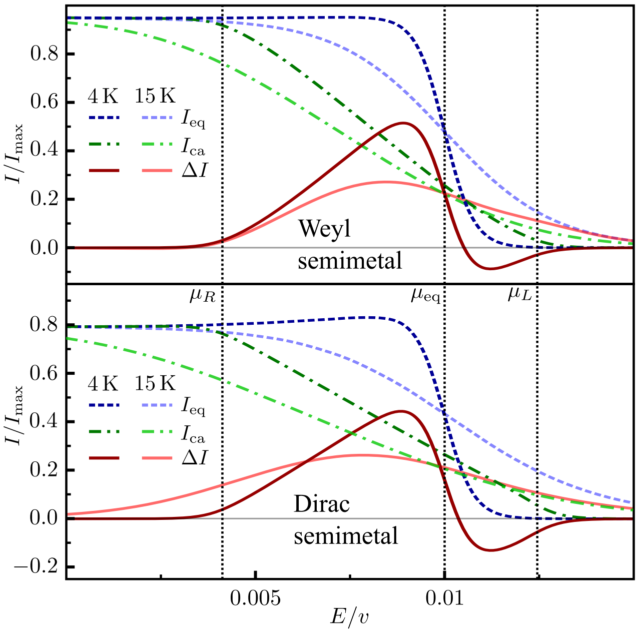

FIGURE 3.5: Chiral anomaly in PES spectra for Dirac and Weyl semimetals. Numerically computed PES intensities for Weyl and Dirac semimetals for two different temperatures. In equilibrium the intensity $I_{\rm eq}$ presents a single step around $\mu_{\rm eq}$, that is smeared out by increasing temperature and resembles the occupation of the cones. In non-equilibrium the intensity $I_{\rm ca}$ shows a double-step-profile with steps at μ_R and μ_L. Both $\mu_{R/L}$ include the temperature dependence of the chiral anomaly[51;172]. The difference $\Delta I = I_{\rm eq} - I_{\rm ca}$ highlights the effect of the chiral anomaly by a characteristic peak-dip structure for low temperatures, resulting from the shift in occupation of the two cones, that evolves into a single peak as temperature is increased. The parameters used to obtain these plots are $\mu_{\rm eq} = 0.020\,v$, $\mu_L = 0.025\,v$, $\mu_R = 0.008\,v$ at 4 K and $\mu_L = 0.024\,v$, $\mu_L = 0.005\,v$ at 15 K. The temperatures are chosen to be $T = 8 \cdot 10^{-4}\,v$ and $T = 2.9 \cdot 10^{-3}\,v$, corresponding to 4 K and 15 K for a typical value of $v = 0.45\,\mathrm{eV}$. The rest of parameters are chosen as in Fig. 3.2 and 3.3 for the upper and lower panel respectively.

of the chiral anomaly is within the state of the art. Were it to be realized experimentally in the way proposed here, a revealing light would be shed on the relation between two fundamental concepts: quantum anomalies and topological states of matter.

3.4 The Consistent and Covariant Anomalies

Historically, the nonconservation of chiral charge was first realized by a perturbative analysis of the divergence of the chiral current $\partial_\mu j_5^\mu$.[28;29] Since the nonconservation of chiral charge apparently violates the classical expectation from the field theory,[164] the perturbative result created a dispute about the applicability of the path integral approach that was resolved by Fujikawa, who took into account the change in the *measure* of the path integral, as we saw in Sec. 3.1.[61;190;191] In this section, we follow the original path by Adler, Bell and Jackiw and calculate the response of massless Dirac fermions to external fields perturbatively.[28;29] We see that an ambiguous result is obtained via the perturbative approach that can be fixed in two different ways, giving the so-called consistent and covariant anomalies.[67]

Instead of transforming the action via a chiral rotation, we calculate the Feyman diagrams that give the coupling the the vector potential A_μ. To obtain the chiral anomaly, we compute the triangle diagrams for the current. Adler and Bardeen showed that the contribution of triangle diagrams to observables is exact:[192] there are no higher-order corrections to these diagrams, which is the reason why perturbation theory and the approach based on manipulations of the path integral[190;191] give the same result. To distinguish between the responses of left- and right-handed chiralities, we project on each chirality χ with the operator $\mathcal{P}_\pm = (1 \pm \gamma^5)/2$. This allows to split the action of massless Dirac fermions into a sum of the contribution of both chiralities $\mathcal{S} = \mathcal{S}_+ + \mathcal{S}_-$ with

$$\mathcal{S}_\pm = \int d^4x\, \bar{\psi}\gamma^\mu \left(i\partial_\mu - A_\mu\right) \mathcal{P}_\pm \psi \tag{3.33}$$

and the corresponding partition function

$$\mathcal{Z}_\pm = e^{i\mathcal{S}_{\mathrm{eff},\pm}[A]} = \int \mathcal{D}(\bar{\psi}, \psi) \exp(i\mathcal{S}_\pm). \tag{3.34}$$

The chiral anomaly states that the chiral current is not conserved $\partial_\mu(j^\mu_+ - j^\mu_-) \neq 0$, while the vector current is, $\partial_\mu(j^\mu_+ + j^\mu_-) = 0$. Thus, it is sufficient to show that both contributions $j^\mu_\pm$ are not conserved individually. The nonvanishing contribution to $\partial_\mu j^\mu_\pm$ comes from the triangle diagrams,[28] which give the current

$$j^\mu_\pm(p) = \int \frac{d^4q}{(2\pi)^4} \int \frac{d^4k}{(2\pi)^4} \delta(p+q+k) \Delta^{\mu\nu\rho}_\pm(p,q,k) A_\nu(q) A_\rho(k) \tag{3.35}$$

with the three-point correlation function

$$\Delta^{\mu\nu\rho}_\pm(p,q,k) = \mathcal{Z}^{-1}_\pm \left.\frac{\delta^3 \mathcal{Z}_\pm}{\delta A_\mu(p) \delta A_\nu(q) \delta A_\rho(k)}\right|_{A=0}. \tag{3.36}$$

It comprises two triangle triagrams that are shown in Fig. 3.6 and explicitly reads, obeying momentum conservation $p + q + k = 0$,[193]

$$i\Delta^{\mu\nu\rho}_\pm(p,q,k) = \int \frac{d^4\ell}{(2\pi)^4} \frac{\mathrm{tr}\left[(-\not{\ell} + \not{p})\gamma^\mu(-\not{\ell})\gamma^\nu(-\not{\ell} - \not{q})\gamma^\rho \mathcal{P}_\pm\right]}{(\ell - p)^2 \ell^2 (\ell + q)^2} + (\mu \leftrightarrow \nu, p \leftrightarrow q). \tag{3.37}$$

where we inserted the Green's function for massless Dirac fermions $\mathcal{G}_0(p) = -i\not{p}/p^2$ and employed the Feyman slash notation $\not{p} \equiv \gamma^\mu p_\mu$.

Ultimately, we are interested in the divergence of $j^\mu_\pm$. Instead of evaluating the three-point correlation function $\Delta^{\mu\nu\rho}_\pm$, we can use a shortcut to the divergence of $j^\mu_\pm$ by computing the divergence of $\Delta^{\mu\nu\rho}_\pm$. To calculate $p_\mu \Delta^{\mu\nu\rho}_\pm(p,q,k)$, we use $p_\mu\gamma^\mu = (\not{p} - \not{\ell}) + \not{\ell}$ in first integral and $p_\mu\gamma^\mu = (\not{p} + \not{\ell}) - \not{\ell}$ in the second integral, giving

$$ip_\mu \Delta^{\mu\nu\rho}_\pm = \int \frac{d^4\ell}{(2\pi)^4} \left[I_1(\ell + q) - I_1(\ell) + I_2(\ell + p - q) - I_2(\ell)\right] \tag{3.38}$$

with the functions

$$I_1(\ell) = \frac{\mathrm{tr}\left[(-\not{\ell} + \not{q})\gamma^\nu(-\not{\ell})\gamma^\rho \mathcal{P}_\pm\right]}{(\ell - q)^2 \ell^2}, \quad I_2(\ell) = \frac{\mathrm{tr}\left[(-\not{\ell} + \not{p})\gamma^\nu(-\not{\ell} - \not{q})\gamma^\rho \mathcal{P}_\pm\right]}{(\ell - p)^2 (\ell + q)^2}. \tag{3.39}$$

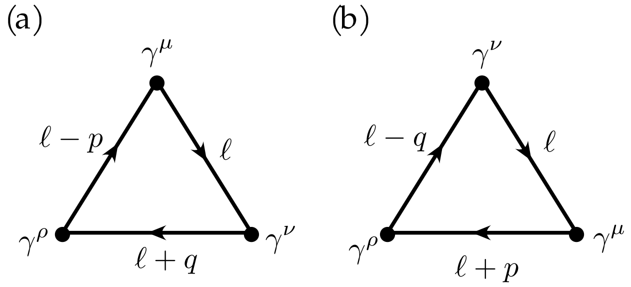

FIGURE 3.6: Two triangle diagrams contribution to the chiral anomaly. The matrices γ^ν and γ^ρ are connected to the vector potential $A_\nu(q)$ and $A_\rho(k)$, respectively. The matrix $\gamma^\mu \mathcal{P}_\pm$ is connected to the current operator $j_\mu(p)$.

One is tempted to argue that the integral in Eq. (3.38) gives zero: shifting the integration variable $\ell \to \ell + q$ in $I_1(\ell)$ and $\ell \to \ell + p - q$ in $I_2(\ell)$ results in mutually canceling contributions of I_1 and I_2, respectively. However, this approach is incomplete. Since the integral is linearly divergent, its value changes with the substitution.[61] Thus, we chose the most general substitution $\ell \to \ell + c(p-q) + d(p+q)$, which gives[193]

$$p_\mu \Delta_\pm^{\mu\nu\rho} = \pm \frac{-i}{8\pi^2}(1-c)\epsilon^{\nu\rho\alpha\beta} q_\alpha k_\beta. \tag{3.40a}$$

Analogue, we can compute the divergences with respect to the other momenta, giving[193]

$$q_\nu \Delta_\pm^{\mu\nu\rho} = \pm \frac{-i}{8\pi^2}(1-c)\epsilon^{\mu\rho\alpha\beta} k_\alpha p_\beta \tag{3.40b}$$

$$k_\rho \Delta_\pm^{\mu\nu\rho} = \pm \frac{-i}{8\pi^2} 2c\epsilon^{\nu\rho\alpha\beta} q_\alpha p_\beta. \tag{3.40c}$$

This means that the one-loop three-point function of the chiral current is finite but undetermined. The value of c depends on the physical constraints the three-point function is supposed to obey.

One one hand, we can demand that the function obeys Bose symmetry on the external legs, i.e., it is indeed given by Eq. (3.36) where the order of differentiation does not play a role.[193] Then, all legs of the triangle diagram are the same, implying that all divergences must be equal, which is satisfied by $c = 1/3$. This gives the *consistent* form of the anomaly,

$$\partial_\mu \mathcal{J}_\pm^\mu = \pm \frac{1}{96\pi^2} \epsilon^{\mu\nu\rho\sigma} F_{\mu\nu} F_{\rho\sigma}. \tag{3.41}$$

One the other hand, we can demand that the current couples without the anomaly to external gauge fields. This singles out one particular vertex and demands that the divergence of the other two vanishes, $q_\nu \Delta_\pm^{\mu\nu\rho} = p_\mu \Delta_\pm^{\mu\nu\rho} = 0$, implying $c = 1$. This gives the *covariant* form of the anomaly,

$$\partial_\mu J_\pm^\mu = \pm \frac{1}{32\pi^2} \epsilon^{\mu\nu\rho\sigma} F_{\mu\nu} F_{\rho\sigma}. \tag{3.42}$$

In the following, we use the notation shown above for the two current resulting from the chiral anomaly—the covariant current $\mathcal{J}_\pm^\mu$ and the consistent current $J_\pm^\mu$.

The difference between consistent and covariant current becomes evident when we introduce different right- and left-handed vector potentials, $A_\mu^\chi = A_\mu + \chi A_\mu^5$ that act on the Weyl node of chirality χ. From the action of Weyl fermions, Eq. (3.24), we see how it is possible that different vector potentials act on the two chiralities: the Weyl spinors are eigenfunctions of γ^5, but with a different eigenvalue that gives their chirality.[117] Thus, the term $A_\mu + b_\mu \gamma^5$ acts differently on each chirality, effectively resulting in $A_\mu^\chi = A_\mu + \chi b_\mu$ for the chirality χ, i.e., the Weyl node separation acts as an effective axial gauge field.[54] We acknowledge the different effective potentials by replacing $A_\mu \to A_\mu^\pm$ in Eq. (3.41), which allows to rewrite the divergence of the consistent vector and axial currents $\mathcal{J}$ and $\mathcal{J}_5$ in terms of A_μ and A_μ^5,

$$\partial_\mu \mathcal{J}^\mu = \frac{1}{24\pi^2} \epsilon^{\mu\nu\rho\sigma} F_{\mu\nu} F^5_{\rho\sigma} \tag{3.43}$$

$$\partial_\mu \mathcal{J}_5^\mu = \frac{1}{48\pi^2} \epsilon^{\mu\nu\rho\sigma} \left(F_{\mu\nu} F_{\rho\sigma} + F^5_{\mu\nu} F^5_{\rho\sigma} \right) \tag{3.44}$$

with $F_{\mu\nu} = \partial_\mu A_\nu - \partial_\nu A_\mu$ and $F^5_{\mu\nu} = \partial_\mu A^5_\nu - \partial_\nu A^5_\mu$. This result is highly problematic, since Eq. (3.43) violates charge conservation. As we saw above, in Eqs. (3.40), the consistent anomaly also violates gauge invariance.[67] Loosing gauge invariance is not our concern here: one could argue that, since the Weyl node separation b_μ that acts as A_μ^5 is a physical observable (visible, e.g., in the anomalous Hall conductance, Eq. (3.26)) rather than a gauge field, no gauge invariance is necessary. Readers who feel uncomfortable about this argument have the right intuition—we leave the subtle issue of gauge invariance aside for now, but address it again in Sec. 3.5. As soon as gauge invariance is lost, more gauge-violating terms can be added to the action.[194] Following Bardeen, we add an additional contribution to the action, the so-called Bardeen counterterms that modify

$$\mathcal{S}_{\text{eff}} \left[A, A^5 \right] \to \mathcal{S}_{\text{eff}} \left[A, A^5 \right] + \frac{1}{12\pi^2} \int d^4x \, \epsilon^{\mu\nu\rho\sigma} A_\mu A^5_\nu F_{\rho\sigma}. \tag{3.45}$$

Computing the consistent current as a variation of the new effective action, we find the currents[193]

$$\partial_\mu \mathcal{J}^\mu = 0, \qquad \partial_\mu \mathcal{J}_5^\mu = \frac{1}{16\pi^2} \epsilon^{\mu\nu\rho\sigma} \left(F_{\mu\nu} F_{\rho\sigma} + \frac{1}{3} F^5_{\mu\nu} F^5_{\rho\sigma} \right), \tag{3.46}$$

which is the consistent anomaly. It is charge-conserving, which we ensured by choosing the particular form of the Bardeen counterterm in Eq. (3.45). It does not, however, conserve the chiral charge. The first contribution to the anomaly in the chiral charge $\partial_\mu \mathcal{J}_5^\mu$ is familiar—we already found the same response from the chiral transformation of the action, Eq. (3.23). The second term is new and it results from considering the Weyl node separation as an axial field $b_\mu \to A_\mu^5$. Thus, spatial and temporal fluctuations in the Weyl node separation give rise the axial fields

$$\mathbf{B}_5 = \nabla \times \mathbf{b}, \qquad \mathbf{E}_5 = -\nabla b_0 - \partial_t \mathbf{b}. \tag{3.47}$$

As elaborated in Ref. 195, strain in Weyl semimetals can induce such fluctuations in the node separation that give the axial fields $\mathbf{B}_5$ and $\mathbf{E}_5$.

The covariant anomaly, on the other hand, is gauge-invariant. Adding a Bardeen counterterm such as (3.45) would spoil this gauge invariance, so that we can compute directly the covariant currents from Eq. (3.42), giving

$$\partial_\mu J^\mu = \frac{1}{2\pi^2} \left(\mathbf{E} \cdot \mathbf{B}_5 + \mathbf{E}_5 \cdot \mathbf{B} \right), \qquad \partial_\mu J_5^\mu = \frac{1}{2\pi^2} \left(\mathbf{E} \cdot \mathbf{B} + \mathbf{E}_5 \cdot \mathbf{B}_5 \right). \tag{3.48}$$

These relations are gauge-invariant, but violate charge conservation. Consistent and covariant currents are related by additional Chern-Simons currents, the so-called Bardeen-Zumino polynomials.[67] In Weyl semimetals, this current has a topological origin and it is directly related to the Hall conductance.[196]

What is the physical meaning of the two different currents and the Bardeen-Zumino polynomial connecting them? The answer depends on the physical context. For example, in quantum Hall systems, the one-dimensional chiral edge modes exhibit both anomalies. The Bardeen-Zumino polynomial is the current provided by the Hall effect in the bulk that ensures charge-conservation.[197;198] In this example, the total charge is conserved—however, if we consider the two chiral edge modes just around the Fermi surface, without a connection to the bulk, charge is (apparently) created and annihilated in the two counterpropagating modes. In the following section, we show a similar identification of the consistent and covariant anomalies in Weyl semimetals.

3.5 Consistent and Covariant Anomalies on a Lattice

How do the consistent and covariant anomalies manifest themselves in Weyl semimetals? In this section, we consider a space- and time-dependent Weyl node separation b_μ, as in strained or inhomogenously magnetized Weyl semimetals[195] or Helium-3.[34;199] A space- and time-dependent node separation generates axial magnetic ($\mathbf{B}_5$) and electric ($\mathbf{E}_5$) fields, Eq. (3.47), which couple with opposite signs to opposite chiralities.[200–205] These axial fields lead to a rich phenomenology including strain-enhanced conductivity,[203;204] pseudo-chiral magnetic effects,[204;206–208] chiral lensing,[209;210] pseudomagnetic helicons,[211] chiral plasmons,[212] and a chiral Hall effect[213] among higher order effects.[214–216] Unlike a magnetic field $\mathbf{B}$, which generates Landau levels dispersing in opposite direction for opposite chiralities, $\mathbf{B}_5$ generates pseudo-Landau levels that disperse in the same direction for both chiralities. This property allows the left and right chirality to be depleted and filled, respectively, when $\mathbf{E}_5$ is applied.

The combined electromagnetic and pseudo-electromagnetic field contribution to the chiral anomaly is expressed as a finite four-divergence of the difference between left and right (consistent) currents $\mathcal{J}_5^\mu = \mathcal{J}_L^\mu - \mathcal{J}_R^\mu$,[164;193]

$$\partial_\mu \mathcal{J}_5^\mu = \frac{1}{2\pi^2}\left(\mathbf{E}\cdot\mathbf{B} + \frac{1}{3}\mathbf{E}_5\cdot\mathbf{B}_5\right) \tag{3.49}$$

while the consistent vector current $\mathcal{J}^\mu = \mathcal{J}_L^\mu + \mathcal{J}_R^\mu$ is naturally conserved, cf. Eq. (3.46). While Fermi arcs have been interpreted as the zeroth pseudo-Landau level of $\mathbf{B}_5$,[204] their precise role in the chiral anomaly is still to be systematically addressed.[66] Moreover, $\mathbf{B}_5$ contributes to the covariant version of the anomaly, which only counts charges that traverse the original Fermi surface, leading to the non-conservation of the covariant vector current J^μ, Eq. (3.48). The covariant currents are formally related to the consistent currents at the field theory or semiclassical level by additional currents known as Bardeen polynomials, which act like boundary conditions for the accumulated charge at the cut-off energy.[55;64;194;196;217] Although the consistent anomaly sets observables[217;218] such as the anomalous Hall conductivity[217] or chiral pseudo magnetic plasmons[218] and discards unphysical responses,[55;62;193;217] the Bardeen polynomials sacrifice the Fermi surface based intuition[219] of the covariant picture and more specifically how a lattice implementation of Weyl fermions restores charge conservation. Similar to the previously discussed connection between the anomaly for chiral edge states of the quantum Hall effect,[197;198] consistent and covariant currents can be defined for a 3+1D Weyl fermion living at the edge of a 4+1D Quantum Hall effect.

The above considerations signal the need for a unifying approach where Landau and pseudo-Landau levels, consistent and covariant anomalies, and Fermi arcs are treated on the same footing from a lattice perspective. In this section, we develop such a framework, with the main benefit of providing a simple physical intuition applicable to a variety of physical systems and field profiles. We exemplify its usefulness by identifying Fermi arcs as a source for the covariant anomaly terms of Eq. (3.48) and relating them to the Bardeen polynomials, the topological content of which was pointed out in Ref. 196. By separately examining each of the anomalous terms in Eqs. (3.49) and (3.48) in a realistic lattice implementation of Weyl semimetals with arbitrary profiles of $\mathbf{B}_5$, we provide a lattice interpretation of the consistent and covariant anomalies.

3.5.1 Model and Methods

Our starting point is the microscopic Weyl semimetal model[62] used before in Eq. (3.30) with $b_\mu \to v b_\mu$ and isotropic velocities v for convenience,

$$\begin{aligned}\mathcal{H} =& v\left[\sin(ak_y)\sigma_x - \sin(ak_x)\sigma_y\right]\tau_z + v\sin(ak_z)\tau_y + m\tau_x \\ &+ t\sum_i \left[1-\cos(ak_i)\right]\tau_x + va\sum_\mu u^\mu b_\mu,\end{aligned} \tag{3.50}$$

with a the lattice constant and where σ and τ denote two sets of Pauli matrices, which typically correspond to spin and orbital degrees of freedom, respectively. The matrices associated with $b_\mu = (b_0, \mathbf{b})$ are $u^\mu = (\sigma_z\tau_y, -\sigma_x\tau_x, -\sigma_y\tau_x, \sigma_z)$. Neglecting higher orders in b_μ, the model has one pair of Weyl nodes for $m^2 < v^2|\mathbf{b}^2 - b_0^2|$.[62] Unless stated otherwise, we set $m = 0$ and $t = 2v/\sqrt{3}$; with $\mathbf{b}$ oriented along a reciprocal lattice vector, this parameter choice gives two Weyl nodes located at $\pm\mathbf{b}[1+\mathcal{O}(b_0^2)] + \mathcal{O}(b_j^5)$ and energies $\pm vab_0[1+\mathcal{O}(b_j^2)] + \mathcal{O}(b_0^3)$. Simple generalizations of Eq. (3.50) that do not modify the essential physics described in this work can be used to model Dirac (e.g., Cd_3As_2, Na_3Bi) and Weyl semimetal (e.g., TaAs family) materials.[36;121;184]

To introduce a chiral density $\rho_5 = \mathcal{J}_5^0$, we define the gamma matrices with the signature $(+---)$, $\gamma^\mu = (\tau_x, i\sigma_y\tau_y, -i\sigma_x\tau_y, i\tau_z)$ and their product $\gamma^5 = i\gamma^0\gamma^1\gamma^2\gamma^3 = \sigma_z\tau_y$, such that $u^\mu = \gamma^0\gamma^\mu\gamma^5$. The space dependent chiral density is

$$\rho_5(\mathbf{x}) = \sum_{n\in\mathrm{occ.}} \langle\psi_n(\mathbf{x})|\gamma^5|\psi_n(\mathbf{x})\rangle, \tag{3.51}$$

in analogy with the total density $\rho(\mathbf{x})$, which is defined by replacing γ^5 with the identity in Eq. (3.51).

As briefly mentioned in Sec. 3.3.2, the Hamiltonian Eq. (3.50) is a lattice regularization of an effective field theory that describes the physics of two species of Weyl fermions of opposite chiralities via the action

$$\mathcal{S} = \int d^4x\,\bar{\psi}\left[\gamma^\mu\left(i\partial_\mu - A_\mu - b_\mu\gamma^5\right) - m\right]\psi, \tag{3.52}$$

cf. Eq. (3.24). The Weyl fermions are coupled to an emergent chiral field b_μ and they are regularized via the Wilson fermion map $k_i \to \sin k_i$, and $m \to m + t\sum_i(1-\cos k_i)$.[60] The space-like component $\mathbf{b}$ denotes their separation in momentum, and the time-like component b_0 in energy. Spatial and temporal variations of $\mathbf{b}$ generate the chiral fields $\mathbf{B}_5 = \nabla \times \mathbf{b}$ and $\mathbf{E}_5 = -\partial_0 \mathbf{b}$.

We compute the response of the Weyl semimetal to external fields $\mathbf{E}$ and $\mathbf{E}_5$ numerically by perturbing the system infinitesimally. A time-dependent vector potential $\mathbf{A} = -\mathbf{E}t$ gives an electric field $\mathbf{E}$, and analogously a time-dependent node separation $\mathbf{b} = -\mathbf{E}_5 t$. The time-derivative of any expectation value f is expressed in terms of the response to changes in $\mathbf{A}$ and $\mathbf{b}$,

$$\frac{df}{dt} = -\mathbf{E} \cdot \partial_{\mathbf{A}} f - \mathbf{E}_5 \cdot \partial_{\mathbf{b}} f, \tag{3.53}$$

which is especially handy when evaluating time-derivatives proportional to $\mathbf{E}$ and $\mathbf{E}_5$, such as $\partial_\mu j^\mu$ and $\partial_\mu j_5^\mu$, where f corresponds to ρ or ρ_5 in the following. The response of the density to external fields $\mathbf{E}$ and $\mathbf{E}_5$ is the response to a shift $\mathbf{A} \to \mathbf{A} + d\mathbf{A}$ and $\mathbf{b} \to \mathbf{b} + d\mathbf{b}$, respectively. In particular, the chiral density at site y,

$$\rho_5(y) = \sum_{n \in \text{occ.}} \langle \psi_n | \gamma^5 \Pi_y | \psi_n \rangle, \tag{3.54}$$

with Π_y the projection of site y changes for an infinitesimal variation $\mathbf{b} \to \mathbf{b} + d\mathbf{b}$. The single-particle states change as

$$|\psi_n(\mathbf{b} + d\mathbf{b})\rangle = |\psi_n\rangle + d\mathbf{b} \cdot \sum_{m \neq n} \frac{|\psi_m\rangle \langle \psi_n | \partial_{\mathbf{b}} \mathcal{H} | \psi_m \rangle}{\varepsilon_n - \varepsilon_m} \tag{3.55}$$

resulting in the response of the chiral density

$$\frac{d\rho_5(y)}{d\mathbf{b}} = \sum_{n \in \text{occ.}} \sum_{m \neq n} \frac{\langle \psi_n | \gamma^5 \Pi_y | \psi_m \rangle \langle \psi_n | \partial_{\mathbf{b}} \mathcal{H} | \psi_m \rangle}{\varepsilon_n - \varepsilon_m} + \text{h.c.} \tag{3.56}$$

with the sum over the states n that are initially occupied at a node separation $\mathbf{b}$.

The Fermi surface contribution, on the other hand, just counts the subset of states that are lifted above the Fermi level for $\mathbf{b} \to \mathbf{b} + d\mathbf{b}$, minus the states that are pushed below the Fermi level, $d\rho_5^{FS} = d\rho_5^+ - d\rho_5^-$ with

$$d\rho_5^+(y) = \sum_{\substack{\varepsilon_n < \mu, \\ \varepsilon_n + d\varepsilon_n > \mu}} \langle \psi_n | \gamma^5 \Pi_y | \psi_n \rangle, \qquad d\rho_5^-(y) = \sum_{\substack{\varepsilon_n > \mu, \\ \varepsilon_n + d\varepsilon_n < \mu}} \langle \psi_n | \gamma^5 \Pi_y | \psi_n \rangle \tag{3.57}$$

or, expressed in terms of Heaviside functions,

$$d\rho_5^\pm(y) = \pm \sum_n \langle \psi_n | \gamma^5 \Pi_y | \psi_n \rangle \Theta(\pm d\varepsilon_n) \left[\Theta(\mu - \varepsilon_n) - \Theta(\mu - (\varepsilon_n + d\varepsilon_n)) \right].$$

To first order in perturbation theory, the infinitesimal change in the energies is

$$d\varepsilon_n = d\mathbf{b} \cdot \langle \psi_n | \partial_{\mathbf{b}} \mathcal{H} | \psi_n \rangle \tag{3.58}$$

and the sum of Heaviside functions reduces to

$$\Theta(\mu - \varepsilon_n) - \Theta(\mu - (\varepsilon_n + d\varepsilon_n)) = d\varepsilon_n \delta(\mu - \varepsilon_n), \tag{3.59}$$

finally giving

$$\frac{d\rho_5^{FS}(y)}{d\mathbf{b}} = \sum_n \langle \psi_n | \gamma^5 \Pi_y | \psi_n \rangle \langle \psi_n | \partial_{\mathbf{b}} \mathcal{H} | \psi_n \rangle \delta(\mu - \varepsilon_n). \tag{3.60}$$

The delta function is implemented as a Lorentz function $\delta(x) = \lim_{\eta \to 0} \eta / (\pi(\eta^2 + x^2))$.

3.5.2 Lattice Results for Consistent and Covariant Anomalies

The simplest realization of $\mathbf{B}_5$ occurs at the boundary of any Weyl semimetal, where the Weyl node separation b_μ must go to zero.[193;201;204] For concreteness we take periodic boundaries along x and z but open along $y \in [-L/2, L/2]$, modeled by a discontinuous spatial component $\mathbf{b}$

$$\mathbf{b}(y) = b_z[\Theta(y - L/2) - \Theta(y + L/2)]\hat{z}, \tag{3.61}$$

with b_z a constant, leading to

$$\mathbf{B}_5(y) = b_z[\delta(y - L/2) - \delta(y + L/2)]\hat{x}, \tag{3.62}$$

localized at the surface. As discussed in Ref. 204, this $\mathbf{B}_5$ generates surface pseudo-Landau levels dispersing along $\pm k_x$, with opposite signs at each surface. The Fermi surface traces an arc, establishing the correspondence between surface pseudo-Landau levels induced by $\mathbf{B}_5$ and the topological surface states of Weyl semimetals. This is analogous to the effect of a uniform external magnetic field; a $\mathbf{B} = B\hat{z}$ parallel to the Weyl node separation leads to a spectrum hosting bulk Landau levels dispersing along $\pm k_z$, where the sign is set by the Weyl node chirality. When both $\mathbf{B}$ and surface $\mathbf{B}_5$ are present, Landau and pseudo-Landau levels coexist and the Fermi surface at the Fermi energy ε_F traces a square (or parallelogram for general orientations of $\mathbf{B}$)[187;220] shown in Fig. 3.7 (a) for $\varepsilon_\mathrm{F} = 0$, which we assume in what follows.

The occurrence of Landau levels under pseudo-magnetic and magnetic fields motivates us to discuss all the anomaly contributions in this framework. We first recall the origin of the most familiar $\mathbf{E} \cdot \mathbf{B}$ term in Eq. (3.49) in this picture.[30] An electric field along z, $\mathbf{E} = E\hat{z}$, pumps charges of one chirality to the other via the Landau levels created by $\mathbf{B}$ connected through the band bottom, realizing the chiral anomaly in the lattice[30] (see Fig. 3.7 (b)). Interestingly, since the Fermi surface is a connected parallelogram,[187;220] internode scattering is not required to equilibrate the chiral imbalance,[40] but rather intranode scattering suffices.[66]

The pseudo-Landau level interpretation of the Fermi arcs similarly suggests the existence of a term $\mathbf{E} \cdot \mathbf{B}_5$ in the lattice picture, as in Eq. (3.48). Since the pseudo-Landau levels disperse along $\pm k_x$ on each surface, applying an electric field along x, $\mathbf{E} = E\hat{x}$, will deplete charges from one surface and generate charges on the other. This is visualized in Fig. 3.7 (c). In analogy with the arguments of Ref. 30 we can interpret this as an anomaly of *each* surface state due to $\mathbf{E} \cdot \mathbf{B}_5$. In contrast to the usual chiral anomaly, where the total charge is locally conserved, the spatial separation of the two surfaces leads to an apparent violation of local charge conservation, as in Eq. (3.48). This otherwise subtle difference is evident in our Landau and pseudo-Landau level picture.

The spectral flow between the pseudo-Landau levels at each surface happens via the bulk bands connecting them, fixing charge conservation. As time increases, the electric field shifts k_x, which due to position-momentum locking[204] determines the average y position, creating a Hall current

$$\delta\mathbf{j} = -\frac{1}{2\pi^2} b_z E_x \hat{y}, \tag{3.63}$$

which we can interpret as the net current flowing along the y-direction from one surface to the other through the bottom of the band. In the bulk, b_z is a constant leading to $\nabla \cdot \delta\mathbf{j} = 0$ and no accumulation of charge in the bulk. At the surface, the Weyl node

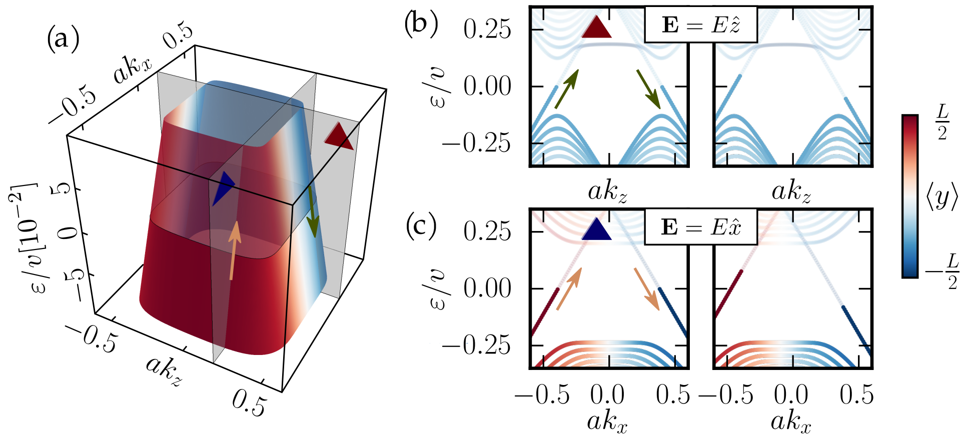

FIGURE 3.7: Unified lattice picture of $\mathbf{E}\cdot\mathbf{B}$ and $\mathbf{E}\cdot\mathbf{B}_5$. (a) The spectrum of Eq. (3.50) with periodic boundaries along x and z but open along y showing the coexisting Fermi arcs and Landau levels of $\mathbf{B} = B\hat{z}$. The color denotes the position of the wave function along y, with red/blue corresponding to $y = \pm L/2$. States up to $\varepsilon = 0$ are occupied; unoccupied states are shown semi-transparent. (b) (c) The Landau (pseudo Landau) levels of $\mathbf{B}$ ($\mathbf{B}_5$) on the red (blue) triangle plane show the anomaly in the presence of $\mathbf{E} = E\,\hat{z}$ ($\mathbf{E} = E\hat{x}$), where the spectral flow at the Fermi surface is schematically shown by the green (orange) arrows. The left panels in (b) and (c) show the occupation in equilibrium, while the right panels show the dispersion for $A_z = 0.08/a$ ($A_x = 0.08/a$) with the same momenta occupied as in the left panels. We use open boundary conditions with $L/a = 100$ sites; the magnetic field has the magnetic length $\ell_B = 11.2a$.

separation varies, leading to the spatial current having a finite divergence, positive on one surface and negative on the other.

We can similarly understand a more general $\mathbf{B}_5$ profile, and its interplay with magnetic field $\mathbf{B}$, in terms of Landau and pseudo-Landau levels. For instance, a uniform bulk $\mathbf{B}_5$ along $\hat{z}$ arises from $\mathbf{b} = B_5 y\hat{x}$; its spectrum is shown in Fig. 3.8 (a). It shows a characteristic butterfly Fermi surface that is obtained from the square Fermi surface of Fig. 3.7 (a) by noticing that the two bulk Landau levels have lengths given by $\mathbf{B} \pm \mathbf{B}_5$. When $\mathbf{B}_5$ surpasses $\mathbf{B}$, the Fermi surface acquires a twist leading to the characteristic butterfly of Fig. 3.7 (a). The butterfly Fermi surface resembles the spectrum found in Ref. 221 in a seemingly unrelated context, and thus is an alternative way to achieve the peculiar quantum oscillation signals associated to it. Now, as Fig. 3.8 (b) and (c) shows, an electric field $\mathbf{E} = E\hat{z}$ parallel to $\mathbf{B}_5$ makes the bulk gain charge above the Fermi level (upward arrows), while the surface loses charge (downward arrows). This is further corroborated in Fig. 3.8 (e) where the spatial profile of the charge relative to that at $t = 0$ is shown for different times. While the bulk gains charge uniformly throughout space, as both $\mathbf{E}$ and $\mathbf{B}_5$ are constant in the bulk, the surfaces lose the same charge within a smaller real-space extend, due to the sharp drop of $\mathbf{b}$ (and thus large $\mathbf{B}_5$) at the boundary.

Our previous examples, summarized in Figs. 3.7 and 3.8, are a consequence of the covariant anomaly that only considers the depletion and growth of charges at the Fermi level. By construction, the corresponding covariant current J^μ misses information from states away far from the Fermi level, and thus it is not conserved as dictated by Eq. (3.48).[193] The conserved physical (consistent) current, $\mathcal{J}^\mu$, can be obtained from the covariant current by adding the Bardeen Polynomials δj^μ such that $\partial_\mu(J^\mu + \delta j^\mu) = \partial_\mu \mathcal{J}^\mu = 0$.[55;217]

Using Eq. (3.48) and the definition of the pseudo-fields it is simple to write the Bardeen Polynomials as

$$\delta j^0 = \frac{1}{2\pi^2}\mathbf{b}\cdot\mathbf{B}; \qquad \delta\mathbf{j} = \frac{1}{2\pi^2}\left(b_0\mathbf{B} - \mathbf{b}\times\mathbf{E}\right). \tag{3.64}$$

Comparing (3.64) to Eq. (3.63) of our first example (Fig. 3.7), one can identify the latter as a part of the Bardeen polynomials.[193] The benefit of the Landau level approach is to retain the physical meaning: in this example, $\mathbf{E}_5 = 0$ and the finite $\mathbf{E}\cdot\mathbf{B}_5$ pumps charge from one surface to another via the Hall effect Eq. (3.63) through $\partial_t J^0 = \mathbf{E}\cdot\mathbf{B}_5/(2\pi^2)$. Our second example (Fig. 3.8) can be interpreted in a similar fashion. In the bulk charge grows as $\partial_t J^0 = \mathbf{E}\cdot\mathbf{B}_5/(2\pi^2)$ locally,[§] while at the surface charge is depleted since $\mathbf{B}_5$ has an opposite sign compared to the bulk. There is a corresponding current that pumps charge from the surface to the bulk, which is given by the Bardeen polynomial, read of from (3.64) $\delta\mathbf{j} = -\mathbf{b}\times\mathbf{E}/(2\pi^2)$. Since we have $\mathbf{b} = B_5 y\hat{x}$, there are local currents in the bulk of the system $\delta\mathbf{j} = B_5 E y\hat{y}/(2\pi^2)$. The divergence of this current, $\nabla\cdot\delta\mathbf{j} = \mathbf{B}_5\cdot\mathbf{E}/(2\pi^2)$, is precisely the growth rate of local charge observed in Fig. 3.8 (c), hence reconciling from a lattice perspective the Fermi surface (covariant) picture with charge conservation (consistent anomaly).

Using our approach, it is also possible to understand physically $\mathbf{E}_5\cdot\mathbf{B}$ in (3.48) and $\mathbf{E}_5\cdot\mathbf{B}_5$ in Eq. (3.49) by allowing for more general spatio-temporal variations of the Weyl node separation. We consider first $\mathbf{b} = -E_5 t\hat{z}$ that leads to a uniform $\mathbf{E}_5 \parallel \hat{z}$. The presence of $\mathbf{B}$ activates the second term of (3.48), suggesting that charge is being created at the Fermi surface at rate $\mathbf{E}_5\cdot\mathbf{B}/(2\pi^2)$. The above statement can be tested on the lattice model Eq. (3.50). The effect of $\mathbf{E}_5$ is to shift the band bottom, pushing charge above a fixed energy, cf. Fig. 3.9 (a) and (c). A rigid shift of the band conserves total charge and is the consistent picture of the anomaly. However, in the linearized regime (gray region in Fig. 3.9 (a) and (b)), the apparent effect is a creation of charge from the vacuum. This is the covariant version of the anomaly, Eq. (3.48), which ignores the band bottom shift. To connect the covariant and consistent pictures quantitatively, we compute the rate of change of charge in the shaded region and band bottom, to compare it to the relevant Bardeen polynomial in Eq. (3.64), δj^0. The rate of anomalous charge growth equals the band bottom charge loss and the Bardeen polynomial, Fig. 3.9 (d). This correction accounts for the change in fermion density at the band bottom, as the Streda formula relates the change of electron density below the Fermi level to the Hall conductivity.[222]

3.5.3 Influence of the Mass Term

The response of the chiral and total charge to fields $\mathbf{E}$ and $\mathbf{E}_5$ computed on a lattice can deviate from the expectation based on the simplest quantum field theory expectations due to corrections set by the mass term. In this section, we carefully investigate one example, the electromagnetic contribution to the chiral anomaly on a lattice, $\partial_\mu j_5^\mu = \mathbf{E}\cdot\mathbf{B}/(2\pi^2)$, and argue how a mass term influences the chiral anomaly. We further show that the mass term does not play the same role for the covariant anomaly $\partial_\mu J^\mu_{\text{cov}} = \mathbf{E}_5\cdot\mathbf{B}/(2\pi^2)$.

The main source of lattice corrections to the anomaly is that the Wilson fermion Hamiltonian[60] used for all tight-binding calculations, Eq. (3.50), has a momentum-dependent

---

[§] Since we work in the setting of a closed quantum system, the spatial component of the covariant current is zero.

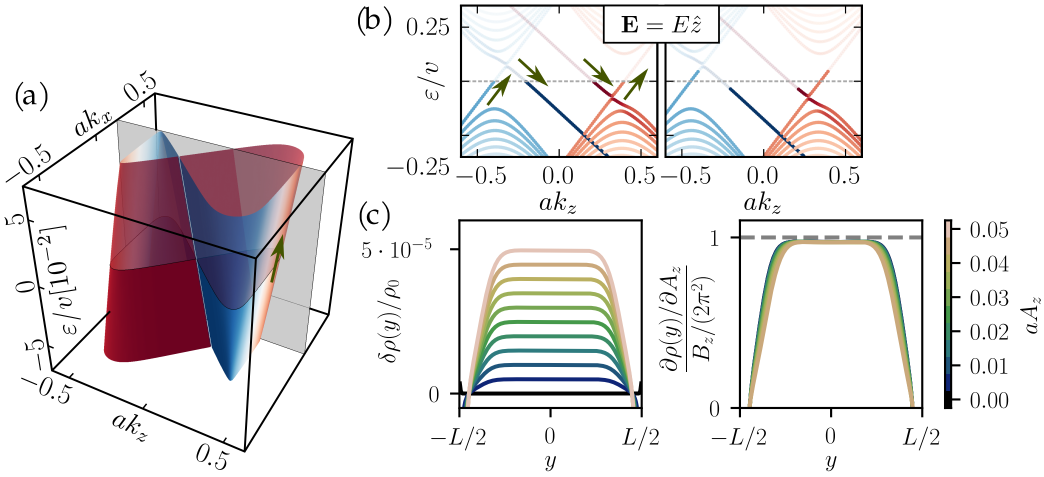

FIGURE 3.8: Anomaly due to $\mathbf{E} \cdot \mathbf{B}_5$ with a constant $\mathbf{B}_5$ in the bulk. (a) The energy spectrum shows the pseudo-Landau levels of $\mathbf{B}_5$, where the color coding and boundary conditions are those of Fig. 3.7. The pseudo-Landau levels of $\mathbf{B}_5$ show an anomaly when $\mathbf{E} = E\hat{z}$ and the spectral flow is schematically shown via the green arrows. (b) The spectrum at $k_x = 0.2/a$, marked by the gray plane in (a), is shown at both $t = 0$ and $t > 0$ (corresponding to $A_z = 0$ and $A_z = 0.05/a$) with $\varepsilon_{\mathrm{F}} = 0$. (c) Left: The spatial profile of the charge relative to that at $t = 0$ is shown at different times (by different colors), evidencing a surface to bulk charge redistribution. The y-axis is chosen such that just the (positive) bulk contribution is visible. The (negative) surface contribution exactly cancels the charge accumulation in the bulk. Right: From Eq. (3.48) the density time derivative equals $\partial_t\rho = \mathbf{E} \cdot \partial_{\mathbf{A}}\rho$, i.e., for $\mathbf{B}_5 \parallel \mathbf{E} \parallel \hat{z}$, the bulk response is $\partial_{A_z}\rho = B_5/(2\pi^2)$, as indicated by the dashed line. In panels (a) and (b), we use open boundary conditions with $L/a = 100$ sites and an axial magnetic field with the magnetic length $\ell_5 = 11.1a$; in panel (c), we use $L/a = 200$ sites and an axial magnetic field with the magnetic length $\ell_5 = 15.8a$.

mass term

$$M_{\mathbf{k}} = m + t\sum_i (1 - \cos k_i), \tag{3.65}$$

that ensures the absence of copies of the Weyl nodes, or doublers, on the lattice.[60] When $t > 0$, the minimum of $M_{\mathbf{k}}$ is at the Γ point and its maximum at (π, π, π); for $m = 0$, the term is zero at $\mathbf{k} = 0$ and increases away from Γ. The term $M_{\mathbf{k}}$ corresponds to the momentum-independent mass term m in the action (3.52) that couples both chiralities and changes the response to electric and magnetic fields.[161;223;224] Such a term results in an additional classical contribution to the chiral anomaly, $\partial_\mu j^\mu_{5,\text{class}} = 2mi\bar{\psi}\gamma^5\psi$,[164] that is zero in all equilibrium situations we consider, which we confirm numerically. Instead, another consequence of m affects the chiral anomaly: when $m \neq 0$ in the field theory, the eigenfunctions of the corresponding Hamiltonian are no longer eigenfunctions of the chiral matrix γ^5. Instead, close to the Weyl node of chirality χ, the overlap with γ^5 for the low-energy eigenstates with a linear dispersion can be obtained analytically to be

$$\langle\psi^\chi|\gamma^5|\psi^\chi\rangle = \chi\sqrt{1 - \frac{m^2}{|b^2|}}, \tag{3.66}$$

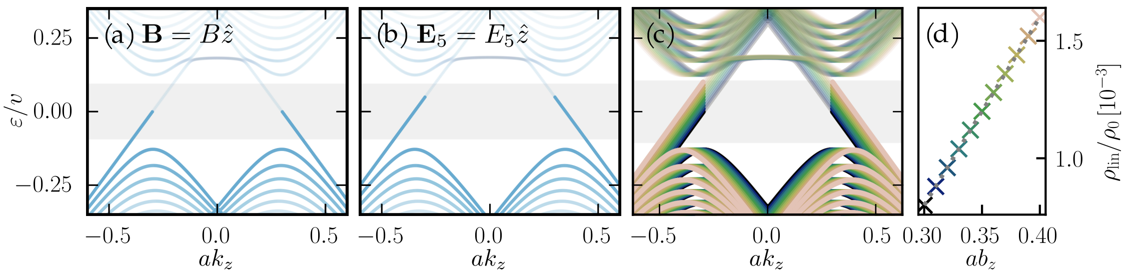

FIGURE 3.9: Anomaly due to $\mathbf{E}_5 \cdot \mathbf{B}$. The original Fermi level (a) is rigidly pushed to higher energies due to a band bottom shift (b) representing the charge conserving consistent anomaly. Considering only the linearized regimes shown by the gray shaded regions, one isolates the Fermi surface contribution or covariant anomaly. (c) The dispersion in presence of $\mathbf{B}$ is plotted for different values of b_z (different colors) where again dark (light) colors represent filled empty states and the gray shaded region is taken to be linearized regime. (d) The charge in the linearized linearized regime, ρ_{lin}, linearly increases with b_z. Since the total charge stays conserved, the charge in the band bottom, below the linearized regime, changes with the same slope, but opposite sign (not shown here). We use open boundary conditions with $L/a = 100$ sites; the magnetic field has the magnetic length $\ell_B = 11.2a$.

with $b^2 = b_\mu b^\mu$, i.e., the chiral density around the Weyl is reduced by a nonzero mass term. We note that a similar factor appears in the effective action for this model and is related to the Weyl node separation.[161;224]

On a lattice, the eigenstates of the Hamiltonian (3.50) are only eigenstates of γ^5 for those momenta $\mathbf{k}$ where $M_{\mathbf{k}} = 0$. In particular, the overlap with γ^5 of states of chirality χ close to the Weyl nodes at $\chi\mathbf{k}_W$ is

$$\langle \psi^{\chi}_{\chi\mathbf{k}_W} | \gamma^5 | \psi^{\chi}_{\chi\mathbf{k}_W} \rangle = \chi \sqrt{1 - \frac{M^2_{\mathbf{k}_W}}{|b^2|}}, \tag{3.67}$$

i.e., it scales with the value of $M_{\mathbf{k}}$ at the Weyl nodes, $\bar{m} \equiv M_{\mathbf{k}_W}$. In the presence of $\bar{m} \neq 0$, the eigenstates are not strictly eigenstates of γ^5 yet in order to define the chiral anomaly using Eq. (3.51) we effectively assume that they are. An alternative definition of chirality that does not possess this problem is to partition the Brillouin zone into two and declare left and right chiral charges as done in Ref. 225. While it has the advantage of having a clear definition of chirality, it does not reduce to any representative matrix at the field theory level and so we retain the first definition.

With these definitions it is tempting to upgraded the chiral anomaly to

$$\partial_\mu j^\mu_5 = \frac{1}{2\pi^2} \sqrt{1 - \frac{\bar{m}^2}{b^2}}\, \mathbf{E} \cdot \mathbf{B}. \tag{3.68}$$

It is interesting to note that a similar equation would be obtained if one interprets the prefactor as an effective renormalization of the chiral electric charge $e_5 = e\sqrt{1 - \bar{m}^2/b^2}$ that would enter the chiral anomaly throughout the coupling to an external chiral gauge field $e_5 A_{\mu,5}$, in analogy with ordinary charge. We have unsuccesfully attempted to derive Eq. (3.68) from the effective field theory responses for the action Eq. (3.52) discussed in Refs. 161;223;224. However, our numerical results on the corrections presented below suggest a richer structure when the mass is non-zero, which has motivated us to leave

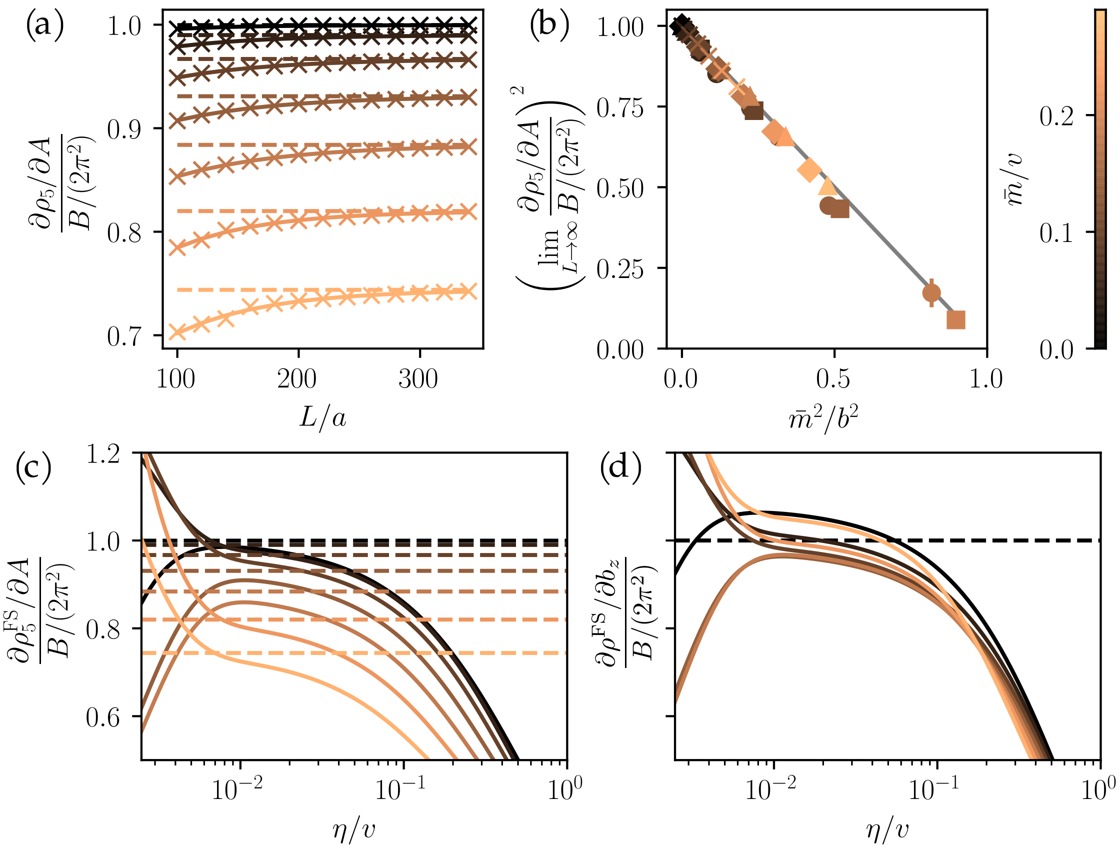

FIGURE 3.10: (a) Convergence of the response $\partial\rho_5/\partial A_z$ for a tight-binding system governed by the Hamiltonian (3.50) with periodic boundary conditions in y-directions of length L and a node separation $\mathbf{b} = b\hat{z}$. A magnetic field $\mathbf{B} = B\hat{z}$ that satisfies periodic boundary conditions is included, with a magnetic length $\ell_B/a = \sqrt{2\pi L/a}$. The crosses denote the numerical results from tight-binding calculations , the solid line the results of a fit with $f(L) = c_0 + c_1 \exp(-L/\xi)$, and the dashed line the coefficient c_0, i.e., the result in the limit $L/a \to \infty$. The color denotes different values of $\bar{m}$, as shown in panel (b), and we further choose $b = 0.4/a$. (b) The response $\partial\rho_5/\partial A_z$ in the limit $L \to \infty$ as a function of $\bar{m}^2/b^2$. The different symbols denote different combinations of b and t and the gray line shows the expectation (3.68). (c) Response of the chiral charge around the Fermi surface to an electric field, $\partial\rho_5^{\mathrm{FS}}/\partial A$, as a function of the level broadening η for $b = 0.4/a$. The dashed lines denote the result from panel (a), $\lim_{L\to\infty}\partial\rho_5/\partial A$. (d) Response of the total charge around the Fermi surface to an axial field, $\partial\rho^{\mathrm{FS}}/\partial A_5$, as a function of the level broadening η. The dashed line denotes the field theory result $\partial\rho/\partial A_5 = B/(2\pi^2)$ as a guide for the eyes.

the precise connection between the quantum field theory discussed in these works and our results are worthy of a separate study. At the end of the section we specify the conditions where our numerics coincide with the massless field theory expectation validating our results, up to a given order in momentum.

To gain insight on the above expectation numerically, we investigate how the chiral anomaly changes with $\bar{m}$. Differentiating between the total charge and the charge around the Fermi surface, we compute the response to external fields $\mathbf{E}$ and $\mathbf{E}_5$ via Eqs. (3.56)

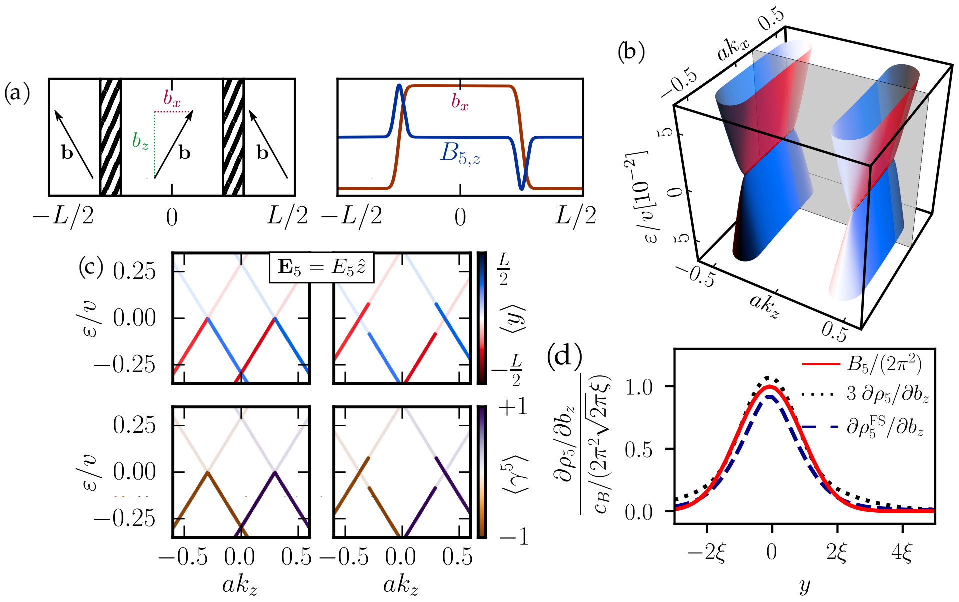

FIGURE 3.11: Anomaly due to $\mathbf{E}_5 \cdot \mathbf{B}_5$. (a) The profile Eq. (3.69) implements two neighboring Weyl semimetals with node separations $\mathbf{b} = (\pm b_x, 0, b_z)$ with a finite $\mathbf{B}_5 \parallel \hat{z}$ at their interface, Eq. (3.70). (b) Energy spectrum with a real space color encoding. (c) In the region of positive $\mathbf{B}_5$ (red), a parallel $\mathbf{E}_5$ pushes left and right-handed chiral charges above and below the Fermi level respectively, annihilating chiral charge. Accordingly, in the region of negative $\mathbf{B}_5$ (blue), chiral charge is created. (d) The spatial distribution of chiral charge creation and annihilation follows and equals $\mathbf{B}_5$ when taking into account solely charges transversing the original Fermi surface (FS). By including all bands, the total chiral charge creation is $\sim 1/3$ of the chiral charge creation at the Fermi surface, as predicted by the consistent anomaly (here shown enlarged by a factor of 3). There is a small mismatch between the profile of B_5 and the two response functions. We use $L/a = 360$ lattice sites, $c_B = 1.25/a$, a B_5 broadening $\xi = 9a$ (cf. Eq. (3.70)), and a delta function broadening $\eta/v = 10^{-6}$.

and (3.60) on a lattice with periodic boundary conditions and a constant $\mathbf{B}$.

We show the response of the total charge in Fig. 3.10 (a) and (b). In panel (a), we show the convergence with system size, whereas in panel (b), we show that, in the limit of $L \to \infty$, the response of the chiral charge scales with $\sqrt{1 - \bar{m}^2/b^2}$ as dictated by Eq. (3.68).

Taking into account just states around the Fermi surface via Eq. (3.60), the chiral charge response approximately in the same way as shown in Fig. 3.10 (b). Thus, the consistent and covariant anomalies are the same for the term $\mathbf{E} \cdot \mathbf{B}$, even in the presence of a mass m. In panel (d), we show the response of the total charge around the Fermi surface to a field $\mathbf{E}_5$: due to the covariant anomaly, $\partial\rho^{\mathrm{FS}}/\partial A_5 \neq 0$. In contrast to $\partial\rho_5^{\mathrm{FS}}/\partial A$, the contribution $\partial\rho^{\mathrm{FS}}/\partial A_5$ is not much affected by $\bar{m} \neq 0$.

3.5.4 The Quest for One Third

We end this section by addressing the conditions to observe the 1/3 factor in the second term of Eq. (3.49). We aim to clarify, under the lattice perspective, the field theory prediction that this prefactor is unity for the covariant version of Eq. (3.49). In particular, it implies that the band bottom current must add $-2/3$ to the Fermi surface contribution leading to the consistent $1/3$ factor, irrespective of the precise pseudo-field profile. This insensitivity could be argued to be a consequence of topological nature of the Bardeen polynomials, yet we find that this alone cannot explain the conditions under which the $1/3$ can be isolated. We find that an additional requirement is that the profile of $\mathbf{b}$, and hence $\mathbf{B}_5$, allows for a separation of the two chiralities in momentum space space. We further require that regions of positive and negative $\mathbf{B}_5$ are well-separated in real space, which avoids mixing of the Landau levels created by the different axial fields. These requirements, which have been overlooked before, become apparent in our Landau and pseudo Level based picture. The profile

$$\mathbf{b} = \left(\frac{c_B}{2} \left[\operatorname{erf}\left(\frac{y - L/4}{\sqrt{2}\xi} \right) - \operatorname{erf}\left(\frac{y + L/4}{\sqrt{2}\xi} \right) \right], 0, b_z \right), \tag{3.69}$$

with the error function $\operatorname{erf}(x)$ and schematically in Fig. 3.11 (a), smoothly varies in real space and realizes the desired separation of all states at the Fermi energy in real and momentum space, Fig. 3.11 (b) and (c). In a periodic system of length L in the y direction, this profile effective realizes two interfaces at $y = \pm L/4$ between two Weyl semimetals with different node separations, connected by regions where $\mathbf{b}$ smoothly changes such that

$$\mathbf{B}_5 = \frac{c_B}{\sqrt{2\pi}\xi} \left[\exp\left(\frac{-(y - L/4)^2}{2\xi^2} \right) + \exp\left(\frac{-(y + L/4)^2}{2\xi^2} \right) \right] \hat{z}. \tag{3.70}$$

Promoting $b_z \to b_z - E_5 t$, we implement $\mathbf{E}_5 \parallel \mathbf{B}_5$, activating the second term in Eq. (3.49). As t increases, the chiral charge, Eq. (3.51), is created/annihilated in spatially separated regions, Fig. 3.11 (b), at a rate that follows the spatial profile of $\mathbf{B}_5$ as expected from Eq. (3.49), Fig. 3.11 (d). This profile allows to isolate the Fermi surface contribution, which from Fig. 3.11 (d) is three times larger than that of the full spectrum. This sets the $\mathbf{E}_5 \parallel \mathbf{B}_5$ coefficient to $\sim 1/3$, approximately the value set by the consistent version of the anomaly, while ~ 1 when restricting to the Fermi surface, as expected from the covariant version.

A finite gap is created due to the finite overlap between states localized in different regions, preventing us to extract $1/3$ exactly. This sets a region in both momentum (light/dark regions in Fig. 3.11 (c)) and real space where chirality is not well defined. This implies that the value $1/3$ is corrected for generic profiles of $\mathbf{B}_5$; only profiles like (3.69) minimize such effect. The detrimental overlap is minimized if $L \gg \xi \gg a$ is satisfied. Additionally all anomaly terms are affected by finite size and quadratic corrections to the low energy field theory Eq. (3.52), similar to those discussed in Sec. 3.5.3.

Based on Landau and pseudo-Landau levels, we have provided an intuitive and generalizable lattice approach that connects the consistent and covariant anomalies, the Bardeen polynomials incorporating the role of the Fermi arcs. Our discussion adds to our general understanding of the chiral anomaly in condensed matter, and we expect that it will prove useful to provide physical intuition for the study of strained and magnetized Weyl and Dirac materials.

3.6 The Action of Nodal Line Semimetals

The description of gapless topological phases in a field-theory language easily extends to nodal line semimetals. It was realized by Burkov *et al.* that the low-energy theories of both Weyl and nodal line semimetals arise from a perturbation of massive Dirac fermions by several momentum-independent terms.[33] To describe the 4×4 basis of the underlying

Hamiltonian, we use Euclidean gamma matrices Γ^μ with signature $(++++)$, and $\Gamma^5 = -\Gamma^1\Gamma^2\Gamma^3\Gamma^4$. Together with the commutator $\Sigma^{\mu\nu} = -\frac{i}{2}\left[\Gamma^\mu, \Gamma^\nu\right]$, these gamma matrices constitute the basis for the low-energy Hamiltonian describing perturbed Dirac fermions, given by

$$\mathcal{H} = \Gamma^j k_j + u^\mu b_\mu + v^j b'_j + w^j p_j + m\Gamma^4 \tag{3.71}$$

with $u^\mu = \left(\Sigma^{45}, \Sigma^{23}, \Sigma^{31}, \Sigma^{12}\right)$, $v^j = \Sigma^{j5}$, and $w^j = \Sigma^{j4}$. This Hamiltonian is a basis-independent formulation of Eq. (2.41) with the same definitions of b_μ, b'_j and p_j.

We rewrite the Hamiltonian as a Lagrangian in terms of gamma matrices γ^μ that realize a metric with signature $(+---)$. We define $\Gamma^j \equiv \gamma^0\gamma^j$ and $\Gamma^4 = \gamma^0$. This definition implies $\Gamma^5 = i\gamma^0\gamma^5$, $\Sigma^{ij} = -\sigma^{ij}$, $\Sigma^{j4} = i\gamma^j$, and $\Sigma^{j5} = -\gamma^j\gamma^5$, with the commutator $\sigma^{\mu\nu} = -\frac{i}{2}[\gamma^\mu, \gamma^\nu]$. The Lagrangian in terms of γ matrices is therefore

$$\mathcal{L} = \psi^\dagger \left(i\partial_t - \mathcal{H}\right)\psi = \bar{\psi}\left(i\partial_t\gamma^0 - \gamma^0\mathcal{H}\right)\psi \tag{3.72}$$

$$= \bar{\psi}\left(\gamma^\mu\left(i\partial_\mu - b_\mu\gamma^5\right) - m - i\gamma^0\gamma^j p_j + \gamma^0\gamma^j\gamma^5 b'_j\right)\psi. \tag{3.73}$$

We further introduce a vector potential A_μ and identify $-i\gamma^0\gamma^j = \sigma^{0j}$ and $\gamma^0\gamma^j\gamma^5 = \epsilon^{jkl}\sigma^{lk}$ to obtain a general form of the Lagrangian of perturbed Dirac fermions

$$\mathcal{L} = \bar{\psi}\left(\gamma^\mu\left(i\partial_\mu - A_\mu - b_\mu\gamma^5\right) - m + \frac{1}{2}\sigma^{\mu\nu}H_{\mu\nu}\right)\psi, \tag{3.74}$$

with $H_{0j} = p_j$, $H_{j0} = -p_j$, and $H_{jk} = -\varepsilon^{jkl}b'_l$. This is a generalization of the action of Weyl fermions, Eq. (3.24), where the mass term is promoted to a Lorentz-invariance-breaking[226] form $m \to m - \sigma^{\mu\nu}H_{\mu\nu}/2$.

The tensor $H_{\mu\nu}$ is analogue to the electromagnetic field tensor $F_{\mu\nu}$ with $\mathbf{E} \to \mathbf{p}$ and $\mathbf{B} \to \mathbf{b}'$. Although one is tempted to drive this analogy further, it is important to keep in mind that there are, different from $\mathbf{E}$ and $\mathbf{B}$, no restrictions on $\mathbf{p}$ and $\mathbf{b}'$. This especially means that generally $\nabla \times \mathbf{b}' \neq 0$. In order to rewrite $H_{\mu\nu}$ in terms of gauge fields, we have to introduce two fields Q_μ and M_μ, similar to the extension of classical electrodynamics to magnetic monopoles,[227;228]

$$H_{\mu\nu} = \partial_\mu Q_\nu - \partial_\nu Q_\mu + \varepsilon_{\mu\nu\alpha\beta}\partial^\alpha M^\beta. \tag{3.75}$$

In momentum space, this replacement gives

$$\sigma^{\mu\nu}H_{\mu\nu} = \gamma^\mu k_\mu \gamma^\nu Q_\nu - \gamma^\mu Q_\mu \gamma^\nu k_\nu + \varepsilon_{\mu\nu\alpha\beta}\gamma^\mu\gamma^\nu k^\alpha M^\beta. \tag{3.76}$$

Further contracting $\varepsilon_{\mu\nu\alpha\beta}\gamma^\mu\gamma^\nu = i[\gamma^\alpha, \gamma^\beta]\gamma^5$ allows to use the simple notation

$$\sigma^{\mu\nu}H_{\mu\nu} = [\not{k}, \not{Q}] + i\left[\not{k}, \not{M}\right]\gamma^5. \tag{3.77}$$

There are now three different gauge fields in the action: A_μ, Q_μ, and M_μ. In contrast to the previous discussion about the axial gauge field A^5_μ in Weyl semimetals, Secs. 3.4 and 3.5, the fields Q_μ and M_μ do not correspond to any physical observables, i.e., a gauge transformation $Q_\mu \to Q_\mu + \partial_\mu\xi$ does not change any observables, not even at high energies. Similar to the previous discussion, temporal and spatial fluctuations in the parameters $\mathbf{b}'$ and $\mathbf{p}$ are captured by these gauge fields. Response functions for the current j_μ now include terms that depend on all gauge fields A_μ, Q_μ, and M_μ. For example, the three-point correlation function

$$\Delta^{\mu\nu\rho}_{AQM}(p,q,k) = \mathcal{Z}^{-1}\left.\frac{\partial^3\mathcal{Z}[A,Q,M]}{\partial A_\mu(p)\partial Q_\nu(q)\partial M_\rho(k)}\right|_{A=Q=M=0} \tag{3.78}$$

enters into the derivation of j_μ. More contributions are given by the exchange $Q_\mu \to M_\mu$ and vice versa.

This construction allows for the evaluation of the triangle diagrams, similar to the chiral anomaly, and provides another example for a Lorentz-invariance breaking quantum field theory that is realized in a condensed-matter system. While the evaluation of the triangle diagrams is left for further study, we note that they may be connected to known anomalies in nodal line semimetals.[47;48]

4 Transport in Topological Semimetals

This chapter is dedicated to several transport phenomena in topological semimetals that either reveal the topological nature of the semimetal or the effect of quantum anomalies. One key ingredient is, again, the chiral anomaly in Weyl semimetals. Since longitudinal magnetotransport, i.e., transport parallel to an applied magnetic field, reflects the chiral anomaly,[30;40] we first discuss the anomaly-related contribution, Sec. 4.1, before focusing on one particular signature observed in experiments: a strongly peaked conductivity for parallel electric and magnetic fields.[175] We concentrate on the so-called quantum limit, where transport is dominated by Landau levels, although some conclusions are also valid in the semiclassical limit, where, at higher energies, the Landau level mix due to disorder.

When a magnetic field orthogonal to the transport direction is applied, magnetotransport in Weyl semimetals differs fundamentally from the usual paradigm in metallic systems.[26] Besides various experiments that show a linear and unsaturated growth of the resistivity with magnetic field,[43;173;229] transversal magnetotransport has been investigated analytically by using perturbation theory.[26;44] We extend this previous work and show how the strong-disorder regime that is not captured by perturbation theory can be accessed numerically, Sec. 4.2.

After discussing magnetotransport, we investigate axial fields generated by strain and show that these fields can give an unusual scaling of the conductance, Sec. 4.3. Finally, we briefly discuss transport in nodal line semimetals and show that the prediction from the Kubo formula fails for transport along a direction in the plane of the nodal line, Sec. 4.4 We further show that the conductance orthogonal to the plane of the nodal line grows with the disorder strength, similar to graphene.[46]

4.1 Longitudinal Magnetoresistance in Weyl Semimetals

An experimentally relevant consequence of the chiral anomaly, a large negative longitudinal magnetoresistance, was obtained by Nielsen and Ninomiya and discussed in their lucid 1983 paper.[30] The magnetoconductivity takes the form

$$\sigma_{ii} = f(B)\,\tau_v \tag{4.1}$$

with $f(B) \propto B$ in the quantum limit with quantized Landau levels[30] and $f(B) \propto B^2$ in the semiclassical limit,[40;230] where this quantization can be neglected. Importantly, it is the internode scattering time τ_v—the time for scattering between different chiralities, which is generally much larger than the intranode chirality preserving scattering time τ_c—that enters, resulting in an unusually large magnetoresistance.

Early transport experiments[41;172;175;179;229;231;232] obtained results consistent with this prediction (albeit in some cases interpreted as a result of current jetting[41]), although not all features of these experiments are fully understood. Measurements for Na_3Bi, where two Dirac nodes split up into four Weyl nodes due to Zeeman coupling, show a strong angular dependence of the conductivity,[175] which at weak magnetic field is consistent with expectations, but at large magnetic field it is even much more strongly peaked at parallel electric and magnetic fields than can be explained assuming an angle-independent internode scattering time.[233]

In this section, following Ref. 42, we address this observation by reviewing previous work on longitudinal magnetotransport and studying the angular dependence of the magnetoresistance in the presence of long-range disorder, extending previous work on the interplay of long-range disorder and magnetic field in Weyl semimetals.[234–237] We show analytically that, within the Born approximation, the internode scattering time τ_v is exponentially reduced when the magnetic field is tilted away from the momentum-space separation of the Weyl nodes.[*] We limit ourselves to the simplest case of two Weyl fermions of opposite chirality separated in momentum space by the vector $\mathbf{b}$.[†] The essential reason for the observed effect is understood from noting that tilting the magnetic field $\mathbf{B} = B\,\hat{r}$ away from $\mathbf{b}$ reduces the effective node separation to $b_r = \mathbf{b}\cdot\hat{r}$. In the presence of long-range disorder, the internode scattering time decays rapidly with decreasing node separation, since this corresponds to a large momentum transfer, resulting, via the relation (4.1), to sharply peaked magnetoresistance. The long-range nature of the disorder potential is essential—for short-range disorder the separation in momentum space does not influence the scattering rate.[181] In addition to this effect, there is a slightly more subtle effect due to the shift of the Landau-level wave-function-center with momentum, which affects the internode scattering time in the opposite direction by increasing the real space distance between the closest states in momentum space. Remarkably, these two effects counterbalance each other at low magnetic field (magnetic length $\ell_B \gg \xi$ the disorder correlation length) such that the internode scattering time is independent of the angle. At large magnetic field ($\ell_B \ll \xi$) the shift of the node separation dominates and results in the aforementioned exponential decrease of the internode scattering time τ_v.

The argument just given is valid for low energies where the chemical potential $\mu < \sqrt{2}\,\hbar v/\ell_B$ such that one can ignore all but the lowest Landau level. In this limit we provide explicit analytical results, and further extend them to higher energies, with the results remaining qualitatively the same, by taking into account scattering between different Landau levels. This provides the detailed chemical potential dependence of the magnetoresistance. Finally, these quantum limit results are confirmed by a numerical computations of the conductance at zero energy, using a transfer matrix technique.[46]

Given that we are interested in the internode scattering time $\tau_v = -\hbar/\mathrm{Im}\Sigma^R_{\chi\neq\chi'}$, with χ denoting the chirality, we need to compute the self-energy Σ. The Hamiltonian describing two Weyl nodes in a magnetic field is

$$\mathcal{H} = v\,(\hbar\mathbf{k} + e\,\mathbf{A})\cdot\boldsymbol{\sigma}\,\tau_z + V, \tag{4.2}$$

where the Pauli matrices τ_μ act in the space of chiralities. The disorder potential V has Gaussian correlations

$$\langle\!\langle V(\mathbf{r})\,V(\mathbf{r}')\rangle\!\rangle = \frac{K_0}{(2\,\pi)^{3/2}}\left(\frac{\hbar v}{\xi}\right)^2 \exp\left[-\frac{|\mathbf{r}-\mathbf{r}'|^2}{2\,\xi^2}\right] \tag{4.3}$$

---

[*] The angle defined here differs from the experiments, where the magnetic and electric fields are tilted away from each other.

[†] The definition of $\mathbf{b}$ differs from the rest of this work by a factor of 2. The extra factor of two results in more symmetric expressions.

of dimensionless strength K_0, with $\langle\!\langle\cdot\rangle\!\rangle$ denoting the disorder average. The vector potential $\mathbf{A}$ lies in the y–z-plane with

$$\mathbf{B} = B\,\hat{r}, \qquad \mathbf{A} = B\,x\,\hat{\theta} \tag{4.4}$$

$$\hat{r} = \cos\theta\,\hat{z} + \sin\theta\,\hat{y}, \qquad \hat{\theta} = \cos\theta\,\hat{y} - \sin\theta\,\hat{z}. \tag{4.5}$$

In a clean system $V = 0$, the two chiralities are decoupled and their eigenfunctions can be found separately. Rotating the 2×2 Hamiltonian of chirality χ allows us to express it in terms of creation and annihilation operators in a Landau-level basis[238;239]

$$\mathcal{H}_\chi = \chi\frac{\hbar v}{\ell_B}\begin{pmatrix} \ell_B k_r & i\sqrt{2}a_{k_\theta} \\ -i\sqrt{2}a^\dagger_{k_\theta} & -\ell_B k_r \end{pmatrix} \tag{4.6}$$

with the magnetic length $\ell_B = \sqrt{\hbar/(eB)}$, rotated momenta $k_{r,\theta} = \mathbf{k}\cdot(\hat{r},\hat{\theta})$, and annihilation operator

$$a_{k_\theta} = \frac{1}{\sqrt{2}}\left(\frac{x}{\ell_B} + \ell_B\,k_\theta + i\ell_B\,k_x\right). \tag{4.7}$$

The energy spectrum consists of dispersive Landau levels, which at positive energy are given by

$$E^\chi_{n>0} = \hbar\omega_B\sqrt{2\,n + \ell_B^2 k_r^2},\;\; E^\chi_0 = \chi\,\hbar v\,k_r \tag{4.8}$$

where the cyclotron frequency $\omega_B = v/\ell_B$. The corresponding eigenstates are[26;44]

$$|\Phi^\chi_{n>0\,\mathbf{k}_\parallel}\rangle = \frac{1}{\sqrt{N_\chi}}\left(\frac{-i\sqrt{2\,n}\,|n-1\rangle}{\ell_B\,k_r - \chi\sqrt{2\,n + \ell_B^2 k_r^2}}, |n\rangle\right)^T, \;\; |\Phi^\chi_{0\,\mathbf{k}_\parallel}\rangle = (0, |0\rangle)^T \tag{4.9}$$

with $N_\chi = 2\sqrt{2\,n + \ell_B^2 k_r^2}/(\sqrt{2\,n + \ell_B^2 k_r^2} - \chi\ell_B k_r)$ a normalization constant. The wave functions describing the eigenstates of the number operator $a^\dagger_{k_\theta}a_{k_\theta}|n\rangle = n\,|n\rangle$,

$$\phi_{n\mathbf{k}_\parallel}(x) = \langle x, \mathbf{k}_\parallel|n\rangle = \frac{1}{\sqrt{\ell_B}}\psi_n\left(\frac{x}{\ell_B} + \ell_B\,k_\theta\right), \tag{4.10}$$

are proportional to the Hermite functions ψ_n centered at $x = -\ell_B^2\,k_\theta$, such that the position along x and the momentum along $\hat{\theta}$ are locked. While the energies depend only on the single momentum component k_r, the wave functions depend only on k_θ. Lines of equal energy are parallel to k_y when $\theta = 0$ and tilt towards k_z when θ increases.[187]

We corroborate these low energy results by calculating the band structure in a tight-binding system, Eq. (2.37), with a low-energy bulk dispersion that is well reproduced by two isolated Weyl nodes.[124] The Fermi-arc structure[187] is captured by taking the system finite in the x direction. A magnetic field in the y-z plane changes the linear dispersion to a Landau-level structure with momentum-space separation of the chiralities $b_r = b\,\cos\theta$ [see Fig. 4.1(a)]. At low energies $\mu < \sqrt{2}\hbar\omega_B$, the Fermi surface consists of the two zeroth Landau levels (tilted lines) that are connected by Fermi arcs (at fixed k_y) [see Fig. 4.1(b)]. As the zeroth Landau levels tilt towards k_z with increasing angle between the magnetic field and node separation, the distance in real space $\delta x = \ell_B^2\,\delta k_\theta$, with k_θ measured from

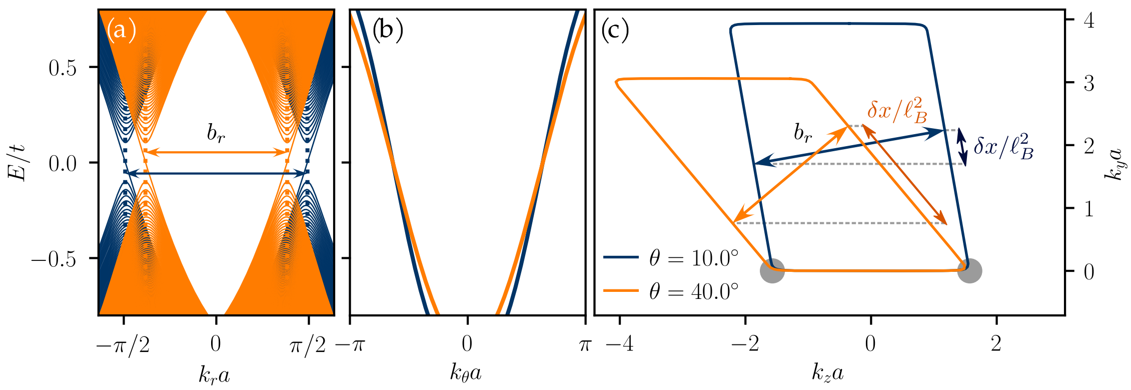

FIGURE 4.1: Energy dispersion of a tight binding system[124], Eq. (2.37) with $v = t$ and $m = 0$, giving two Weyl nodes separated by $\mathbf{b} = \pi\hat{z}$, (a) as a function of k_r at $k_\theta = 0$, (b) as a function of k_θ at $k_r = 0$, and (c) Fermi surface at a chemical potential $\mu = 0$ and a magnetic field of $\mathbf{B} = B\cos\theta\hat{z} + B\sin\theta\hat{y}$ for two different angles θ with $\ell_B = 14.1a$, and a the lattice constant. The system is finite in the x direction with $L/a = 768$ sites and infinite in the other two directions. The dashed lines in the energy dispersion (a) show the position of the zeroth Landau level at zero energy expected from the continuum model, at $k_r a = \pm\pi/2\,\cos\theta$. The positions of the Weyl nodes in absence of a magnetic field are indicated by gray circles in (c).

the Weyl nodes in absence of a magnetic field, simultaneously increases for those states with minimal momentum-space distance.

The essential reason for the enhanced internode scattering can now be intuitively understood from the band structure: for a disorder potential with long-range correlations, the amplitude for internode scattering increases when the magnetic field is tilted away from the Weyl-node momentum axis, due to the reduced momentum-space distance b_r, while simultaneously decreasing because of the increased real-space distance δx. To substantiate this argument, we explicitly calculate the self-energy.

The disorder-induced self-energy correction for a Landau level of certain chirality can be split up into two contributions: scattering within the chirality, which defines the intranode scattering time τ_c, and scattering between different chiralities, which defines the internode scattering time τ_v. These corrections are expressed to lowest order in the disorder potential via the Born approximation, with $\mathbf{k}_\parallel = (k_r, k_\theta)$,

$$\Sigma^m_{\chi\chi'}(i\omega_n, \mathbf{k}_\parallel) = \sum_{m',k'_r} \mathcal{G}_{m'\chi'}(i\omega_n, k'_r) \sum_{k'_\theta} \Gamma^{\chi\chi'}_{mm'} \tag{4.11}$$

with the disorder correlation in the Landau-level basis

$$\Gamma^{\chi\chi'}_{mm'} = \left\langle\!\!\left\langle \langle \Phi^{\chi}_{m\,\mathbf{k}_\parallel} | V | \Phi^{\chi'}_{m'\,\mathbf{k}'_\parallel} \rangle \langle \Phi^{\chi'}_{m'\,\mathbf{k}'_\parallel} | V | \Phi^{\chi}_{m\,\mathbf{k}_\parallel} \rangle \right\rangle\!\!\right\rangle \tag{4.12}$$

and the Green's function of the clean system $\mathcal{G}_{m\chi}(i\omega_n, k_r) = 1/(i\omega_n - E^{\chi}_m)$. The splitting up of the momentum summation in this expression is possible since the energies only depend on the momentum component k'_r. The diagonal elements of Σ with $\chi = \chi'$ give intranode scattering, while off-diagonal elements with $\chi \neq \chi'$ give internode scattering. Inserting a general form of the disorder correlation $\langle\!\langle V(\mathbf{q})V(-\mathbf{q}')\rangle\!\rangle = K(\mathbf{q})\delta_{\mathbf{q},\mathbf{q}'}$, the disorder correlation in Landau level basis is

$$\Gamma^{\chi\chi'}_{mm'} = \sum_{q_x} K(\mathbf{q}^{\chi\chi'}) \int dx \Phi^{\chi\dagger}_{m\mathbf{k}_\parallel}(x) \Phi^{\chi'}_{m'\mathbf{k}'_\parallel}(x) e^{iq_x x} \int dx' \Phi^{\chi'\dagger}_{m'\,\mathbf{k}'_\parallel}(x') \Phi^{\chi}_{m\mathbf{k}_\parallel}(x') e^{-iq_x x} \tag{4.13}$$

where $\mathbf{q}^{\chi\chi'} = q_x\hat{x} + \mathbf{k}_\parallel - \mathbf{k}'_\parallel - (\chi - \chi')\mathbf{b}/2$ is the momentum transfer between the involved states. Scattering is therefore dominated by small momentum transfer $\mathbf{q}^{\chi\chi'} \approx 0$. Note that $\Phi^{\chi}_{n\,\mathbf{k}_\parallel}(x) = \langle x | \Phi^{\chi}_{n\,\mathbf{k}_\parallel} \rangle$ are two-component wave functions.

In the ultra-quantum limit at energies $\mu < \sqrt{2}\,\hbar\omega_B$, it is sufficient to compute $\Gamma^{\chi\chi'}_{mm'}$ by including scattering only between zeroth Landau levels. With the wave functions (4.9), the disorder correlations (4.13) simplifies to

$$\Gamma^{\chi\chi'}_{00} = \frac{K_0\,\hbar^2 v^2}{\sqrt{2\,\pi}\,L^2} \frac{\xi}{\sqrt{\ell_B^2 + \xi^2}} e^{-\frac{1}{2}\left(\xi\,\delta\mathbf{q}^{\chi\chi'}_\parallel\right)^2 - \frac{1}{2}\,\ell_B^2\,\left(k_\theta - k'_\theta\right)^2}. \tag{4.14}$$

The self-energy correction for scattering within the same chirality is now straightforward. Integration over momenta $\mathbf{k}'_\parallel$ results in an inverse intranode scattering time

$$\frac{1}{\tau_c} = -\frac{1}{\hbar} \mathrm{Im}\,\Sigma^{0\,R}_{\chi\chi}\big|_{k_r = \chi\frac{\varepsilon}{\hbar v}} = \frac{K_0}{4\,\pi}\,\frac{v}{\xi}\,\frac{\xi^2}{\ell_B^2 + \xi^2}. \tag{4.15}$$

For the internode scattering time the momentum difference between the chiralities is enlarged by the node separation, resulting in

$$\frac{1}{\tau_v} = \frac{K_0}{4\,\pi}\,\frac{v}{\xi}\,\frac{\xi^2}{\ell_B^2 + \xi^2}\,e^{-\frac{1}{2}\xi^2\left[\left(\frac{2\,\mu}{\hbar v} - b_r\right)^2 - \frac{\ell_B^2}{\ell_B^2 + \xi^2}\,b_\theta^2\right]} \tag{4.16}$$

with $b_{r,\theta} = \mathbf{b} \cdot (\hat{r}, \hat{\theta})$. The ratio of inter- and intranode scattering time at zero energy is therefore

$$\frac{\tau_v}{\tau_c} = \exp\left[\frac{1}{2}\xi^2\,b^2\,\left(\cos^2\theta + \frac{\ell_B^2}{\ell_B^2 + \xi^2}\,\sin^2\theta\right)\right]. \tag{4.17}$$

In the limit of small magnetic fields, $\ell_B \gg \xi$, the ratio does not depend on the angle θ between the node separation and magnetic field. In contrast, for large magnetic fields, $\ell_B \ll \xi$, the ratio decreases exponentially when the magnetic field is tilted away from the node separation. This functional behavior is illustrated in Fig. 4.2, and constitutes one of our main results.

To extend our results to energies larger than $\sqrt{2}\,\hbar\omega_B$, where higher Landau levels are occupied, a full solution for the disorder correlation (4.13) is needed. The integrals over both momentum components are similar to those appearing in the treatment of the integer quantum Hall effect[240], resulting in analogous expressions. Since the full analytical expression is too complicated to give additional insight, we relegate its display to Appendix C.1.

In Fig. 4.3(a) we show the ratio of the internode scattering times with the node separation orthogonal and parallel to the magnetic field, $\tau_v(\theta = \pi/2)/\tau_v(\theta = 0)$, as a function of the chemical potential for different magnetic field strengths. As in the ultra quantum limit, the change of the internode scattering time is more pronounced for large fields. For small ℓ_B/ξ, the decrease persists up to higher energies than for large ℓ_B/ξ. The behavior

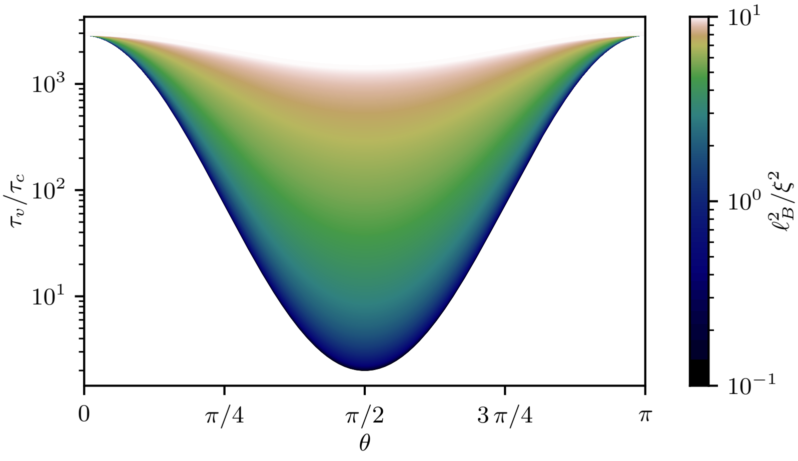

FIGURE 4.2: Ratio of inter- and intranode scattering times τ_v/τ_c, for two isolated Weyl nodes in the presence of long-range disorder, as a function of the angle θ between the node separation $\mathbf{b}$ and the externally applied magnetic field $\mathbf{B}$. The ratio is evaluated at $\mu = 0$ with a node separation $\xi\, b = 4$. The color scale shows different magnetic field strengths given by ℓ_B^2/ξ^2, with the two limits $\ell_B/\xi \to 0$ and $\ell_B/\xi \to \infty$ described in the main text.

for energies in the ultra-quantum limit with $\mu < \sqrt{2}\hbar\omega_B$ can be best understood from Eq. (4.16), which gives a linearly increasing logarithm of the ratio due to the reduced momentum-space distance with increasing energy. In Fig. 4.3(b), we further compare the ratio of scattering times for the node separation anti-parallel and parallel to the applied field. These two scattering times are not identical due to the dispersion of the zeroth Landau levels: their momentum-space separation is reduced when $\mu > 0$, while changing the direction of the magnetic field $\mathbf{B} \to -\mathbf{B}$ reverses this effect and increases the node separation when $\mu > 0$. This effect could be visible in experiments since other reasons for an angle-dependent magnetoresistance, such as non-isotropic Fermi velocities, do not change upon reversing the magnetic field direction.

We verify the approximation that the internode scattering time is the relevant transport time, and thereby our results, by numerically calculating the conductance using a transfer matrix representation[46;241] of the solutions of the Weyl equation $\mathcal{H}\,\psi = E\,\psi$, previously employed for disordered Weyl nodes in the absence of a magnetic field[27;242–244]. A random scattering potential with correlations as in Eq. (4.3) is transformed into the Landau-level basis and added to the Hamiltonian in terms of the raising and lowering operators, Eq. (4.6). The details of this approach are given in Appendix D.1. With this method, we obtain the matrix of transmission amplitudes t for a system that has periodic boundary conditions in the transverse x and y directions and a finite length L in the z direction; the conductance is then given by the Landauer formula

$$G = \frac{e^2}{h}\mathrm{Tr}\left[t^\dagger t\right]. \tag{4.18}$$

In Fig. 4.4(a), we show the dimensionless resistance $\bar{R} = G^{-1}\,N\,e^2/h$, normalized by N transverse modes, for fixed node separation $b\xi$ and ratio ℓ_B/ξ, as a function of system length for various disorder strengths. The resistance increases linearly with L, giving a constant

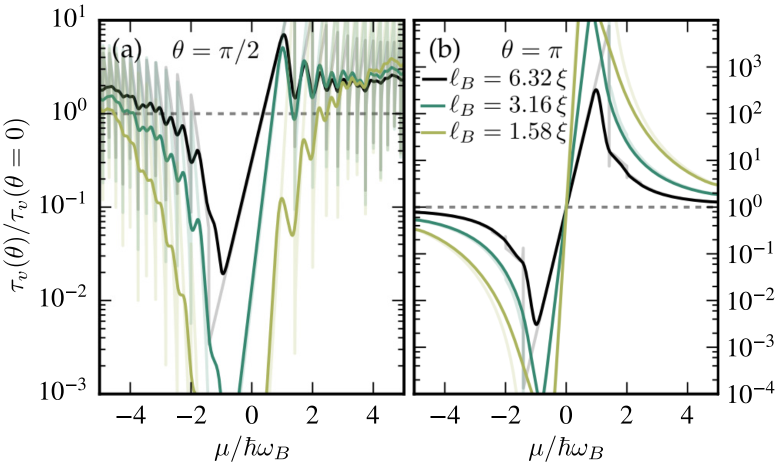

FIGURE 4.3: Ratio of internode scattering times $\tau_v(\theta)/\tau_v(\theta = 0)$ at different tilt angles θ as a function of the chemical potential μ, evaluated away from the ultra quantum limit, at (a) $\theta = \pi/2$ and (b) $\theta = \pi$. The opaque lines show temperature-broadened results (with $\tau_v(\mu) = -\int d\omega \tau_v^{T=0}(\omega)\partial n_F/\partial\omega$ and $T = 0.067\,\hbar\omega_B$) for a better visibility of the overall trend, while the semitransparent lines in the background show zero-temperature results. The node separation at zero field is fixed to $b\xi = 10$. The dashed gray line depicts a ratio of 1 as a guide for the eyes.

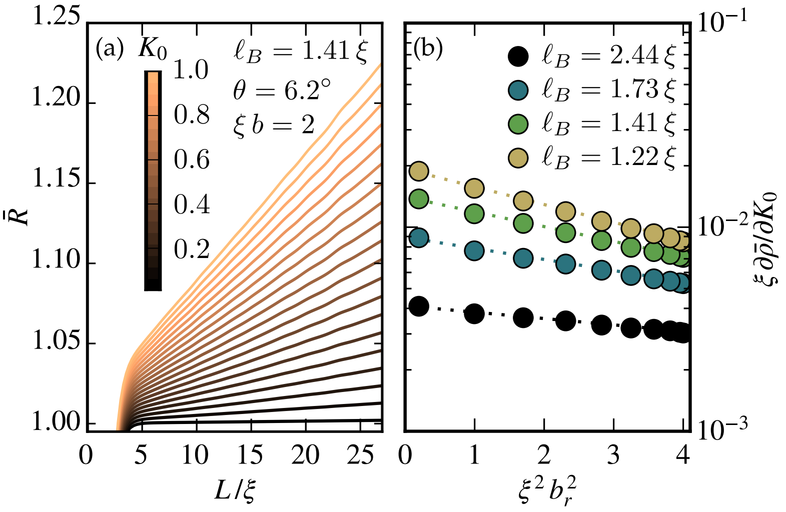

FIGURE 4.4: Numerically obtained resistance for two isolated Weyl cones with long-range internode disorder at zero chemical potential. (a) The disorder-averaged dimensionless resistance $\bar{R}$ normalized by the number of modes increases with the system size with constant slope $\bar{\rho} = \partial\bar{R}/\partial L$. The slope is proportional to the inverse scattering time τ_v^{-1} and therefore linearly increases with disorder strength K_0. (b) The logarithm of the derivative $\xi\,\partial\bar{\rho}/\partial K_0$ scales quadratically with $\xi\,b_r$. Circles represent numerical results, and the dotted line shows the results from the analytical expectation given in Eq. (4.19). All numerical data are averaged over 200 different disorder realizations.

resistivity $\bar{\rho} = \partial \bar{R}/\partial L$. For small disorder strength $K_0 \lesssim 1$, $\bar{\rho}$ increases linearly with K_0. Figure 4.4(b) shows the dimensionless quantity $\xi\, \partial\bar{\rho}/\partial K_0$ as a function of the squared effective node separation $b_r^2 = b^2 \cos^2\theta$, where we included the analytical expectation

$$\xi \frac{\partial \bar{\rho}}{\partial K_0} = 2\, \frac{1}{K_0}\, \frac{\xi}{v}\, \tau_v^{-1} \tag{4.19}$$

as a guide for the eye. The good agreement provides a numerical confirmation of the main finding of this work: magnetotransport is not just dominated by the size of the node separation itself, but also by the tunable angle between applied magnetic field and the node separation.

In conclusion, we find that the internode scattering time in Weyl semimetals at zero energy exponentially decreases when an external magnetic field is tilted away from the Weyl node separation. For small magnetic fields, this drop vanishes and the internode scattering time is angle independent. Numerically, we confirm that the internode scattering time is the relevant transport time and proportional to the conductivity. Away from the ultra-quantum limit, where transport is dominated by the zeroth Landau level, the internode scattering time remains angle dependent, and decreases for large magnetic fields tilted away from the Weyl node separation. The angle-dependent internode scattering time may be related to the experimentally observed sharply peaked magnetoresistance at large magnetic fields. Our predictions can, in principle, be experimentally confirmed by measuring the conductivity along the axis of parallel electric and magnetic fields with all fields tilted against the node separation. The predictions can be extended for a larger number of Weyl nodes. The behavior presented in this work especially applies when the separation between pairs of Weyl nodes is smaller than the separation of the pairs. The difference in conductivity for magnetic fields parallel and anti parallel to the node separation is another experimentally accessible signature.

4.2 Transversal Magnetoresistance in Weyl Semimetals

Different from the longitudinal magnetotransport investigated in the previous section, the chiral anomaly is not operational for transversal magnetotransport transport that is considered in this section, following Ref. 42. However, despite the absence of the chiral anomaly, Weyl and Dirac semimetals show very peculiar magnetotransport properties: a large transversal magnetoresistivity has been observed experimentally in a variety materials at low temperatures around $T = 2\,\mathrm{K}$. Early studies of the Dirac semimetal Cd_3As_2[179;245–247] with multiple Dirac cones were followed by measurements on the single-Dirac cone material TiBiSSe[248] and Weyl materials NbAs,[43] TaAs,[173] and NbP.[229] The transversal resistivity can increase up to a factor of a thousand compared to the $(B = 0)$-resistivity upon the application of a magnetic field with a strength on the order of $10\,\mathrm{T}$,[248] and it does not saturate with growing magnetic field.

The observed linear and unsaturated growth of the resistivity with the applied magnetic field is in stark contrast to Boltzmann magnetotransport theory in metals where the magnetoresistivity is much smaller, quadratic in B for small B and saturating if the cyclotron frequency exceeds the scattering time. Thus, alternative theoretical approaches are necessary to explain the experimental results.

Abrikosov studied the problem of transverse magnetoresistance long before the confirmation of Weyl and Dirac materials in the lab. He developed a perturbative analytical approach for transversal magnetotransport of a single Weyl node Hamiltonian,[26] using

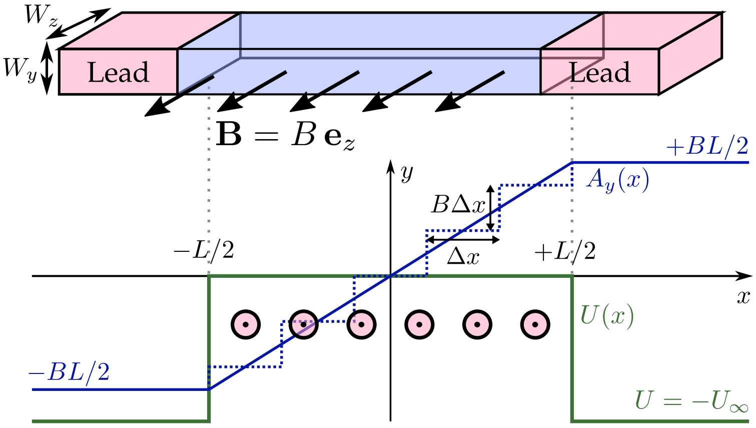

FIGURE 4.5: Sketch of modeled transport experiment. The magnetic field points in the z-direction perpendicular to the transport direction (x). The lower panel shows the doping distribution $V(x)$ (green) that defines the leads, and the choice for the vector potential A_y (blue). The piecewise constant approximation of A_y, shown with a dotted dotted line, is used in the scattering matrix approach for the situation including disorder $U(\mathbf{r})$.

the Kubo formula and Born approximation to include the effect of weak disorder while focusing on the quantum limit. Indeed, this approach gives a linear and non-saturating magnetoresistance under the assumption of screened Coulomb impurities.

The recent experiments triggered a renewed interest in the problem leading to the appearance of a number of theoretical studies reproducing and extending Abrikosov's earlier results.[44;236;249–254] Notably, the more realistic situation with a pair of nodes was accounted for in Refs. 236;249;250;253, while disorder was assumed to be of (uncorrelated) Gaussian white noise type in Refs. 44;250;252 and to have a finite range in Ref. 236. However, most of the approaches in the recent papers follow Abrikosov's method by treating disorder using the Born approximation and computing the conductivity making use of the Kubo formula with bare current vertices. Some slight but noteworthy variations are the numerical evaluation of overlap integrals for disorder scattering in Ref. 251 and the extension to the self-consistent Born approximation (SCBA) in Refs. 44;252. Moreover, the role of vertex corrections was scrutinized in Refs. 44;252. Staying in the quantum limit, all of these recent works have confirmed Abrikosov's result for the transversal magnetoconductivity, $\sigma_{xx}(B) \sim 1/B$ (screened Coulomb disorder) and $\sigma_{xx}(B) \sim B$ (short-range correlated disorder). Results for finite chemical potential μ and finite temperature T are also available.[251;252] However, the extent to which the above theories are applicable to experiments is still under debate.[251]

Here, we complement the existing analytical and perturbative approaches to transversal magnetotransport in a Weyl node by introducing a numerical method, which treats disorder and the magnetic field exactly. This is of relevance in the limit $B \to 0$ due to the known failure of the SCBA, which misses relevant crossed disorder diagrams.[27] It also allows us to study the interplay between magnetic field and strong disorder, the latter of which is known to drive a phase transition[255;256] between a semimetal and a diffusive metal in the case $B = 0$. Finally, by being formulated in the framework of scattering theory, our formalism applies to mesoscopic systems while the bulk limit is well within reach.

Although we formulate our method for undoped Weyl nodes $\mu = 0$, it can be straightforwardly generalized to include finite μ. Similarly, although the disorder type could be freely specified, we limit ourselves to Gaussian disorder with correlation length ξ.

4.2.1 Model

We study magnetotransport in a Weyl semimetal slab of length L and transversal widths $W_y, W_z \gg L$ shown schematically in Fig. 4.5. The scattering between several Weyl nodes can be neglected if their separation in reciprocal space is large compared to the inverse disorder correlation length and we consequently focus on a single node. We assume the magnetic field $\mathbf{B} = B\hat{z}$ in the z-direction and transport in the x-direction. The Hamiltonian has the same form as the one previously considered, Eq. (4.2),

$$\mathcal{H} = v\left(\hbar\mathbf{k} + e\mathbf{A}\right)\cdot\boldsymbol{\sigma} + U\left(x\right) + V\left(\mathbf{r}\right), \tag{4.20}$$

with the position-dependent potential $U(x)$ that models the system's leads. Using Landau gauge, the vector potential is

$$\mathbf{A} = \begin{cases} -B\frac{L}{2}\,\hat{y} & : x \leq -\frac{L}{2}, \\ Bx\,\hat{y} & : |x| < \frac{L}{2}, \\ B\frac{L}{2}\,\hat{y} & : x \geq \frac{L}{2}. \end{cases} \tag{4.21}$$

The leads at $|x| \geq L/2$ are modeled with the potential $U(x)$,

$$U(x) = \begin{cases} 0 & : |x| < L/2, \\ -U_\infty & : \text{otherwise}, \end{cases} \tag{4.22}$$

and are free of magnetic field. In the central scattering region, the Fermi energy is located at the nodal point. The disorder potential $V\left(\mathbf{r}\right)$ is assumed to be present in the scattering region only and is modeled with a Gaussian distribution, zero mean and the same Gaussian correlations used in the previous section, Eq. (4.3), with correlation length ξ and the dimensionless disorder strength K_0.

4.2.2 Mesoscopic Transport in Clean Samples

We start by considering transport in the clean limit, i.e., $K_0 = 0$. In the transversal y and z-directions, we apply periodic boundary conditions and use the resulting translational symmetry to make the ansatz $\psi(\mathbf{r}) = \psi(x)e^{i(k_y y + k_z z)}$ with $\psi(x) = \left(\psi_\uparrow(x), \psi_\downarrow(x)\right)^{\mathrm{T}}$. We solve the scattering problem by assuming an incoming state from $x = -\infty$ and finding the transmission coefficient t. In the central scattering region, $|x| \leq L/2$, the Schrödinger equation for a zero-energy state leads to the following system of equations

$$\ell_B\partial_x\psi_\uparrow(x) = +\left(\ell_B k_y + \frac{x}{\ell_B}\right)\psi_\uparrow(x) + i\ell_B k_z\psi_\downarrow(x), \tag{4.23a}$$

$$\ell_B\partial_x\psi_\downarrow(x) = -\left(\ell_B k_y + \frac{x}{\ell_B}\right)\psi_\downarrow(x) - i\ell_B k_z\psi_\uparrow(x), \tag{4.23b}$$

where we again introduced the magnetic length $\ell_B = \sqrt{\hbar/(eB)}$. In the limit of infinite doping in the leads, $U_\infty \to \infty$, the following boundary conditions are enforced by the lead states from wave-function matching

$$\psi(-L/2) = \frac{1}{\sqrt{2}}\begin{pmatrix} 1 \\ 1 \end{pmatrix} + \frac{r}{\sqrt{2}}\begin{pmatrix} 1 \\ -1 \end{pmatrix}, \tag{4.24}$$

with the reflection coefficient r and

$$\psi(L/2) = \frac{t}{\sqrt{2}}\begin{pmatrix}1\\1\end{pmatrix}. \tag{4.25}$$

To obtain solutions for t, we redefine $\psi_\pm(x) \equiv \psi_\uparrow(x) \pm \psi_\downarrow(x)$, such that the coupled system of equations reads

$$\ell_B \partial_x \psi_\pm(x) = \left(\ell_B k_y + \frac{x}{\ell_B} \mp i\ell_B k_z\right)\psi_\mp(x), \tag{4.26}$$

and the boundary conditions become $\psi_-(L/2) = 0$ and $\psi_+(-L/2) = 2/\sqrt{2}$. The transmission coefficient $t = \psi_+(L/2)/\sqrt{2}$ can be found by numerically solving Eq. (4.26).

In Fig. 4.6 (d), the transmission eigenvalue $T = |t|^2$ is shown as a function of $(k_y, k_z) \equiv \mathbf{k}_\perp$ for $L/\ell_B = 3$. We observe that the presence of the magnetic field causes a gauge-dependent k_y-k_z asymmetry whereas the $B = 0$ result $T = \cosh^{-2}(L|\mathbf{k}_\perp|)$[27] is rotationally symmetric. Nevertheless, the $\mathbf{k}_\perp = 0$ mode still shows perfect transmission. The conductance G is calculated via the Landauer formula, Eq. (4.18), and is shown in Fig. 4.6 (a) where the dotted line represents the known result in the limit of vanishing magnetic field,[27]

$$G\frac{\ell_B^2}{W^2} = \frac{e^2}{h}\frac{\ln 2}{2\pi}\left(\frac{\ell_B}{L}\right)^2 \tag{4.27}$$

with the transversal width $W = W_y = W_z$. For $L/\ell_B \gg 1$, when the magnetic field becomes relevant, the conductance vanishes rapidly with L/ℓ_B. The plot of $G(\ell_B/W)^2 h/e^2$ vs. $(L/\ell_B)^2$ on a semi-logarithmic scale in Fig. 4.6 (b) reveals a functional form $G\ell_B^2/W^2 \propto \exp(-\alpha(L/\ell_B)^2)$ with $\alpha = 1/4$ (dotted line).

Although we did not succeed in deriving an analytical expression for G in the limit $L/\ell_B \gg 1$, the exponential localization can be understood from the form of the bulk wave functions in the vicinity of zero energy. As known from the previous discussion of the Landau level physics, the zeroth Landau level is chiral and its x position is locked to the transversal momentum k_y, i.e., the wave function is exponentially localized at $x = \ell_B^2 k_y$, cf. Eq. (4.10) with $k_\theta = -k_y$. Due to translational invariance (i.e., the absence of disorder), k_y is conserved and coherent transport between the leads only proceeds via the exponential tail of the orbitals leaking across the sample. This explains the observed exponential suppression of the conductance with length.

The Fano factor

$$F = \frac{\operatorname{tr}\left[tt^\dagger\left(1 - tt^\dagger\right)\right]}{\operatorname{tr}\left[tt^\dagger\right]} \tag{4.28}$$

is a measure of shot noise in quantum transport and is shown in Fig. 4.6 (c). In the limit $L \ll \ell_B$, we find $F = 0.57$ in agreement with the pseudo-ballistic regime described in Ref. 27. With increasing field B, the Fano factor also increases and reaches up to $F = 0.74$ in the large-B regime.

Upon the inclusion of disorder, i.e., $K_0 > 0$, the momenta are no longer conserved and we expect a diffusion process between localized orbitals leading to drastic change of transport behavior. Indeed, we show in the next section that in the large system limit the transport with $K_0 > 0$ becomes diffusive.

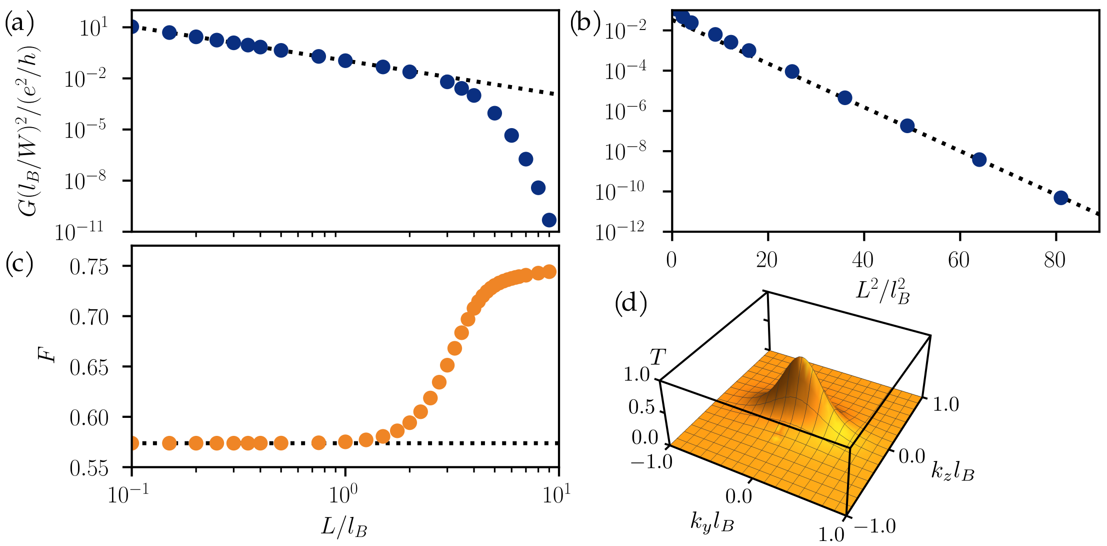

FIGURE 4.6: Numerical results for clean transversal magnetotransport. (a) Conductance versus system length, the dotted line indicates the $B = 0$ result $G \sim L^{-2}$. (b) Conductance versus $(L/\ell_B)^2$. For the case $L/\ell_B \gg 1$, the logarithm of the conductance obeys a linear relation with $(L/\ell_B)^2$. (c) The Fano factor versus system length. The dotted line corresponds to the $B = 0$ result, $F = 0.57$. The slope of the dotted line is $-1/4$. (d) Transmission eigenvalue T as a function of transversal momenta for $L/\ell_B = 3$.

4.2.3 Numerical Magnetotransport in the Presence of Disorder

As done in the previous section, we use the transport matrix method to find the scattering matrix of the magnetotransport problem in the presence of a specific disorder realization. Some modifications are necessary to incorporate the effect of the transversal magnetic field. The magnetic flux is concentrated between x and $x + \Delta x$ in an infinitely thin sheet at $x + \Delta x$ where the vector potential $A_y(x)$ accordingly has a jump, cf. Fig. 4.5. Likewise, the disorder potential in the slice is represented by an infinitely thin sheet at $x + \Delta x$. The scattering matrix $S_{x,x+\Delta x}$ of a slice can be found from concatenation of the scattering matrix $S^{(0)}_{x,x+\Delta x}$ for free propagation from x to $x+\Delta x$ and the scattering matrices resulting from the vector potential step $S^{(B)}_{x+\Delta x}$ and the disorder sheet $S^{(\mathrm{dis})}_{x+\Delta x}$. The scattering matrix of the full system is found from concatenation of slice scattering matrices. This approach to transport in the presence of disorder has been applied previously for two-dimensional Dirac dispersions[46] and Weyl nodes,[27] and also in the presence of parallel magnetic fields.[42] We refer to these references for the specific form of the disorder-sheet scattering matrix $S^{(\mathrm{dis})}_{x+\Delta x}$ and the derivation of the scattering matrix for free propagation within the (clean and field-free) slice

$$S^{(0)}_{x,x+\Delta x} = \begin{pmatrix} t^{(0)} & r^{(0)\prime} \\ r^{(0)} & t^{(0)\prime} \end{pmatrix} \tag{4.29}$$

with the following transmission and reflection blocks,

$$t^{(0)} = t^{(0)\prime} = \frac{1}{\cosh\left(\Delta x\sqrt{\tilde{k}_y^2 + k_z^2}\right)}, \tag{4.30}$$

$$r^{(0)} = \frac{\tilde{k}_y + ik_z}{\sqrt{\tilde{k}_y^2 + k_z^2}} \tanh\left[\Delta x\sqrt{\tilde{k}_y^2 + k_z^2}\right] = -r^{(0)\prime\star}, \tag{4.31}$$

where $\tilde{k}_y = k_y + eA_y(x)/\hbar$ is x-dependent. Finally, we compute the scattering matrix $S^{(B)}_{x+\Delta x}$ for an abrupt jump in vector potential representing a magnetic field $B(x) = \delta(x+\Delta x)B\Delta x$. This scattering matrix is found by considering two leads meeting at $\tilde{x} = 0$ in the presence of a jump in the vector potential,

$$A_y(\tilde{x}) = \begin{cases} A_{y,L} & : \tilde{x} < 0, \\ A_{y,R} & : \tilde{x} > 0. \end{cases} \tag{4.32}$$

At $\tilde{x} = 0$, we match the wave functions (with incoming state from $\tilde{x} = -\infty$) and use $a_{L,R} \equiv \frac{e}{\hbar}A_{yL,yR}$ and $v_\infty \equiv V_\infty/\hbar v$ to write

$$\begin{aligned} &\mathcal{N}_L \begin{pmatrix} v_\infty + k_z \\ k_x^L + i(k_y - a_L) \end{pmatrix} + r\mathcal{N}_L \begin{pmatrix} v_\infty + k_z \\ -k_x^L + i(k_y - a_L) \end{pmatrix} \\ &= t\mathcal{N}_R \begin{pmatrix} v_\infty + k_z \\ k_x^R + i(k_y - a_R) \end{pmatrix}, \end{aligned} \tag{4.33}$$

where $\mathcal{N}_{L,R}$ represents spinor normalizations and $k_x^{L,R} = \sqrt{v_\infty^2 - (k_y - a_{L,R})^2 - k_z^2}$ are the momenta in transport direction in the left and right lead, respectively. Solving Eq. (4.33) and taking the limit $V_\infty \to \infty$ as above, we find $t = 1$ and $r = 0$. Thus, the scattering across a localized transverse field is trivial. Note, however, that the magnetic field also enters the free slice scattering matrix $S^{(0)}_{x,x+\Delta x}$ via the appearance of $A_y(x)$. In summary, we obtain the total scattering matrix of a slice as $S^{(0)}_{x,x+\Delta x} \otimes S^{(\text{dis})}_{x+\Delta x}$ (here $\otimes$ denotes scattering matrix concatenation[257]).

We discretize the transversal momenta in accordance with the periodic boundary conditions, $k_{y,z} = 2\pi m_{y,z}/W_{y,z}$, $m_{y,z} \in \mathbb{Z}$ and choose a cutoff $R_{y,z}$ such that the transversal momenta $|k_{y,z}|\xi \leq R_{y,z}$. We are interested in the physical limit $R_{y,z} \to \infty$ and claim convergence if the conductance and Fano factor (computed from Eqs. (4.18) and (4.28), respectively) do not vary with increased $R_{y,z}$ or reduced Δx. We increase transversal dimensions until $G/(W_yW_z)$ and F are independent of the widths. We further check that the results do not change when antiperiodic transversal boundary conditions are applied.

We have checked that the stepwise approach presented in this section reproduces the results of Sec. 4.2.2 obtained for a smooth vector potential. Building up the scattering matrix of the full system $S_{-L/2,L/2}$ from concatenating slices and labeling the intermediate scattering matrices $S_{-L/2,x}$ with $-L/2 \leq x \leq L/2$, we observe that the position of the maximum of the transmission T, denoted $(\tilde{k}_y, 0)$ is at $\tilde{k}_y = -L\ell_B^{-2}/2$ for $x = -L/2$ and shifts to $\tilde{k}_y = 0$ for $x = L/2$, cf. Fig. 4.6(a), inset. Qualitatively, such a shift is also observed for the disordered case. With increasing x, $\tilde{k}_y$ moves to larger values. We can keep $\tilde{k}_y$ in the center of the k_y mode range considered, if we apply redefinitions $S\left(k_y, k_z; k'_y, k'_z\right) \to S\left(k_y - \delta_y, k_z; k'_y - \delta_y, k'_z\right)$ along with $A(x) \to A(x) - \hbar\delta_y/e$ whenever $\tilde{k}_y$ increases above a threshold value. Here, $\delta_y = 2\pi/W_y$ is the mode separation. This shift operation can be expressed as a concatenation with the scattering matrix,[258]

$$S_s = \begin{pmatrix} t_s & r'_s \\ r_s & t'_s \end{pmatrix}, \tag{4.34}$$

where

$$t_s(k_y, k_z; k'_y, k'_z) = \delta_{k_z,k'_z}\delta_{k_y,k'_y-\delta_y}, \quad r_s(k_y, k_z; k'_y, k'_z) = e^{i\phi}\delta_{k_z,k'_z}\delta_{k_y,k_{y,\max}}\delta_{k'_y,k_{y,\max}},$$
$$t'_s(k_y, k_z; k'_y, k'_z) = \delta_{k_z,k'_z}\delta_{k_y,k'_y+\delta_y}, \quad r'_s(k_y, k_z; k'_y, k'_z) = e^{i\phi}\delta_{k_z,k'_z}\delta_{k_y,k_{y,\min}}\delta_{k'_y,k_{y,\min}}.$$

Here, ϕ is an arbitrary phase and $k_{y,\min} \simeq -R_y/\xi$ and $k_{y,\max} \simeq R_y/\xi$ are the minimal and maximal wave vectors considered.

4.2.4 Born-Kubo Analytical Bulk Conductivity

We apply our numerical approach in the important and experimentally relevant bulk limit $L \to \infty$. As mentioned in the introduction, under the additional assumption of weak disorder, the transversal magnetotransport is expected to be diffusive. The conductivity σ_{xx} can be calculated using the Kubo formula along with the Born approximation, following Abrikosov's seminal work[26]. Here, weak disorder is understood to fulfill two conditions: (i) $K_0 < K_c$ where K_c is the critical disorder strength that, for $B = 0$, drives the semimetal to a diffusive metal phase. From Ref. 27, we know that $K_c \simeq 5$ for the specific disorder model in Eq. (4.3). (ii) The disorder-induced level broadening Γ should be small compared to the Landau level separation $\sim \hbar v/\ell_B$.

In Appendix C.2, we present a self-contained derivation for the transversal magnetoconductivity in the weak disorder case for the model defined in Sec. 4.2.1. The calculation is carried out in the limit $T \to 0$ such that it can be compared to the exact numerical data but the result remains valid for finite $k_B T$ as long as $k_B T \ll \hbar v/\ell_B$. We find

$$\sigma_{xx} = \frac{e^2}{h\xi}\frac{K_0}{8\pi^2}\frac{1}{1+(\ell_B/\xi)^2}. \tag{4.35}$$

The disorder broadening of the lowest non-chiral Landau level is found to be

$$\Gamma = \frac{K}{4\pi}\frac{\hbar v\xi}{\ell_B^2+\xi^2}. \tag{4.36}$$

For chemical potential at the nodal point, $\mu = 0$, the Hall conductivity σ_{xy} vanishes[26;44] and $\rho_{xx} = 1/\sigma_{xx}$.

4.2.5 Numerical Results in Disordered Samples

We now turn to the discussion of the results of our numerical approach from Sec. 4.2.3 with finite disorder strength. We start with the weak disorder case and check for the validity of the analytical approach in Sec. 4.2.4. The numerical results for $K_0 = 3$ and $\ell_B/\xi = 1.8, 2.1, 2.5, 3.0$ and 3.6 are presented in Fig. 4.7. In the bulk limit $L \to \infty$, the disorder averaged conductance behaves diffusively, i.e., $\partial R/\partial L = \text{const.}$, cf. panel (a). The red dashed lines denote the slope that is expected on the basis of the analytical conductivity σ_{xx} from Eq. (4.35), panel (e). The agreement is excellent and confirms the validity of the Born-Kubo calculation. As a further confirmation of diffusive transport, the Fano factor in the bottom panel asymptotically converges to $F = 1/3$, cf. panel (c).

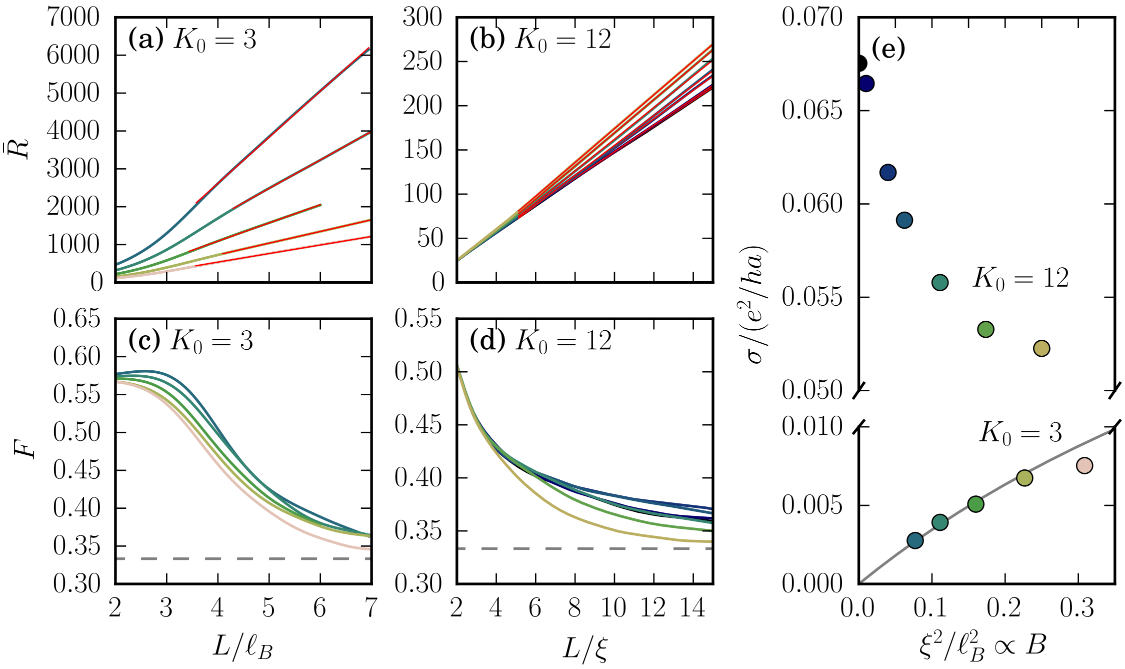

FIGURE 4.7: Numerical results for transversal magnetotransport in a disordered Weyl node. (a) The normalized resistance $\bar{R} = G^{-1}e^2W_yW_z/(h\xi^2)$ as function of system length for small disorder $K_0 = 3$ is linear in L for $L/\ell_B \gg 1$, shown here for different values of $\ell_B/\xi = 1.8, 2.1, 2.5, 3$ and 3.6 (color coding in panel (e)), averaged over 100 disorder configurations. The slope $\partial\bar{R}/\partial L$ is obtained from a numerical fit (red curves), giving the resistivity. (b) For large (supercritical $K_0 > K_c$) disorder, $K_0 = 12$, the normalized resistance $\bar{R}$ is linear in L for $L/\xi \gg 1$, shown here for different values $\ell_B/\xi = 2, 2.4, 3, 4, 5, 10$, and 10^4 (color coding in panel (e)), averaged over 500 disorder configurations. In panels (c) and (d), the Fano factor is shown as a function length, which approaches for both $K_0 = 3$ and $K_0 = 12$ the diffusive value of $F = 1/3$ (dashed line). (e) The conductivity as a function of magnetic field, more precisely ξ^2/ℓ_B^2, follows the analytical expectation (gray line) for $K_0 = 3$ (lower data points). For $K_0 = 12$, the conductivity decreases with the magnetic field, different from the behavior at small disorder that is covered by the analytical treatment.

In the case of strong (supercritical) disorder, the Weyl node at $B = 0$ behaves as a diffusive metal with a finite conductivity[27]. In Fig. 4.7 (b) we show the resistance in the case $K_0 = 12$, indicating a decreasing conductivity with system size, panel (e). Unfortunately, due to the limitations in system length, the bulk limit ($L \gg \ell_B$ and constant $\partial R/\partial L$) cannot be assessed for $\ell_B \gtrsim 5\xi$ and the weak field scaling of $\Delta\sigma_{xx}(B) = \sigma_{xx}(B) - \sigma_{xx}(0)$ cannot be identified unambiguously. If longer system sizes become available in the future, it would be interesting to check if the predicted[44] scaling $\Delta\sigma_{xx}(B) \propto B^2$ holds. For larger B, we observe a saturation at $\Delta\sigma_{xx}(B)/\sigma_{xx}(0) \simeq -0.25$. For completeness, the Fano factor is shown in panel Fig. 4.7 (d), approaching the diffusive limit $F = 1/3$.

4.2.6 Conclusion

In this work, we developed a numerical approach to transversal magnetotransport in an undoped Weyl node. Our method is based on a real space formulation and is thus suitable for mesoscopic systems as well as capable of capturing the bulk limit. Building on the scattering matrix technique, we circumvent the fermion doubling theorem and faithfully describe single node physics. Our method treats both disorder and magnetic field exactly. Starting from the clean limit, the following qualitative picture emerges: the wave functions of the Landau levels are localized along the transport direction, and centered around a position determined by the crystal momentum in the direction perpendicular to both transport- and magnetic field direction. The wave functions decay exponentially in transport direction leading to a conductance exponentially decaying with system length. However, this picture is unstable under the inclusion of any finite amount of disorder, which breaks crystal momentum conservation and consequently allows for hopping between localized orbitals Eventually, with increasing length, diffusive transport characteristics emerge.

In the case of weak but finite disorder strength, our exact numerical data are in excellent agreement with results from an existing analytical approach that we adapted to the correlated disorder potential assumed. The analytical approach is perturbative in disorder and is frequently used to explain experimental observations. Further, our exact numerical method has been applied to situations beyond the validity of the analytic result, namely the clean and the strongly disordered limit.

An important ingredient in the theory of transversal magnetotransport is the type of disorder. We have chosen to work with Gaussian disorder with finite range correlations. Recently, finite range correlated disorder was also investigated analytically in Ref. 236 with the claim that it leads to decreasing transversal conductivity with increasing magnetic field if the correlation length exceeds the magnetic length, different from our analytic result in Eq. (4.35) that is backed up with numerics. We remark that the celebrated linear magnetoresistance observed in experiments is believed to be due to the presence of screened Coulomb type disorder. Our method, of course, can be easily adapted to any kind of Gaussian disorder correlator.

An interesting direction for further study is the straightforward generalization of our method to finite chemical potential. First, this would be relevant for experiments. Second, in the semiclassical limit, Song *et al.* proposed a guiding center picture of linear magnetoresistance that could be checked with our exact and fully quantum-mechanical approach.[259]

4.3 Transport in the Presence of Axial Magnetic Fields

As discussed in Sec. 3.5, strain in Weyl semimetals has peculiar consequences: it creates effective axial electric and magnetic fields,[195;203;204] similar to pseudo-fields in graphene that are created by strain.[260;261] Axial magnetic fields result in pseudo-Landau levels at low energies[203;204] and axial electric fields induce chirality-dependent transport,[204] similar to real electromagetic fields. However, different from electromagnetic fields, axial fields act with an opposite sign on opposite chiralities.[193] Thus, the pseudo-Landau levels created by the axial magnetic fields have the same dispersion for both chiralities.

The axial fields are created via a time- and space dependent Weyl node separation $b_\mu \to b_\mu(t, \mathbf{b})$ due to fluctuations in the hopping amplitudes created by strain.[203;204] Such a variation in $\mathbf{b}$ results in the axial fields[164]

$$\mathbf{B}_5 = \nabla \times \mathbf{b}, \;\; \mathbf{E}_5 = -\nabla b_0 - \partial_t \mathbf{b}. \tag{4.37}$$

By requiring $b_\mu = 0$ in the vacuum, we can understand the emergence of Fermi arcs: they result from an effective field $\mathbf{B}_5$ at the surface created by the change of $\mathbf{b}$ from its bulk value to zero.[204] For a bulk $\mathbf{B}_5$ created by strain, charge conservation ensures that states with an opposite velocity to the bulk pseudo-Landau levels must exist somewhere in the spectrum. This is ensured by the surface: since $b_\mu = 0$ outside the sample, any $\mathbf{B}_5$ in the bulk is counteracted at the surface, creating an axial magnetic field of opposite sign. Over the whole sample, $\mathbf{B}_5$ always averages to zero.[204]

Axial magnetic fields are expected to give rise to pseudo-magnetic quantum oscillations[262;263] and enhance the conductivity by an additional anomaly-induced contribution.[203;204] The chiral fields give rise to collective excitations[217] and they can be simulated in cold atom systems.[213] The careful determination of robust transport signatures, however, is still lacking. Especially phenomena related to a local redistribution of charge, such as the chiral-anomaly induced contribution to semiclassical transport,[40;203] may suffer from screening effects.

In this section, we predict another experimental signature: the scaling of conductance with the system's width. We find that the conductance for transport along $\mathbf{B}_5$ increases with the width cubed, different from the usual scaling in diffusive systems.[97] This different scaling originates in the spatial separation of left- and right-moving modes, as described above as the effect of a surface $\mathbf{B}_5$ that counteracts its bulk counterpart. We explicitly demonstrate the scaling by employing tight-binding simulations to compute the conductance.

4.3.1 Model and Methods

The starting point of our investigation is the action of massive Dirac fermions subjected to a Lorentz-breaking perturbation $b_\mu = (b_0, \mathbf{b})$,

$$\mathcal{S} = \int d^4x \bar{\psi} \left[\gamma^\mu \left(i\partial_\mu - A_\mu - b_\mu \gamma^5 \right) - m \right] \psi, \tag{4.38}$$

the same action (3.24) used in Secs. 3.2 and 3.4 to derive the chiral anomaly. The field b_μ acts as a chiral gauge field such that the different chiralities of Weyl fermions are subjected to different effective gauge fields, $A^\chi_\mu = A_\mu + \chi b_\mu$. These have consequences for space- and time-dependent b_μ fields: the effective electric and magnetic fields are different for the two chiralities, $\mathbf{E}^\chi = \mathbf{E} + \chi \mathbf{E}_5$ and $\mathbf{B}^\chi = \mathbf{B} + \chi \mathbf{B}_5$.

In this section, we discuss the consequences of an axial magnetic field on charge transport driven by electric fields, so we set $\mathbf{E}_5 = 0$ in the following. These consequences can be intuitively understood by considering the electronic dispersion in presence of an axial magnetic field, shown in Fig. 4.8, where the effect of $\mathbf{B}$ (panels (a) and (b)) is compared to $\mathbf{B}_5$ (panels (c) and (d)). Landau levels form as a consequence of $\mathbf{B}_5$, similar to the Landau levels due to a magnetic field. However, while the zeroth Landau levels of the two chiralities disperse in opposite directions when created by a magnetic field, the axial magnetic field acts with an opposite sign on the two chiralities, resulting in the same velocity for the two chiralities. Modes that are counterprogating to the bulk states exist at the surface where the Weyl node separation goes to zero, cf. Fig. 4.8 (c) and (d), i.e., counter-propagating modes are localized at different real-space positions. Modes deep in

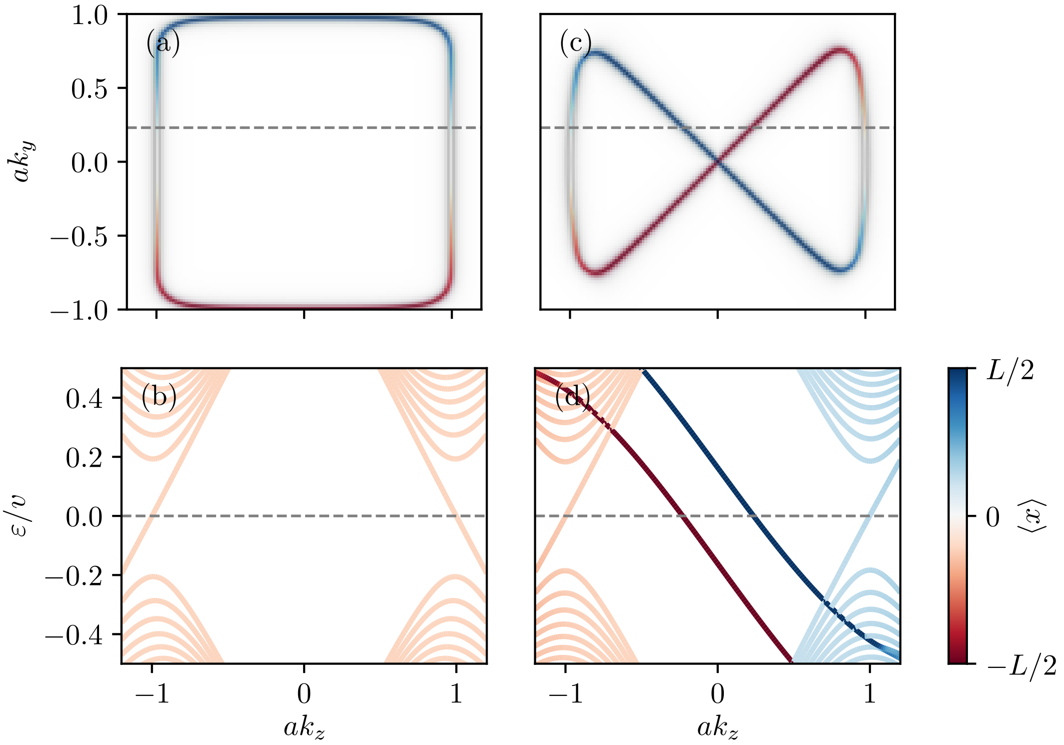

FIGURE 4.8: Fermi surface and dispersion of a Weyl semimetal, Eq. (4.39), subjected to a magnetic field or to strain, where the color denotes the real-space localization $\langle x \rangle$ of the states. We choose open boundary conditions with $L/a = 100$ sites in the x-direction. (a) Fermi surface in presence of a magnetic field $\mathbf{B} = B\hat{z}$. The Fermi arcs separate in momentum space (top and bottom) and the bulk Weyl nodes become Landau levels with position-momentum locking. (b) Dispersion at constant $ak_y = 0.23$ (dashed lines in panels (a) and (c)). In presence of a magnetic field, counter-propagating states in z-direction are both located in the bulk. The transport time at low energies equals the internode scattering time.[42] The dashed line shows the Fermi energy $\varepsilon_F = 0$ as a guide for the eyes. (c) Fermi surface in presence of a pseudo-magnetic field $\mathbf{B}_5 = B_5\hat{z}$ in the bulk that pseudo-Landau levels with opposite position-momentum locking. As elaborated in the main text, the bulk field results in a tilted pseudo-magnetic field in the surface, thus, in tilted Fermi arcs. (d) For a pseudo-magnetic field, bulk states propagate in the same direction. Backscattering is just possible via the surface states.

the bulk have to scatter all the way to the surface to relax,[203] i.e., the relaxation time enhances with the real-space separation of the counterpropagating modes. Thus, we expect that the scattering time for those modes deep in the bulk increases with the system's width. The arguments given above apply in the ultra-quantum limit, i.e., when the physics is dominated by the zeroth Landau levels. Semiclassical charge transport at much higher chemical potential might also show signatures of the the axial magnetic fields.[203] We leave an investigation of semiclassical transport for future studies.

To quantitatively investigate transport in presence of disorder, we employ a lattice model that realizes the action (4.38). We employ the Wilson fermion map[60] $-i\partial_j \to v \sin k_j$ and $m \to m + t\sum_j (1-\cos k_i)$, which gives the momentum-space Hamiltonian given in Eq. (3.30). Here, we chose isotropic velocities and change $b_\mu \to v b_\mu$ for simplicity, resulting in

$$\mathcal{H}_{\mathbf{k}} = v\left(\sin k_y \sigma_x - \sin k_x \sigma_y\right)\tau_z + v \sin k_z \tau_y + m\tau_x + t\sum_i \left(1-\cos k_i\right)\tau_x + v\sum_\mu u^\mu b_\mu. \quad (4.39)$$

If not otherwise stated, we use $t = 2v/\sqrt{3}$ throughout this section.

A spatial variation of the components of $\mathbf{b}$ generates the pseudo-field $\mathbf{B}_5 = \nabla \times \mathbf{b}$ in z-direction. To be precise, we chose $b_\mu = (0, 0, B_5 x, b_z)$, such that it has a constant component in the z-direction that separates the different chiralities in momentum space and a x-dependent component in the y-direction, with $x \in [-L/2, L/2]$. We always take periodic boundary conditions in the y direction and open boundary conditions in the x-direction. The transport direction is always z, parallel to $\mathbf{B}_5$.

All transport calculations are performed using the Kwant code.[264] The total system consists of a wire of length $L_{||}$ connected to two semi-infinite clean leads at a different chemical potential μ_{lead}. The chemical potential is chosen such that the density of states in the leads is much higher than in the sample, in order to mimic metallic leads. The limit $\mu_{\text{lead}} \to \infty$ taken with the transfer matrix method[46] cannot be reached in the lattice model with a bounded spectrum.

4.3.2 Longitudinal Magnetotransport for Axial Fields

For clean systems and $\mu_{\text{lead}} = 0$, the conductance $G = ne^2/h$ for n propagating modes. For both $\mathbf{B}$ and $\mathbf{B}_5$, the number of propagating modes increases linearly with the sample's cross section, i.e., the sample's width squared, and the field strength. This can be understood from Fig. 4.8, panels (a) and (c): the number of propagating modes equals the length of the zeroth (pseudo-) Landau level in momentum space times the density of momenta k_y. The latter increases linearly with L_y, and the length of the (pseudo-) Landau level increases linearly with both L_x and B (or B_5, respectively). Given the same dimensions and the same (pseudo-) magnetic length, the conductance for axial fields is twice as big as for magnetic fields, since both Landau levels contribute for one particular value of k_y. There is no difference in the scaling of the conductance in the clean case between real and axial magnetic fields.

In Fig. 4.9, we compare these expectations with lattice results for clean samples with $\mu_{\text{lead}} = 0$. In panels (a) and (b), we show the conductance as a function of B_5 and B and see that it indeed increases linearly with B. In presence of B_5, the linear regime breaks down at a certain field strength, characterized by $B_5 \propto a^2/\ell_5^2 \gtrsim 0.1$. This breakdown is a lattice effect: the implementation of the Weyl node separation b_μ as a constant in the Hamiltonian is not valid for large $b_\mu \gg 1/a$. In presence of B_5, the condition $b_\mu \ll 1/a$ is not satisfied for $B_5 \gg 1/a^2$ and/or $L_\perp \gg a$. The consequences of the second conditions

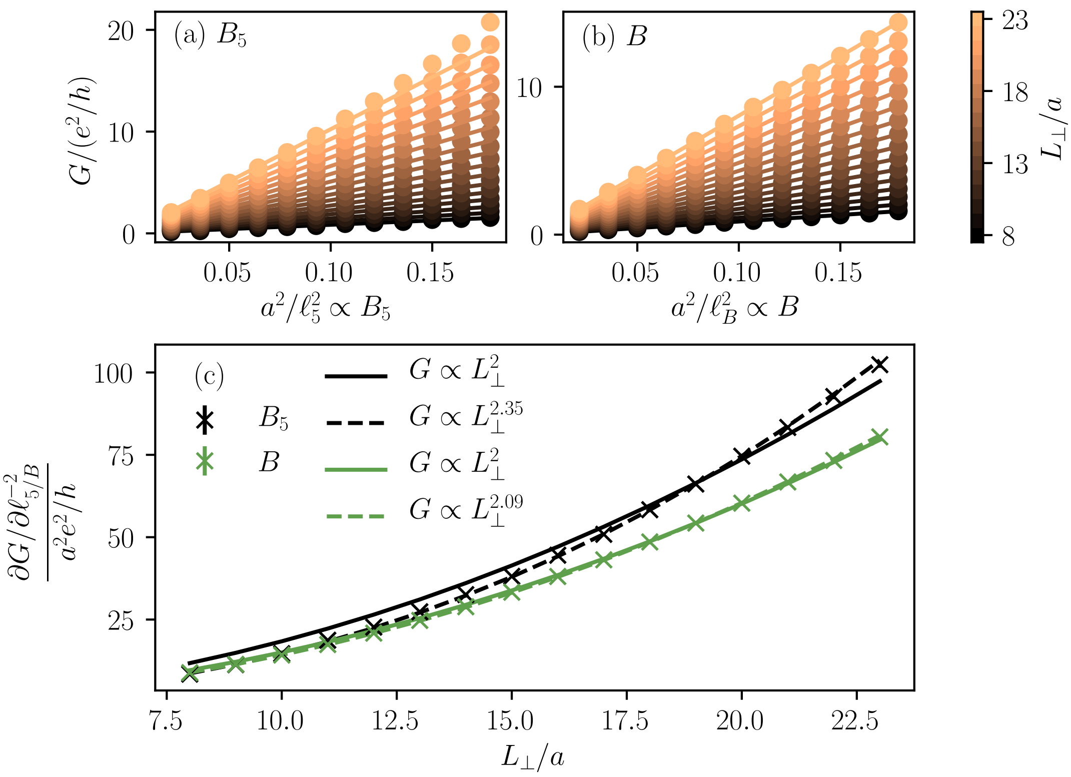

FIGURE 4.9: Conductance of clean samples in presence of (axial) magnetic fields. (a) Conductance as a function of B_5 ($\mathbf{B} = 0$) for transport along $\hat{z} \parallel \mathbf{B}_5$. For small fields a^2/ℓ_5^2, the conductance grows linearly with B_5 (linear fit by solid line), whereas the growth increases for larger values of $a^2/\ell_5^2 \gtrsim 0.1$. (b) The conductance as a function of B ($\mathbf{B}_5 = 0$) grows linearly with B, even at large field strengths. (c) The slope of the conductance $\partial G/\partial B$, obtained from panel (a), increases quadratically with $L_\perp$, the system's width (solid green line; a power-law fit gives a value slightly larger than 2, dashed green line). The slope in presence of $\mathbf{B}_5$, $\partial G/\partial B_5$, obtained from panel (b), however, increases faster: a power-law fit gives $\partial G/\partial B_5 \propto L_\perp^{2.35}$ (dashed black line).

are evident from Fig. 4.9 (c): while the conductance in presence of B grows with $L_\perp^2$, as expected, the a power-law fit of the conductance in presence of B_5 gives a larger power and a scaling $G \propto L_\perp^{2.35}$. To avoid these lattice-induced scaling effects, we limit the size of both B_5 and $L_\perp$ in the subsequent discussion.

To discuss (axial) longitudinal magnetotransport in presence of disorder, we add both vector and scalar disorder by introducing a random on-site matrix $V(\mathbf{r}_i)$ that has the form and disorder correlation

$$V(\mathbf{r}_i) = \sum_{\mu\nu} v_{\mu\nu}(\mathbf{r}_i)\sigma_\mu \tau_\nu, \qquad \langle\!\langle v_{\mu\nu}(\mathbf{r}_i) v_{\rho\sigma}(\mathbf{r}_j) \rangle\!\rangle = g_{\mu\nu} K(\mathbf{r}_i - \mathbf{r}_j)\delta_{\mu\rho}\delta_{\nu\sigma} \tag{4.40}$$

to the lattice Hamiltonian. The function $K(\mathbf{r}_i - \mathbf{r}_j)$ is the disorder correlator. Since the presence of Weyl nodes in the Hamiltonian (4.39) does not rely on the presence of any symmetries, no restrictions are put on the matrix form of disorder and we set for convenience $g_{\mu\nu} = 1$.

For a better comparison between real and axial magnetic fields, we briefly review known results for external magnetic fields. For any, even infinitesimally small,[152] disorder, charge transport along the direction of the magnetic field is diffusive, i.e., the conductance $G = \sigma L_\perp^2/L_\parallel$ with the length along the transport direction $L_\parallel$, the width $L_\perp$, and the conductivity σ that is independent of the system's dimensions. The scaling of the conductivity with the magnetic field depends on the type of disorder correlator $K(\mathbf{r}_i - \mathbf{r}_j)$. For white-noise disorder

$$K(\mathbf{r}_i - \mathbf{r}_j) = \frac{W^2}{12}\delta_{ij}, \tag{4.41}$$

the conductivity in the ultra-quantum limit is independent of the magnetic field,[235] as observed in TaAs.[265] A disorder potential with correlations mimics physical disorder more realistically, which creates a potential that varies on some scale ξ. Gaussian correlations in the disorder potential change the conductivity scaling to $\sigma \propto (\xi^2 + \ell_B^2)/\ell_B^2$.[236;237;250] In the strong-field limit $\ell_B \ll \xi$, such that σ increases with the inverse magnetic length squared, i.e., with the magnetic field. When $\ell_B \gg \xi$, the scaling for white-noise disorder is recovered.

Two things change when we replace the magnetic field by an axial magnetic field: first, the conductivity increases linearly with B_5 for white-noise disorder and quadratically with B_5 for correlated disorder.[203] Second, as argued above using Fig. 4.8, the conductivity increases with the system's width due to the spatial separation of counterpropagating modes. Both expectations only hold in the ultra-quantum regime. As soon as disorder becomes large enough to mix the zeroth and higher Landau levels, all effects dominated by the zeroth Landau levels start to wash out—especially phenomena driven by the same propagation direction of the zeroth Landau levels for $\mathbf{B}_5$ and counterpropagation for $\mathbf{B}$. We thus expect that the conductance scales similarly for axial and magnetic field in strongly disordered systems.

To account for the scaling of the conductivity with the system's width, we define the dimensionless conductivity $g(L_\perp)$, a quantity that is *not* independent of the system's dimensions, via

$$G = \frac{e^2}{ha}\frac{L_\perp^2}{L_\parallel}g(L_\perp) \tag{4.42}$$

with the lattice constant a. We consider the regime where we observe $g(L_\perp)$ independent of $L_\parallel$, i.e., the diffusive regime where $G \propto 1/L_\parallel$.

In the tight-binding simulations, we need to be careful to observe the diffusive regime. When $L_\parallel \gg L_\perp$, the system is essentially one dimensional and the charge carriers always localize, giving an exponentially decreasing conductance.[266] Similarly, large disorder also leads to localization in the correct three-dimensional limit $L_\parallel \ll L_\perp$.[267] Finite-size effects also play an important role: if, for small disorder, the disorder-induced level broadening is smaller than the level spacing, transport is ballistic. Averaging over twisted boundary conditions eliminates another finite-size effect, the restriction of few momenta k_y.

Numerically, we investigate the conductance as a function of the longitudinal system size $L_\parallel$ in presence of white-noise disorder (4.41). We focus on the regime where the inverse conductance increases linearly with $L_\parallel$, which we can observe up to $L_\parallel \lesssim 3L_\perp$ before reaching the one-dimensional limit that shows the onset of localization. In Fig. 4.10, we compare transport in presence of axial fields with magnetic fields for different field strengths characterized by the magnetic length $\ell_B = \sqrt{\hbar/(eB)}$ and the pseudo-magnetic length $\ell_5 = 1/\sqrt{B_5}$. The dimensionless conductivity (4.42) is the inverse slope of G^{-1} when plotted as a function of $L_\parallel$, panels (a) and (b). We find that the dimensionless conductivity

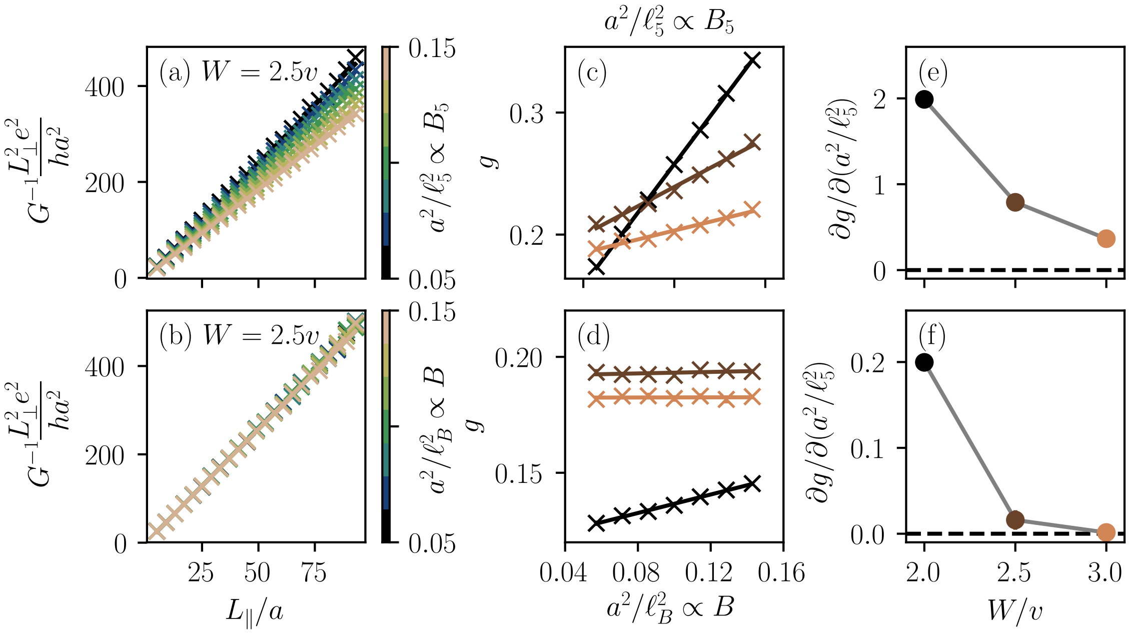

FIGURE 4.10: Numerically obtained inverse conductance (a) in presence of $\mathbf{B}_5$ and (b) in presence of $\mathbf{B}$ a function of $L_\parallel$, the system size in transport direction. The different colors denote different values of the (axial) magnetic length ℓ_B (ℓ_5). The slope from panels (a) and (b) is the inverse of the dimensionless conductivity g, which is shown in panels (c) and (d) as a function of the (axial) magnetic field strength for different disorder strengths W/v. While g clearly increases with B_5, it stays almost constant in presence of magnetic fields B and disorder $W/v \gtrsim 2.5$. In panels (e) and (f), we plot the slope $\partial g/\partial B_5$ ($\partial g/\partial B$) as a function of disorder. All results are averaged over twisted boundary conditions and 100 disorder configurations; the chemical potential in the lead is $\mu_{\text{lead}} = 1.5v$, and the transversal width $L_\perp = 21a$.

increases with the strength of the axial field B_5, panel (c), while it does does not increase with B for sufficiently large disorder, panel (d). In presence of axial fields, the slope $\partial g/\partial B_5$ decreases with the disorder strength W before it eventually reaches zero. This is due to the influence of higher Landau levels that start to contribute to the conductance, especially for small fields in comparison to the disorder strength, i.e., large (axial) magnetic lengths $\ell_B > \hbar v/W$ ($\ell_5 > \hbar v/W$).

The additional factor of B_5 in the conductance was explained in Ref. 203: to relax between counterpropagating modes, the states deep in the bulk need to scatter all the way to the surface. To travel the distance $L_\perp$, $(L_\perp/\ell_5)^2$ scattering events are necessary.[203] The scaling of the conductivity with B_5 is different from the one obtained in Ref. 203 since we take the scaling of the microscopic scattering time into account.

In Fig. 4.11 (a) and (b), we show the inverse conductance for different values of $L_\perp$. The dimensionless conductivity increases with $L_\perp$ in presence of B_5, panel (c) but stays constant in presence of B, panel (d). This is one of the main results of this section: the dimensionless conductance depends on the system's dimensions; in particular, it increases linearly in the regime that we consider. Similar to the scaling with B_5 itself, the slope with $L_\perp$ decreases with the disorder strength, due to the mixing with higher Landau levels.

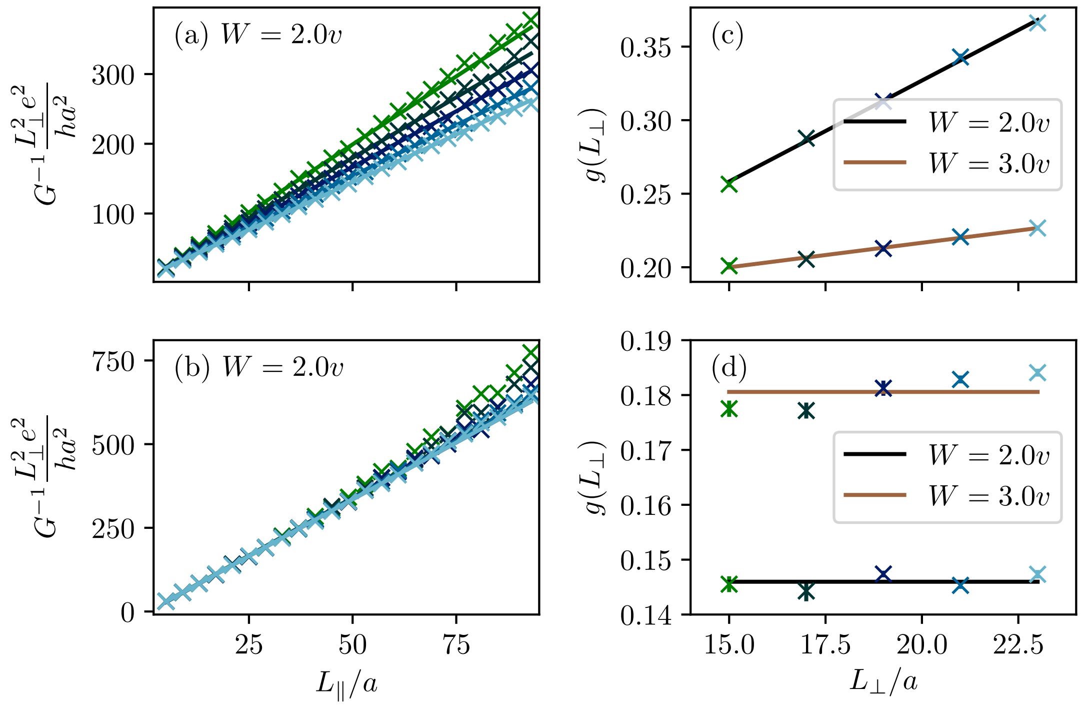

FIGURE 4.11: Numerically obtained inverse conductance (a) in presence of $\mathbf{B}_5$ and (b) in presence of $\mathbf{B}$ as a function of $L_\parallel$, the system size in transport direction. The different colors denote different values of the transversal dimension $L_\perp$, cf. panels (c) and (d). The slope from panels (a) and (b) is the dimensionless conductivity g, shown in panels (c) and (d) as a function of the transversal dimension $L_\perp$ for different disorder strengths W/v. While g increases linearly with $L_\perp$ in presence of axial fields, it stays, apart from finite-size effects, constant in presence of magnetic fields B. All results are averaged over twisted boundary conditions and 100 disorder configurations; the chemical potential in the lead is $\mu_{\text{lead}} = 1.5v$, and (axial) magnetic length $\ell_B = 2.65a$ ($\ell_5 = 2.65a$).

4.3.3 Conclusion

In this section, we numerically showed how transport is affected in presence of axial magnetic fields and white-noise disorder. We explicitly demonstrated that the dimensionless conductivity increases with both B_5, the strength of the axial field, and $L_\perp$, the transversal width of the system. Both observations can be intuitively understood by considering the band structure of the sample, Fig. 4.8.

We leave a more detailed analysis for future studies: in particular, we cannot explain the scaling with $L_\perp$ based on simple analytical arguments, which calls for a perturbative treatment of disorder scattering. We further did not evaluate the energy scales that give the mixing with higher Landau levels carefully—especially how the disorder strength W is related to the cyclotron frequency $\omega_B = v/\ell_5$.

We are confident that the discussed behavior can be observed in the near future, considering the recent efforts in manufacturing microstructured Weyl semimetals.[268] Such an experiment would not require the generation of large magnetic fields to reach the quantum limits; instead, strain can easily induce axial field strengths equivalent to a few Tesla.[261]

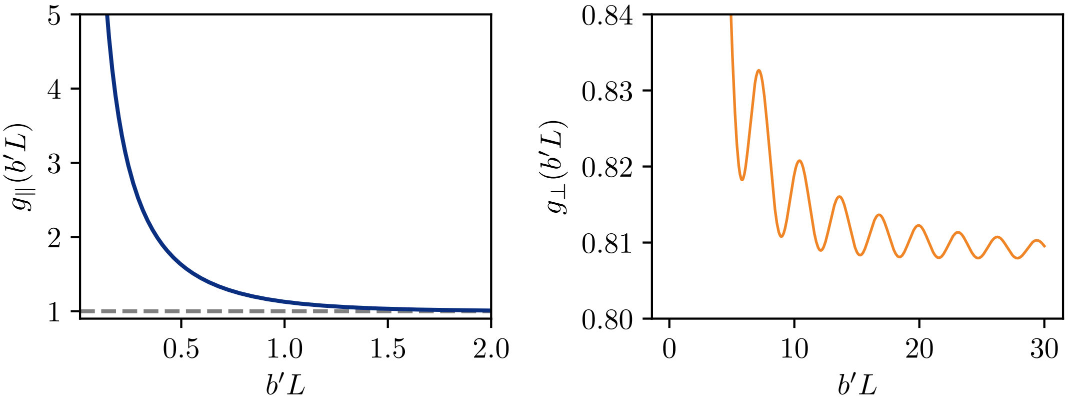

FIGURE 4.12: Dimensionless conductivity of a clean nodal line semimetal (4.43) as a function of $b'L$ for both transport along the vector $\mathbf{b}'$ (a) and orthogonal to $\mathbf{b}'$ (b). For transport along $\mathbf{b}'$, the dimensionless conductivity (4.50) reaches the value obtained using the Kubo formula.[33] The dimensionless conductivity orthogonal to $\mathbf{b}'$ (4.54) does not reach the prediction from the Kubo formula ($g_{\perp} = 1$) in the limit $b'L \gg 1$, but rather oscillates around a different, smaller value.

4.4 Transport in Nodal Line Semimetals

Transport in semimetals is largely determined by the codimension of the Fermi surface, i.e., the system's dimension minus the dimension of the Fermi surface.[32] This means that in three-dimensional nodal line semimetals, transport is similar to graphene.[33] This has two important implications: first, in clean systems, the conductance decreases with the inverse system length, as in diffusive systems. We are thus able to define the conductivity of a clean nodal line semimetal, which is not possible for clean metals or clean Weyl semimetals.[27;269] Second, quantum anomalies also play an important role in the charge transport of nodal line semimetals. The parity anomaly observed in graphene[185] may have a parametrized counterpart in nodal line semimetals.[47;48]

In this section, we discuss the possibility of another analogy to graphene: the unsaturated growth of the conductivity with disorder.[46] We extend the transfer matrix method to nodal line semimetals and investigate transport in clean samples, before presenting preliminary results for disordered samples. These preliminary results clearly show a growth of the conductivity with disorder, although the exact scaling remains left for future studies.

The starting point of our investigation is the low-energy Hamiltonian for nodal line semimetals, Eq. (2.41), with the simplifications $b_{\mu} = \mathbf{p} = m = 0$. Without loss of generality, we choose $\mathbf{b}' = b'\hat{z}$ in the subsequent discussion. Further reintroducing the velocity gives the Hamiltonian

$$\mathcal{H}_0 = \hbar v \left(\mathbf{k} \cdot \boldsymbol{\sigma} \tau_z + b' \sigma_z \tau_x \right) . \tag{4.43}$$

To investigate transport parallel to $\mathbf{b}'$, we rotate the matrices $\tau_z \to \tau_x$ and $\tau_x \to -\tau_z$ before performing the canonical transformation

$$\sigma_{\pm} \to \sigma_{\pm} \tau_z, \qquad \tau_{\pm} \to \sigma_z \tau_{\pm} \tag{4.44}$$

and rotating back $\tau_x \to \tau_z$, $\tau_z \to -\tau_x$. The rotation of the Pauli matrices has the advantage that the velocity operator in transport direction is τ_z, which allows to easily distinguish left- and right-moving modes. The eigenstates of the disordered Hamiltonian $\mathcal{H}_0+V$ satisfy $(\mathcal{H}_0+V-\varepsilon)\psi=0$, which can be rewritten as

$$i\partial_z\tau_z\psi=\left(\frac{V-\varepsilon}{\hbar v}+\left(k_x\sigma_y-k_y\sigma_x\right)\tau_y+b'\sigma_z\tau_x\right)\psi. \tag{4.45}$$

The eigenfunctions have the formal solution $\psi(z)=T(z,z')\psi(z')$ with the transfer matrix

$$T(z,z')=P_{z''}\exp\left[\int_{z'}^{z}dz''\left(i\frac{\varepsilon-V}{\hbar v}\tau_z+(k_x\sigma_y-k_y\sigma_x)\tau_x-b'\sigma_z\tau_y\right)\right] \tag{4.46}$$

where $P_{z''}$ denotes position ordering. At $E=V=0$, all summands in the exponent commute and we can solve the integral and the matrix exponential exactly. Introducing cylindrical coordinates allows to write the transfer matrix connecting states at $z'=0$ with $z=L$ in the compact form

$$T(L,0)=\left(\cosh(kL)+e^{-i\phi\sigma_z}\sinh(kL)\sigma_y\tau_x\right)\left(\cosh(b'L)-\sinh(b'L)\sigma_z\tau_y\right). \tag{4.47}$$

The elements of the transfer matrix can be identified with the elements of the scattering matrix, cf. Appendix D. In particular, the transmission for samples of length L reads

$$t^{\dagger-1}=\begin{pmatrix}\cosh(b'L)\cosh(kL) & e^{-i\phi}\sinh(b'L)\sinh(kL)\\ e^{i\phi}\sinh(b'L)\sinh(kL) & \cosh(b'L)\cosh(kL)\end{pmatrix}, \tag{4.48}$$

which results in the conductance in the limit where the width W is much larger than the length, i.e., $W\gg L$,

$$G_\parallel=\frac{e^2}{h}\mathrm{Tr}\left[t^\dagger t\right]=\frac{e^2}{h}\frac{W^2}{2\pi}\int_0^\infty dk\,k\frac{4\left[\cosh^2(L(b'-k))+\cosh^2(L(b'+k))\right]}{(\cosh(2b'L)+\cosh(2kL))^2} \tag{4.49}$$

$$=\frac{e^2}{h}\frac{W^2}{L}\frac{b'}{\pi}\frac{\log\left(4\cosh^2(b'L)\right)}{2b'L}\equiv\frac{e^2}{h}\frac{W^2}{L}\frac{b'}{\pi}g_\parallel(b'L) \tag{4.50}$$

with the dimensionless conductivity $g_\parallel(b'L)$ defined in the last equation. From Eq. (4.50), we can easily recover the conductance of a clean Weyl semimetal by setting $b'=0$.[27;269] We further realize that the conductance scales as in metallic systems for $b'L\gg 1$,

$$\lim_{b'L\to\infty}G_\parallel=\frac{e^2}{h}\frac{W^2}{L}\frac{b'}{\pi} \tag{4.51}$$

since $\lim_{x\to\infty}g_\parallel(x)=1$. This implies that the conductivity is $\sigma_\parallel/(e^2/h)=b'/\pi$, the same result that Burkov *et al.* found using the Kubo formula.[33] The dimensionless conductivity $g_\parallel(b'L)$ approaches 1 very fast, with less than 1 % deviation for $b'L=2$, as shown in Fig. 4.12 (a).

For transport orthogonal to $\mathbf{b}'$, we do not recover the expectation from the Kubo formula. After computing the transfer matrix for transport from $x=0$ to $x=L$, we isolate the transmission t that is used to obtain the conductance,

$$G_\perp=\frac{e^2}{h}\sum_{\mathbf{k}_\parallel}\frac{4}{1+\cos q_+\,\cos q_-+\frac{\sin q_+\,\sin q_-}{q_-\,q_+}L^2(b'^2+k^2)} \tag{4.52}$$

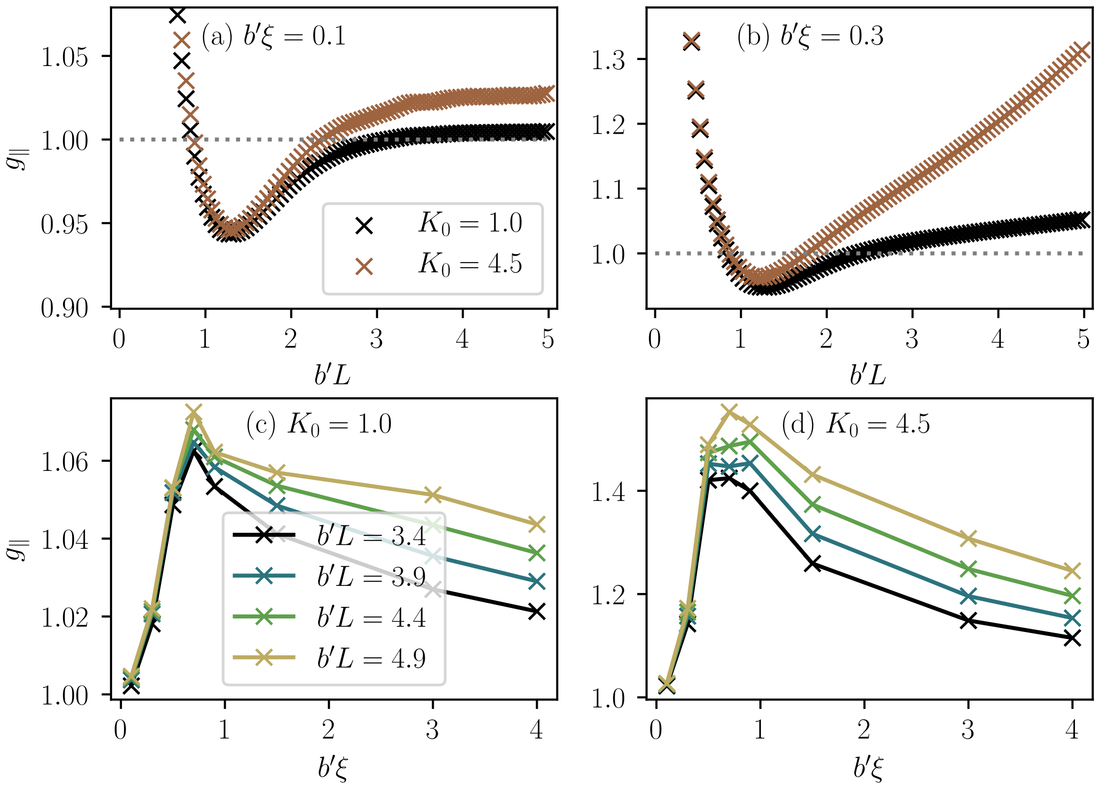

FIGURE 4.13: Dimensionless conductivity $g_\parallel$ of a disordered nodal line semimetal (4.43) for transport along the vector $\mathbf{b}'$, orthogonal to the plane of the nodal line. In (a) and (b), we show $g_\parallel$ as a function of $b'L$, the system's length, for two different disorder strengths K_0 and radii of the line b'. Different from the clean case, Eq. (4.50) and Fig. 4.12 (a), the conductivity increases with the length of the sample. The bulk result $g_\parallel = 1$ obtained in the clean case is included as a guide for the eyes. In (c) and (d), we show $g_\parallel$ as a function of $b'\xi$ for two different disorder strengths and different lengths $b'L$.

with $q_\pm \equiv L\sqrt{b'^2 - k^2 \pm 2ikb' \cos\phi}$ with the transversal momenta $k_y = k\sin\phi$, $k_z = k\cos\phi$. For large transversal widths, i.e., in the limit $W \gg L$, the sum can be transformed to an integral, giving

$$G_\perp = \frac{e^2}{h}\frac{W^2}{L}\frac{b'}{2\pi}\frac{2}{\pi}\int d\bar{k}\,\bar{k}\,d\phi \frac{b'L}{1+\cos q_+\,\cos q_- + \frac{\sin q_+}{q_-}\frac{\sin q_-}{q_+}b'^2L^2(1+\bar{k}^2)} \tag{4.53}$$

$$\equiv \frac{e^2}{h}\frac{W^2}{L}\frac{b'}{2\pi}g_\perp(b'L) \tag{4.54}$$

with the dimensionless conductivity $g_\perp(b'L)$ and $\bar{k} = k/b'$. The integral above does not have an analytical solution, but it can be evaluated numerically. We present the numerical solution $g_\perp(b'L)$ as a function of $b'L$ in Fig. 4.12 (b). In the limit $b'L \gg 1$, the dimensionless conductivity does not approach the result expected from the Kubo formula that gives $\sigma^\perp_{\text{Kubo}} = e^2b/(2\pi h)$ (note the factor of 2 compared to $\sigma^\parallel_{\text{Kubo}}$), implying $\lim_{x\to\infty} g_\perp(x) = 1$. Instead, the dimensionless conductivity oscillates around $g_\perp \approx 0.81$, where the oscillations decay approximately with $1/\sqrt{b'L}$. This mismatch suggests that the Kubo formula does not capture the clean limit properly.

What happens in the presence of disorder? In this section, we discuss the consequences of scalar disorder for transport along $\mathbf{b}'$ and leave transport orthogonal to $\mathbf{b}'$ for future studies. We add correlated disorder, Eq. (4.3), characterized by the correlation length ξ and the dimensionless disorder strength K_0, to the transfer matrix (4.46) while keeping the chemical potential in the sample at $\varepsilon = 0$. All results are in the limit $W \gg L$ where the system is characterized by three different length scales: its length L, the disorder correlation length ξ and the inverse of the nodal line's radius, $1/b'$.

In Fig. 4.13 (a) and (b), we show the dimensionless conductivity $g_{||}$ as a function of $b'L$ for various disorder strengths and correlations lengths ξ. Different from the clean case, the conductivity does not saturate for $b'L \gg 1$, but keeps increasing. This behavior is similar to graphene, where the conductivity shows an unsaturated growth in absence of intervalley scattering.[46] It might be possible to drive this analogy further and introduce a one-parameter scaling at a fixed radius b'; however, finding such a scaling is beyond the scope of this thesis.

We show the conductivity as a function of different radii characterized by $b'\xi$ in panels (c) and (d). The conductivity first increases until it reaches a maximum around $b'\xi = 1$ and eventually decreases with larger radius. This behavior is independent of the disorder strength and system length in the regime we analyzed numerically, although the shape of the peak and the value of the conductivity changes.

In conclusion, we find that the conductance for transport orthogonal to $\mathbf{b}'$ does not scale with the system's length as expected from the Kubo formula. We further show that, for transport parallel to $\mathbf{b}'$, the conductivity increases with the system's length, similar to graphene.[46] Further studies are necessary to investigate this behavior further, especially with regard to the scaling as a function of the nodal line's radius. We also leave the investigation of transport orthogonal to $\mathbf{b}'$ in presence of disorder for future work.

5 Nodal Line Semimetals from Weyl Superlattices

How can we realize nodal line semimetals? As we saw in Sec. 2.3.2, the existence of nodal lines is tied to the crystal symmetries of the underlying lattice system. Artificially engineered lattices, such as heterostructures and other superlattices, provide promising avenues to realize desired crystal symmetries that protect lower-dimensional Fermi surfaces. In this chapter, following Ref. 152, we investigate a Weyl semimetal subjected to a spatially periodic onsite potential, giving rise to several phases, including a nodal-line semimetal phase. In contrast to proposals that focus purely on lattice symmetries, the emergence of the nodal line in this setup does not require small spin-orbit coupling, but rather relies on its presence. We show that the stability of the nodal line is understood from reflection symmetry and a combination of a fractional lattice translation and charge-conjugation symmetry, giving one possible extension of the tenfold symmetry classification introduced in Sec. 2.2. Depending on the choice of parameters, this model exhibits drumhead surface states that are exponentially localized at the surface, or weakly localized surface states that decay into the bulk at all energies.

Symmetries play a crucial role in the realization of lower-dimensional Fermi surfaces: while Dirac semimetals with degenerate Fermi points require time-reversal in combination with crystal symmetries, such as reflection or rotational invariance, Weyl semimetals are stable even in absence of these.[31] However, Weyl nodes may be gapped by coupling two nodes of opposite chirality.[270] Although isolated Weyl nodes are generally stable towards small disorder,[27] scattering between different Weyl nodes couples them and may open up a gap in the spectrum by annihilating the Weyl nodes. Alternatively, we demonstrate that Weyl nodes can couple such that a new phase arises: a nodal-line semimetal with a one-dimensional Fermi surface.[33;125;150;271–282]

Nodal-line semimetals exhibit surface bands at a limited range of momenta.[134] These bands may serve as a basis for correlated physics in the presence of interactions.[283] In the bulk, the implications of the nodal line include a sharply peaked magnetic susceptibility at zero energy,[284;285] three-dimensional integer quantum Hall effect,[286] and intriguing transport and density response properties.[33;287–295] However, nodal-line phases generically do not survive the inclusion of spin-orbit coupling,[36;271–275;296;297] which lifts the nodal degeneracy leading to isolated Weyl points. It is thus desirable to conceive realizations of nodal-line semimetals that do not rely on a small or vanishing spin-orbit coupling, as already suggested in previous proposals[129;298;299] that require time-reversal and inversion symmetry, or nonsymmorphic symmetries.[300;301]

In this chapter, we show that a Weyl semimetal subjected to a spatially periodic modulation of the onsite potential can undergo a transition to various phases, including a nodal-line semimetal. Since spin-orbit coupling is usually a requirement to have a Weyl phase,[36;37] the nodal-line semimetal also relies on it, contrary to other proposals that require small spin-orbit coupling.[271–275;297] We present the topological classification of the nodal line, showing that its stability relies on reflection symmetry[116] and a combination of a fractional lattice translation and charge-conjugation symmetry.

The nodal-line semimetal phase that we predict exhibits surface states that are not pinned to zero energy, similar to previously studied models with drumhead surface states at low energies.[134;276;282] The extra charge accumulation due to states at the surface is tied to the intercellular Zak phase, cf. Sec. 2.4.[113] This implies that realizations without surface states exponentially localized to the boundary are possible. Nodal-line semimetals without surface states at low energies enable the direct study of the bulk properties of the nodal line.

Periodic superlattices can be implemented both in solid-state[302–304] and synthetic systems.[305–307] Multilayer heterostructures can effectively realize superlattices for Weyl fermions in crystalline solids. A Weyl phase realized on an optical lattice[308] can be supplemented with a superlattice[309] to obtain the nodal-line semimetal phase proposed here. Since Weyl fermions are realized in photonic crystals,[310–312] and superlattice structures have been engineered to observe Brillouin zone folding effects,[307] these systems may also serve as a natural platform for the phenomena we study.

5.1 Weyl Semimetal on a Superlattice

We start from the time-reversal-breaking two-band lattice Hamiltonian, Eq. (2.37),[124]

$$\mathcal{H}_0(\mathbf{k}) = v\left(\sin k_x \sigma_x + \sin k_y \sigma_y\right) + M_{\mathbf{k}} \sigma_z, \tag{5.1}$$

where $M_{\mathbf{k}} = t(2 - \cos k_x - \cos k_y) + v(\cos k_z - m)$ and the lattice constant is set to $a = 1$. For certain values of m, e.g., $-1 < m < 5$ at $v = t$, the model describes a Weyl semimetal.[125] The Hamiltonian obeys a charge-conjugation symmetry, which may be broken in higher-energy bands in more realistic systems. In the course of this work, we consider this symmetry to be fulfilled. Here, we focus on $0 < m < 1$, when there is one pair of Weyl nodes at $(0, 0, \pm \arccos m)$. This Hamiltonian is perturbed by the periodic potential

$$U(\mathbf{r}) = 2 \sum_{\mu=\{0,x,y,z\}} u_\mu \cos\left(\mathbf{r}\cdot\mathbf{K} - \theta_\mu\right) \sigma_\mu, \tag{5.2}$$

where $\sigma_\mu = (\sigma_0, \boldsymbol{\sigma})$, σ_0 is the 2×2 identity matrix, $\boldsymbol{\sigma}$ is the vector of Pauli matrices, and $\mu = 0, x, y, z$. Depending on the physical realization of this low-energy Hamiltonian, σ_μ may act in spin or orbital space, or, when realized on an optical lattice, in sublattice space.[308] The angles θ_μ denote a shift of each component of the periodic potential towards the original lattice.

In the interest of clarity, we make two provisional simplifying assumptions: first, we assume that $\mathbf{K}$ is commensurate with a reciprocal-lattice vector in the z-direction, which sets $\mathbf{K} = (2\,\pi/n)\,\hat{z}$ for a folding degree $n \in \mathbb{N}$ and the unit vector $\hat{z}$. Second, the vector $\mathbf{K}$ is chosen to match the wave vector connecting the two Weyl nodes, $\mathbf{K} = 2 \arccos m\,\hat{z}$, thereby restricting our discussion to the specific values of $m = \cos \pi/n$. We postpone discussing the consequences of relaxing these two assumptions to Sec. 5.5.

Such choice of $\mathbf{K}$ enlarges the unit cell by the folding degree n in the z-direction, as shown in Fig. 5.1 (a). The full Hamiltonian can be written in a form representing the larger unit cell

$$\mathcal{H}_{n\mathbf{k}} = \begin{pmatrix} h_{\mathbf{k}} + U_0 & & & \text{h.c.} \\ \frac{v}{2}\,\sigma_z & h_{\mathbf{k}} + U_1 & & \\ & \ddots & \ddots & \\ \frac{v}{2}\,e^{-i\,n\,k_z}\,\sigma_z & & \frac{v}{2}\,\sigma_z & h_{\mathbf{k}} + U_{n-1} \end{pmatrix}. \tag{5.3}$$

There is a gauge freedom in choosing the phases of the basis functions for the sites that constitute the superlattice. Our gauge choice ensures that the Hamiltonian is invariant under a shift by a reciprocal-lattice vector. The j-th diagonal element of the Hamiltonian is $h_{\mathbf{k}} + U_j$ with

$$h_{\mathbf{k}} = \mathcal{H}_0(\mathbf{k}) - v\,\cos k_z\,\sigma_z,\;\; U_j = U\left(\mathbf{r} = j\,\hat{z}\right). \tag{5.4}$$

To gain further intuition of the nature of the perturbation, one can express Eq. (5.3) as n copies of a Weyl Hamiltonian at different momenta, coupled by the superlattice perturbation (5.2). To this end, we rotate the Hamiltonian using the unitary transformation $\mathcal{V} = \mathcal{V}_0 \otimes \sigma_0$ with elements

$$(\mathcal{V}_0)_{jl} = \frac{1}{\sqrt{n}}\,\exp\left[-i\,l\left(k_z + \frac{2\,\pi\,j}{n}\right)\right], \tag{5.5}$$

to obtain $\tilde{\mathcal{H}}_{n\mathbf{k}} = \mathcal{V}\,\mathcal{H}_{n\,\mathbf{k}}\,\mathcal{V}^\dagger$,

$$\tilde{\mathcal{H}}_{n\mathbf{k}} = \begin{pmatrix} \mathcal{H}_0(\mathbf{k}) & U_+ & & U_- \\ U_- & \mathcal{H}_0(\mathbf{k} + \frac{2\pi\hat{z}}{n}) & U_+ & \\ & & \ddots & \\ U_+ & & U_- & \mathcal{H}_0(\mathbf{k} + \frac{2\pi(n-1)\hat{z}}{n}) \end{pmatrix} \tag{5.6}$$

with the Weyl Hamiltonian $\mathcal{H}_0(\mathbf{k})$ and the perturbation $U_\pm = \sum_\mu u_\mu\,e^{\pm i\,\theta_\mu}\,\sigma_\mu$. Thus, the periodic perturbation couples Weyl Hamiltonians evaluated at momenta that differ by $2\,\pi/n\,\hat{z}$.

To begin understanding the physics of the Hamiltonian (5.6), we diagonalize it to obtain the band structure shown in Fig. 5.1. Anticipating the key differences between even and odd n, and the central role played by the presence or absence of reflection symmetry along z, we show the band structure along the path through momentum space defined in panel (b) for representatives of the four possible cases in panels (c) to (f). We find that in all but the reflection-symmetry broken case with odd n, the low-energy band structure has a nodal line. All realizations have low-energy surface states that are degenerate in the presence of reflection symmetry. To obtain a deeper understanding of these observations, in the next two sections we derive an effective low-energy theory and then provide a symmetry classification of the emergent nodal line.

For our later symmetry analysis, it is important to note that there are n equivalent definitions of the bulk unit cell [an example is shown in Fig. 5.1 (g)]. It will therefore prove useful to define the translation operator

$$T_{n,m} = \begin{pmatrix} & \mathbb{1}_m \\ \mathbb{1}_{n-m}\,e^{i\,n\,k_z} & \end{pmatrix} \otimes \sigma_0, \tag{5.7}$$

where $\mathbb{1}_m$ is the an identity matrix of size m. The operator $T_{n,m}$ translates the Hamiltonian's unit cell by m sites and satisfies $T_{n,m}T_{n,n-m} = e^{i\,n\,k_z}$. The transformation

$$T_{n,m}\,\mathcal{H}_{n\,\mathbf{k}}\,T_{n,m}^\dagger \to \mathcal{H}'_{n\,\mathbf{k}} \tag{5.8}$$

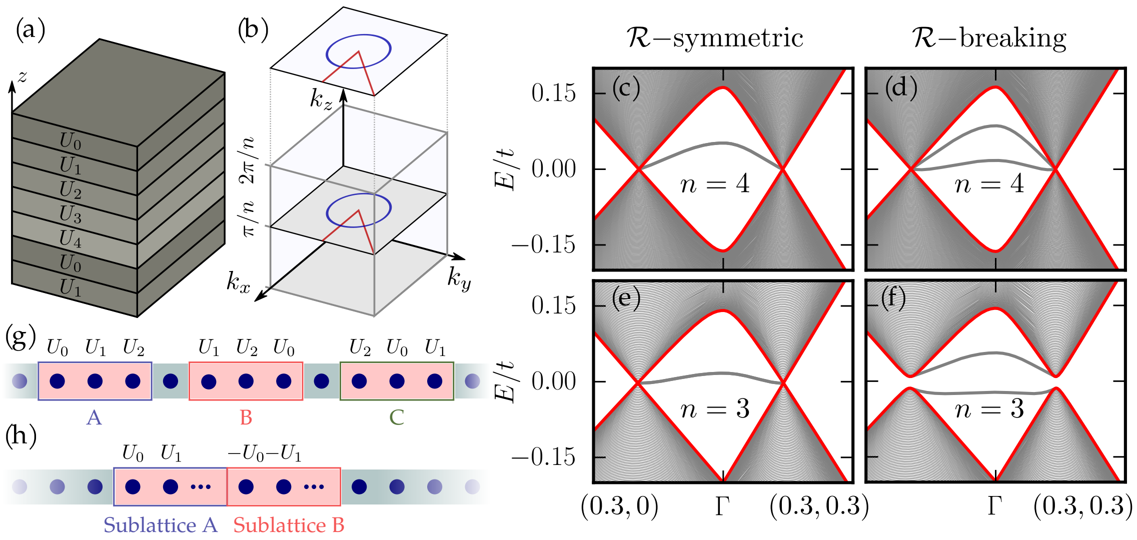

FIGURE 5.1: (a) Stacking of layers of Weyl semimetals subjected to different potentials U_0 with a folding degree $n = 5$, realizing the superlattice discussed in this work. (b) Brillouin zone and surface Brillouin zone projected on the (001) surface with the position of the nodal line that may emerge in the k_x-k_y plane at $k_z = \pi/n$, depending on the choice of parameters. The dispersion of the full Hamiltonian, Eq. (5.3), along the two dark red lines in the bulk and surface Brillouin zone is plotted in (c) to (f), with $v = t, u_0 = 0.2\,t$ and $u_{x,y,z} = 0$ for different angles θ_0. The red lines show the dispersion at $k_z = \pi/n$ and the gray lines the dispersion for open boundary conditions in the z-direction with 256 sites, including surface states. The different plots show (c) folding degree $n = 4$, obeying reflection symmetry with $\theta_0 = 3/4\,\pi$, (d) $n = 4$, breaking reflection symmetry with $\theta_0 = 3/4\,\pi + 0.15$, (e) $n = 3$, obeying reflection symmetry with $\theta_0 = 2/3\,\pi$, (f) $n = 3$, breaking reflection symmetry with $\theta_0 = 2/3\,\pi + 0.15$. (g) Illustration of the equivalent definitions of the bulk unit cell for a folding degree of $n = 3$. All bulk properties stay invariant when the definition of the unit cell is changed between the three different options A,B and C. (h) For an even folding degree n, each unit cell can be split up into two sublattices A and B where the superlattice potential has opposite sign.

is equivalent to changing all angles of the perturbation (5.2) as $\theta_\mu \to \theta_\mu + 2\,\pi\, m/n$. All bulk properties stay invariant upon such a transformation.

5.2 Emergent Nodal Phases

To understand the emergence of a nodal line, we introduce a low-energy approximation developed by projecting the full Hamiltonian to bands close to the Weyl nodes. As described above, the system may be seen as n copies of the Hamiltonian that realize the Weyl phase, Eq. (5.1), coupled at different momenta, Eq. (5.6). For a folding degree of $n = 2$, this especially means that the full Hamiltonian equals two copies of the Weyl Hamiltonian that are coupled at opposite chirality,

$$\tilde{\mathcal{H}}_{n=2,\mathbf{k}} = \begin{pmatrix} \mathcal{H}_0(\mathbf{k} - \pi\,\hat{z}) & U_+ + U_- \\ U_+ + U_- & \mathcal{H}_0(\mathbf{k} + \pi\,\hat{z}) \end{pmatrix}. \tag{5.9}$$

This relatively simple 4×4 Hamiltonian allows a detailed investigation of the model's properties in this special case of $n = 2$, including an extensive phase diagram. This is discussed in detail in Ref. 152.

For $n > 2$, the full Hamiltonian can be expanded around the Weyl nodes at $(0, 0, \pm\pi/n)$ and projected down to the lowest bands, giving a form similar to Eq. 5.9, i.e., two Weyl nodes of opposite chirality that are coupled by the potential $U_\pm$. We shift the Weyl node position slightly to $m \to \cos(\pi/n) + \eta/v$, creating a small mismatch between the Weyl node separation and the superlattice's wave vector. Up to linear order in momentum and first order* in U, the low-energy Hamiltonian has the form

$$\mathcal{H}^{\mathrm{low}}_{\mathbf{k}} = v\,(k_x\sigma_x + k_y\sigma_y) + (v\sqrt{1-m^2}q_z\tau_z + \eta)\sigma_z + U_+\tau_+ + U_-\tau_-, \tag{5.10}$$

where q_z is the momentum along z measured from $(0, 0, \pi/n)$. The matrices τ_μ act in the space of the different Weyl nodes that are coupled by $U_\pm$. We introduce the Euclidean Dirac matrices with signature $(++++)$

$$\gamma_1 = \sigma_x, \qquad \gamma_2 = \sigma_y, \qquad \gamma_3 = \sigma_z\tau_z, \qquad \gamma_4 = \tau_x\sigma_z, \tag{5.11}$$

and $\gamma_5 = \gamma_1\gamma_2\gamma_3\gamma_4 = -\tau_y\sigma_z$ plus the identity and the commutators $\gamma_{ij} = -\frac{i}{2}[\gamma_i, \gamma_j]$ to rewrite Eq. (5.10) in terms of perturbed Dirac fermions. It reads, after eliminating the phase $u_z \exp(\pm i\theta_z)$ by a rotating and upon rescaling of momenta

$$\mathcal{H}^{\mathrm{low}}_{\mathbf{k}} = \sum_{i=1}^{3} k_i\gamma_i + u_z\gamma_4 + \mathbf{b}\cdot\mathbf{u} + \mathbf{b}'\cdot\mathbf{v} + \mathbf{p}\cdot\mathbf{w}, \tag{5.12}$$

with the definitions[33]

$$\begin{gathered}\mathbf{w} = (\gamma_{14}, \gamma_{24}, \gamma_{34})\,,\ \ \mathbf{v} = (\gamma_{15}, \gamma_{25}, \gamma_{35})\,,\ \ \mathbf{u} = (\gamma_{23}, \gamma_{31}, \gamma_{12}) \\ \mathbf{p} = \begin{pmatrix} -u_y\,\cos(\theta_y - \theta_z) \\ u_x\,\cos(\theta_x - \theta_z) \\ -u_0\,\sin(\theta_0 - \theta_z) \end{pmatrix},\ \mathbf{b}' = \begin{pmatrix} -u_y\,\sin(\theta_y - \theta_z) \\ u_x\,\sin(\theta_x - \theta_z) \\ u_0\,\cos(\theta_0 - \theta_z)) \end{pmatrix},\ \mathbf{b} = \begin{pmatrix} 0 \\ 0 \\ \eta \end{pmatrix}.\end{gathered} \tag{5.13}$$

This Hamiltonian has same form as the generic four-band Hamiltonian introduced in Eq. (2.41), although not all components of b_μ are realized here. As discussed in Ref. 33, a perturbation u_z introduces a mass to the Dirac Hamiltonian and all other terms can lead to Weyl or nodal-line semimetal phases. However, as shown before in Fig. 5.1 (f), the nodal line that forms is not necessarily stable: it may gap out when taking into account higher orders in momentum and U. In Sec. 5.3, the stability of the nodal line is investigated beyond the low-energy approximation. The detailed discussion of a term $\eta \neq 0$ is postponed to Sec. 5.5; for now, it is set to $\eta = 0$.

Let us focus on a case where the emergence of a nodal line in the spectrum simply follows from the low-energy perspective. For a perturbation $U_\pm = u_0\,e^{\pm i\,\theta_0}\sigma_0$ and $\eta = 0$, we may rotate the low-energy Hamiltonian, Eq. (5.10) by a unitary transformation

$$\mathcal{U} = \frac{1}{\sqrt{2}}\,(\sigma_x + \sigma_z)\,e^{i\,\phi/2\,\sigma_z}, \tag{5.14}$$

with ϕ being the polar angle in the k_x-k_y plane. This transformation gives

$$\mathcal{U}\,\mathcal{H}^{\mathrm{low}}_{\mathbf{k}}\,\mathcal{U}^\dagger = v\,q\,\sigma_z + v\sqrt{1-m^2}\,q_z\,\sigma_x\,\tau_z + u_0\,e^{i\,\theta_0\,\tau_z}\,\tau_x, \tag{5.15}$$

---

*Orders of $\mathcal{O}(U^2)$ appear on the diagonal of this matrix. They are additionally suppressed by the eigenvalues of $\mathcal{H}_{\mathbf{k}\pm 3\,\mathbf{k}_0}$, i.e., they do not play a role close to the nodal line.

with $q = \sqrt{k_x^2 + k_y^2}$. After applying the canonical transformation

$$\sigma_\pm \to \sigma_\pm \, \tau_z , \quad \tau_\pm \to \tau_\pm \, \sigma_z , \tag{5.16}$$

the Hamiltonian takes the simple form

$$\mathcal{H}'_{\mathbf{k}} = \Delta_\pm \, \sigma_z - v\sqrt{1-m^2}\, q_z \, \sigma_x , \tag{5.17}$$

where we replaced the operator $\hat{\Delta} = v\, q + u_0 \, e^{i\,\theta_0\, \tau_z} \, \tau_x$ by its eigenvalues $\Delta_\pm = v\, q \pm u_0$. The nodal line therefore emerges at $q_z = 0, v\, q = u_0$.

5.3 Symmetry Classification of the Nodal Line

Generally, there are two different ways to obtain a protected nodal line in the model (5.3): by fulfilling reflection symmetry or a combination of a fractional lattice translation and charge-conjugation symmetry—we explain this in the current section. The symmetry classification of the nodal line depends on the folding degree of the unit cell n. In its most general form, the full Hamiltonian, Eq. (5.3), does not possess any commuting anti-unitary or anticommuting unitary symmetries, i.e., it is in symmetry class A. The system is reflection symmetric along z if the operator

$$\mathcal{R} = \begin{pmatrix} & & \sigma_0 \\ & \iddots & \\ \sigma_0 & & \end{pmatrix} \tag{5.18}$$

commutes with $\mathcal{H}_{n\,\mathbf{k}}$ or with any shifted Hamiltonian $T_{n,m} \, \mathcal{H}_{n\,\mathbf{k}} \, T^\dagger_{n,m}$ at momenta that are invariant under reflection along z, i.e., $k_z = 0$ and $k_z = \pi/n$, where we choose $\mathcal{R}$ such that $\mathcal{R}^2 = +1$, using the convention by Ref. 116. This is the case when all angles θ_μ are the same and equal $\theta_\mu = m\,\pi/n$ for all μ with the integer m. At $k_z = 0$ and $k_z = \pi/n$, the eigenstates of the Hamiltonian are simultaneously eigenstates of $\mathcal{R}$, $\mathcal{R}|\psi\rangle = r\,|\psi\rangle$ with eigenvalues $r = \pm 1$ (the bands are either even or odd under reflection). Bands with different eigenvalues r cannot mix, which is the mechanism that protects the nodal line, cf. Fig. 5.2 (a). The invariant characterizing this protection is the mirror Chern number:[116] the difference in the number of occupied bands that are even under reflection within and outside the nodal line.

For odd folding degree n, reflection symmetry is the only symmetry that protects the nodal line. In absence of reflection symmetry, the nodal line gaps out, giving rise to two Weyl nodes. This can be achieved in two ways. One relies on setting at least one angle to be $\theta_\mu \neq m\,\pi/n$, which opens up a gap along the nodal line, cf. Fig. 5.1 (f) for $n = 3$. A second option is to break mirror symmetry by adding a term $\gamma \sin k_z \, \sigma_0$ to the Weyl Hamiltonian, Eq. (5.1). A nonzero γ shifts the Weyl nodes to different energies, breaking mirror symmetry and opening up a gap in the nodal line, cf. Fig. 5.3.

For even n, the system is partitioned into two sublattices A and B, cf. Fig. 5.1 (h), where the superpotential has opposite sign. The system can be understood as a one-dimensional system in the z-direction, parametrized by the other momentum components $\mathbf{k}_\parallel = (k_x, k_y)$. For a perturbation $U_\pm = u_0 e^{\pm i\,\theta_0} \sigma_0$, it obeys a one-dimensional charge-conjugation symmetry

$$C_{\mathbf{k}} \, \mathcal{H}_{\mathbf{k}_\parallel, k_z} \, C_{\mathbf{k}}^{-1} = -\mathcal{H}_{\mathbf{k}_\parallel, -k_z} \tag{5.19}$$

where the operator $C_{\mathbf{k}}$ consists of a combination of a fractional lattice translation and the anti-unitary charge-conjugation symmetry

$$C_{\mathbf{k}} = \begin{pmatrix} 0 & e^{-i\,n\,k_z} \\ 1 & 0 \end{pmatrix} \otimes \sigma_x \mathcal{K}, \tag{5.20}$$

with the outer matrix acting in the sublattice space of A, B and $\mathcal{K}$ denoting complex conjugation. The operator $C_{\mathbf{k}}$ squares to $C_{\mathbf{k}}\,C_{-\mathbf{k}} = e^{-i\,n\,k_z}$. Similar to one-dimensional superconductors, the one-dimensional Zak phase

$$\gamma_j\left(\mathbf{k}_{\|}\right) = i \int_0^{\frac{2\pi}{n}} dk_z \,\langle u_{j\,\mathbf{k}} | \partial_{k_z} | u_{j\,\mathbf{k}} \rangle \tag{5.21}$$

is related to the determinant of the matrix $W(\mathbf{k})$ that diagonalizes the Hamiltonian via

$$\exp\left[i \sum_{j \in \text{occ.}} \gamma_j \right] = \frac{\det W(\mathbf{k}_{\|}, 0)}{\det W(\mathbf{k}_{\|}, \frac{\pi}{n})}. \tag{5.22}$$

At planes in momentum space defined by $k_z = 0$, the operator $C_{\mathbf{k}}$ squares to -1, i.e., the Hamiltonian that respects Eq. (5.19) is in symmetry class C. The matrix $W(\mathbf{k}_{\|}, 0)$ is symplectic,[83] which implies that $\det W(\mathbf{k}_{\|}, 0) = 1$. Similarly, at $k_z = \pi/n$, the operator $C_{\mathbf{k}}$ squares to $+1$, i.e., the Hamiltonian is in symmetry class D. Hamiltonian matrices in class D can be rewritten in terms of Majorana modes as a skew symmetric matrix $X^T = -X$, which can be diagonalized by an orthogonal matrix,[114;313] i.e., $\det W(\mathbf{k}_{\|}, \pi/n) = \pm 1$. The value of $\det W(\mathbf{k}_{\|}, \pi/n) = \text{sign}\left(\text{Pf}\left[X_{\mathbf{k}_{\|}}\right]\right)$ is a zero-dimensional invariant that characterizes the two distinct sectors, which are separated by the nodal line. This invariant is shown in Fig. 5.2 (b) at both planes $k_z = 0$ and $k_z = \pi/n$. Its value is $\det W = -1$ inside the nodal line in the plane defined by $k_z = \pi/n$ and $\det W = 1$. The gap closing cannot vanish without breaking the symmetry protecting this invariant. Alternatively, the Zak phase can be interpreted as a one-dimensional invariant that is quantized for loops enclosing the nodal line.

Note that the presence of charge-conjugation symmetry does not change the previous statements about the protection of the nodal line in presence of reflection symmetry, since the mirror Chern number is inherited from class A.[114]

A particularly simple instance of an even n is the case with folding degree $n = 2$. In this case the Hamiltonian is always invariant upon a reflection along z, i.e.,

$$\mathcal{R}_{k_z}\, \mathcal{H}_{n=2,\mathbf{k}_{\|},-k_z}\, \mathcal{R}^{\dagger}_{k_z} = \mathcal{H}_{n=2,\mathbf{k}_{\|},k_z} \tag{5.23}$$

with $\mathcal{R}_{k_z} = \cos k_z - i\,\sin k_z\,\tau_z$. Analogous to the other reflection-symmetric cases, the bands in the plane defined by $k_z = \pi/2$ have different eigenvalues of $\mathcal{R}_{\pi/2}$, $r = \pm 1$, and cannot mix. The nodal line is therefore protected by a mirror $M\mathbb{Z}$ Chern number. Additionally, the presence of charge-conjugation symmetry protects the nodal line even if reflection symmetry is broken by a term $\gamma\,\sin k_z\,\sigma_0$, a fact that holds for all systems with even folding degree n.

5.4 Surface States

In the model investigated here, surface states play a crucial role: it is possible to have realizations of a stable nodal-line phase with drumhead surface states as well as surface

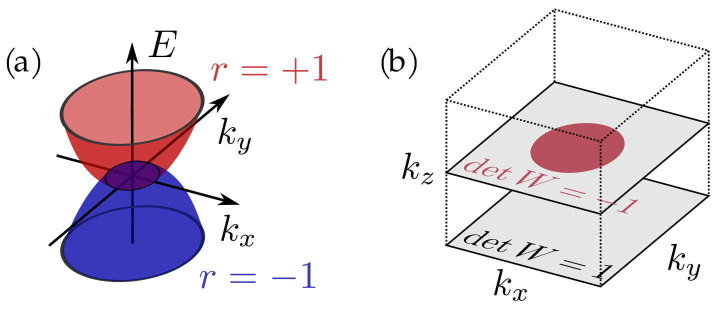

Figure 5.2: Topological protection of the nodal line. The nodal line at $k_z = \pi/n$ is protected by two mechanisms: (a) In the presence of reflection symmetry, the two bands that form the nodal line at the reflection invariant momentum $k_z = \pi/n$ have different eigenvalues under reflection, $r = \pm 1$. The number of occupied bands that are even under reflection changes by 1 when crossing the nodal line. (b) When the Hamiltonian respects the symmetry induced by $C_{\mathbf{k}}$, the determinant of the matrix that diagonalizes the Hamiltonian, $W(\mathbf{k})$, is quantized to $\det W(\mathbf{k}) = 1$ in the plane defined by $k_z = 0$ and quantized to $\det W(\mathbf{k}) = \pm 1$ in the plane defined by $k_z = \pi/n$, as shown in the figure. The red area, within the nodal line, denotes $\det W(\mathbf{k}) = -1$, while the gray area denotes $\det W(\mathbf{k}) = +1$. This protection mechanism is only possible for even folding degree n.

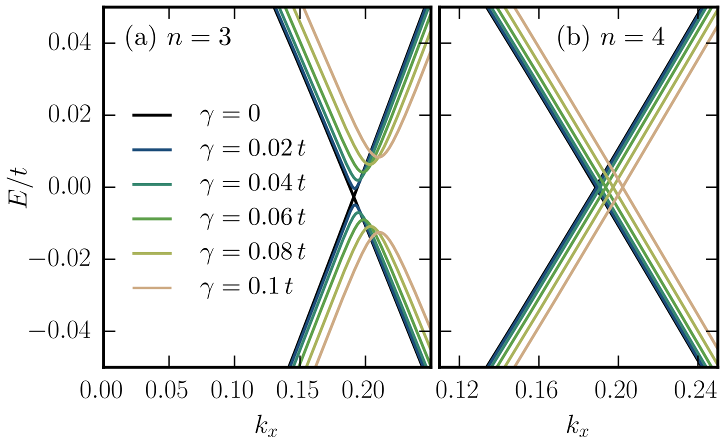

Figure 5.3: Dispersion of the system close to the nodal line in presence of the reflection-symmetry-breaking term $\gamma \sin k_z \, \sigma_0$, with $v = t$, $u_0 = 0.2\,t$, and $u_{x,y,z} = 0$, evaluated at $k_y = 0.05$, $k_z = \pi$. (a) For odd folding degree n, the reflection-symmetry-breaking term γ immediately opens a gap in the spectrum. (b) For even folding degree, the gap is stable due to the combination of a fractional lattice translation and charge-conjugation symmetry.

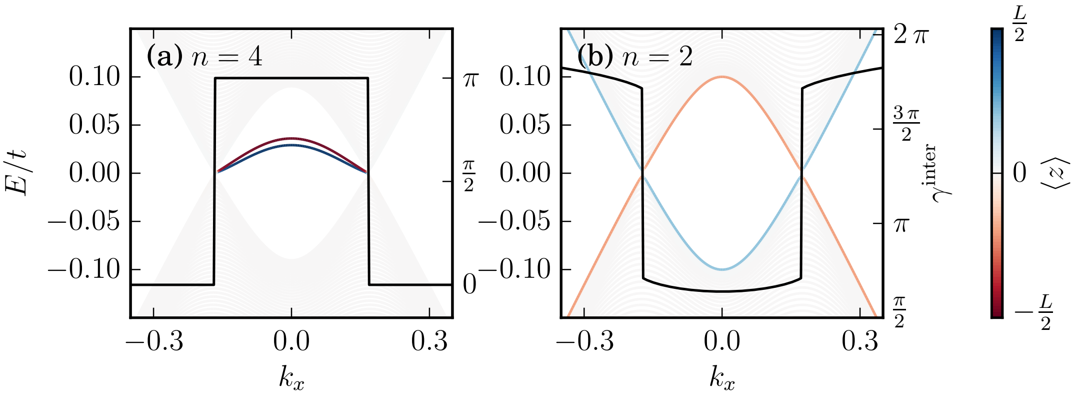

FIGURE 5.4: Energy dispersion and intercellular Zak phase of a periodically perturbed Weyl semimetal that is finite in z with $L = 512$ sites, $-L/2 < z < L/2$, evaluated at $k_y = 0.05$. The intercellular Zak phase is summed over all occupied bands $\gamma^{\text{inter}} \equiv \sum_{j \in \text{occ.}} \gamma_j^{\text{inter}}$. The color of the lines encodes the average real-space position. (a) Folding degree $n = 4$ and perturbation strength $u_0 = 0.2\,t$ with $\theta_0 = 3/4\,\pi$. Intercellular Zak phase and total Zak phase coincide and are both quantized to 0 (outside the nodal line) and π (within the nodal line). The intercellular Zak phase predicts the extra-charge accumulation at the surface, which results in exponentially localized surface states (the degeneracy of the surface states is lifted by an extra energy $\eta = 0.005\,t$). (b) Folding degree $n = 2$ and perturbation strength $u_0 = 0.1\,t$ with $\theta_0 = 0$. Although the total Zak phase is quantized, the intercellular Zak phase is not; this results in surface states that are not exponentially localized at the surface. Furthermore, the surface states are not locked to small energies.

states that are not exponentially localized at the boundary. The emergence of surface states close to zero energy is discussed in this section.

In Fig. 5.4 (a), the energy dispersion of a finite system with folding degree $n = 4$ that respects reflection symmetry is plotted, along with the location of the states encoded by a color scale. The system exhibits drumhead surface states at small energies that are exponentially localized at the surface. However, not all realizations of a stable nodal line share this feature: an example without drumhead surface states is given in Fig. 5.4 (b), where the dispersion for a finite system with folding degree $n = 2$ is shown. It is not possible to find a surface termination that respects the reflection symmetry of the bulk system. This results in states that are not exponentially localized at the surfaces of the system. To explain the properties of the surface states, we introduce and compute the Zak phase.

In the modern theory of polarization[93], the Zak phase is associated with the surface charge. Here, we employ the intercellular Zak phase that reflects the choice of a bulk unit cell to relate the extra charge accumulation at the surface with bulk properties of the system.[113] The intercellular Zak phase and extra charge accumulation are proportional when the finite system is commensurate with the unit cell used to compute the intercellular Zak phase. While the Zak phase is generally given by

$$\gamma_j(k_x, k_y) = i \int_0^{2\pi/n} dk_z \langle u_{j\,\mathbf{k}} | \partial_{k_z} | u_{j\,\mathbf{k}} \rangle \tag{5.24}$$

with the lattice-periodic part of the wave function $u_{j\,\mathbf{k}}(\mathbf{r}) = e^{-i\,\mathbf{k}\cdot\mathbf{r}}\,\psi_{j\,\mathbf{k}}(\mathbf{r})$, we rather focus on

$$\gamma_j^{\text{inter}}(k_x, k_y) = i\int_0^{2\,\pi/n} dk_z\,\langle\psi_{j\,\mathbf{k}}|\partial_{k_z}|\psi_{j\,\mathbf{k}}\rangle, \tag{5.25}$$

as defined in Sec. 2.4, neglecting the “classical” contribution to the surface charge, coming from the polarization within a unit cell. The functions $|\psi_{j\,\mathbf{k}}\rangle$ are chosen such that all sites in one unit cell carry the same Bloch phase.[113] This quantity can be numerically evaluated efficiently by calculating the corresponding Wilson loop.[145]

The intercellular Zak phase is only quantized to $0, \pi$ for a reflection-symmetric unit cell, when it equals the total Zak phase, otherwise it can take an arbitrary value. Extra charge accumulation $Q^{L(R)}_{\text{acc.}}$ and intercellular Zak phase are related via[113]

$$Q^{L(R)}_{\text{acc.}} = +(-)\frac{e}{2\,\pi}\sum_{j\in\text{occ.}}\gamma_j^{\text{inter}}(\text{mod } e) \tag{5.26}$$

where $L(R)$ stands for the left (right) surface region commensurate with the bulk unit cell used for the calculation of the intercellular Zak phase. Furthermore, Eq. (5.26) does not allow us to make a statement about the energy of the extra-charge accumulation. It has been shown that the above relation leads to the $\mathbb{Z}_2$ bulk-boundary correspondence for the reflection symmetric insulators: we have $\gamma^{\text{inter}}/\pi$ (mod 2) in-gap surface modes, with $\gamma^{\text{inter}} = \sum_{j\in\text{occ.}}\gamma_j^{\text{inter}}$, if the finite system (i) respects the reflection symmetry and (ii) is commensurate with the bulk unit cell.[113]

As shown in Fig. 5.4 (a), the intercellular Zak phase for a reflection symmetric system with folding degree $n = 4$ is quantized to $0, \pi$, correctly predicting the number of in-gap surface modes. However, the $n = 2$ case violates the condition (i) for the bulk-boundary correspondence, and surface modes are not guaranteed to exist although the total Zak phase is quantized. Instead, the intercellular Zak phase explains the extra charge accumulations for both surfaces correctly as plotted in Fig. 5.4 (b).

5.5 Stability against Wave Vector Mismatch

In the previous discussion, the focus was on a perfect match of the superlattice's wave vector and the node separation of the underlying Weyl semimetal. In any realistic system, such a perfect agreement may be hard to realize. There are two possibilities for a vector mismatch: we can change the superlattice's wave vector $\mathbf{K} = (2\,\pi/n + \delta k)\,\hat{z}$ or we can change the node separation by changing $m \to \eta/v + \cos\pi/n$.

When the wave vector $\mathbf{K}$ is changed, it generally fits neither the node separation nor the lattice. In such a case, translational invariance is lost, as investigated in Ref. 309. Here, we are interested in the fate of the nodal line in presence of a wave vector that does not match the node separation, i.e., we choose a vector $\mathbf{K}$ that is commensurate with periodic boundary conditions. In Fig. 5.5, the radius of the nodal line is shown for several lattices with periodic boundary conditions that allow certain $\mathbf{K}$. The diameter of the nodal line shrinks with increasing δk until it vanishes at a critical value that depends on u_0 and the folding degree n.

By changing $m \to \eta/v + \cos\pi/n$, the position of the Weyl nodes in the original unperturbed system are modified. The position of the nodal line can be obtained from modifying Eq. (5.17). This gives the condition for the position in the x-y-plane with $q = \sqrt{k_x^2 + k_y^2}$

$$v\,q = \sqrt{u_0^2 - \eta^2}, \tag{5.27}$$

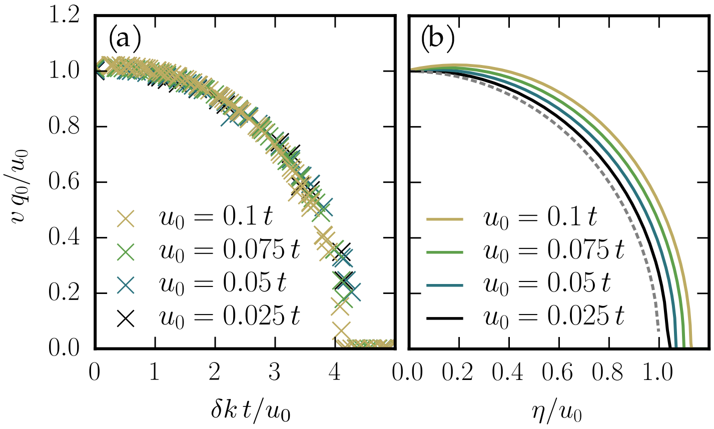

FIGURE 5.5: Stability of nodal line. Position of nodal line $(q_0, 0, \pi/n)$ for a periodically perturbed Weyl semimetal with a superlattice of folding degree $n = 7$ for different potential strengths u_0, with $v = t$ and $u_{x,y,z} = 0$. (a) The superlattice is varied $\mathbf{K} \to (2\pi/n + \delta k)\,\hat{z}$ so that is does not match the node separation. (b) The mass parameter is varied $m \to \cos\pi/n + \eta/v$ so that the node separation does not match the superlattice. Solid lines and crosses show the results using the full Hamiltonian, and the dashed line shows the lowest order prediction.

i.e., we expect that the nodal line stays stable up to $|\eta| \leq |u_0|$. In Fig. 5.5, the lowest-order prediction is compared with numerical results for the full Hamiltonian. As in the previous case, the diameter of the nodal line shrinks for nonzero η, but it generally persists up to a critical value, in agreement with the symmetry classification that generally predicts the stability of the nodal line and does not rely on specific values of the mass term.

5.6 Time-reversal Symmetric Weyl Semimetal

The previous findings can be extended to a model that is closer to currently available materials that respect time-reversal symmetry. Two copies of the Weyl Hamiltonian

$$\mathcal{H}_0^{(\pm)}(\mathbf{k}) = v\,\left(\pm\sin k_x\,\sigma_x + \sin k_y\,\sigma_y\right) + M_{\mathbf{k}}\,\sigma_z \tag{5.28}$$

with $M_{\mathbf{k}}$ from Eq. (5.1) give rise to several phases, including Dirac semimetals, Weyl semimetals with four Weyl nodes and strong topological insulators, all described by [121]

$$\mathcal{H}_{\mathbf{k}} = \begin{pmatrix} \mathcal{H}_0^{(+)}(\mathbf{k}-\mathbf{k}_1) & B_1\,e^{i\,\phi}\,\sin(k_z)\,\sigma_x \\ B_1\,e^{-i\,\phi}\,\sin(k_z)\,\sigma_x & \mathcal{H}_0^{(-)}(\mathbf{k}+\mathbf{k}_1) \end{pmatrix}. \tag{5.29}$$

The vector $\mathbf{k}_1$ lies in the k_x-k_y-plane and it breaks inversion symmetry. The outer matrix structure is described by the Pauli matrices s_μ acting in spin space. This Hamiltonian is time-reversal symmetric with $\Theta = i\,s_y\,\mathcal{K}$ and has reflection symmetry along z with $\mathcal{R} = s_z$. When $\mathbf{k}_1 = 0$ and $B_1 = 0$, the system has a C_4 rotational symmetry in the k_x-k_y-plane. Then, there are two degenerate Dirac nodes at $(0, 0, \pm\arccos m)$. In absence of inversion and rotational symmetry, the Dirac nodes either split up into four Weyl nodes for $|\mathbf{k}_1| > B_1$ or gap out when $|\mathbf{k}_1| < B_1$.

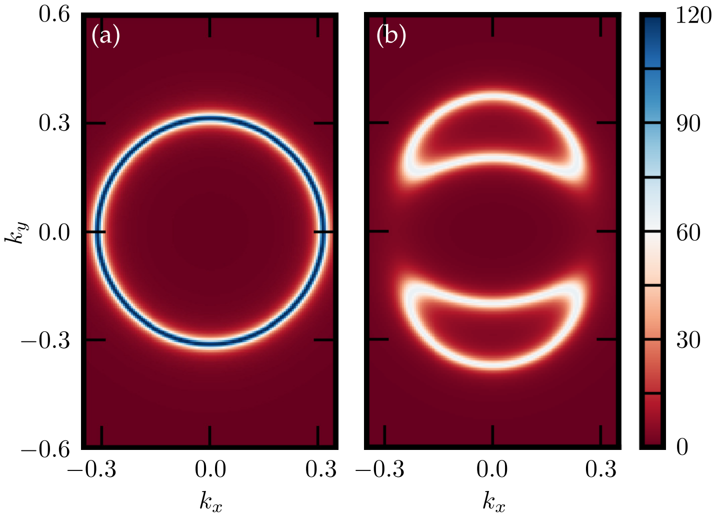

FIGURE 5.6: Density of states at zero energy for the time-reversal invariant system subjected to a periodic perturbation $U(\mathbf{r}) = 2\, u_{00}\, \cos\left(2\,\mathbf{r}\cdot\mathbf{K} - \theta_{00}\right)\, s_0\, \sigma_0$ with folding degree $n = 4$ and $v = t, u_{00} = 0.3\,t,\ \theta_{00} = 3/4\,\pi$. The level broadening η is chosen $\eta = 0.01\,t$. (a) Starting from the Dirac phase with $B_1 = \mathbf{k}_1 = 0$, a fourfold-degenerate nodal line emergence. Splitting up the original Dirac node into two Weyl nodes with $B_1 = 0.1\,t$ and $\mathbf{k}_1 = (0, 0.15, 0)$ lifts one degeneracy and splits the fourfold-degenerate nodal line into two twofold-degenerate nodal lines.

A periodic perturbation with a wave vector $\mathbf{K} = 2\,\arccos m\,\hat{z}$ can lead to protected line nodes. The most general perturbation

$$U(\mathbf{r}) = \sum_{\mu,\nu} u_{\mu\nu}\, \cos\left(\mathbf{r}\cdot\mathbf{K} - \theta_{\mu\nu}\right)\, \sigma_\mu\, s_\nu \tag{5.30}$$

may give rise to a plethora of different phases. For simplicity, we just discuss the simplest case of a onsite potential, i.e., only u_{00} is nonzero (see Fig. 5.6). In the Dirac phase, such a perturbation can give rise to a fourfold-degenerate nodal line. In presence of reflection symmetry, the symmetry class is AII with R_-, i.e., $\mathcal{R}$ and Θ anti-commute.[116] Although this symmetry class only allows a $\mathbb{Z}_2$ classification that does not protect the nodal line, the $M\,\mathbb{Z}$ classification inherited from A remains.[114]

Breaking inversion and C_4 symmetry by $\mathbf{k}_1$ and B_1 splits up the fourfold-degenerate nodal line into two twofold-degenerate nodal lines. The protection mechanism of these nodal lines is analogous to the previously considered time-reversal-breaking case, since the additional time-reversal symmetry does not change the classification. The operator

$$\bar{C}_{\mathbf{k}} = \begin{pmatrix} & e^{-i\,n\,k_z} \\ 1 & \end{pmatrix} \otimes \left(\sin\phi\, s_0 - i\,\cos\phi\, s_z\right) \sigma_y \mathcal{K} \tag{5.31}$$

anti-commutes with the Hamiltonian and squares to $C_{\mathbf{k}}\, C_{-\mathbf{k}} = -e^{-i\,n\,k_z}$, giving a $\mathbb{Z}_2$ invariant defined in the $k_z = \pi/n$ plane, analogous to the classification for the time-reversal breaking case in Sec. 5.3.

5.7 Conclusion

We showed that a Weyl semimetals subjected to a periodic modulation of the onsite potential can give rise to a nodal-line semimetal that is not gapped out by spin-orbit coupling. Since the nodal line is protected by mirror symmetry and/or the combination of a fractional lattice translation and charge-conjugation symmetry, its presence does not rely on details of the Hamiltonian. Although we focused in this chapter, because of its simplicity, on a Weyl semimetal with two Weyl nodes as a starting point, we further show that nodal lines also arise in periodically perturbed Weyl semimetals that respect time-reversal symmetry, by using a model that has four Weyl nodes without the perturbation.

An unusual feature of this proposal are the surface states that are not necessarily exponentially localized at the surface close to zero energy; this may open possibilities for experimental investigations of bulk properties that are not disturbed by any low-energy surface states. Similarly, quasiparticle interference[314] is a promising tool for probing the nodal line at the Fermi level.

6 Symmetry Classification of the SYK Model

So far, we have only encountered examples of noninteracting topological phases. These noninteracting models represent a subgroup of a much wider class of Hamiltonians that realize symmetry-protected topological phases, or SPT phases.[70;72;315] In this chapter, we provide one example of an SPT phase, the SYK model,[73;74] named after Sachdev, Ye and Kitaev. It is a zero-dimensional model with random four-body interactions between particles that can be solved exactly in the limit of infinite particle number.[73] It is believed to have an AdS_2 dual in its conformal limit[74] at $\beta J \gg 1$, with the coupling strength J and the inverse temperature β. This potentially constitutes an example for the AdS/CFT correspondence:[316] a conjectured relationship between anti-de Sitter spaces (AdS) and lower-dimensional conformal quantum field theories (CFT).[317–319] Here, we do not discuss the nature of the AdS/CFT correspondence or the related high-energy background. We rather focus on experimental consequences of the symmetry classification of the SYK model.

In Kitaev's formulation, the SYK model describes random interactions between Majorana operators.[74] With the advent of Majorana modes in topological superconductors,[21;24;320] realizations of the SYK model in condensed-matter systems come in sight: e.g., by trapping Majoranas in a superconducting vortex[321] or by connecting Majorana wires to a random quantum dot.[322] Irregularly-shaped graphene flakes realize the SYK model in terms of conventional fermions,[323] i.e., in the original formulation by Sachdev and Ye.[73] In this thesis, we concentrate on the formulation in terms of Majorana operators. Naturally, any condensed matter realization has a finite number of particles. Depending on the particle number, the system is in a different symmetry class,[71] with the consequences on the spectrum extensively studied.[324;325]

Based on the condensed-matter realizations, we investigate experimentally accessible consequences of the symmetry class for a finite number of Majorana modes. We find that the symmetry class manifests itself in features of the spectral function at zero energy that stable against temperature: the spectral function has a peak, a hole, or it is featureless. We discuss the accessibility of the spectral function via scanning tunneling microscopy and the influence of finite temperatures.

6.1 Model and Topological Classification

We discuss the variant of the SYK Hamiltonian that describes random four-body interactions[73;74;326]

$$H = \sum_{p=0}^{k-1} \sum_{q=0}^{p-1} \sum_{r=0}^{q-1} \sum_{s=0}^{r-1} J_{pqrs} \gamma_p \gamma_q \gamma_r \gamma_s \tag{6.1}$$

between k Majorana modes that obey the anticommutation relation $\{\gamma_p, \gamma_q\} = 2\delta_{pq}$ with $\gamma_p^\dagger = \gamma_p$. When comparing to the discussion of the gamma matrices in Sec. 3, we see that the Majorana operators realize a Clifford algebra with signature $(++++\ldots)$, cf. Eq. (3.2). Thus, they can be represented by higher-dimensional gamma matrices of dimension $M \times M$, with $M = 2^{\lfloor k/2 \rfloor}$ and $\lfloor \cdots \rfloor$ the floor function.[327] We choose the action of complex conjugation $\mathcal{K}$ on the Majorana operators such that it does not affect Majoranas with an even index $\mathcal{K}\gamma_{2p}\mathcal{K} = \gamma_{2p}$, but changes the sign of Majoranas with an odd index $\mathcal{K}\gamma_{2p+1}\mathcal{K} = -\gamma_{2p+1}$. The random interaction J_{pqrs} between the different particles defines the system's only energy scale J via its variance

$$\langle\!\langle J_I \rangle\!\rangle = 0, \;\; \langle\!\langle J_I J_{I'} \rangle\!\rangle = \frac{3!}{k^3} J^2 \, \delta_{I,I'}, \tag{6.2}$$

where $\langle\!\langle \cdots \rangle\!\rangle$ denotes averaging over different realizations of the random interactions J_{pqrs}, and with joint indices $I = (pqrs)$.

The SYK model is time-reversal symmetric, i.e., the Hamiltonian (6.1) commutes with the antiunitary operator $\hat{T}$ that commutes with all Majorana operators.[71] The properties of $\hat{T}$, which determine the symmetry class of this SPT phase, change with the number of Majorana modes k, thus, the class depends solely on k. To understand the topological classification, we discuss the general properties of the Hilbert space spanned by k Majorana operators, summarizing previous work on higher dimensional Clifford algebras[327–329] and their connection to topology.[71] This topology has direct consequences for the overlap of the Hamiltonian's eigenstates with certain operators.

For an even number of Majoranas k, one can find two unitary matrices C_+ and C_- with the properties[327]

$$C_\pm \, \gamma_p^* \, C_\pm^\dagger = \pm \gamma_p. \tag{6.3}$$

The combination of each of these matrices with complex conjugation commutes with the Hamiltonian $[C_\pm \mathcal{K}, H] = 0$. We identify the time reversal operator $\hat{T} = C_+\mathcal{K}$ since it commutes with both the Hamiltonian and all Majorana modes.[71] Combining both signs from Eq. (6.3) gives

$$C_+ C_- \gamma_p C_-^\dagger C_+^\dagger = -C_+ \gamma_p^* C_+^\dagger = -\gamma_p, \tag{6.4}$$

i.e., the joint operator C_+C_- anticommutes with all γ_p. Since the operator γ_p changes the parity of a state $|\psi\rangle$,[320] C_+C_- equals the parity operator up to a phase, $\hat{P} = C_+C_-e^{i\phi}$. The phase is chosen such that the parity operator itself is hermitian, which is satisfied by the choice

$$\hat{P} \equiv \gamma_{\text{chir}} = i^{k/2} \gamma_0 \gamma_1 \cdots \gamma_{k-1}, \tag{6.5}$$

i.e., equals the chiral matrix, the product of all Majorana operators times a phase.[327] Given the definition of $\hat{P}$, we realize that, since $\hat{T}$ commutes with all γ_p, just the number of Majorana operators k determines if $\hat{T}$ and $\hat{P}$ commute or anticommute

$$\hat{T}\hat{P}\hat{T}^{-1} = (-1)^{k/2} \hat{P} \equiv a\hat{P}. \tag{6.6}$$

Using that $\hat{P}$ equals C_+C_- up to a phase, it is evident that a equals the product of $(C_-\mathcal{K})^2$ and $(C_+\mathcal{K})^2$

$$a = \hat{T}\hat{P}\hat{T}^{-1}\hat{P} = C_+ C_+^* C_-^* e^{-i\phi} C_+^\dagger C_+ C_- e^{i\phi} = C_+ C_+^* \, C_-^* C_-, \tag{6.7}$$

k mod 8	$C_+C_+^*$	$C_-C_-^*$	$\hat{T}^2$	a	$\langle\psi\|\gamma_p\|\psi\rangle$	$\langle\psi\|\gamma_p\hat{T}\|\psi\rangle$	Cartan label[71]
0	+1	+1	+1	+1	0	0	AI
1	+1	0	+1	+1	finite	finite	BDI
2	+1	−1	+1	−1	0	finite	D
3	0	−1	−1	−1	finite	finite	DIII
4	−1	−1	−1	+1	0	0	AII
5	−1	0	−1	+1	finite	0	CII
6	−1	+1	−1	−1	0	0	C
7	0	+1	+1	−1	0	0	CI

TABLE 6.1: Square of the operators[327] $C_\pm\mathcal{K}$ (the label 0 means that the matrix does not exist), expectation value of γ_p, $\gamma_p\hat{T}$, and corresponding Cartan labels[71]. For even k, the symmetry class is given by square of time-reversal symmetry $\hat{T}^2 = C_+C_+^* = \pm1$ and the commutation relation between $\hat{T}$ and the parity operator $\hat{P}$ with $\hat{T}\hat{P} = a\hat{P}\hat{T}$ and $a = \pm1$, giving 4 distinct possibilities. For odd k, it is necessary to compute the square of time-reversal symmetry and the commutation between $\hat{T}$ and $\hat{Z}$ as defined in the main text, with $\hat{T}\hat{Z} = a\hat{Z}\hat{T}$, again giving 4 distinct possibilities. In the last two columns, we summarize the findings that are relevant for the spectral function at zero energy. The matrix elements $\langle\psi|\gamma_p|\psi\rangle$ and $\langle\psi|\gamma_p\hat{T}|\psi\rangle$ are not necessarily different, since $\hat{T}|\psi\rangle$ and $|\psi\rangle$ may just differ by a phase.

with both squares $C_+C_+^*$ and $C_-C_-^*$, along with a, shown in Tab. 6.1 for different numbers of Majoranas k. Together with the square of $\hat{T}$, $\hat{T}^2 = C_+C_+^* = \pm1$, there are four distinct possibilities for the properties of $\hat{T}$ for even k: two possible signs for $a = \pm1$ and two possible signs for $\hat{T}^2 = \pm1$. Fidkowski and Kitaev made a connection between the properties of $\hat{T}$ and the Altland-Zirnbauer classification,[83] which we briefly discuss later.[71] Here, we state the result without going into details and show the Cartan labels of the symmetry class along with the properties of $\hat{T}$ in Tab. 6.1.[71]

When considering a subsystem with an odd number of Majorana modes, it is required to add an additional Majorana located at infinity, γ_∞, to work in a physical Hilbert space that necessarily incorporates an even number of Majoranas. The parity operator is then the product

$$\hat{P} = i^{(k+1)/2}\gamma_0\gamma_1\cdots\gamma_{k-1}\gamma_\infty. \tag{6.8}$$

It turns out useful to define the hermitian and unitary operator $\hat{Z}$

$$\hat{Z} = i^{(k-1)/2}\gamma_0\gamma_1\cdots\gamma_{k-1} \tag{6.9}$$

that anticommutes with $\hat{P}$. We chose the action of time-reversal of γ_∞ such that $\hat{T}$ and $\hat{P}$ commute,[71] giving

$$\hat{T}\gamma_\infty\hat{T}^{-1} = -a\gamma_\infty \tag{6.10}$$

with the sign a defined by $\hat{T}\hat{Z}\hat{T}^{-1} = a\hat{Z}$, different from its definition for an even number of Majorana modes, Eq. (6.6).

For an odd number of Majorana modes, it is not possible to find both matrices $C_\pm$, Eq. (6.3). For $k = 4n + 1$, only the matrix C_+ exists and time reversal has the same form as for even k, $\hat{T} = C_+\mathcal{K}$. As before, we determine if $\hat{T}$ and $\hat{Z}$ commute or anticommute by simply counting the imaginary units in the definition of $\hat{Z}$,

$$\hat{T}\hat{Z}\hat{T}^{-1} = (-1)^{4n/2}\hat{Z} = \hat{Z}, \tag{6.11}$$

i.e., $\hat{Z}$ and $\hat{T}$ commute for $k = 4n+1$. For $k = 4n+3$, only the matrix C_- exists, which defines the antiunitary operator $\hat{T}' = C_-\mathcal{K}$. To construct time-reversal symmetry, an operator that commutes with all Majorana operators, we define it as the product $\hat{T} = \hat{T}'\hat{P}$, where both $\hat{P}$ and $\hat{T}'$ anticommute with all γ_p. Since $\hat{Z}$ and $\hat{P}$ anticommute,

$$\hat{T}\hat{Z}\hat{T}^{-1} = -\hat{T}'\hat{Z}\hat{T}'^{-1} = -(-1)^{2n+1}(-1)^k\hat{Z} = -\hat{Z}, \tag{6.12}$$

where the first factor of $(-1)^{2n+1}$ originates in the number of imaginary units in Eq. (6.9) and $(-1)^k$ in the number of Majoranas since $\hat{T}'\gamma_p\hat{T}'^{-1} = -\gamma_p$. Using that $\hat{P}$ is hermitian and unitary, we conclude that $\hat{T}^2 = \hat{T}'^2 = C_-C_-^*$, with the square $C_-C_-^*$ summarized in Tab. 6.1.

For an odd number of Majorana modes, there are the same four distinct possibilities for the properties of $\mathcal{T}$ as for an even k: $\hat{T}^2 = \pm 1$ and $a = \pm 1$. Different from an even number of Majoranas, only one of the matrices $C_\pm$ exists, such that $\hat{P}$ is not part of the (unphysical) Hilbert space that incorporates an even number of Majoranas.

As shown by Fidkowski and Kitaev, the eight possible symmetry classes (four classes for even k, four classes for odd k) can be connected to the tenfold Atland-Zirnbauer classification of topological insulators presented in Sec. 2.2.[71] If we consider the action of $\hat{T}$ on a non-interacting Hamiltonian written in terms of Majorana operators $H = i/4\sum_{p,q} A_{pq}\gamma_p\gamma_q$[320] with a real antisymmetric matrix A, $\hat{T}$ either acts as *single-particle* "time-reversal symmetry" T_+ or "particle-hole symmetry" T_-.[*] When $\hat{T}$ and $\hat{P}$ commute, $\hat{T}$ does not exchange the parity sectors and we can define the single-particle time-reversal symmetry by $T_+ = \hat{T}$ ($k \mod 8 \in [0,1,3,4,5,7]$). Otherwise, $\hat{T}$ acts as single-particle particle-hole symmetry $T_- = \hat{T}$ ($k \mod 8 \in [2,6]$, classes C and D). For an even number of Majoranas, the sublattice symmetry $\hat{Z}$ is always present and, since $\hat{Z} = T_+T_-$, particle-hole symmetry is present with $T_- = \hat{T}^{-1}\hat{Z}$. Note that the latter definition only makes sense when the physical Hilbert space that includes γ_∞ is considered, such that $\hat{Z}$ does not equal the identity operator (see below, Sec. 6.2.2).

The symmetry classes found in this section give the energy level statistics of the many-body Hamiltonian (6.1).[83;324;325] To evaluate the level statistics in terms of Gaussian ensembles, we need to eliminate the role of the density of states that does not follow a simple distribution function.[330] Following Ref. 325, we collect the eigenenergies of the Hamiltonian and sort them in ascending order $E_1 < E_2 < \ldots$ to compute the level spacing $\Delta E_n = E_{n+1} - E_n$. The density of states is canceled out in the ratio of adjacent level spacings $r_n = \Delta E_n / \Delta E_{n+1}$.[325;331] The ratio r_n is distributed according to Wigner-Dyson statistics with the distribution function[332]

$$p(r) = \frac{1}{Z_\beta}\frac{(r+r^2)^\beta}{(1+r+r^2)^{1+3\beta/2}}. \tag{6.13}$$

The parameter β and the normalization Z_β depend on the Gaussian ensemble: for the Gaussian orthogonal ensemble $\beta = 1$ and $Z_\beta = 8/27$ (classes CI, AI, BDI), for the Gaussian unitary ensemble $\beta = 2$ (classes C,D) and $Z_\beta = 4\pi/(81\sqrt{3})$, and for the Gaussian

---

[*] We denote the single particle operators without a hat, following the notation of Ref. 86. The quotation marks emphasize that the expressions are only meaningful in a single-particle context.

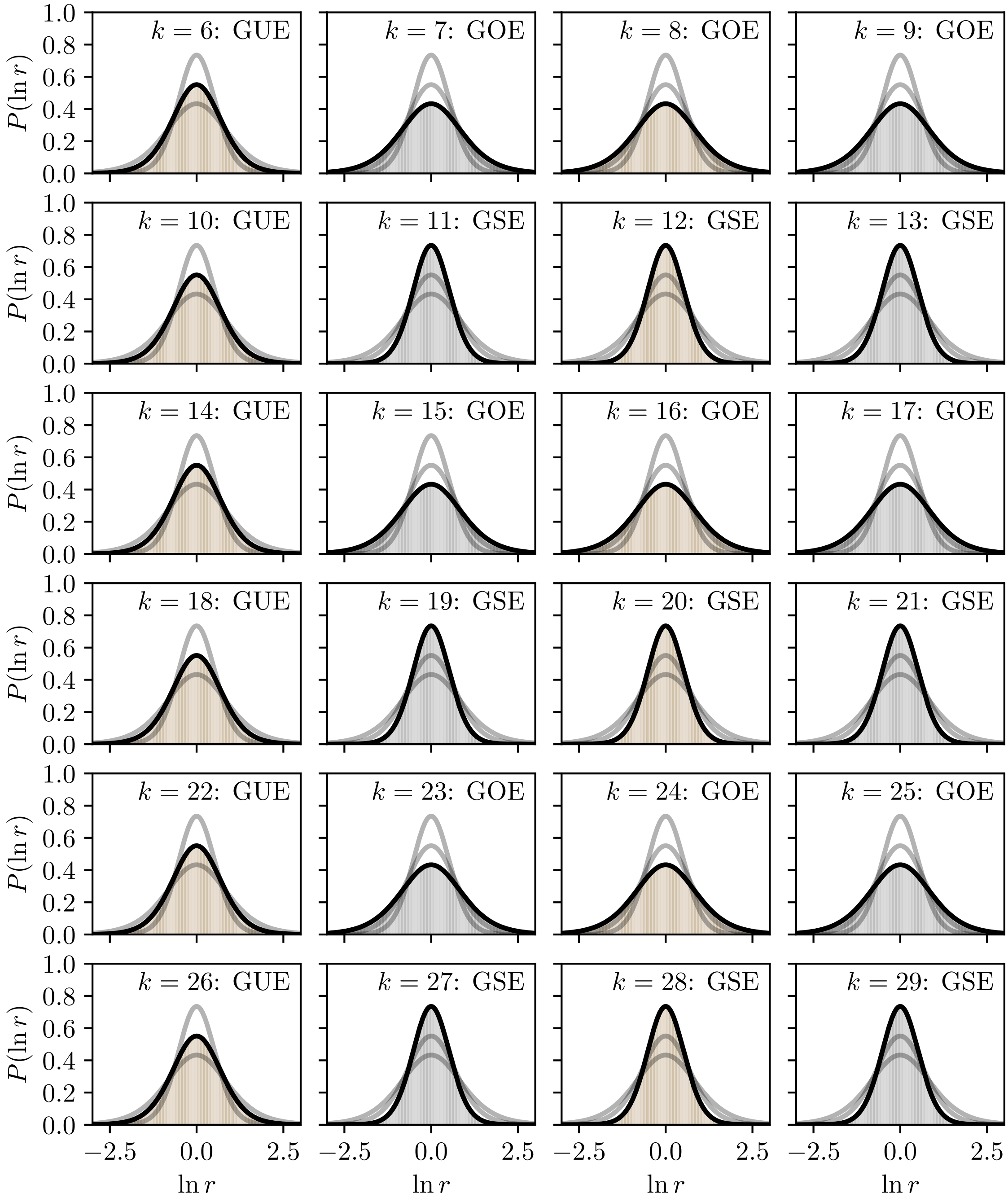

FIGURE 6.1: Level spacing statistics of the SYK model for a finite particle number. The ensemble averaged ratio of adjacent level spacings r_n from the Hamiltonian (6.1) follows either a Gaussian orthogonal, unitary, or symplectic ensemble (GOE/GUE/GSE). We plot the distribution as a function of $\ln r$, together expectation from random matrix theory, Eq. (6.13). The solid lines in black show the expected behavior from the symmetry classification, Tab. 6.1, and the solid lines in gray the other ensembles for a comparison. For an even number of Majoranas, the Hamiltonian is decomposed into two different parity sectors, cf. Eq. (6.14). The resulting r_n from both two parity sectors are plotted in red and green and they are indistinguishable. For an odd number of Majoranas, only one parity sector exists, with the single sector of r_n plotted in gray.

symplectic ensemble $\beta = 4$ and $Z_\beta = 4\pi/(729\sqrt{3})$ (classes DIII, AII, CII).[332] The difference between the different levels statistics is clearer to see when plotting $\ln r$ and the corresponding distribution $P(\ln r) = p(r)r$. In Fig. 6.1, we show the numerically obtained level statistics for the Hamiltonian (6.1). The expectation from the symmetry classification is well-reflected in the distribution of the eigenvalues that follow the different Gaussian ensembles.

6.2 Overlap of Time-reversed Partners

The different symmetry classes have peculiar consequences that exceed the level spacing statistics. Similar to random matrices,[83] the spectral function's behavior at low energies $\omega \to 0$ depends on the symmetry class. Surprisingly, it is the many-body spectral function that shows this feature.

Before we investigate the spectral function itself, we investigate how its features originate solely in the properties of the Hilbert space discussed in the previous section. The behavior at zero energy is given by the overlap of a Majorana operator with two states $|\psi\rangle$ and $|\psi'\rangle$ that have the same energy eigenvalue, $\langle\psi|\gamma_p|\psi'\rangle$. In this section, we show when these matrix elements have to be zero due to symmetry constraints. In general, if no symmetries constrain them to zero, we expect a finite contribution by those elements.

6.2.1 Even Number of Majoranas

For even k, the Hamiltonian commutes with the parity operator $\hat{P}$, thus the eigenstates of the Hamiltonian are automatically eigenstates of the parity operator. The operator $\hat{P}$ is hermitian and unitary with eigenvalues are $p = \pm 1$. We can therefore label any eigenstate of the Hamiltonian by its parity eigenvalue

$$H|\psi^\pm\rangle = E_\pm|\psi^\pm\rangle, \;\; \hat{P}|\psi^\pm\rangle = \pm|\psi^\pm\rangle. \tag{6.14}$$

Since γ_p anticommutes with $\hat{P}$, i.e., it changes the parity eigenvalue, the expectation value of γ_p for any eigenstate must always vanish, $\langle\psi|\gamma_p|\psi\rangle = 0$.

The only way to construct non-vanishing matrix elements $\langle\psi|\gamma_p|\psi'\rangle$ with $|\psi\rangle$ and $|\psi'\rangle$ having the same energy eigenvalue is to use that H and $\hat{T}$ commute: any energy eigenstate $|\psi\rangle$ with energy E has a time-reversed partner $|\hat{T}\psi\rangle$ with the same energy,

$$\hat{T}E|\psi\rangle = \hat{T}H|\psi\rangle = H\hat{T}|\psi\rangle = H|\hat{T}\psi\rangle. \tag{6.15}$$

Using Eq. (6.6), we realize that

$$\hat{T}\hat{P}\hat{T}^{-1}|\hat{T}\psi^\pm\rangle = \pm\hat{T}|\psi^\pm\rangle = a\hat{P}|\hat{T}\psi^\pm\rangle \tag{6.16}$$

with $a = (-1)^{k/2}$. Thus, when $a = +1$, $\hat{T}$ does not change the parity of an eigenstate, otherwise, it does. Accordingly, for $k = 4n + 2$ Majoranas (classes C and D, $a = -1$), $|\hat{T}\psi^\pm\rangle$ has a different parity eigenvalue than $|\psi^\pm\rangle$. Then, the joint operator $\gamma_p\hat{T}$ does not change the parity, which means that the matrix element $\langle\psi|\gamma_p\hat{T}|\psi\rangle$ is not necessarily zero. However, it must be zero in those cases when $O \equiv \gamma_p\hat{T}$ squares to $O^2 = -1$, and it can be nonzero for $O^2 = +1$. The square is easy to compute. Using $[\hat{T}, \gamma_p] = 0$ gives

$$O^2 = \gamma_p\hat{T}\gamma_p\hat{T} = \hat{T}^2 \tag{6.17}$$

with $\hat{T}^2 = +1$ in class D and $\hat{T}^2 = -1$ in class C. We conclude that

$$\langle\psi|\gamma_p\hat{T}|\psi\rangle = \begin{cases} \text{finite} & \text{class D} \\ 0 & \text{class C,} \end{cases} \tag{6.18}$$

i.e., it is possible to find eigenstates of the same energy that have vanishing matrix elements with γ_p. The vanishing matrix element is directly visible in the spectral function at zero energy, as elaborated further in Sec. 6.3.

6.2.2 Odd Number of Majoranas

For an odd number of Majoranas, $\hat{P}$ and $\hat{T}$ always commute, so applying time reversal $\hat{T}$ to a state $|\psi\rangle$ does never change its parity. However, $\hat{Z}$ and $\hat{P}$ anticommute, so $\hat{Z}|\psi\rangle$ has a different parity than $|\psi\rangle$, and the matrix element

$$\langle\psi|\gamma_p\hat{Z}|\psi\rangle = \langle\psi|\hat{Z}\gamma_p|\psi\rangle \tag{6.19}$$

is not necessarily zero. Let us first investigate $\langle\psi|\hat{Z}\gamma_p\hat{T}|\psi\rangle$, where the square of the antiunitary operator $\left(\hat{Z}\gamma_p\hat{T}\right)^2 = a\hat{T}^2$ is either $+1$ or -1, resulting in

$$\langle\psi|\hat{Z}\gamma_p\hat{T}|\psi\rangle = \begin{cases} 0 & \text{classes CI, CII} \\ \text{finite} & \text{classes BDI, DIII.} \end{cases} \tag{6.20}$$

In those cases where $\hat{T}^2 = +1$, $|\psi\rangle$ and $\hat{T}|\psi\rangle$ are not necessarily different states. If they just differ by a phase, then

$$|\langle\psi|\hat{Z}\gamma_p\hat{T}|\psi\rangle| = |\langle\psi|\hat{Z}\gamma_p|\psi\rangle| = \begin{cases} 0 & \text{class CI} \\ \text{finite} & \text{class BDI} \end{cases}. \tag{6.21}$$

If $|\psi\rangle$ are $\hat{T}|\psi\rangle$ are different states, then above relation holds for the linear combinations

$$|\phi_\pm\rangle = \frac{1}{\sqrt{2}}\left(|\psi\rangle \pm \hat{T}|\psi\rangle\right) \tag{6.22}$$

that change only by a phase when applying $\hat{T}$.

Since $\hat{Z}$ commutes with all γ_p, $p \in [0, k-1]$ and therefore with all combinations $\gamma_p\gamma_q\cdots\gamma_r$, we can replace $\hat{Z} \to 1$ when only considering the space spanned by an odd number of Majoranas. The results are summarized in the last columns of Tab. 6.1 for both odd and even k.

6.3 Spectral Function

The spectral function close to zero energy reflects the value of the overlap of the Majorana operator with states at the zero energy. In particular, the same matrix elements computed above enter in the correlation function[52]

$$C^+_{pq}(\omega) = \frac{1}{\mathcal{Z}}\sum_{\alpha,\beta}\frac{\langle\psi_\alpha|\gamma_p|\psi_\beta\rangle\,\langle\psi_\beta|\gamma_q|\psi_\alpha\rangle}{\omega + \varepsilon_\alpha - \varepsilon_\beta + i\eta}\left(e^{-\beta\varepsilon_\alpha} + e^{-\beta\varepsilon_\beta}\right) \tag{6.23}$$

with the many-body states $|\psi_\alpha\rangle$ and energies ε_α. At $\omega = 0$, the sum over all states α, β only gives a contribution if $\varepsilon_\alpha = \varepsilon_\beta$, which is true if those states are identical or if they are time-reversed partners. As shown above, a contribution arises in classes BDI, DIII, and CII if both states are identical, and in classes BDI, DIII and D if the states are time-reversed partners, whereas there is no contribution at zero energy in classes C and CI. In classes AI and AII, time-reversed partners are in within the same parity sector, so that no contribution arises at zero energy.

The results in a particular signature in the spectral function: at zero energy, it has a peak in classes BDI, D, DIII, CI and D, a hole in classes C and CI, and it is featureless in classes AI and AII. We confirm this signature numerically, by evaluating the imaginary part of the diagonal elements C^{+}_{pp} at zero temperature and at infinite temperature. These diagonal elements are related to the spectral function

$$A(\omega) = -\frac{1}{k}\,\frac{1}{\pi}\mathrm{Im}\sum_{p} C^{+}_{pp}(\omega) \tag{6.24}$$

that is experimentally accessible with scanning tunneling microscopy.[333]

6.3.1 Zero Temperature

At zero temperature, the imaginary part of the diagonal elements of the spectral function (6.23) simplifies to

$$\mathrm{Im}C^{+}_{pp}(\omega) = -\,\pi \sum_{\alpha} |\langle\psi_0|\gamma_p|\psi_\alpha\rangle|^2 \left[\delta(\omega+\varepsilon_0-\varepsilon_\alpha)+\delta(\omega+\varepsilon_\alpha-\varepsilon_0)\right]. \tag{6.25}$$

We define the characteristic energy scale Δ as the ensemble average of the first excited state's energy $\Delta = \langle\!\langle \varepsilon_1 - \varepsilon_0 \rangle\!\rangle$ and obtain an approximation by numerically evaluating a large number of ensembles. For large k, it is possible to give an analytical expression for Δ, using known approximations[324;334] for the single-particle spectral function at energies $\omega \sim \varepsilon_0$; however, since we are especially interested in a small number of Majoranas, the more pragmatic numerical approach suits better. In all numerical evaluations, we replace the delta function by a Lorentz function $\delta(x) = \lim_{\eta\to 0} \eta/(\pi(\eta^2+x^2))$ with level broadening η.

In Fig. 6.2, we show the numerically evaluated spectral function at zero temperature, averaged over disorder. The upper two panels show those cases where a peak at zero energy is expected. We distinguish between CII and the other three cases, since the weight of the peak differs. In the lower two panels, we show the classes AI and AII, where no peak nor hole is observed, and C and CI with a hole at zero energy since all overlaps that enter are strictly zero, cf. Tab. 6.1.

6.3.2 Infinite Temperature

The signatures visible at zero temperature persist at any other temperature. We demonstrate this explicitly by computing the spectral function at infinite temperature numerically. For $T \to \infty$, the partition function simply equals $\mathcal{Z} = M$, the number of many-body states, and the diagonal matrix elements of the correlation function are

$$\mathrm{Im}C^{+}_{pp}(\omega) = -\,\frac{2\pi}{M} \sum_{\alpha,\beta} |\langle\psi_\alpha|\gamma_p|\psi_\beta\rangle|^2\, \delta(\omega+\varepsilon_\alpha-\varepsilon_\beta). \tag{6.26}$$

For infinite temperature, we are able to compute the mean level spacing Δ analytically, using the variance of the energy eigenvalues. By employing the Majorana anticommutation

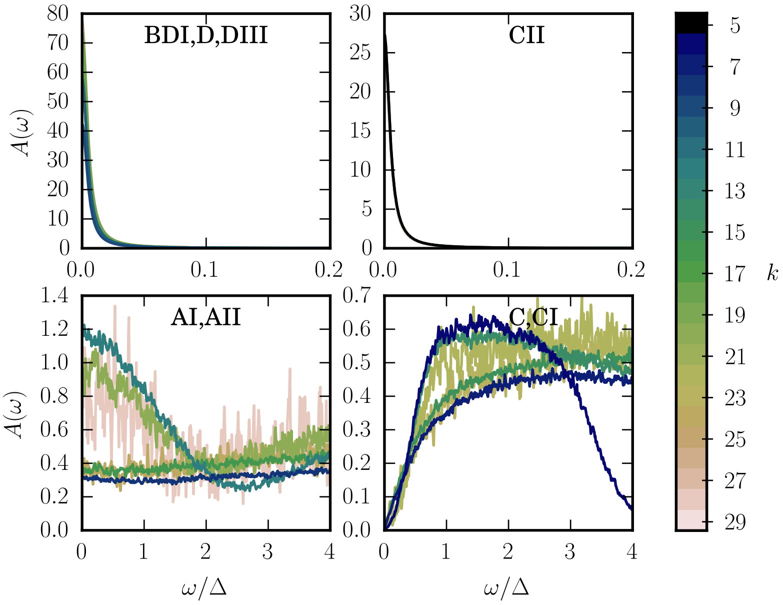

FIGURE 6.2: Spectral function at zero temperature close to zero energy, where the energy is rescaled by Δ, the mean energy of the first excited state. The level broadening is chosen $\eta = 0.005\Delta$.

relations, and the mean and variance of J_{pqrs}, Eq. (6.2), we find that the variance of the energy eigenvalues ($\langle\!\langle \varepsilon_n \rangle\!\rangle = 0$)

$$\langle\!\langle \varepsilon_n^2 \rangle\!\rangle = \langle\!\langle H^2 \rangle\!\rangle = J^2 \frac{3!}{k^3} \binom{k}{4}. \tag{6.27}$$

Since the eigenvalues do not follow a Wigner semicircle distribution,[324] we need to take into account the correction[330]

$$\zeta = \binom{k}{4}^{-1} \sum_{r=0}^{4} (-1)^r \binom{4}{r} \binom{k-4}{4-r}. \tag{6.28}$$

to obtain the minimal and maximal eigenvalues

$$\varepsilon_\pm = \pm \frac{2\sqrt{\langle\!\langle \varepsilon_n^2 \rangle\!\rangle}}{\sqrt{1-\zeta}} \tag{6.29}$$

($\zeta = 0$ for the Wigner semicircle distribution). The mean level spacing Δ is therefore

$$\frac{\Delta}{J} \equiv J^{-1} \langle\!\langle \varepsilon_{n+1} - \varepsilon_n \rangle\!\rangle = \begin{cases} \frac{\sqrt{(k-1)!/(k-4)!}}{k\, 2^{\lfloor k/2 \rfloor - 1} \sqrt{1-\zeta}} & \text{no degeneracies} \\ \frac{\sqrt{(k-1)!/(k-4)!}}{k\, 2^{\lfloor k/2 \rfloor} \sqrt{1-\zeta}} & \text{doubly degenerate.} \end{cases} \tag{6.30}$$

The spectrum is degenerate in symmetry classes D, DIII, AII, CII and C. In classes D and C, the two different parity sectors are degenerate, and in classes DIII, AII and CII there are degeneracies within the same parity sector. The degeneracies in classes DIII, AII and CII can be understood from the Kramer's degeneracy in non-interacting systems, since the single-particle time-reversal symmetry squares to $T_+^2 = -1$ in these symmetry classes.[71]

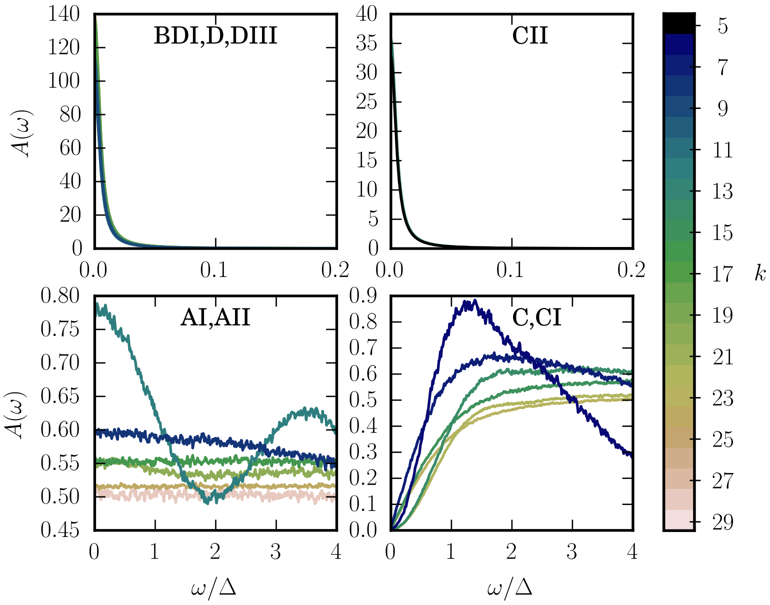

FIGURE 6.3: Spectral function at infinite temperature close to zero energy, where the energy is rescaled by Δ, the mean level spacing, cf. Eq. (6.30). The level broadening is chosen $\eta = 0.005\Delta$.

In Fig. 6.3, we show the spectral function rescaled by Δ in all symmetry classes. The features close to zero energy reflect the overlap of the Majorana operators with eigenstates of the same energy, as expected. The overall behavior is strikingly similar to the spectral function at zero temperature, Fig. 6.2. Less disorder realizations than for zero temperature are necessary to obtain smooth functions of the energy.

6.4 Symmetry-breaking Terms

How do the properties shown above survive once a symmetry-breaking term is added to the Hamiltonian? When the chemical potential is not exactly at zero energy, or if there are random fluctuations in the chemical potential, the condensed-matter realization of the SYK model by Ref. 321 includes an additional random bilinear term that extend the original model, (6.1)

$$H = i \sum_{p<q} K_{pq}\gamma_p\gamma_q + \sum_{p<q<r<s} J_{pqrs}\gamma_p\gamma_q\gamma_r\gamma_s \tag{6.31}$$

and defines a second energy scale

$$K^2 = k\langle\!\langle K_{pq}^2 \rangle\!\rangle. \tag{6.32}$$

This bilinear term breaks time-reversal symmetry, since it anticommutes with $\hat{T}$. Numerically, we find that

$$\frac{1}{k}\sum_p |\langle\psi_0|\gamma_p|\psi_0\rangle|^2 = \mathcal{O}(K^2) \tag{6.33}$$

in classes C and CI, while it stays finite in the other symmetry classes. We show the results for classes C and CI in Fig. 6.4. When replacing the ground state with any state $|\psi_n\rangle$, the

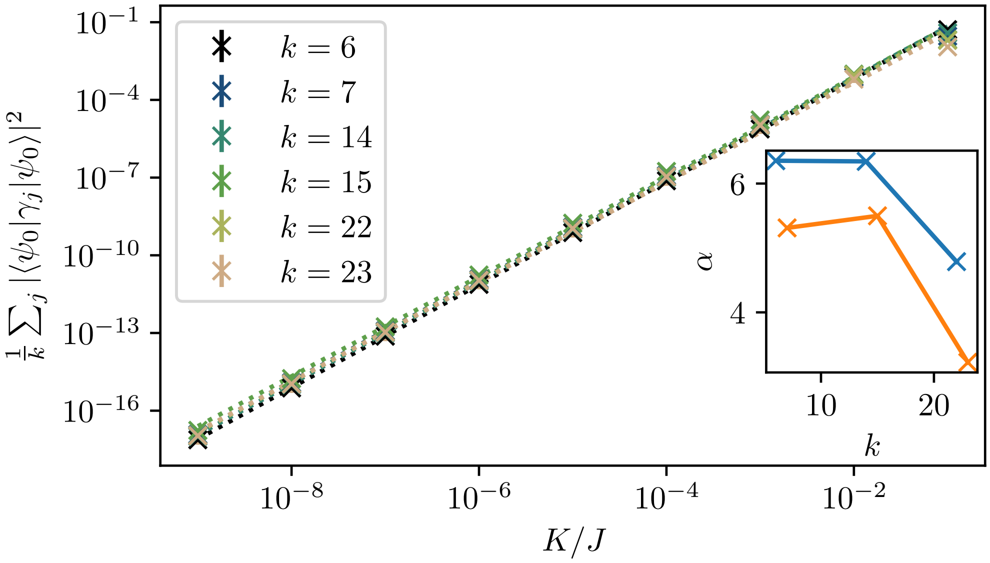

FIGURE 6.4: Ground state overlap for $k \in [6, 7, 14, 15, 22, 23]$ Majoranas (classes C and CI) as a function of K/J, averaged over disorder. The dotted lines are quadratic fits of the data, $\frac{1}{k}\sum_j |\langle\psi_0|\gamma^j|\psi_0\rangle|^2 = \alpha K^2$. The coefficient α is plotted in the inset, in blue for class C and in orange for class CI.

scaling with K^2 stays the same. The spectral hole at zero energy thus gradually fades away once time-reversal symmetry is broken.

6.5 Lattice Model

How can our findings be interpreted in a condensed-matter context? The visibility of the peak and hole at zero energy is a matter of energy scales. In all proposals for a condensed-matter realization of the SYK model,[321–323] the low-energy degrees of freedom are separated by a gap from the rest of the spectrum. In this section, we investigate the gap in a particular model and argue how it affects the experimental visibilty.

Following Ref. 321, we employ a simple lattice model that realizes a Fu-Kane Hamiltonian, i.e., a surface state of a topological insulator in proximity to a superconductor.[21] In absence of the induced superconductivity, the Hamiltonian

$$\mathcal{H}_0 = \lambda(\sin k_x \sigma_x + \sin k_y \sigma_y) + M_{\mathbf{k}}\sigma_z - \mu \tag{6.34}$$

is defined on a two-dimensional square lattice with the mass term $M_{\mathbf{k}} = m\{(2 - \cos k_x - \cos k_y) - [2 - \cos(2k_x) - \cos(2k_y)]/4\}$. The mass term is fine-tuned to $M_{\mathbf{k}=0} = 0$ to have a gapless dispersion without fermion doubling. The mass term breaks time-reversal symmetry, different from a surface state of a topological insulator, but the symmetry-violating term is small close to the Γ point,[321] where it introduces an artificial splitting of the zero modes that we ignore. In proximity to a superconductor, the superconducting pairing potential Δ is induced to the topological insulator surface state by tunneling of quasiparticles.[21] This gives a particle-hole symmetric Hamiltonian that slightly breaks time-reversal

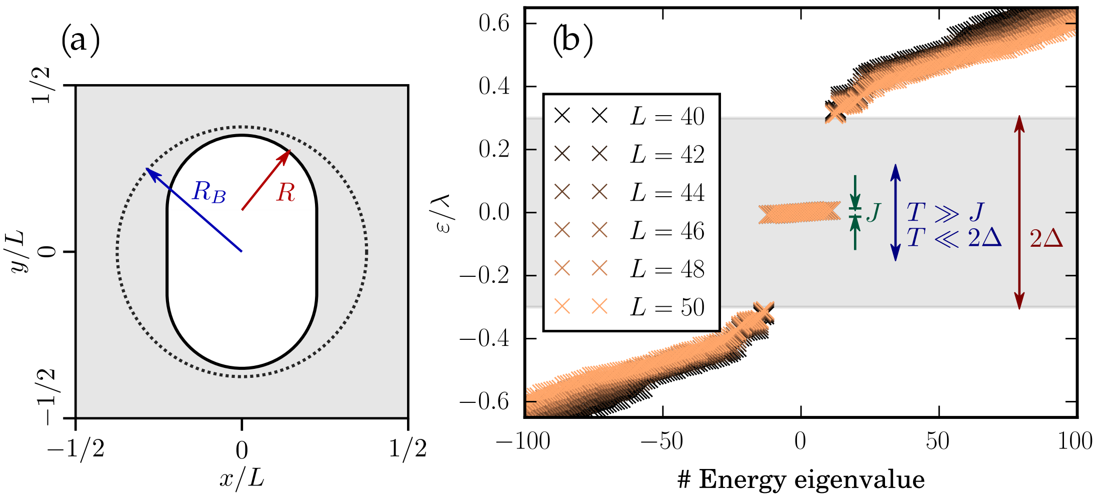

FIGURE 6.5: Energy eigenvalues for the tight-binding Hamiltonian defined in Eq. (6.35) that supports $N = 24$ Majorana zero modes.[321] We chose periodic boundary conditions on a square lattice with $L \times L$ sites. In this system, the limit of infinite temperature is quite transparent: for $T \gg J$, the temperature is the largest energy scale in the subsystem that only consists of randomly interacting Majorana zero modes. As long as the temperature is sufficiently smaller than the energy gap, $T \ll 2\Delta$, only in-gap states contribute to the spectral function at small energies.

symmetry, given by

$$\mathcal{H} = \begin{pmatrix} \mathcal{H}_0 & \Delta \\ \Delta & -\sigma_y \mathcal{H}_0^* \sigma_y \end{pmatrix}. \tag{6.35}$$

An even number of Majorana modes may be trapped in a superconducting vortex. Using the Kwant code,[264] we numerically simulate a geometry with a stadium-sized vortex where $\Delta = 0$ and a magnetic flux of $\Phi = N\Phi_0$ restricted to a circular hole with diameter R_B, Fig. 6.5 (a). This geometry gives N Majorana modes trapped into the hole. In Fig. 6.5 (b), we show the resulting energy spectrum for this particular realization.

Random fluctuations in the system's parameters, e.g., in the hole size, give rise to random interactions between the Majorana modes, effectively realizing the SYK model in a condensed-matter context.[321] Since the Majorana modes are separated by a gap from the rest of the system, the SYK model is only realized when the strength of the interactions J and the temperature T are much smaller than the gap size 2Δ. Since J has an upper boundary, the conformal limit $J/T \to \infty$ can only be reached for $T \to 0$. The infinite-temperature limit that was considered before is given by $T \gg J$. To avoid mixing with higher-energy states, this limit further requires $T \ll 2\Delta$, i.e., well-separated energy scales $2\Delta \gg T \gg J$.

6.6 Conclusion

In this chapter, we identified the spectral function as a manifestation of the symmetry class in the interacting SYK model. We summarized previous work[71] that deal with the role of symmetries for the topology in interacting systems. As a direct consequence of the symmetry class, the expectation value of the Majorana operators with respect to states at the same energy is either finite or zero. Since the many-body spectral function depends these expectation values, it shows signatures of the symmetry class close to zero energy, either peak-like, hole-like, or featureless behavior. These signatures are robust against the temperature, which we explicitly showed by numerically computing the spectral function at infinite temperature.

In experiment, the many-body spectral function can be measured with scanning tunneling microscopy,[333] i.e., it can be observed in the condensed-matter realizations of the SYK model.[321–323] The observability depends on the correct cascade of energy scales.

The features in the many-body spectral function show a strong similarity to the features in the single-particle density of states of noninteracting random Hamiltonians.[83] For example, the peak or hole close to zero energy in classes C and D are also visible in single-particle density of states for those classes.[83] We cannot provide reasons for this analogy, which are left for future studies.

7 Conclusion and Outlook

In this thesis, we identified several experimental signatures of topological semimetals, advanced methods to compute transport in noninteracting systems, and provided a link between high-energy and condensed-matter physics by showing how the consistent and covariant anomalies manifest on a lattice. One main experimental signature identified in this work is the blue note: a characteristic pattern of the chiral anomaly that emerges in ARPES measurements of Weyl semimetals.[58] Although it has yet not been experimentally observed, we are confident that such an experiment can be carried out in the near future.

Another relevant signature is the strongly peaked magnetoresistance in Weyl semimetals.[42] Even though related work[335] gives an alternative explanation of the peaked magnetoresistance observed in recent experiments,[175] the signature we found can be observed in experiments where magnetic and electric fields remain parallel and are both tilted away from the node separation. For transversal magnetotransport, we mostly focused on a proof-of-principle, i.e., that we are able to access strong-disorder regimes that are not captured by a perturbative approach.[45] Along the way, we showed that strong scalar disorder gives a conductivity that decreases with the applied magnetic field, contrary to the weak-disorder regime where it increases with the field. The decreasing conductivity results in a positive magnetoresistivity that is observed experimentally. Despite this qualitative agreement, strong evidence suggests that charged impurities in Weyl semimetals cause the unsaturated growth of the magnetoresistivity.[26;44]

A key experimental signature of strained Weyl semimetals has been identified in this thesis: the growth of the conductance with the sample's width cubed, different from the usual scaling in diffusive systems.[97] The unusual behavior originates in the spatial separation of counterpropagating modes in strained Weyl semimetals.

We further identified a manifestation of the symmetry class of the SYK model for a finite particle number. The density of states, which can be accessed via scanning tunneling microscopy (STM), is either peaked, gapped, or featureless at low energies. This feature depends solely on the system's symmetry class. Surprisingly, the feature in the density of states remains independent of the temperature, although the visibility in STM measurements might be compromised at large temperatures.[333]

Besides the identification of experimental signatures, we further advanced methods used to compute transport. In particular, we extended the transfer matrix method[46] in two ways to include magnetic fields. We showed how the transfer matrix method can be modified using another degree of freedom than momentum, e.g., Landau levels.[42] For transversal magnetotransport, we suggested a way to avoid the shift of the maximal transmission in disordered systems by employing a gauge transformation.[45] This allowed to access regimes that are not captured by a perturbative treatment of disorder in such systems. Besides these improvements, we found a description of nodal line semimetals in terms of transfer matrices and showed that the Kubo formula fails to give correct predictions for transport in the plane of the nodal line. The study of disorder is left for future work.

A more conceptual result is the manifestation of predictions from high-energy physics, i.e., the consistent and covariant anomaly, on a lattice. We showed that both anomalies can be observed by either considering energies up to a small cutoff or by including the whole spectrum. A similar approach was introduced for nodal line semimetals, with some implications left for future studies.

Besides the field-theory description, we further analyzed a lattice realization of a nodal line semimetal that is based on a Weyl semimetal subjected to a superlattice.[152] We especially focused on the stability of this model and on the surface states. The surface states were used as an example for a reformulated bulk-boundary correspondence that connects the intercellular Zak phase with the number of gapless surface states.[113]

Although we presented novel results for transport in nodal line semimetals and strained Weyl semimetals, the discussion of these results is, however, not complete: in the case of nodal line semimetals, it is not settled if a one-parameter scaling similar to graphene[46] exists, due to the lack of data for disordered systems. Similarly, the scaling of the conductivity with the strength of the strain is not known, and the effect of the disorder model on this scaling remains unknown.

The methods introduced in this work can be extended to gain insights into other gapless topological phases. Most notably, the field-theory approach for nodal line semimetals introduced in Sec. 3.6 has not been exhausted yet. To understand quantum anomalies in nodal line semimetals, we need to combine lattice simulations with field-theory methods to evaluate and interpret the triangle diagrams, Eq. (3.78). This may help to connect recently predicted anomalies in nodal line semimetals[47;48] and quantum field theory.

Another extension of this work is the use of superlattices to generate more topological phases. By using more complex structures and models than the ones introduced in Chapter 5, other topological phases can potentially be realized, e.g., topologically protected two-dimensional Fermi surfaces embedded in three-dimensional systems.[336;337]

How do our results affect the big picture? The results presented in this work are small contributions to a much bigger project: to understand topological materials and to find applications that use their outstanding properties. For example, since transport in strained Weyl semimetals reflects that counterpropagating channels are spatially separated, microstructured materials based on strained Weyl semimetals may be engineered and used in electronic devices where charge transport needs to be channeled into fine structures. Similarly, we showed indirectly that the chiral magnetic effect, a current proportional to an external magnetic field, exists when only energies close to the Fermi surface are considered, as already argued in previous work.[62] This potentially renders devices possible that use this feature.

The investigation of the surface states in nodal line semimetals, especially with respect to the model introduced in Sec. 5, can help to find materials with almost flat surface states.[113;152] In combination with interactions, exotic phenomema can be created at those surfaces with flat bands.[283]. Similar to fractional Chern insulators,[338] anyonic excitations might be created, the building block of topological quantum computation.[339;340]

Finally, a condensed-matter realization of the SYK model massively simplifies the investigation of the AdS/CFT correspondence, ultimately enabling us to gain a deeper understanding of the universe.

A Zak Phase and Extra Charge Accumulation

To show how the intercellular Zak phase is related to the extra charge accumulation at the surface, we use an explicit representation of the eigenstates of the Hamiltonian that satisfy periodic boundary conditions[113]

$$\psi_{n,k}(x) = \frac{1}{\sqrt{N}} \sum_{m}^{N} \sum_{j=1}^{N_b} \sum_{\zeta=1}^{N_{\text{orb}}^{j}} \alpha_k^{n,j,\zeta} \phi_m^{j,\zeta}(x) e^{ikma} \tag{A.1}$$

where N is the number of unit cells, and m and n are the unit cell and band index. There are N_b atomic sites per unit cell with N_{orb}^{j} orbital degrees of freedom for the atomic site with index j. Here,

$$\phi_m^{j,\zeta}(x) = \phi^{\zeta}(x - ma - b_j a) \tag{A.2}$$

is the ζ-th atomic orbital centered at $ma + b_j a$, which is the position of the j-th atomic site in the m-th unit cell. Atomic orbitals at the same site are orthonormal and the overlaps between orbitals on different sites are assumed to be exponentially vanishing in accordance with the tight-binding condition. The coefficients $\alpha_k^{n,j,\zeta}$ are obtained from solving the eigenvalue problem with the tight-binding Hamiltonian. We choose the gauge in which every atomic orbital in the m-th unit cell has the same phase factor e^{ikma} in (A.1); the coefficients α then satisfy the periodic boundary condition $\alpha_{k+G}^{n,j,\zeta} = \alpha_k^{n,j,\zeta}$, where G is a reciprocal lattice vector.[151]

Using Eq. (A.1), the intercellular Zak phase can be rewritten as

$$\gamma_n^{\text{inter}} = i \int dx\, \psi_{n,k}^{*}(x) \partial_k \psi_{n,k}(x) = i \sum_{j=1}^{N_{\text{b}}} \sum_{\zeta=1}^{N_{\text{orb}}^{i}} \alpha_k^{n,j,\zeta *} \partial_k \alpha_k^{n,j,\zeta}. \tag{A.3}$$

We also rewrite the Wannier functions $W_{n,m}(x)$, Eq. (2.18), by introducing the explicit form of the eigenstates,

$$W_{n,m}(x) = \frac{1}{\sqrt{N}} \sum_{k \in \text{BZ}} \psi_{n,k}(x) e^{-ikma} = \sum_{m'}^{N} \sum_{i=j}^{N_b} \sum_{\zeta=1}^{N_{\text{orb}}^{j}} \underbrace{\frac{1}{N} \sum_{k \in \text{BZ}} e^{ik(m'-m)a} \alpha_k^{n,j,\zeta}}_{\equiv A_{m'-m}^{n,j,\zeta}} \phi_{m'}^{j,\zeta}(x) \tag{A.4}$$

where we defined $A^{n,j,\zeta}_{m'-m}$ as the Fourier transform of $\alpha^{n,j,\zeta}_k$. The reverse transformation, $\alpha^{n,j,\zeta}_k = 2\pi/a \sum_m A^{n,j,\zeta}_m e^{-ikma}$, allows for another form of the intercellular Zak phase

$$\gamma_n^{\text{inter}} = 2\pi \sum_m \sum_{j=1}^{N_\text{b}} \sum_{\zeta=1}^{N^i_\text{orb}} m \left| A^{n,j,\zeta}_m \right|^2 \tag{A.5}$$

$$= \underbrace{2\pi \sum_{m=-\infty}^{-1} \sum_{j=1}^{N_\text{b}} \sum_{\zeta=1}^{N^i_\text{orb}} m \left| A^{n,j,\zeta}_m \right|^2}_{-\gamma_n^{R\to L}} + \underbrace{2\pi \sum_{m=0}^{\infty} \sum_{j=1}^{N_\text{b}} \sum_{\zeta=1}^{N^i_\text{orb}} m \left| A^{n,j,\zeta}_m \right|^2}_{\gamma_n^{L\to R}}, \tag{A.6}$$

where we defined $\gamma_n^{R\to L}$ and $\gamma_n^{L\to R}$ and set our system boundaries to infinity. The two parts of the intercellular Zak phase can now be rewritten in terms of Wannier functions[113]

$$\gamma_n^{R\to L} = -2\pi \sum_{m=-\infty}^{0} \sum_{j=1}^{N_\text{b}} \sum_{\zeta=1}^{N^i_\text{orb}} m \left| A^{n,j,\zeta}_m \right|^2 = 2\pi \sum_{m'=0}^{\infty} \sum_{m=-\infty}^{-1} \sum_{j=1}^{N_\text{b}} \sum_{\zeta=1}^{N^i_\text{orb}} \left| A^{n,j,\zeta}_{m-m'} \right|^2 \tag{A.7a}$$

$$= 2\pi \sum_{m'=0}^{\infty} \int_{-\infty}^{x_b} dx |W_{n,m'}(x)|^2 \tag{A.7b}$$

$$\gamma_n^{L\to R} = 2\pi \sum_{m=0}^{\infty} \sum_{j=1}^{N_\text{b}} \sum_{\zeta=1}^{N^i_\text{orb}} m \left| A^{n,j,\zeta}_m \right|^2 = 2\pi \sum_{m'=-\infty}^{-1} \sum_{m=0}^{\infty} \sum_{j=1}^{N_\text{b}} \sum_{\zeta=1}^{N^i_\text{orb}} \left| A^{n,j,\zeta}_{m-m'} \right|^2 \tag{A.7c}$$

$$= 2\pi \sum_{m'=-\infty}^{-1} \int_{x_b}^{\infty} dx |W_{n,m'}(x)|^2 \tag{A.7d}$$

where x_b is between the sites $m = -1$ and $m = 0$. The relationships in Eqs. (A.7a) and (A.7c) can be understood by a simple counting argument: it is $\sum_{m=1}^{\infty} \sum_{m'=0}^{\infty} a_{m+m'} = \sum_{m=0}^{\infty} m a_m$ for arbitrary a_m. From the expressions (A.7), we realize that $\gamma_n^{R\to L}$ and $\gamma_n^{L\to R}$ have a transparent meaning: $\gamma_n^{R\to L}$ amounts to the weight left of x_b of the Wannier functions that are centered right of x_b; $\gamma_n^{L\to R}$, accordingly, amounts to the weight right of x_b of the Wannier functions that are centered left of x_b; This relationship is visualized in the main text, in Fig. 2.4.

B Material-specific Details for ARPES

B.1 Relaxation Rates

The experimental feasibility of detecting the chiral anomaly with photoemission spectroscopy relies firstly on the correct hierarchy of the different relaxation rates involved. As discussed in the main text, for Weyl semimetals the intra-valley relaxation rate at fixed chirality must be faster than the inter-valley relaxation rate, $\tau_c^{-1} \gg \tau_v^{-1}$. For Dirac semimetals it is also required that the relaxation rate between the two isospins forming each Dirac node must be shorter than the intra-valley relaxation, $\tau_i \gg \tau_c$. The intra-valley relaxation relaxation rate τ_c can be deduced from the experimental values for the carrier mobilities μ_e given in Tab. B.1 using that

$$\mu_e = \frac{\sigma}{en} = \frac{e}{\hbar}\frac{v_F}{k_F}\tau_c, \tag{B.1}$$

where σ denotes the DC conductivity, e is the electric charge, and n is the carrier density. A theoretical estimate of the ratio τ_v/τ_c can be calculated in the first Born approximation following Ref. 181, rendering the values included in Tab. B.1 that justify the assumptions used in the main text.

Experimentally, τ_v can be determined via non-local transport measurements.[181] The corresponding inter-valley scattering length ℓ_v was obtained experimentally in Ref. 341 for Cd_3As_2. This length is connected to the scattering time via $\ell_v = \sqrt{D\,\tau_v}$, where $D = \mu_e\,k_B\,T/e$ is the charge diffusion coefficient at temperature T. Together with mobility measurements, the inter-valley scattering time τ_v at $T = 4\,\mathrm{K}$ can be determined to be $\tau_v \sim 10^{-9}\,\mathrm{s}$, similar to the theoretical estimate for Na_3Bi.

B.2 ARPES in Finite Magnetic Fields

ARPES experiments in magnetic fields are challenging. External magnetic fields affect electron trajectories (especially those with low energies) and compromise angle resolution. Typical ARPES equipment is protected from external magnetic fields using μ-metal shields made from a metallic alloy with high magnetic permeability μ. This material offers the magnetic field lines a path with a low magnetic resistance (or reluctance) that is inversely proportional to μ, preventing them going to the energetically costly exterior. In typical ARPES experiments, for instance the set-up of Ref. 188, high resolution requires the field inside the ARPES lens to be of the order of μT or less. In practice up to $\sim 6\,\mu$T can be handled.[188] These small magnetic fields typically induce a rigid shift of the electron trajectories that can in principle be corrected.[188] As we discuss in the next section, already

---

[*] Ilya Belopolski, private communication.

[†] Measurement of ℓ_v, the inter-valley relaxation time was obtained as described in the text.

	Dirac semimetals				Weyl semimetals	
	Cd_3As_2	Ref.	Na_3Bi	Ref.	TaAs	Ref.
μ_e ($cm^2\,V^{-1}\,s^{-1}$)	10^4 – 10^5	245;342–344	10^3–10^4	232*	$5 \cdot 10^5$	345
τ_c (s) [Eq. (B.1)]	10^{-14}–10^{-13}		10^{-13}		10^{-12}	
τ_v/τ_c [theory]	-		10^4	181	500	181
τ_i/τ_c [theory]	-		10^3	181	τ_i not defined	
τ_v (s) [experiment]	10^{-9}	$341^\dagger$	-		-	
v $(\frac{m}{s})$	$7.6 \cdot 10^5$	346	$3.74 \cdot 10^5$	347	$3.1 - 3.6 \cdot 10^5$ (W1)	173
	$9.3 \cdot 10^5$	246			$2.6 - 4.3 \cdot 10^5$ (W2)	173
	$1.1 \cdot 10^6$	344				
	$1.3 \cdot 10^6$	348				
	$1.5 \cdot 10^6$	343				
v_z $(\frac{m}{s})$	10^5	343	$2.89 \cdot 10^5$	347	$3.4 \cdot 10^5$ (W1)	173
	$3.3 \cdot 10^5$	348			$4.1 \cdot 10^4$ (W2)	173

TABLE B.1: Summary of experimentally measured Fermi velocities v and v_z, mobilities μ_e, and theoretical estimates for the relevant scattering times. For TaAs W1 (W2) nomenclature classifies the eight (sixteen) Weyl points falling on (away) the $k_z = 2\pi/c$ plane. The scattering rate τ_c is estimated for an isotropic Weyl or Dirac cone with $E_F = \hbar v k_F \sim 10\,\text{meV}$.

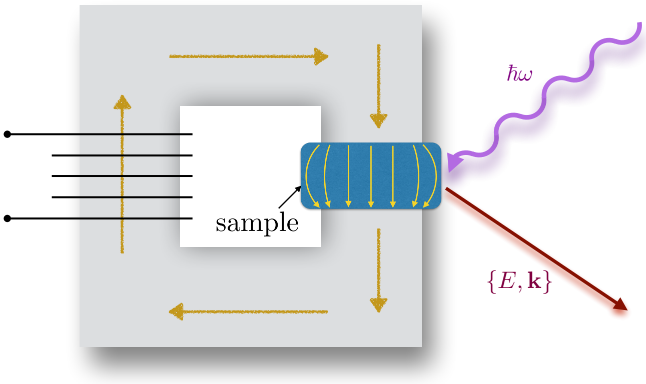

FIGURE B.1: Proposed magnetic circuit for studying the chiral anomaly and ARPES in a magnetic field, based on ARPES experiments on ferromagnetic materials.[189] The sample is included in a magnetic circuit to minimize stray fields effects on photo-electron trajectories. The yellow arrows show the confined magnetization in the ferromagnetic material (e.g. nickel or iron) shaped into the picture-frame geometry. The Weyl or Dirac semimetal sample, a photon of energy $\hbar\omega$ and a photo-electron with energy and momentum $\{E, \mathbf{k}\}$ are depicted schematically as a blue rectangle, a purple curved arrow and a red straight arrow respectively.

these small fields can result in observable values of the chiral potential difference $\delta\mu \sim 4\,\mathrm{meV}$.

To allow for measurements in larger magnetic fields, without altering electron trajectories, it would be advantageous to go one step beyond existing set-ups. We suggest that a possible experimental design can be based on early ideas used to perform ARPES on ferromagnetic materials.[189;349] Stray fields around ferromagnetic materials, like nickel, can severely alter photo-electron trajectories and jeopardize ARPES measurement accuracy. An elegant experimental solution studied these materials in the so-called picture frame geometry or remnant state[189;349] (see Fig. B.1). In this geometry, the magnetic field lines are confined within the material in a magnetic loop, minimizing their effect on electron trajectories that can spoil ARPES measurements. To reach a uniform field within a Weyl or Dirac semimetal sample, while minimizing the external stray fields, one possible solution is to open up a small gap in the magnetic circuit as shown in Fig. B.1. In this set-up, a very uniform field is obtained within the gap, with possible additional fringing fields depicted as curved field lines. The effect of the fringing field is to increase the effective area of the gap, thus reducing its reluctance and increasing the effective magnetic field felt by the sample.[350] The magnitude and spatial extent of the fringing field can therefore be optimized by increasing the gap's length or cross section. In addition, if the sample cross section is designed to be slightly larger than the cross section of the gap, the fringing fields could enter the sample as well, not affecting photo-electron trajectories as shown in Fig. B.1. Finally we note that external current loops were commonly used in experiments to orient the magnetization.[189;349] Therefore it is plausible that these set-ups can admit modifications to incorporate electric fields as well.

B.3 Estimates of the Chiral Chemical Potential Difference

To observe the note-shaped pattern that signals the chiral anomaly it is essential that the induced chemical potential difference $\delta\mu$ is larger than the energy resolution of the experiments, which is of the order of $\sim$ meV[351] if magnetic fields are kept of the order of $\sim \mu$T. To estimate the difference $\delta\mu = \mu_L - \mu_R$, we use the definition of the chiral chemical potentials given by equation (3) of the main text. For the particular case where $\mu_{\mathrm{eq}} = 0$, this difference is given by

$$\delta\mu = 2\left(\frac{3}{2}\,\hbar\, v^2\, v_z\, e^2\, \tau_v\, \mathbf{E}\cdot\mathbf{B}\right)^{1/3}, \tag{B.2}$$

where v and v_z are the anisotropic cone Fermi velocities defined in Section 3.3.2 of the main text and reproduced in Table B.1 as measured by ARPES for $\mathrm{Na_3Bi}$ and $\mathrm{Cd_3As_2}$. From Eq. (B.2) we observe that it is the magnitude of the Fermi velocities, rather than τ_v or $\mathbf{B}$, that can most effectively enhance the chiral anomaly.

To calculate $\delta\mu$ we choose two different magnetic field values $|\mathbf{B}| = 6\,\mu\mathrm{T}$ and $|\mathbf{B}| = 1\,\mathrm{mT}$. The first corresponds to a reasonable magnetic environment that can be achieved in ARPES as discussed in the previous section, while the second is a very conservative estimate of the magnetic fields that can be achieved with the frame geometry also introduced above. All our following estimates are calculated for $|\mathbf{E}| = 1\cdot 10^4\,\mathrm{V\,m^{-1}}$. For the relaxation rates, we choose the experimentally obtained time $\tau_v = 10^{-9}\,\mathrm{s}$ for $\mathrm{Cd_3As_2}$ and the theoretical estimate $\tau_v/\tau_c = 10^4$ for $\mathrm{Na_3Bi}$, both justified in appendix B.1. These are also conservative estimates since τ_v is expected to be even larger for small chemical potentials.[181] Given these values, we find for $\mathrm{Cd_3As_2}$ and field strengths of $|\mathbf{B}| = 1\,\mathrm{mT}$ ($6\,\mu\mathrm{T}$)

a chiral chemical potential difference of $\delta\mu \sim 30\,\mathrm{meV}$ ($5.4\,\mathrm{meV}$). For $\mathrm{Na_3Bi}$, we find that $\delta\mu \sim 15\,\mathrm{meV}$ ($2.7\,\mathrm{meV}$) for $|\mathbf{B}| = 1\,\mathrm{mT}$ ($6\,\mu\mathrm{T}$).

C Weyl Nodes in a Magnetic Field

Weyl nodes in a magnetic field can be analytically treated by writing the Hamiltonian in terms of creation and annihilation operators, as shown in Sec. 4.1. In this Appendix, we summarize the results for a clean system, which enables us to include the effects of disorder perturbatively.

The Weyl Hamiltonian describing two Weyl nodes in a magnetic field is

$$\mathcal{H} = v\left(\hbar\mathbf{k} + e\mathbf{A} + \hbar\mathbf{b}\tau_z\right)\cdot\boldsymbol{\sigma}\tau_z + b_0\tau_z + m\tau_x \tag{C.1}$$

with $\gamma^5 = \tau_z$, cf. Sec. 3.2. The vector potential $\mathbf{A}$ lies in the y–z-plane with

$$\mathbf{B} = B\hat{r}, \qquad \hat{r} = \cos\theta\hat{z} + \sin\theta\hat{y} \tag{C.2}$$

$$\mathbf{A} = Bx\hat{\theta}, \qquad \hat{\theta} = \cos\theta\hat{y} - \sin\theta\hat{z}. \tag{C.3}$$

In a clean and massless system, $m = 0$, the two chiralities are decoupled and their eigenfunctions can be found separately. Momenta in the 2×2 Hamiltonian of chirality χ are shifted $\mathbf{k}\to\mathbf{k}-\chi\mathbf{b}$, such that they measured from the Weyl point. Rotating the Hamiltonian allows us to express it in terms of creation and annihilation operators in a Landau-level basis[238;239]

$$\mathcal{H}_\chi = \chi\frac{\hbar v}{\ell_B}\begin{pmatrix} \ell_B k_r & i\sqrt{2}a_{k_\theta} \\ -i\sqrt{2}a^\dagger_{k_\theta} & -\ell_B k_r \end{pmatrix} \tag{C.4}$$

with the magnetic length $\ell_B = \sqrt{\hbar/(eB)}$, rotated momenta $k_{r,\theta} = \mathbf{k}\cdot(\hat{r},\hat{\theta})$, and annihilation operator

$$a_{k_\theta} = \frac{1}{\sqrt{2}}\left(\frac{x}{\ell_B} + \ell_B\,k_\theta + i\ell_B\,k_x\right). \tag{C.5}$$

The energy spectrum consists of dispersive Landau levels at positive and negative energy. While there is just one zeroth Landau level for each chirality with energy $\varepsilon_0^\chi = \chi\hbar v k_r$, two different solutions exist for higher Landau levels, denoted by different signs of the Landau level index n,

$$\varepsilon^\chi_{|n|>0,\sigma} = \chi\mathrm{sgn}\left(n\right)\hbar\omega_B\sqrt{2|n| + \ell_B^2k_r^2} \tag{C.6}$$

where the cyclotron frequency $\omega_B = v/\ell_B$. The corresponding eigenstates are[26;44]

$$|\Phi^\chi_{|n|>0,\mathbf{k}_\parallel}\rangle = \frac{1}{\sqrt{N}}\left(\frac{-i\sqrt{2|n|}\,||n-1|\rangle}{\ell_B k_r - \mathrm{sgn}\left(n\right)\sigma\sqrt{2|n| + \ell_B^2k_r^2}}, ||n|\rangle\right)^T, \quad |\Phi^\chi_{0,\mathbf{k}_\parallel}\rangle = \left(0, |0\rangle\right)^T \tag{C.7}$$

with the normalization N and the eigenstates of the number operator $a^\dagger_{k_\theta} a_{k_\theta}|n\rangle = n|n\rangle$, $n \in \mathbb{N}$. Its eigenfunctions are harmonic oscillator wave functions centered at $x_c = \ell_B^2 k_\theta$

$$\phi_{n\,\mathbf{k}_\parallel}(x) = \langle x, \mathbf{k}_\parallel | n\rangle = \frac{1}{\sqrt{l_B}}\psi_n\left(\frac{x}{\ell_B} + \ell_B k_\theta\right), \quad \int dx \phi_{n,k_\perp}(x)\phi_{n',k_\perp}(x) = \delta_{nn'}, \quad \text{(C.8)}$$

with the Hermite functions $\psi_n(x) = H_n(x)\exp(-x^2/2)/\sqrt{2^n n!\sqrt{\pi}}$ and the Hermite polynomials $H_n(x)$. The clean Matsubara Green's function is a 2×2 matrix, given by

$$\mathcal{G}_{n\chi}(i\omega_n, \mathbf{k}_\parallel) = \frac{|\Phi^\chi_{n,\mathbf{k}_\parallel}\rangle\langle\Phi^\chi_{n,\mathbf{k}_\parallel}|}{i\omega_m - \varepsilon_{n,\mathbf{k}_\parallel}}. \quad \text{(C.9)}$$

This notation is used in the following sections to compute scattering between different Landau levels, necessary for the computation of the internode scattering time for energies $\varepsilon \neq 0$ in Sec. 4.1. Further, we compute the transversal magnetoresistance of a single Weyl node, closely following an approach first formulated by Abrikosov, but for disorder with a finite correlation length ξ.[26]

C.1 Scattering between Different Landau Levels

To include scattering between Landau levels $m \geq 0$ and $m' \geq 0$ (the case $m, m' < 0$ is analogue) in the self energy calculation, we insert the eigenspinors, Eq. (C.7), into the expression for the disorder correlator in Landau level basis, Eq. (4.13). Using the correlated disorder in momentum space, $K(\mathbf{q}$, the disorder correlator reads

$$\sum_{k'_\theta} \Gamma^{\chi\chi'}_{m\,m'} = \frac{K_0}{2\,\pi\,L}\frac{\hbar^2 v^2}{\xi}\frac{\xi^2}{\ell_B^2+\xi^2}\frac{e^{-\frac{1}{2}\xi^2\delta k_r^2}}{N_m\,N_{m'}}\left[I^{m,m'}_{m,m'} + 2\,\zeta\, I^{m-1,m'-1}_{m,m'} + \zeta^2\, I^{m-1,m'-1}_{m-1,m'-1}\right], \quad \text{(C.10)}$$

with the integrals

$$\begin{aligned} I^{n'm'}_{nm} =& \frac{\ell_B^2+\xi^2}{2\pi}\int dk'_\theta dq_x e^{-\frac{1}{2}\xi^2(\delta^2+q_x^2)}\int dx e^{iq_x x}\phi_{n\,k_\theta}(x)\phi_{m\,k'_\theta}(x) \\ & \int dx' e^{-iq_x x'}\phi_{m'\,k'_\theta}(x')\phi_{n'\,k_\theta}(x'), \end{aligned} \quad \text{(C.11)}$$

that are independent of k'_r. The momenta δk_θ, δk_r are the two components of the momentum difference of the states involved in scattering, $\delta\mathbf{k}_\parallel = \mathbf{k}_\parallel - \mathbf{k}'_\parallel - (\chi - \chi')\mathbf{b}/2$. Note that $\mathbf{k}_\parallel$ is measured from the Weyl nodes, thus, the additional difference of the node separation $\mathbf{b}$ for internode scattering. In Eq. (C.10), we further use the definition

$$\zeta \equiv \frac{\sqrt{2m}}{\ell_B k_r - \chi\sqrt{2m+\ell_B^2 k_r^2}}\,\frac{\sqrt{2m'}}{\ell_B k'_r - \chi'\sqrt{2m'+\ell_B^2 {k'_r}^2}}. \quad \text{(C.12)}$$

Substituting

$$\frac{x}{\ell_B} + \ell_B\frac{k_\theta+k'_\theta}{2} \to x, \quad \frac{x'}{\ell_B} + \ell_B\frac{k_\theta+k'_\theta}{2} \to x', \quad \frac{\ell_B}{\sqrt{2}}\left(k'_\theta - k_\theta\right) \to q_\theta, \quad \frac{\ell_B}{\sqrt{2}}q_x \to q_x \quad \text{(C.13)}$$

and inserting the eigenfunctions $\phi_{m\,k_\theta}(x)$, Eq. (C.8), gives an expression for $I_{nm}^{n'm'}$ in terms of a momentum-integral over the product of two real-space integrals,

$$I_{nm}^{n'm'} = \frac{\ell_B^2+\xi^2}{\pi\ell_B^2}\int dq_x dq_\theta e^{-\frac{\xi^2}{\ell_B^2}q_x^2-\frac{1}{2}\xi^2\delta k_\theta^2}\mathcal{I}^+_{nm}\mathcal{I}^-_{n'm'} \tag{C.14}$$

with the two independent integrals over real space[352]

$$\begin{aligned}\mathcal{I}^{\pm}_{nm} &= \int dx\,\psi_n\left(x-\tfrac{q_\theta}{\sqrt{2}}\right)\psi_m\left(x+\tfrac{q_\theta}{\sqrt{2}},\right)e^{\pm i\sqrt{2}\,q_x x} \\ &= \sqrt{\frac{\min(n,m)!}{\max(n,m)!}}\,e^{-\frac{1}{2}\left(q_x^2+q_\theta^2\right)}\,L^{(|n-m|)}_{\min(n,m)}\left(q_x^2+q_\theta^2\right)\left(\pm i\,q_x-\operatorname{sgn}\left(m-n\right)\,q_\theta\right)^{|n-m|},\end{aligned} \tag{C.15}$$

where $L_n^{(\alpha)}$ are the Associated Laguerre polynomials. To solve the momentum integration in Eq. (C.14), we introduce polar coordinates $q_x = q\sin\varphi$, $q_\theta = q\cos\varphi$. For all cases of interest that appear in Eq. (C.10), the product $\mathcal{I}^+_{nm}\mathcal{I}^-_{n'm'}$ depends only on the radial coordinate q. As mentioned above, the momentum difference between the states involved is $\delta k_\theta = \sqrt{2}q_\theta/\ell_B$ for intranode and $\delta k_\theta = \sqrt{2}(q_\theta \pm \tilde{b}_\theta)/\ell_B$ for internode scattering, with $\tilde{b}_\theta = \ell_B b_\theta/\sqrt{2}$. Focusing on internode scattering, the integral over φ in Eq. (C.14) gives

$$I_{nm}^{n'm'} = 2(1+\gamma)\int dq\,q\,e^{-\gamma(q^2+\tilde{b}_\theta^2)}I_0\left(2\gamma\tilde{b}_\theta\,q\right)\mathcal{I}^+_{nm}\mathcal{I}^-_{n'm'} \tag{C.16}$$

with the modified Bessel function of the first kind $I_0(x)$ and $\gamma = \xi^2/\ell_B^2$. We substitute $s = q^2$ and use the abbreviations $\alpha = |n-m| = |n'-m'|$ (with the restriction coming from Eq. (C.14)), $p = \min(n,m)$ and $l = \min(n',m')$

$$I_{nm}^{n'm'} = 2(1+\gamma)\sqrt{\frac{p!\,\ell!}{(p+\alpha)!(\ell+\alpha)!}}e^{-\gamma\tilde{b}_\theta^2}\int ds\,I_0(2\gamma\tilde{b}_\theta\sqrt{s})e^{-(1+\gamma)s}s^\alpha L_p^{(\alpha)}(s)L_l^{(\alpha)}(s). \tag{C.17}$$

To solve the integral over s, we rewrite the product of Laguerre polynomials as a double sum

$$L_p^{(\alpha)}(s)\,L_\ell^{(\alpha)}(s) = \sum_{i=0}^{p}\sum_{j=0}^{\ell}(-1)^{i+j}\binom{\ell+\alpha}{\ell-i}\binom{p+\alpha}{p-i}\frac{s^{i+j}}{i!\,j!} \tag{C.18}$$

such that

$$\begin{aligned}I_{nm}^{n'm'} =& \frac{(1+\gamma)\,\sqrt{p!\,\ell!}\,e^{-\gamma\,\tilde{b}_\theta^2}}{\sqrt{(p+\alpha)!\,(\ell+\alpha)!}}\sum_{i=0}^{p}\sum_{j=0}^{\ell}\frac{(-1)^{i+j}}{i!\,j!}\binom{\ell+\alpha}{\ell-i}\binom{p+\alpha}{p-i} \\ &\times\int ds\,I_0(2\,\gamma\,\tilde{b}_\theta\sqrt{s})\,s^{\alpha+i+j}\,e^{-(1+\gamma)s}.\end{aligned} \tag{C.19}$$

The integral over s gives an explicit expression expressed in terms of Laguerre polynomials,

$$\int ds\,s^{\alpha+i+j}\,e^{-(1+\gamma)s}I_0(2\gamma\tilde{b}_\theta\sqrt{s}) = \frac{(\alpha+i+j)!}{(1+\gamma)^{1+\alpha+i+j}}e^{\frac{\gamma^2\,\tilde{b}_\theta^2}{1+\gamma}}\,L_{\alpha+i+j}\left(-\tfrac{\gamma^2\,\tilde{b}_\theta^2}{1+\gamma}\right) \tag{C.20}$$

Changing back $\tilde{b}_\theta = \ell_B\, b_\theta/\sqrt{2}$ finally gives for internode scattering

$$I_{nm}^{n'm'} = e^{-\frac{1}{2}\frac{\xi^2\ell_B^2}{\xi^2+\ell_B^2}\,b_\theta^2}\sqrt{\frac{p!\,(\ell+\alpha)!}{\ell!\,(p+\alpha)!}}\sum_{i=0}^{p}\sum_{j=0}^{\ell}\frac{(-1)^{i+j}}{(1+\gamma)^{\alpha+i+j}}\binom{\ell}{j}\binom{\alpha+i+j}{\alpha+j}\binom{p+\alpha}{p-i}$$
$$\times L_{\alpha+i+j}\left(-\tfrac{1}{2}\tfrac{\xi^4}{\xi^2+\ell_B^2}\,b_\theta^2\right). \tag{C.21}$$

One has to be careful when numerically evaluating $I_{nm}^{n'm'}$ since the terms to be summed are exponentially large with alternating signs. For internode scattering at $b_\theta = 0$, the integral (C.14) gives the more simple closed form[353]

$$I_{nm}^{n'm'} = \sqrt{\frac{(p+\alpha)!\,\ell!}{(\ell+\alpha)!\,p!}}\binom{p+\ell+\alpha}{\ell}\frac{\gamma^{\ell+p}}{(1+\gamma)^{\ell+p+\alpha}}\,{}_2F_1\left(-p,-\ell;-p-\ell-\alpha;\tfrac{\gamma^2-1}{\gamma^2}\right). \tag{C.22}$$

with the hypergeometric function ${}_2F_1$.

We are ultimately interested in the self-energy correction

$$\Sigma^m_{\chi\chi'}(i\,\omega_n,\mathbf{k}_\parallel) = \sum_{m',k'_r}\mathcal{G}_{m'\chi'}(i\,\omega_n,k'_r)\sum_{k'_\theta}\Gamma^{\chi\chi'}_{mm'}, \tag{C.23}$$

which requires another integration over the momentum component k'_r. This integral can be easily solved since the imaginary part of the clean single-particle Green's function, $\mathrm{Im}G^R_{m\chi}$, is a delta function. The analytical results sketched here are used to compute the angle dependence of the internode scattering time shown in Sec. 4.1.

C.2 Analytical Born-Kubo Calculation of Transversal Magnetoconductivity

Based on Abrikosov's seminal work, we calculate the transversal magnetoconductivity of a single Weyl node assuming correlated disorder, Eq. (4.3). Since we want to give a comprehensive derivation, the calculation of the transversal magnetoconductivity σ_{xx} is presented in two sections. First, we determine the relevant disorder-induced self-energies in the Born approximation, following by an application of the Kubo formula is applied to find σ_{xx}.

The only Green functions necessary to calculate the conductivity at zero energy carry indices $m = 0$ and $m = \pm 1$. Dropping the index for the chirality that is fixed in this section to $\chi = +1$, the Green's functions read

$$\mathcal{G}_0\left(i\omega_n,\mathbf{k}_\perp\right) = \frac{1}{i\omega_n - \hbar v k_z}\begin{pmatrix}|0\rangle\langle 0| & 0\\ 0 & 0\end{pmatrix}, \tag{C.24}$$

$$\mathcal{G}_{\pm 1}\left(i\omega_n\mathbf{k}_\perp\right) = \frac{1}{i\omega_n - \varepsilon_{\pm 1}}\begin{pmatrix}\left(1+\frac{\hbar v k_z}{\varepsilon_{\pm 1}}\right)|1\rangle\langle 1| & \pm i\sqrt{1-\frac{(\hbar v k_z)^2}{\varepsilon_{\pm 1}^2}}|1\rangle\langle 0|\\ \mp i\sqrt{1-\frac{(\hbar v k_z)^2}{\varepsilon_{\pm 1}^2}}|0\rangle\langle 1| & \left(1-\frac{\hbar v k_z}{\varepsilon_{\pm 1}}\right)|0\rangle\langle 0|\end{pmatrix} \tag{C.25}$$

with the momentum $\mathbf{k}_\perp = (k_y, k_z)$ perpendicular to the transport direction, x.

C.2.1 Disorder Scattering in Born Approximation

In the Kubo calculation of the transverse magnetoconductivity σ_{xx}, which follows below, we need the imaginary part of the disorder-averaged retarded self-energy correction for $m = \pm 1$ and $k_z = 0$

$$\Gamma_{\pm}(k_y) \equiv -\mathrm{Im}\Sigma^{R}_{\downarrow\downarrow}(m = \pm 1, \omega = 0, k_y, k_z = 0). \tag{C.26}$$

The Born-approximation diagram is a loop including a free propagator, which we can restrict to the $(m = 0)$-Green function due to its small energy denominator. After averaging over disorder, the diagram reads

$$\Gamma_{\pm}(\mathbf{k}_\perp) = -\mathrm{Im} \int_{\mathbf{k}'} \langle 0, \mathbf{k}_\perp | \mathbf{k}' \rangle \langle \mathbf{k}' | \mathcal{G}^{R}_{0,\uparrow\uparrow}(\mathbf{k}'_\perp) | \mathbf{k}' \rangle \langle \mathbf{k}' | 0, \mathbf{k}_\perp \rangle \left\langle\!\!\left\langle V(\mathbf{k} - \mathbf{k}') V(\mathbf{k}' - \mathbf{k}) \right\rangle\!\!\right\rangle. \tag{C.27}$$

The overlap between the Landau level wave function and the momentum eigenstate can be evaluated by inserting a real-space basis giving

$$\begin{aligned} \Gamma_{\pm}(\mathbf{k}_\perp) = &- \mathrm{Im} \int_{\mathbf{k}'} \frac{\int dx e^{ik'_x x} \phi_0(x, \mathbf{k}_\perp) \phi_0(x, \mathbf{k}'_\perp) \int dx' e^{-ik'_x x'} \phi_0(x', \mathbf{k}'_\perp) \phi_0(x', \mathbf{k}_\perp)}{i\eta - \hbar v k'_z} \\ &\times \left\langle\!\!\left\langle V(\mathbf{k} - \mathbf{k}') V(\mathbf{k}' - \mathbf{k}) \right\rangle\!\!\right\rangle. \end{aligned} \tag{C.28}$$

Inserting the disorder correlator in momentum space, i.e.,

$$\left\langle\!\!\left\langle V(\mathbf{q}) V(-\mathbf{q}') \right\rangle\!\!\right\rangle = K_0 \frac{(\hbar v)^2}{\xi^2} \frac{\xi^3}{L^3} e^{-\frac{1}{2}\xi^2 q^2}, \tag{C.29}$$

allows the evaluation of the integrals over real space and momentum giving[42]

$$\begin{aligned} \Gamma_{\pm}(\mathbf{k}_\perp) &= -K_0 (\hbar v)^2 \xi \, \mathrm{Im} \int_{\mathbf{k}'} \frac{e^{-\frac{1}{2}(\ell_B^2 + \xi^2)((k_x - k'_x)^2 + (k_y - k'_y)^2)}}{i\eta - \hbar v k'_z} e^{-\frac{1}{2}\xi^2 {k'_z}^2} && \text{(C.30)} \\ &= \frac{K_0}{4\pi} \frac{\hbar v \xi}{\xi^2 + l_B^2} e^{-\frac{1}{2}\ell_B^2 k_z^2}. && \text{(C.31)} \end{aligned}$$

At $k_z = 0$, we finally obtain a simple expression independent of k_y and the sign of $m = \pm 1$,

$$\Gamma = \frac{K_0}{4\pi} \frac{\hbar v \xi}{\ell_B^2 + \xi^2}, \tag{C.32}$$

the same result we obtained when just considering zeroth Landau levels, Eq. (4.15).

C.2.2 Transversal Magnetoconductivity from Kubo Formula

The transversal magnetoconductivity σ_{xx} is obtained via the Kubo formula

$$\sigma_{xx} = \lim_{\Omega \to 0} \frac{1}{\Omega} \mathrm{Im}\Pi^{R}_{xx}(\Omega) \tag{C.33}$$

for frequencies Ω with the imaginary-time current-current correlation function $\Pi_{xx}(\tau - \tau') = -\mathrm{Tr}\left[\langle T_\tau j_x(\tau) j_x(\tau') \rangle\right]$ where T_τ denotes imaginary-time ordering and j_x is the current operator $j_x = ev\, \psi^\dagger \sigma_x \psi$. By using standards methods,[333] we find

$$\Pi_{xx}(i\Omega_\ell) = \frac{e^2 v^2}{\beta L^2} \sum_{\omega_n} \sum_{\mathbf{k}_\perp} \sum_{m_{1,2} = -\infty}^{\infty} \mathrm{Tr}_{\phi,\sigma} \left[\sigma_x \bar{\mathcal{G}}_{m_1}(i\omega_n + i\Omega_\ell, \mathbf{k}_\perp) \sigma_x \bar{\mathcal{G}}_{m_2}(i\omega_n, \mathbf{k}_\perp) \right], \tag{C.34}$$

where disorder-dressed Green functions are denoted by $\bar{\mathcal{G}}$ and the trace is over spin degrees of freedom, σ, and the Harmonic-oscillator basis, ϕ. In Eq. (C.34), we have neglected the small vertex correction, which can straightforwardly be calculated to be $\Gamma^2/(\hbar v \ell_B^{-1})^2$ in the lowest order. Using rotational invariance in the x-y plane, we write $\Pi_{xx}^R = (\Pi_{xx}^R + \Pi_{yy}^R)/2$ to simplify the trace to

$$\frac{1}{2}\mathrm{Tr}_\sigma\left[\sigma_x \bar{\mathcal{G}}^{(i)}\sigma_x \bar{\mathcal{G}}^{(ii)}\sigma_x + \sigma_x \bar{\mathcal{G}}^{(i)}\sigma_y \bar{\mathcal{G}}^{(ii)}\sigma_y\right] = \bar{\mathcal{G}}^{(i)}_{\uparrow\uparrow}\bar{\mathcal{G}}^{(ii)}_{\downarrow\downarrow} + \bar{\mathcal{G}}^{(i)}_{\downarrow\downarrow}\bar{\mathcal{G}}^{(ii)}_{\uparrow\uparrow}. \tag{C.35}$$

Next, we perform the Matsubara sum using the standard procedures and expand for small Ω. We find

$$\begin{aligned}\mathrm{Im}\Pi_{xx}^R(\Omega) = {}& e^2 v^2 \hbar\Omega \frac{\beta}{2}\int \frac{d\omega}{2\pi}\frac{1}{L^3}\sum_{\mathbf{k}_\perp}\sum_l \sum_{m_{1,2}=-\infty}^{\infty}\frac{1}{\cosh^2\frac{\beta\omega}{2}} \\ & \times \langle l, \mathbf{k}_\perp | \mathrm{Im}\bar{\mathcal{G}}^R_{m_1,\downarrow\downarrow}(\omega, \mathbf{k}_\perp)\,\mathrm{Im}\bar{\mathcal{G}}^R_{m_2,\uparrow\uparrow}(\omega, \mathbf{k}_\perp) + (\uparrow\uparrow)\leftrightarrow(\downarrow\downarrow)|l, \mathbf{k}_\perp\rangle,\end{aligned} \tag{C.36}$$

and let $T \to 0$. This yields

$$\begin{aligned}\sigma_{xx} = {}& \frac{\hbar e^2 v^2}{\pi}\frac{1}{L^3}\sum_{\mathbf{k}_\perp}\sum_l \sum_{m_{1,2}=-\infty}^{\infty}\langle l, \mathbf{k}_\perp | \mathrm{Im}\bar{\mathcal{G}}^R_{m_1,\downarrow\downarrow}(k_y, k_z, 0)\,\mathrm{Im}\bar{\mathcal{G}}^R_{m_2,\uparrow\uparrow}(k_y, k_z, 0) \\ & + (\uparrow\uparrow)\leftrightarrow(\downarrow\downarrow)|l, \mathbf{k}_\perp\rangle.\end{aligned} \tag{C.37}$$

We approximate the sums over m_1 and m_2 with the dominant terms, i.e., using the the minimal $|m_i|$. This is justified in the limit of magnetic energy large compared to level width $\hbar v \ell_B^{-1} \gg \Gamma$ as discussed in the main text. Due to the 2×2 matrix structure of $\bar{\mathcal{G}}^R_{m=0}$ (cf. Eq. (C.25)), the choice $m=0$ is only applicable for the $\uparrow\uparrow$-component. Then by orthogonality of the $|\phi_l(k_y)\rangle$, we only have to consider $m=\pm 1$ for the remaining $\downarrow\downarrow$-Green function component:

$$\begin{aligned}\sigma_{xx} = {}& \frac{2\hbar e^2 v^2}{\pi}\frac{1}{L^3}\sum_{\mathbf{k}_\perp}\left(\mathrm{Im}\frac{\frac{1}{2}\left(1 - \frac{\ell_B k_z}{\sqrt{k_z^2\ell_B^2+2}}\right)}{-\frac{\hbar v}{\ell_B}\sqrt{k_z^2\ell_B^2+2} + i\Gamma} + \mathrm{Im}\frac{\frac{1}{2}\left(1 + \frac{\ell_B k_z}{\sqrt{k_z^2\ell_B^2+2}}\right)}{+\frac{\hbar v}{\ell_B}\sqrt{k_z^2\ell_B^2+2} + i\Gamma}\right) \\ & \times \mathrm{Im}\frac{1}{-\hbar v k_z - \Sigma^R_{\uparrow\uparrow}(0, k_y, k_z, 0)}.\end{aligned} \tag{C.38}$$

In the weak disorder limit discussed above, the last factor can be treated as a δ-function, which yields

$$\sigma_{xx} = \frac{e^2 v}{2\pi}\frac{1}{L^2}\sum_{k_y}\frac{2\Gamma}{2\hbar^2 v^2/\ell_B^2 + \Gamma^2}. \tag{C.39}$$

Along with $\sum_{k_y} = g = L^2/(2\pi\ell_B^2)$ and the value of Γ determined from the Born approximation in Eq. (C.32), the transversal magnetoconductivity is

$$\sigma_{xx} = \frac{e^2}{h\xi}\left(\frac{K_0}{8\pi^2}\times\frac{1}{1+\ell_B^2/\xi^2}\right), \tag{C.40}$$

as quoted in the main text.

D Transfer Matrix Method

Generally, the eigenstates ψ of a Hamiltonian $\mathcal{H}$ need to satisfy

$$(\mathcal{H}-\varepsilon)\psi = 0. \tag{D.1}$$

For a continuum Hamiltonian that has at least one component that is linear in momentum, Eq. (D.1) can be neatly rewritten as a simple real-space differential equation. For example, inserting the Weyl Hamiltonian (2.33) and switching from the k_z-component to real-space gives

$$\partial_z\psi = \left(i\frac{\varepsilon}{\hbar v}\sigma_z + k_x\sigma_y - k_y\sigma_x\right)\psi \equiv M(z)\psi \tag{D.2}$$

with the two-component wave function ψ and matrix $M(z)$ introduced for the sake of a more general notation. Eq. (D.2) has a straightforward analytical solution,

$$\psi(z) = T(z,z')\psi(z'),\ T(z,z') = P_{z''}\exp\left[\int_z^{z'} dz'' M(z'')\right] \tag{D.3}$$

with the path-ordered matrix exponential $P_{z''}\exp(\cdots)$. The matrix $T(z,z')$ is a so-called transfer matrix. It relates the wave function at any position z to itself at position z'. This property can be used to investigate transport: consider a Weyl semimetal that is finite in z-direction with the length L. At both ends at $z=0$ and $z=L$, it is connected to two metallic leads that are modeled by the same Weyl Hamiltonian, but at a large chemical potential to mimic the metallic behavior. Then, the eigenstates around the Fermi surface with small transversal momenta $\mathbf{k}_\perp = (k_x, k_y)$ need to have a large longitudinal momentum $|k_z| \gg k_\perp$ to satisfy $\hbar v\sqrt{k_z^2+k_\perp^2} = \mu \gg 0$. Thus, the eigenstates in the leads are the eigenstates of $\hat{v}_z = v\sigma_z$, $\psi = (1,0)$, right-moving, and $\psi = (0,1)$, left-moving. In this situation, the transfer matrix connects the propagating modes of the two leads

$$\begin{pmatrix}\psi_{\text{out}}(L)\\ \psi_{\text{in}}(L)\end{pmatrix} = T(L,0)\begin{pmatrix}\psi_{\text{in}}(0)\\ \psi_{\text{out}}(0)\end{pmatrix}, \tag{D.4}$$

similar to the scattering matrix S that connects incoming and outgoing modes

$$\begin{pmatrix}\psi_{\text{out}}(0)\\ \psi_{\text{out}}(L)\end{pmatrix} = \underbrace{\begin{pmatrix} r & t'\\ t & r'\end{pmatrix}}_{S}\begin{pmatrix}\psi_{\text{in}}(0)\\ \psi_{\text{in}}(L)\end{pmatrix}, \tag{D.5}$$

with the reflection and transmission amplitudes r, r' and t, t', cf. Fig. D.1. Combining Eqs. (D.4) and (D.5) gives the transfer matrix in term of the reflection and transmission amplitudes[354]

$$T(L,0) = \begin{pmatrix} t^{\dagger -1} & r't'^{-1}\\ -t'^{-1}r & t'^{-1}\end{pmatrix}. \tag{D.6}$$

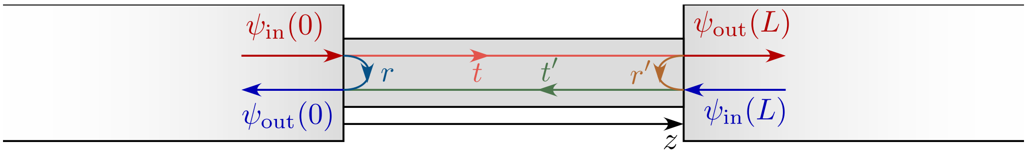

FIGURE D.1: Finite sample of length L in z-direction that is connected to two leads. While the transfer matrix, Eq. D.4, connects the two leads at $z = 0$ and $z = L$, the scattering matrix, Eq. D.5, connects the outgoing modes to the incoming modes via the transmission and reflection amplitudes t, t' and r, r'.

The Landauer formula, Eq (4.18), connect the transmission amplitude to the conductance via $G = \mathrm{Tr}\left[t^\dagger t\right] e^2/h$.

In the case of the clean Weyl Hamiltonian, the matrix $M(z)$ does not depend on the position z, thus, the integration in the exponential can be directly performed. At $\varepsilon = 0$, the transfer matrix has the simple form

$$T(L, 0) = \begin{pmatrix} \cosh(Lk_\perp) & -ie^{-i\phi}\sinh(Lk_\perp) \\ ie^{i\phi}\sinh(Lk_\perp) & \cosh(Lk_\perp) \end{pmatrix} \tag{D.7}$$

with polar coordinates $k_x = k_\perp \cos\phi$, $k_y = k_\perp \sin\phi$. For a sample with a width W much bigger than its length, $W \gg L$, the conductivity is then[27;269]

$$G = \frac{e^2}{h}\mathrm{Tr}\left[\frac{1}{\cosh^2(Lk_\perp)}\right] = \frac{e^2}{h}\frac{W^2}{2\pi L^2}\int dq \frac{q}{\cosh^2(q)} = \frac{e^2}{h}\frac{W^2}{L^2}\frac{\ln 2}{2\pi}, \tag{D.8}$$

i.e., the conductance decreases faster with L than in a diffusive system, where it scales $G \propto 1/L$.

The method we just discussed can be also used in the presence of disorder. The disorder potential $V(\mathbf{r})$ needs to be Fourier transformed to a mixed real- and momentum space representation $V(z, \mathbf{k}_\perp, \mathbf{k}'_\perp)$. Disorder scattering is diagonal in real space, but not in momentum space: it scatters from a transversal momentum $\mathbf{k}'_\perp \to \mathbf{k}_\perp$. This results in a position-dependent matrix $M(z)$, Eq. (D.2), so that the position-ordering $P_{z''}$, Eq. (D.3) becomes relevant. In a numerical calculation, the integral over $M(z)$ is split into N slices of width $\Delta z = L/N$,

$$\int_0^L dz M(z) = \sum_{i=0}^{N-1} \underbrace{\int_{z_i}^{z_{i+1}} dz M(z)}_{=M_i \Delta z}, \; z_i = i\frac{L}{N} \tag{D.9}$$

such that the transfer matrix reads

$$T(L, 0) = \lim_{N\to\infty} T(z_N, z_{N-1})T(z_{N-1}, z_{N-2})) \cdots T(z_2, z_1)T(z_1, z_0) \tag{D.10}$$

$$= \lim_{N\to\infty} \exp(M_{N-1}\Delta z)\exp(M_{N-2}\Delta z)\cdots\exp(M_1\Delta z)\exp(M_0\Delta z). \tag{D.11}$$

It turns out that the direct product of the transfer matrices $T(z_{i+1}, z_i)$ is numerically unstable since all matrices contain exponentially large and exponentially small eigenvalues.[46] Instead, we switch to a scattering matrix representation, Eq. (D.6). The product of scattering matrices is much more stable such that convergence with increasing N can be achieved straightforwardly.

The transfer matrix method has been successfully employed for disordered graphene,[46] and Weyl semimetals.[27] In this work, we investigate numerically the influence of longitudinal and transversal magnetic fields on transport in Weyl semimetals, Secs. 4.1 and 4.2. The modifications that are necessary to employ this method in presence of a magnetic field are discussed in the following.

D.1 Longitudinal Magnetic Field

For a longitudinal magnetic field, it is beneficial to look for solutions of the Weyl equation $\mathcal{H}\psi = E\psi$ in the Landau level basis. In a basis of left- and right-moving channels, such that $\partial\mathcal{H}/\partial p_z = v\sigma_z$, the transfer matrix takes the form

$$\begin{aligned} T(z,z') =& P_{z''} \exp\left\{ \int_z^{z'} \frac{dz''}{\xi} i \left(\frac{E - V_c - V_v\, \sigma_x\tau_x}{\hbar\omega_\xi} \right) \sigma_z + \xi \mathbf{b} \cdot (-\sigma_y, \sigma_x\tau_z, i\tau_z) \right. \\ & \left. - \frac{\xi}{\ell_B} \left(a \frac{\sigma_x + i\sigma_y\tau_z}{\sqrt{2}} + a^\dagger \frac{\sigma_x - i\sigma_y\tau_z}{\sqrt{2}} \right) \right\} . \end{aligned} \tag{D.12}$$

Two different disorder potentials are included here: V_c scatters within the same chirality and is responsible for intranode relaxation, while V_v scatters between different chiralities and is responsible for internode relaxation. The intranode potential V_c does not influence the conductance, but the effect of V_v is investigated in the main text of this paper. The disorder potential needs to be transformed to the Landau level basis,

$$\begin{aligned} V_c^{nm} &= \int dx \phi_{n\,\mathbf{k}_\parallel + \frac{\mathbf{q}_\parallel}{2}}(x) \phi_{m\,\mathbf{k}_\parallel - \frac{\mathbf{q}_\parallel}{2}}(x) V_c(x, \mathbf{q}_\parallel) \\ V_{v\pm}^{nm} &= \int dx \phi_{n\,\mathbf{k}_\parallel + \frac{\mathbf{q}_\parallel}{2}}(x) \phi_{m\,\mathbf{k}_\parallel - \frac{\mathbf{q}_\parallel}{2}}(x) V_v(x, \mathbf{q}_\parallel \pm \mathbf{b}) \end{aligned} \tag{D.13}$$

with the wave function $\phi_{n\,\mathbf{k}_\parallel}(x)$, Eq. (4.10). From Eq. (D.12), the conductance is obtained via the Landauer formula.

Note that there are no symmetry restrictions on the disorder potential, since no symmetries are needed to have Weyl nodes. Thus, more general matrix structures of the disorder potential are possible than the ones that are investigated in this work.

D.2 Transversal Magnetic Field

A magnetic field along z, orthogonal to the transport direction x is generated by the vector potential

$$A(\mathbf{r}) = Bx\hat{y}. \tag{D.14}$$

No basis transformation is necessary to include this vector potential. It is convenient to chose to gauge given above, when the real-space coordinate in the sample ranges from $x \in [-L/2, L/2]$. In contrast to a clean Weyl semimetal without the transversal field, we cannot obtain the transfer matrix analytically when $B \neq 0$. Numerically, we find that the peak of the transmission $|t(k_y, k_z)|^2$ becomes smaller in k_z-direction for $B \neq 0$, cf. Fig. D.2 and Fig. 4.6 (d) in the main text.

In presence of disorder, the transmission stays rotationally symmetric when $B = 0$, as we show in Fig. D.3 (a). When a transversal magnetic field along $\hat{z}$ is added, the maximal transmission amplitude shifts in momentum space, cf. Fig. D.3 (b) which shows the

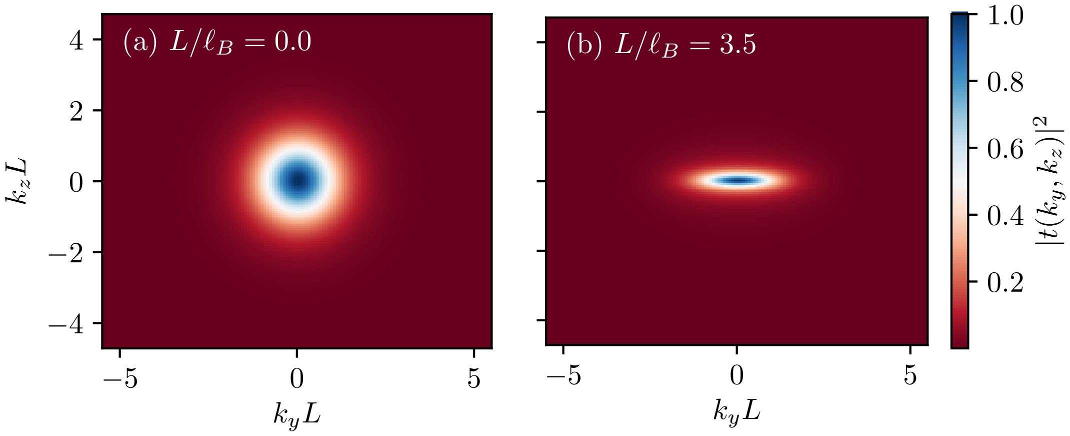

FIGURE D.2: (a) Transmission amplitude $T = |t(k_y,k_z)|^2$ for a clean Weyl node without magnetic field ($1/\ell_B = 0$). The transmission amplitude is rotationally symmetric and can be obtained analytically $|t|^2 = 1/\cosh^2(Lk_\perp)$ with the transversal momentum $k_\perp$. (b) Once a magnetic field in z-direction is introduced, the shape of the transmission amplitude changes, and the width of the peak in k_z direction becomes smaller. At $k_z = 0$, an analytical solution is still possible, giving $|t(k_y,k_z = 0)|^2 = 1/\cosh^2(Lk_y)$ as before. The position of the peak depends on the gauge choice. Disorder broadens this peak again and shifts the position in momentum space.

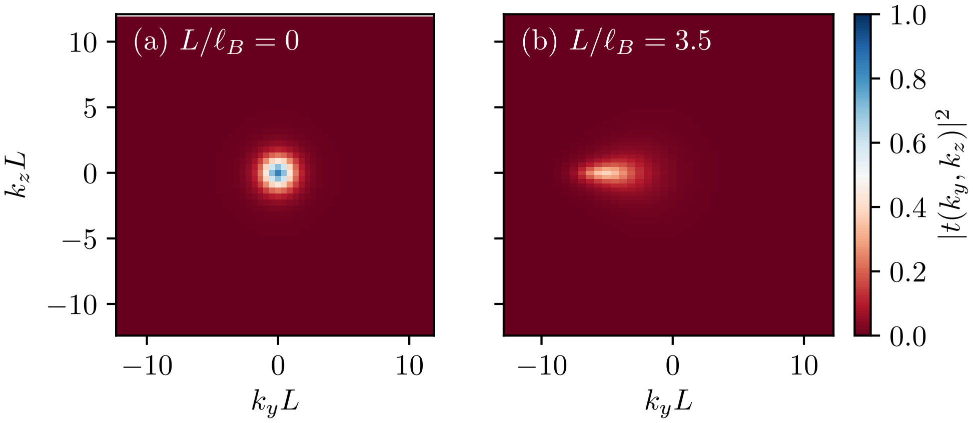

FIGURE D.3: (a) Transmission amplitude $T = |t(k_y,k_z)|^2$ for a disordered Weyl node without magnetic field ($1/\ell_B = 0$). (b) For disordered Weyl nodes in presence of a magnetic field ($L/\ell_B = 3.5$) in the transversal z-direction, not only the shape of the transmission amplitude changes (cf. Fig. D.2 (b)), but also the maximal amplitude is shifted in momentum space. For both panels, we use disorder of strength $K_0 = 3$ and correlation length $L/\xi = 7$, cf. Eq. (4.3).

transmission for same gauge choice as Fig. D.2 (b). To counteract this shift, we perform a gauge transformation of the scattering matrix. This gauge transformation shifts the maximal transmission amplitude $|t(k_y, k_z)|^2$ back to the center of the considered momentum space region. The gauge transformation is described in Sec. 4.2.3.

Bibliography

[1] L. D. Landau, Zh. Eksp. Teor. Fiz. **7**, 19 (1937).

[2] J. M. Kosterlitz and D. J. Thouless, J. Phys. C Solid State Phys. **5**, L124 (1972).

[3] D. J. Thouless and J. M. Kosterlitz, J. Phys. C Solid State Phys. **6**, 1181 (1973).

[4] K. V. Klitzing, G. Dorda, and M. Pepper, Phys. Rev. Lett. **45**, 494 (1980).

[5] B. Jeckelmann and B. Jeanneret, Rep. Prog. Phys. **64**, 1603 (2001).

[6] D. J. Thouless, M. Kohmoto, M. P. Nightingale, and M. Den Nijs, Phys. Rev. Lett. **49**, 405 (1982).

[7] F. D. M. Haldane, Phys. Rev. Lett. **61**, 2015 (1988).

[8] M. Nakahara, *Geometry, Topology and Physics, Second Edition*, Graduate student series in physics (Taylor & Francis, 2003).

[9] K. S. Novoselov, A. K. Geim, S. V. Morozov, D. Jiang, Y. Zhang, S. V. Dubonos, I. V. Grigorieva, and A. A. Firsov, Science **306**, 666 (2004).

[10] C. L. Kane and E. J. Mele, Phys. Rev. Lett. **95**, 226801 (2005).

[11] C. L. Kane and E. J. Mele, Phys. Rev. Lett. **95**, 146802 (2005).

[12] A. H. Castro Neto, F. Guinea, N. M. R. Peres, K. S. Novoselov, and A. K. Geim, Rev. Mod. Phys. **81**, 109 (2009).

[13] B. A. Bernevig, T. L. Hughes, and S.-C. Zhang, Science **314**, 1757 (2006).

[14] M. König, S. Wiedmann, C. Brüne, A. Roth, H. Buhmann, L. W. Molenkamp, X.-L. Qi, and S.-C. Zhang, Science **318**, 766 (2007).

[15] L. Fu, C. L. Kane, and E. J. Mele, Phys. Rev. Lett. **98**, 106803 (2007).

[16] J. E. Moore and L. Balents, Phys. Rev. B **75**, 121306 (2007).

[17] H. Zhang, C.-X. Liu, X.-L. Qi, X. Dai, Z. Fang, and S.-C. Zhang, Nat. Phys. **5**, 438 (2009).

[18] Y. L. Chen, J. G. Analytis, J.-H. Chu, Z. K. Liu, S.-K. Mo, X. L. Qi, H. J. Zhang, D. H. Lu, X. Dai, Z. Fang, S. C. Zhang, I. R. Fisher, Z. Hussain, and Z.-X. Shen, Science **325**, 178 (2014).

[19] A. P. Schnyder, S. Ryu, A. Furusaki, and A. W. W. Ludwig, Phys. Rev. B **78**, 195125 (2008).

[20] A. Kitaev, AIP Conf. Proc. **1134**, 22 (2009).

[21] L. Fu and C. L. Kane, Phys. Rev. Lett. **100**, 096407 (2008).

[22] Y. Oreg, G. Refael, and F. Von Oppen, Phys. Rev. Lett. **105**, 177002 (2010).

[23] R. M. Lutchyn, J. D. Sau, and S. Das Sarma, Phys. Rev. Lett. **105**, 077001 (2010).

[24] V. Mourik, K. Zuo, S. M. Frolov, S. R. Plissard, E. P. a. M. Bakkers, and L. P. Kouwenhoven, Science **336**, 1003 (2012).

[25] W. P. Su, J. R. Schrieffer, and A. J. Heeger, Phys. Rev. Lett. **42**, 1698 (1979).

[26] A. A. Abrikosov, Phys. Rev. B **58**, 2788 (1998).

[27] B. Sbierski, G. Pohl, E. J. Bergholtz, and P. W. Brouwer, Phys. Rev. Lett. **113**, 026602 (2014).

[28] S. L. Adler, Phys. Rev. **177**, 2426 (1969).

[29] J. S. Bell and R. Jackiw, Nuovo Cim. A **60**, 47 (1969).

[30] H. B. Nielsen and M. Ninomiya, Phys. Lett. B **130**, 389 (1983).

[31] C. Herring, Phys. Rev. **52**, 361 (1937).

[32] S. Matsuura, P. Y. Chang, A. P. Schnyder, and S. Ryu, New J. Phys. **15**, 065001 (2013).

[33] A. A. Burkov, M. D. Hook, and L. Balents, Phys. Rev. B **84**, 235126 (2011).

[34] T. D. C. Bevan, A. J. Manninen, J. B. Cook, J. R. Hook, H. E. Hall, T. Vachaspati, and G. E. Volovik, Nature **386**, 689 (1997).

[35] X. Wan, A. M. Turner, A. Vishwanath, and S. Y. Savrasov, Phys. Rev. B **83**, 205101 (2011).

[36] H. Weng, C. Fang, Z. Fang, B. A. Bernevig, and X. Dai, Phys. Rev. X **5**, 011029 (2015).

[37] S.-M. Huang, S.-Y. Xu, I. Belopolski, C.-C. Lee, G. Chang, B. Wang, N. Alidoust, G. Bian, M. Neupane, A. Bansil, H. Lin, and M. Z. Hasan, Nat. Commun. **6**, 7373 (2015).

[38] S.-Y. Xu, I. Belopolski, N. Alidoust, M. Neupane, G. Bian, C. Zhang, R. Sankar, G. Chang, Z. Yuan, C.-C. Lee, S.-M. Huang, H. Zheng, J. Ma, D. S. Sanchez, B. Wang, A. Bansil, F. Chou, P. P. Shibayev, H. Lin, S. Jia, and M. Z. Hasan, Science **349**, 613 (2015).

[39] B. Q. Lv, H. M. Weng, B. B. Fu, X. P. Wang, H. Miao, J. Ma, P. Richard, X. C. Huang, L. X. Zhao, G. F. Chen, Z. Fang, X. Dai, T. Qian, and H. Ding, Phys. Rev. X **5**, 031013 (2015).

[40] D. T. Son and B. Z. Spivak, Phys. Rev. B **88**, 104412 (2013).

[41] F. Arnold, C. Shekhar, S.-C. Wu, Y. Sun, R. D. dos Reis, N. Kumar, M. Naumann, M. O. Ajeesh, M. Schmidt, A. G. Grushin, J. H. Bardarson, M. Baenitz, D. Sokolov, H. Borrmann, M. Nicklas, C. Felser, E. Hassinger, and B. Yan, Nat. Commun. **7**, 11615 (2016).

[42] J. Behrends and J. H. Bardarson, Phys. Rev. B **96**, 060201 (2017).

[43] N. J. Ghimire, Y. Luo, M. Neupane, D. J. Williams, E. D. Bauer, and F. Ronning, J. Phys. Condens. Matter **27**, 152201 (2015).

[44] J. Klier, I. V. Gornyi, and A. D. Mirlin, Phys. Rev. B **92**, 205113 (2015).

[45] J. Behrends, F. K. Kunst, and B. Sbierski, Phys. Rev. B **97**, 064203 (2018).

[46] J. H. Bardarson, J. Tworzydło, P. W. Brouwer, and C. W. J. Beenakker, Phys. Rev. Lett. **99**, 106801 (2007).

[47] W. B. Rui, Y. X. Zhao, and A. P. Schnyder, Phys. Rev. B **97**, 161113 (2018).

[48] A. A. Burkov, Phys. Rev. B **97**, 165104 (2018).

[49] V. L. Ginzburg and L. D. Landau, Zh. Eksp. Teor. Fiz. **20**, 1064 (1950).

[50] M. Schwartz, *Quantum Field Theory and the Standard Model*, Quantum Field Theory and the Standard Model (Cambridge University Press, 2014).

[51] G. E. Volovik, *The Universe in a Helium Droplet*, Int. Ser. Monogr. Phys. (Oxford University Press, 2009).

[52] A. Altland and B. Simons, *Condensed Matter Field Theory* (Cambridge University Press, 2010).

[53] X. L. Qi, T. L. Hughes, and S. C. Zhang, Phys. Rev. B **78**, 195424 (2008).

[54] G. E. Volovik, JETP Lett. **70**, 1 (1999).

[55] K. Landsteiner, Phys. Rev. B **89**, 075124 (2014).

[56] D. Colladay and A. Kostelecky, Phys. Rev. D **55**, 6760 (1997).

[57] D. Colladay and A. Kostelecky, Phys. Rev. D **58**, 116002 (1998).

[58] J. Behrends, A. G. Grushin, T. Ojanen, and J. H. Bardarson, Phys. Rev. B **93**, 075114 (2016).

[59] H. Georgi, Annu. Rev. Nucl. Part. Sci. **43**, 209 (1993).

[60] K. G. Wilson, Phys. Rev. D **10**, 2445 (1974).

[61] A. Zee, *Quantum Field Theory in a Nutshell*, In a Nutshell (Princeton University Press, 2010).

[62] M. M. Vazifeh and M. Franz, Phys. Rev. Lett. **111**, 27201 (2013).

[63] A. A. Zyuzin and A. A. Burkov, Phys. Rev. B **86**, 115133 (2012).

[64] R. Jackiw, Int. J. Mod. Phys. B **14**, 2011 (2000).

[65] M. Peskin and D. Schroeder, *An Introduction To Quantum Field Theory* (Westview Pr., Boulder, Colorado, 2005).

[66] F. D. M. Haldane, Phys. Rev. Lett. **93**, 206602 (2004).

[67] W. A. Bardeen and B. Zumino, Nucl. Phys. B **244**, 421 (1984).

[68] X. G. Wen and Q. Niu, Phys. Rev. B **41**, 9377 (1990).

[69] X. G. Wen, Int. J. Mod. Phys. B **04**, 239 (1990).

[70] F. Pollmann, A. M. Turner, E. Berg, and M. Oshikawa, Phys. Rev. B **81**, 064439 (2010).

[71] L. Fidkowski and A. Kitaev, Phys. Rev. B **83**, 075103 (2011).

[72] A. M. Turner, F. Pollmann, and E. Berg, Phys. Rev. B **83**, 075102 (2011).

[73] S. Sachdev and J. Ye, Phys. Rev. Lett. **70**, 3339 (1993).

[74] A. Kitaev, "A simple model of quantum holography," (2015), proceedings of the KITP Program: Entanglement in Strongly-Correlated Quantum Matter.

[75] R. B. Laughlin, Phys. Rev. B **23**, 5632 (1981).

[76] L. Fu, Phys. Rev. Lett. **106**, 106802 (2011).

[77] J. Kruthoff, J. de Boer, J. van Wezel, C. L. Kane, and R.-J. Slager, Phys. Rev. X **7**, 041069 (2016).

[78] B. Bradlyn, L. Elcoro, J. Cano, M. G. Vergniory, Z. Wang, C. Felser, M. I. Aroyo, and B. A. Bernevig, Nature **547**, 298 (2017).

[79] H. C. Po, A. Vishwanath, and H. Watanabe, Nat. Commun. **8**, 50 (2017).

[80] E. P. Wigner, Math. Proc. Cambridge Philos. Soc. **47**, 790 (1951).

[81] E. P. Wigner, Ann. Math. **67**, 325 (1958).

[82] F. J. Dyson, J. Math. Phys. **3**, 140 (1962).

[83] A. Altland and M. R. Zirnbauer, Phys. Rev. B **55**, 1142 (1997).

[84] X. L. Qi and S. C. Zhang, Rev. Mod. Phys. **83**, 1057 (2011).

[85] A. Bansil, H. Lin, and T. Das, Rev. Mod. Phys. **88**, 021004 (2016).

[86] A. W. W. Ludwig, Phys. Scr. **2016**, 014001 (2016).

[87] J. C. Budich and B. Trauzettel, Phys. Status Solidi - Rapid Res. Lett. **7**, 109 (2013).

[88] A. P. Schnyder, S. Ryu, A. Furusaki, and A. W. W. Ludwig, AIP Conf. Proc. **1134**, 10 (2009).

[89] S. Ryu, A. P. Schnyder, A. Furusaki, and A. W. W. Ludwig, New J. Phys. **12**, 065010 (2010).

[90] S. Ryu, J. E. Moore, and A. W. Ludwig, Phys. Rev. B **85**, 045104 (2012).

[91] R. S. K. Mong, J. H. Bardarson, and J. E. Moore, Phys. Rev. Lett. **108**, 076804 (2012).

[92] M. V. Berry, Proc. R. Soc. A Math. Phys. Eng. Sci. **392**, 45 (1984).

[93] D. Vanderbilt and R. D. King-Smith, Phys. Rev. B **48**, 4442 (1993).

[94] R. D. King-Smith and D. Vanderbilt, Phys. Rev. B **47**, 1651 (1993).

[95] D. J. Thouless, Phys. Rev. B **27**, 6083 (1983).

[96] G. Sundaram and Q. Niu, Phys. Rev. B **59**, 14915 (1999).

[97] N. Ashcroft and N. Mermin, *Solid State Physics* (Cengage Learning, Andover, UK, 2011).

[98] M. Born and V. Fock, Zeitschrift für Phys. **51**, 165 (1928).

[99] B. Bernevig and T. Hughes, *Topological Insulators and Topological Superconductors* (Princeton University Press, 2013).

[100] J. Zak, Phys. Rev. Lett. **62**, 2747 (1989).

[101] D. Xiao, M. C. Chang, and Q. Niu, Rev. Mod. Phys. **82**, 1959 (2010).

[102] G. H. Wannier, Phys. Rev. **52**, 191 (1937).

[103] W. Kohn, Phys. Rev. **115**, 809 (1959).

[104] G. Nenciu, Commun. Math. Phys. **91**, 81 (1983).

[105] G. Panati, Ann. Henri Poincare **8**, 995 (2007).

[106] R. Resta, Rev. Mod. Phys. **66**, 899 (1994).

[107] N. A. Spaldin, J. Solid State Chem. **195**, 2 (2012).

[108] Y. Hatsugai, J. Phys. Soc. Japan **75**, 123601 (2006).

[109] S. Ryu and Y. Hatsugai, Phys. Rev. B **73**, 245115 (2006).

[110] M. Atala, M. Aidelsburger, J. T. Barreiro, D. Abanin, T. Kitagawa, E. Demler, and I. Bloch, Nat. Phys. **9**, 795 (2013).

[111] F. De Juan, A. Rüegg, and D. H. Lee, Phys. Rev. B **89**, 161117 (2014).

[112] C. W. Ling, M. Xiao, C. T. Chan, S. F. Yu, and K. H. Fung, Opt. Express **23**, 2021 (2015).

[113] J.-W. Rhim, J. Behrends, and J. H. Bardarson, Phys. Rev. B **95**, 035421 (2017).

[114] C.-K. Chiu, J. C. Y. Teo, A. P. Schnyder, and S. Ryu, Rev. Mod. Phys. **88**, 035005 (2016).

[115] R. Roy, Phys. Rev. B **79**, 195322 (2009).

[116] C.-K. Chiu and A. P. Schnyder, Phys. Rev. B **90**, 205136 (2014).

[117] H. Weyl, Zeitschrift für Phys. **56**, 330 (1929).

[118] H. B. Nielsen and M. Ninomiya, Phys. Lett. B **105**, 219 (1981).

[119] H. B. Nielsen and M. Ninomiya, Nuclear Physics B **185**, 20 (1981).

[120] H. B. Nielsen and M. Ninomiya, Nuclear Physics B **193**, 173 (1981).

[121] Z. Wang, Y. Sun, X. Q. Chen, C. Franchini, G. Xu, H. Weng, X. Dai, and Z. Fang, Phys. Rev. B **85**, 195320 (2012).

[122] C. Fang, M. J. Gilbert, X. Dai, and B. A. Bernevig, Phys. Rev. Lett. **108**, 266802 (2012).

[123] P. A. M. Dirac, Proc. R. Soc. A Math. Phys. Eng. Sci. **133**, 60 (1931).

[124] K. Y. Yang, Y. M. Lu, and Y. Ran, Phys. Rev. B **84**, 075129 (2011).

[125] C.-Z. Chen, J. Song, H. Jiang, Q.-F. Sun, Z. Wang, and X. C. Xie, Phys. Rev. Lett. **115**, 246603 (2015).

[126] X. L. Qi, Y. S. Wu, and S. C. Zhang, Phys. Rev. B **74**, 085308 (2006).

[127] D. Gosálbez-Martínez, I. Souza, and D. Vanderbilt, Phys. Rev. B **92**, 085138 (2015).

[128] G. Chang, S. Y. Xu, X. Zhou, S. M. Huang, B. Singh, B. Wang, I. Belopolski, J. Yin, S. Zhang, A. Bansil, H. Lin, and M. Z. Hasan, Phys. Rev. Lett. **119**, 156401 (2017).

[129] C. Fang, Y. Chen, H. Y. Kee, and L. Fu, Phys. Rev. B **92**, 081201(R) (2015).

[130] P. Delplace, D. Ullmo, and G. Montambaux, Phys. Rev. B **84**, 195452 (2011).

[131] T. Kariyado and Y. Hatsugai, Phys. Rev. B **88**, 245126 (2013).

[132] F. Grusdt, M. Höning, and M. Fleischhauer, Phys. Rev. Lett. **110**, 260405 (2013).

[133] R. Barnett, Phys. Rev. A **88**, 063631 (2013).

[134] Y.-H. Chan, C.-K. Chiu, M. Y. Chou, and A. P. Schnyder, Phys. Rev. B **93**, 205132 (2016).

[135] A. A. Soluyanov and D. Vanderbilt, Phys. Rev. B **83**, 035108 (2011).

[136] W. B. Hodge, E. D. Welchman, and M. J. Rave, Eur. Phys. J. B **84**, 351 (2011).

[137] S. Longhi, Opt. Lett. **38**, 3716 (2013).

[138] J. C. Budich and E. Ardonne, Phys. Rev. B **88**, 035139 (2013).

[139] Y. Yoshimura, K. I. Imura, T. Fukui, and Y. Hatsugai, Phys. Rev. B **90**, 155443 (2014).

[140] A. Alexandradinata, C. Fang, M. J. Gilbert, and B. A. Bernevig, Phys. Rev. Lett. **113**, 116403 (2014).

[141] A. Przysięzna, O. Dutta, and J. Zakrzewski, New J. Phys. **17**, 013018 (2015).

[142] W. R. Lee and K. Park, Phys. Rev. B **92**, 195144 (2015).

[143] Y. X. Xiao, G. Ma, Z. Q. Zhang, and C. T. Chan, Phys. Rev. Lett. **118**, 166803 (2017).

[144] L. Fidkowski, T. S. Jackson, and I. Klich, Phys. Rev. Lett. **107**, 036601 (2011).

[145] A. Alexandradinata, X. Dai, and B. A. Bernevig, Phys. Rev. B **89**, 155114 (2014).

[146] M. Taherinejad, K. F. Garrity, and D. Vanderbilt, Phys. Rev. B **89**, 115102 (2014).

[147] Z. Wang, A. Alexandradinata, R. J. Cava, and B. A. Bernevig, Nature **532**, 189 (2016).

[148] A. Alexandradinata, Z. Wang, and B. A. Bernevig, Phys. Rev. X **6**, 021008 (2016).

[149] A. Alexandradinata and B. A. Bernevig, Phys. Rev. B **93**, 205104 (2016).

[150] M. Hirayama, R. Okugawa, T. Miyake, and S. Murakami, Nat. Commun. **8**, 14022 (2017).

[151] K. N. Kudin, R. Car, and R. Resta, J. Chem. Phys. **126**, 234101 (2007).

[152] J. Behrends, J.-W. Rhim, S. Liu, A. G. Grushin, and J. H. Bardarson, Phys. Rev. B **96**, 245101 (2017).

[153] M. Kohmoto, Ann. Phys. (N. Y). **160**, 343 (1985).

[154] C. Brouder, G. Panati, M. Calandra, C. Mourougane, and N. Marzari, Phys. Rev. Lett. **98**, 046402 (2007).

[155] A. Balderschi, S. Baroni, and R. Resta, Phys. Rev. Lett. **61**, 734 (1988).

[156] K. N. Kudin, R. Car, and R. Resta, J. Chem. Phys. **127**, 194902 (2007).

[157] J. H. Park, G. Yang, J. Klinovaja, P. Stano, and D. Loss, Phys. Rev. B **94**, 075416 (2016).

[158] C. Wagner, M. F. Green, P. Leinen, T. Deilmann, P. Krüger, M. Rohlfing, R. Temirov, and F. S. Tautz, Phys. Rev. Lett. **115**, 026101 (2015).

[159] R. D. Peccei and H. R. Quinn, Phys. Rev. Lett. **38**, 1440 (1977).

[160] F. Wilczek, Phys. Rev. Lett. **58**, 1799 (1987).

[161] A. G. Grushin, Phys. Rev. D **86**, 45001 (2012).

[162] P. Goswami and S. Tewari, Phys. Rev. B **88**, 245107 (2013).

[163] P. Hosur, S. Ryu, and A. Vishwanath, Phys. Rev. B **81**, 045120 (2010).

[164] R. A. Bertlmann, *Anomalies in Quantum Field Theory*, Int. Ser. Monogr. Phys. (Oxford University Press, Oxford, 2000).

[165] K. Fujikawa and H. Suzuki, *Path Integrals and Quantum Anomalies*, Int. Ser. Monogr. Phys. (Oxford University Press, Oxford, 2004).

[166] D. H. Lee, Phys. Rev. Lett. **103**, 196804 (2009).

[167] E. J. König, P. M. Ostrovsky, I. V. Protopopov, I. V. Gornyi, I. S. Burmistrov, and A. D. Mirlin, Phys. Rev. B **90**, 165435 (2014).

[168] A. A. Burkov, J. Phys. Condens. Matter **27**, 113201 (2015).

[169] D. T. Son and N. Yamamoto, Phys. Rev. Lett. **109**, 181602 (2012).

[170] T. E. O'Brien, C. W. J. Beenakker, and I. Adagideli, Phys. Rev. Lett. **118**, 207701 (2017).

[171] H. J. Kim, K. S. Kim, J. F. Wang, M. Sasaki, N. Satoh, A. Ohnishi, M. Kitaura, M. Yang, and L. Li, Phys. Rev. Lett. **111**, 246603 (2013).

[172] Q. Li, D. E. Kharzeev, C. Zhang, Y. Huang, I. Pletikosic, A. V. V. Fedorov, R. D. D. Zhong, J. A. A. Schneeloch, G. D. D. Gu, T. Valla, I. Pletikosić, A. V. V. Fedorov, R. D. D. Zhong, J. A. A. Schneeloch, G. D. D. Gu, and T. Valla, Nat. Phys. **12**, 550 (2016).

[173] X. Huang, L. Zhao, Y. Long, P. Wang, D. Chen, Z. Yang, H. Liang, M. Xue, H. Weng, Z. Fang, X. Dai, and G. Chen, Phys. Rev. X **5**, 031023 (2015).

[174] C.-L. Zhang, S.-Y. Xu, I. Belopolski, Z. Yuan, Z. Lin, B. Tong, G. Bian, N. Alidoust, C.-C. Lee, S.-M. Huang, T.-R. Chang, G. Chang, C.-H. Hsu, H.-T. Jeng, M. Neupane, D. S. Sanchez, H. Zheng, J. Wang, H. Lin, C. Zhang, H.-Z. Lu, S.-Q. Shen, T. Neupert, M. Zahid Hasan, and S. Jia, Nat. Commun. **7**, 10735 (2016).

[175] J. Xiong, S. K. Kushwaha, T. Liang, J. W. Krizan, M. Hirschberger, W. Wang, R. J. Cava, and N. P. Ong, Science **350**, 413 (2015).

[176] X. Yang, Y. Li, Z. Wang, Y. Zhen, and Z.-A. Xu, "Observation of Negative Magnetoresistance and nontrivial π Berrys phase in 3D Weyl semi-metal NbAs," arXiv:1506.02283 .

[177] J. Du, H. Wang, Q. Mao, R. Khan, B. Xu, Y. Zhou, Y. Zhang, J. Yang, B. Chen, C. Feng, and M. Fang, Sci. China **59**, 657406 (2016).

[178] C. Zhang, C. Guo, H. Lu, X. Zhang, Z. Yuan, Z. Lin, J. Wang, and S. Jia, Phys. Rev. B **92**, 041203 (2015).

[179] H. Li, H. He, H.-Z. Lu, H. Zhang, H. Liu, R. Ma, Z. Fan, S.-Q. Shen, and J. Wang, Nat. Commun. **7**, 10301 (2016).

[180] J. Zhou, H. R. Chang, and D. Xiao, Phys. Rev. B **91**, 035114 (2015).

[181] S. A. Parameswaran, T. Grover, D. A. Abanin, D. A. Pesin, and A. Vishwanath, Phys. Rev. X **4**, 031035 (2014).

[182] G. Başar, D. E. Kharzeev, and H.-U. Yee, Phys. Rev. B **89**, 035142 (2014).

[183] P. Goswami, J. H. Pixley, and S. Das Sarma, Phys. Rev. B **92**, 075205 (2015).

[184] Z. Wang, H. Weng, Q. Wu, X. Dai, and Z. Fang, Phys. Rev. B **88**, 125427 (2013).

[185] R. V. Gorbachev, J. C. W. Song, G. L. Yu, A. V. Kretinin, F. Withers, Y. Cao, A. Mishchenko, I. V. Grigorieva, K. S. Novoselov, L. S. Levitov, and A. K. Geim, Science **346**, 448 (2014).

[186] S. Y. Xu, C. Liu, S. K. Kushwaha, R. Sankar, J. W. Krizan, I. Belopolski, M. Neupane, G. Bian, N. Alidoust, T. R. Chang, H. T. Jeng, C. Y. Huang, W. F. Tsai, H. Lin, P. P. Shibayev, F. C. Chou, R. J. Cava, and M. Z. Hasan, Science **347**, 294 (2015).

[187] D. Bulmash and X. L. Qi, Phys. Rev. B **93**, 081103(R) (2016).

[188] C. Enderlein, *Graphene and its interaction with different substrates studied by angular-resolved photoemission spectroscopy*, Ph.D. thesis, Freie Universität, Berlin (2010).

[189] R. Raue, H. Hopster, and R. Clauberg, Phys. Rev. Lett. **50**, 1623 (1983).

[190] K. Fujikawa, Phys. Rev. Lett. **42**, 1195 (1979).

[191] K. Fujikawa, Phys. Rev. D **21**, 2848 (1980).

[192] S. L. Adler and W. A. Bardeen, Phys. Rev. **182**, 1517 (1969).

[193] K. Landsteiner, Acta Phys. Pol. B **47**, 2617 (2016).

[194] W. A. Bardeen, Phys. Rev. **184**, 1848 (1969).

[195] A. Cortijo, Y. Ferreirós, K. Landsteiner, and M. A. Vozmediano, Phys. Rev. Lett. **115**, 177202 (2015).

[196] E. V. Gorbar, V. A. Miransky, I. A. Shovkovy, and P. O. Sukhachov, Phys. Rev. B **96**, 085130 (2017).

[197] S. Chandrasekharan, Phys. Rev. D **49**, 1980 (1994).

[198] M. Stone, Phys. Rev. B **85**, 184503 (2012).

[199] F. R. Klinkhamer and G. E. Volovik, Int. J. Mod. Phys. A **20**, 2795 (2005).

[200] C. X. Liu, P. Ye, and X. L. Qi, Phys. Rev. B **87**, 235306 (2013).

[201] M. N. Chernodub, A. Cortijo, A. G. Grushin, K. Landsteiner, and M. A. Vozmediano, Phys. Rev. B **89**, 081407 (2014).

[202] T. Schuster, T. Iadecola, C. Chamon, R. Jackiw, and S. Y. Pi, Phys. Rev. B **94**, 115110 (2016).

[203] D. I. Pikulin, A. Chen, and M. Franz, Phys. Rev. X **6**, 041021 (2016).

[204] A. G. Grushin, J. W. Venderbos, A. Vishwanath, and R. Ilan, Phys. Rev. X **6**, 041046 (2016).

[205] Z. M. Huang, J. Zhou, and S. Q. Shen, Phys. Rev. B **96**, 085201 (2017).

[206] J.-H. Zhou, H. Jiang, Q. Niu, and J.-R. Shi, Chinese Phys. Lett. **30**, 027101 (2013).

[207] H. Sumiyoshi and S. Fujimoto, Phys. Rev. Lett. **116**, 166601 (2016).

[208] A. Cortijo, D. Kharzeev, K. Landsteiner, and M. A. H. Vozmediano, Phys. Rev. B **94**, 241405 (2016).

[209] A. Westström and T. Ojanen, Phys. Rev. X **7**, 041026 (2017).

[210] E. V. Gorbar, V. A. Miransky, I. A. Shovkovy, and P. O. Sukhachov, Phys. Rev. B **95**, 241114 (2017).

[211] E. V. Gorbar, V. A. Miransky, I. A. Shovkovy, and P. O. Sukhachov, Phys. Rev. B **95**, 115422 (2017).

[212] E. V. Gorbar, V. A. Miransky, I. A. Shovkovy, and P. O. Sukhachov, Phys. Rev. B **95**, 205141 (2017).

[213] S. Roy, M. Kolodrubetz, N. Goldman, and A. G. Grushin, 2D Mater. **5**, 024001 (2017).

[214] S. A. Yang, H. Pan, and F. Zhang, Phys. Rev. Lett. **115**, 156603 (2015).

[215] Q. D. Jiang, H. Jiang, H. Liu, Q. F. Sun, and X. C. Xie, Phys. Rev. Lett. **115**, 156602 (2015).

[216] A. Cortijo and M. A. Zubkov, Ann. Phys. (N. Y). **366**, 45 (2016).

[217] E. V. Gorbar, V. A. Miransky, I. A. Shovkovy, and P. O. Sukhachov, Phys. Rev. Lett. **118**, 127601 (2017).

[218] E. V. Gorbar, V. A. Miransky, I. A. Shovkovy, and P. O. Sukhachov, Phys. Rev. B **95**, 115202 (2017).

[219] F. D. M. Haldane, "Attachment of Surface "Fermi Arcs" to the Bulk Fermi Surface: "Fermi-Level Plumbing" in Topological Metals," arXiv:1401.0529 .

[220] Y. Ominato and M. Koshino, Phys. Rev. B **93**, 245304 (2016).

[221] N. Bovenzi, M. Breitkreiz, T. E. O'Brien, J. Tworzydło, and C. W. Beenakker, New J. Phys. **20**, 023023 (2018).

[222] P. Streda, J. Phys. C Solid State Phys. **15**, 717 (1982).

[223] R. Jackiw and A. Kostelecky, Phys. Rev. Lett. **82**, 3572 (1999).

[224] M. Pérez-Victoria, Phys. Rev. Lett. **83**, 2518 (1999).

[225] S. Roy, M. Kolodrubetz, J. E. Moore, and A. G. Grushin, Phys. Rev. B **94**, 161107 (2016).

[226] V. A. Kostelecký, C. D. Lane, and A. G. M. Pickering, Phys. Rev. D **65**, 056006 (2002).

[227] S. Shanmugadhasan, Can. J. Phys. **30**, 218 (1952).

[228] D. Fryberger, Found. Phys. **19**, 125 (1989).

[229] C. Shekhar, A. K. Nayak, Y. Sun, M. Schmidt, M. Nicklas, I. Leermakers, U. Zeitler, Y. Skourski, J. Wosnitza, Z. Liu, Y. Chen, W. Schnelle, H. Borrmann, Y. Grin, C. Felser, and B. Yan, Nat. Phys. **11**, 645 (2015).

[230] T. Morimoto, S. Zhong, J. Orenstein, and J. E. Moore, Phys. Rev. B **94**, 245121 (2016).

[231] C.-Z. Li, L.-X. Wang, H. Liu, J. Wang, Z.-M. Liao, and D.-P. Yu, Nat. Commun. **6**, 10137 (2015).

[232] J. Xiong, S. Kushwaha, J. Krizan, T. Liang, R. J. Cava, and N. P. Ong, Europhys. Lett. **114**, 27002 (2016).

[233] A. A. Burkov and Y. B. Kim, Phys. Rev. Lett. **117**, 136602 (2016).

[234] D. A. Pesin, E. G. Mishchenko, and A. Levchenko, Phys. Rev. B **92**, 174202 (2015).

[235] H.-Z. Lu and S.-Q. Shen, Front. Phys. **12**, 127201 (2017).

[236] S. B. Zhang, H. Z. Lu, and S. Q. Shen, New J. Phys. **18**, 053039 (2016).

[237] C. Z. Chen, H. Liu, H. Jiang, and X. C. Xie, Phys. Rev. B **93**, 165420 (2016).

[238] P. E. C. Ashby and J. P. Carbotte, Phys. Rev. B **87**, 245131 (2013).

[239] T. Meng, A. G. Grushin, K. Shtengel, and J. H. Bardarson, Phys. Rev. B **94**, 155136 (2016).

[240] X. C. Xie, Q. P. Li, and S. Das Sarma, Phys. Rev. B **42**, 7132 (1990).

[241] E. Xypakis and J. H. Bardarson, Phys. Rev. B **95**, 035415 (2017).

[242] B. Sbierski, E. J. Bergholtz, and P. W. Brouwer, Phys. Rev. B **92**, 115145 (2015).

[243] B. Sbierski, M. Trescher, E. J. Bergholtz, and P. W. Brouwer, Phys. Rev. B **95**, 115104 (2017).

[244] M. Trescher, B. Sbierski, P. W. Brouwer, and E. J. Bergholtz, Phys. Rev. B **95**, 045139 (2017).

[245] J. Feng, Y. Pang, D. Wu, Z. Wang, H. Weng, J. Li, X. Dai, Z. Fang, Y. Shi, and L. Lu, Phys. Rev. B **92**, 081306 (2015).

[246] T. Liang, Q. Gibson, M. N. Ali, M. Liu, R. J. Cava, and N. P. Ong, Nat. Mater. **14**, 280 (2015).

[247] Y. Zhao, H. Liu, C. Zhang, H. Wang, J. Wang, Z. Lin, Y. Xing, H. Lu, J. Liu, Y. Wang, S. M. Brombosz, Z. Xiao, S. Jia, X. C. Xie, and J. Wang, Phys. Rev. X **5**, 031037 (2015).

[248] M. Novak, S. Sasaki, K. Segawa, and Y. Ando, Phys. Rev. B **91**, 041203 (2015).

[249] E. V. Gorbar, V. A. Miransky, and I. A. Shovkovy, Phys. Rev. B **89**, 085126 (2014).

[250] H. Z. Lu, S. B. Zhang, and S. Q. Shen, Phys. Rev. B **92**, 045203 (2015).

[251] X. Xiao, K. T. Law, and P. A. Lee, Phys. Rev. B **96**, 165101 (2017).

[252] J. Klier, I. V. Gornyi, and A. D. Mirlin, Phys. Rev. B **96**, 214209 (2017).

[253] X. T. Ji, H. Z. Lu, Z. G. Zhu, and G. Su, AIP Adv. **7**, 105003 (2017).

[254] A. Cortijo, Phys. Rev. B **94**, 241105 (2016).

[255] E. Fradkin, Phys. Rev. B **33**, 3263 (1986).

[256] S. V. Syzranov and L. Radzihovsky, Ann. Rev. Cond. Mat. Phys **9**, 35 (2017).

[257] S. Datta, *Electronic Transport in Mesoscopic Systems*, Cambridge Studies in Semiconductor Physics (Cambridge University Press, 1997).

[258] J. H. Bardarson and R. S. K. Mong, private communication.

[259] J. C. Song, G. Refael, and P. A. Lee, Phys. Rev. B **92**, 180204 (2015).

[260] C. Lee, X. Wei, J. W. Kysar, and J. Hone, Science **321**, 385 (2008).

[261] F. Guinea, M. I. Katsnelson, and A. K. Geim, Nat. Phys. **6**, 30 (2010).

[262] T. Liu, D. I. Pikulin, and M. Franz, Phys. Rev. B **95**, 041201 (2017).

[263] D. I. Pikulin and R. Ilan, "Bulk-boundary quantum oscillations in inhomogeneous Weyl semimetals," arXiv:1802.00512 .

[264] C. W. Groth, M. Wimmer, A. R. Akhmerov, and X. Waintal, New J. Phys. **16**, 063065 (2014).

[265] B. J. Ramshaw, K. A. Modic, A. Shekhter, Y. Zhang, E.-A. Kim, P. J. W. Moll, M. D. Bachmann, M. K. Chan, J. B. Betts, F. Balakirev, A. Migliori, N. J. Ghimire, E. D. Bauer, F. Ronning, and R. D. Mcdonald, Nat. Commun. **9**, 2217 (2018).

[266] P. W. Anderson, Phys. Rev. **109**, 1492 (1958).

[267] E. Abrahams, P. W. Anderson, D. C. Licciardello, and T. V. Ramakrishnan, Phys. Rev. Lett. **42**, 673 (1979).

[268] M. D. Bachmann, N. Nair, F. Flicker, R. Ilan, T. Meng, N. J. Ghimire, E. D. Bauer, F. Ronning, J. G. Analytis, and P. J. Moll, Sci. Adv. **3**, e1602983 (2017).

[269] P. Baireuther, J. M. Edge, I. C. Fulga, C. W. J. Beenakker, and J. Tworzydło, Phys. Rev. B **89**, 035410 (2014).

[270] A. M. Turner and A. Vishwanath, in *Topological Insulators*, Contemporary Concepts of Condensed Matter Science, Vol. 6, edited by M. Franz and L. Molenkamp (Elsevier, New York, 2013) Chap. 11, pp. 293–324.

[271] Y. Kim, B. J. Wieder, C. L. Kane, and A. M. Rappe, Phys. Rev. Lett. **115**, 036806 (2015).

[272] M. Zeng, C. Fang, G. Chang, Y.-A. Chen, T. Hsieh, A. Bansil, H. Lin, and L. Fu, "Topological semimetals and topological insulators in rare earth monopnictides," arXiv:1504.03492 .

[273] R. Yu, H. Weng, Z. Fang, X. Dai, and X. Hu, Phys. Rev. Lett. **115**, 036807 (2015).

[274] A. Yamakage, Y. Yamakawa, Y. Tanaka, and Y. Okamoto, J. Phys. Soc. Japan **85**, 13708 (2016).

[275] L. S. Xie, L. M. Schoop, E. M. Seibel, Q. D. Gibson, W. Xie, and R. J. Cava, APL Mater. **3**, 083602 (2015).

[276] G. Bian, T. R. Chang, H. Zheng, S. Velury, S. Y. Xu, T. Neupert, C. K. Chiu, S. M. Huang, D. S. Sanchez, I. Belopolski, N. Alidoust, P. J. Chen, G. Chang, A. Bansil, H. T. Jeng, H. Lin, and M. Z. Hasan, Phys. Rev. B **93**, 121113(R) (2016).

[277] Y. Okamoto, T. Inohara, A. Yamakage, Y. Yamakawa, and K. Takenaka, J. Phys. Soc. Japan **85**, 123701 (2016).

[278] M. Phillips and V. Aji, Phys. Rev. B **90**, 115111 (2014).

[279] J. Hu, Z. Tang, J. Liu, X. Liu, Y. Zhu, D. Graf, K. Myhro, S. Tran, C. N. Lau, J. Wei, and Z. Mao, Phys. Rev. Lett. **117**, 016602 (2016).

[280] H. Huang, J. Liu, D. Vanderbilt, and W. Duan, Phys. Rev. B **93**, 201114(R) (2016).

[281] K. Mullen, B. Uchoa, and D. T. Glatzhofer, Phys. Rev. Lett. **115**, 026403 (2015).

[282] Q. Xu, R. Yu, Z. Fang, X. Dai, and H. Weng, Phys. Rev. B **95**, 045136 (2017).

[283] N. B. Kopnin, T. T. Heikkilä, and G. E. Volovik, Phys. Rev. B **83**, 220503(R) (2011).

[284] M. Koshino and I. F. Hizbullah, Phys. Rev. B **93**, 045201 (2016).

[285] G. P. Mikitik and Y. V. Sharlai, Phys. Rev. B **94**, 195123 (2016).

[286] J. W. Rhim and Y. B. Kim, Phys. Rev. B **92**, 045126 (2015).

[287] J. P. Carbotte, J. Phys. Condens. Matter **29**, 045301 (2016).

[288] J. W. Rhim and Y. B. Kim, New J. Phys. **18**, 043010 (2016).

[289] S. P. Mukherjee and J. P. Carbotte, Phys. Rev. B **95**, 214203 (2017).

[290] Y. Wang and R. M. Nandkishore, Phys. Rev. B **96**, 115130 (2017).

[291] E. Emmanouilidou, B. Shen, X. Deng, T. R. Chang, A. Shi, G. Kotliar, S. Y. Xu, and N. Ni, Phys. Rev. B **95**, 245113 (2017).

[292] S. V. Syzranov and B. Skinner, Phys. Rev. B **96**, 161105 (2017).

[293] S. Ahn, E. J. Mele, and H. Min, Phys. Rev. Lett. **119**, 147402 (2017).

[294] M. Matusiak, J. R. Cooper, and D. Kaczorowski, Nat. Commun. **8**, 15219 (2017).

[295] Z. Yan, P. W. Huang, and Z. Wang, Phys. Rev. B **93**, 085138 (2016).

[296] S.-Y. Xu, N. Alidoust, I. Belopolski, Z. Yuan, G. Bian, T.-R. Chang, H. Zheng, V. N. Strocov, D. S. Sanchez, G. Chang, C. Zhang, D. Mou, Y. Wu, L. Huang, C.-C. Lee, S.-M. Huang, B. Wang, A. Bansil, H.-T. Jeng, T. Neupert, A. Kaminski, H. Lin, S. Jia, and M. Zahid Hasan, Nat. Phys. **11**, 748 (2015).

[297] H. Weng, Y. Liang, Q. Xu, R. Yu, Z. Fang, X. Dai, and Y. Kawazoe, Phys. Rev. B **92**, 045108 (2015).

[298] J.-M. Carter, V. V. Shankar, M. A. Zeb, and H.-Y. Kee, Phys. Rev. B **85**, 115105 (2012).

[299] K. Li, C. Li, J. Hu, Y. Li, and C. Fang, Phys. Rev. Lett. **119**, 247202 (2017).

[300] S. M. Young and C. L. Kane, Phys. Rev. Lett. **115**, 126803 (2015).

[301] B. J. Wieder and C. L. Kane, Phys. Rev. B **94**, 155108 (2016).

[302] C. Bouvier, T. Meunier, P. Ballet, X. Baudry, R. B. G. Kramer, and L. Lévy, “Strained HgTe: a textbook 3D topological insulator,” arXiv:1112.2092 .

[303] M. Mogi, M. Kawamura, R. Yoshimi, A. Tsukazaki, Y. Kozuka, N. Shirakawa, K. S. Takahashi, M. Kawasaki, and Y. Tokura, Nat. Mater. **16**, 516 (2017).

[304] I. Belopolski, S.-Y. Xu, N. Koirala, C. Liu, G. Bian, V. N. Strocov, G. Chang, M. Neupane, N. Alidoust, D. Sanchez, H. Zheng, M. Brahlek, V. Rogalev, T. Kim, N. C. Plumb, C. Chen, F. Bertran, P. Le Fèvre, A. Taleb-Ibrahimi, M.-C. Asensio, M. Shi, H. Lin, M. Hoesch, S. Oh, and M. Zahid Hasan, Sci. Adv. **3**, e1501692 (2017).

[305] G. Roati, C. D’Errico, L. Fallani, M. Fattori, C. Fort, M. Zaccanti, G. Modugno, M. Modugno, and M. Inguscio, Nature **453**, 895 (2008).

[306] B. Deissler, M. Zaccanti, G. Roati, C. D’Errico, M. Fattori, M. Modugno, G. Modugno, and M. Inguscio, Nat. Phys. **6**, 354 (2010).

[307] C. Neff and C. Summers, Opt. Express **13**, 3166 (2005).

[308] T. Dubček, C. J. Kennedy, L. Lu, W. Ketterle, M. Soljačić, and H. Buljan, Phys. Rev. Lett. **114**, 225301 (2015).

[309] Y. Wang and S. Chen, Phys. Rev. A **95**, 053634 (2017).

[310] L. Lu, L. Fu, J. D. Joannopoulos, and M. Soljačić, Nat. Photon. **7**, 294 (2013).

[311] L. Lu, Z. Wang, D. Ye, L. Ran, L. Fu, J. D. Joannopoulos, and M. Soljačić, Science **349**, 622 (2015).

[312] L. Wang, S.-K. Jian, and H. Yao, Phys. Rev. A **93**, 061801(R) (2016).

[313] J. C. Budich and E. Ardonne, Phys. Rev. B **88**, 075419 (2013).

[314] M. S. Lodge, G. Chang, C. Y. Huang, B. Singh, J. Hellerstedt, M. T. Edmonds, D. Kaczorowski, M. M. Hosen, M. Neupane, H. Lin, M. S. Fuhrer, B. Weber, and M. Ishigami, Nano Lett. **17**, 7213 (2017).

[315] Y. M. Lu and A. Vishwanath, Phys. Rev. B **86**, 125119 (2012).

[316] J. Maldacena, Int. J. Theor. Phys. **38**, 1113 (1999).

[317] C. R. Stephens, G. 't Hooft, and B. F. Whiting, Class. Quantum Grav. **11**, 621 (1994).

[318] L. Susskind, J. Math. Phys. **36**, 6377 (1995).

[319] C. B. Thorn, "Reformulating String Theory with the $1/N$ Expansion," arXiv:hep-th/9405069 .

[320] A. Kitaev, Physics-Uspekhi **44**, 131 (2000).

[321] D. I. Pikulin and M. Franz, Phys. Rev. X **7**, 031006 (2017).

[322] A. Chew, A. Essin, and J. Alicea, Phys. Rev. B **96**, 121119 (2017).

[323] A. Chen, R. Ilan, F. D. Juan, D. I. Pikulin, and M. Franz, "Quantum holography in a graphene flake with an irregular boundary," arXiv:1802.00802 .

[324] A. M. García-García and J. J. Verbaarschot, Phys. Rev. D **94**, 126010 (2016).

[325] Y. Z. You, A. W. Ludwig, and C. Xu, Phys. Rev. B **95**, 115150 (2017).

[326] J. Maldacena and D. Stanford, Phys. Rev. D **94**, 106002 (2016).

[327] B. de Wit and J. Smith, *Field theory in particle physics*, N H Personal Library, Vol 1 No. v. 1 (North-Holland, Amsterdam, 1986).

[328] R. Brauer and H. Weyl, Am. J. Math. **57**, 425 (1935).

[329] A. Pais, J. Math. Phys. **3**, 1135 (1962).

[330] A. M. García-García and J. J. M. Verbaarschot, Phys. Rev. D **96**, 066012 (2017).

[331] V. Oganesyan and D. A. Huse, Phys. Rev. B **75**, 155111 (2007).

[332] Y. Y. Atas, E. Bogomolny, O. Giraud, and G. Roux, Phys. Rev. Lett. **110**, 084101 (2013).

[333] H. Bruus and K. Flensberg, *Many-Body Quantum Theory in Condensed Matter Physics: An Introduction*, Oxford Graduate Texts (Oxford University Press, 2004).

[334] D. Bagrets, A. Altland, and A. Kamenev, Nucl. Phys. B **911**, 191 (2016).

[335] A. A. Burkov, Phys. Rev. B **96**, 041110 (2017).

[336] Q. F. Liang, J. Zhou, R. Yu, Z. Wang, and H. Weng, Phys. Rev. B **93**, 085427 (2016).

[337] O. Türker and S. Moroz, Phys. Rev. B **97**, 075120 (2018).

[338] N. Regnault and B. Andrei Bernevig, Phys. Rev. X **1**, 021014 (2011).

[339] A. Kitaev, Ann. Phys. (N. Y). **303**, 2 (2003).

[340] C. Nayak, S. H. Simon, A. Stern, M. Freedman, and S. Das Sarma, Rev. Mod. Phys. **80**, 1083 (2008).

[341] C. Zhang, E. Zhang, W. Wang, Y. Liu, Z. G. Chen, S. Lu, S. Liang, J. Cao, X. Yuan, L. Tang, Q. Li, C. Zhou, T. Gu, Y. Wu, J. Zou, and F. Xiu, Nat. Commun. **8**, 13741 (2017).

[342] J. P. Jay-Gerin, M. J. Aubin, and L. G. Caron, Solid State Commun. **21**, 771 (1977).

[343] M. Neupane, S.-Y. Xu, R. Sankar, N. Alidoust, G. Bian, C. Liu, I. Belopolski, T.-R. Chang, H.-T. Jeng, H. Lin, A. Bansil, F. Chou, and M. Z. Hasan, Nat. Commun. **5**, 3786 (2014).

[344] L. P. He, X. C. Hong, J. K. Dong, J. Pan, Z. Zhang, J. Zhang, and S. Y. Li, Phys. Rev. Lett. **113**, 246402 (2014).

[345] C. L. Zhang, Z. Yuan, Q. D. Jiang, B. Tong, C. Zhang, X. C. Xie, and S. Jia, Phys. Rev. B **95**, 085202 (2017).

[346] S. Borisenko, Q. Gibson, D. Evtushinsky, V. Zabolotnyy, B. Büchner, and R. J. Cava, Phys. Rev. Lett. **113**, 27603 (2014).

[347] Z. K. Liu, B. Zhou, Y. Zhang, Z. J. Wang, H. M. Weng, D. Prabhakaran, S.-K. Mo, Z. X. Shen, Z. Fang, X. Dai, Z. Hussain, and Y. L. Chen, Science **343**, 864 (2014).

[348] Z. K. Liu, J. Jiang, B. Zhou, Z. J. Wang, Y. Zhang, H. M. Weng, D. Prabhakaran, S.-K. Mo, H. Peng, P. Dudin, T. Kim, M. Hoesch, Z. Fang, X. Dai, Z. X. Shen, D. L. Feng, Z. Hussain, and Y. L. Chen, Nat. Mater. **13**, 677 (2014).

[349] M. Donath, Surf. Sci. Rep. **20**, 251 (1994).

[350] T. Bécherrawy, *Electromagnetism: Maxwell Equations, Wave Propagation and Emission* (John Wiley and Sons, Inc., Hoboken, NJ, 2012).

[351] G. Liu, G. Wang, Y. Zhu, H. Zhang, G. Zhang, X. Wang, Y. Zhou, W. Zhang, H. Liu, L. Zhao, J. Meng, X. Dong, C. Chen, Z. Xu, and X. J. Zhou, Rev. Sci. Instrum. **79**, 023105 (2008).

[352] H. Groenewold, Physica **12**, 405 (1946).

[353] I. Gradshteyn and I. Ryzhik, in *Table of Integrals, Series, and Products*, edited by D. Zwillinger and V. Moll (Academic Press, Boston, 2014) Eighth ed., pp. 776 – 865.

[354] P. A. Mello, P. Pereyra, and N. Kumar, Ann. Phys. (N. Y). **181**, 290 (1988).

Acknowledgments

First, and most importantly, I want to thank my supervisor Jens H. Bardarson for his constant and unconditional support throughout the whole project. Jens deeply understands many topics in physics and does never stop on a superficial level, which enables him to explain things from a lot of different perspectives. His support was not just limited to physics: his sense of style helped to get things done, and his remarkable skill to give presentations helped me to improve my own talks. Jens thinks python—his computational skills are almost magic. Three lines of code fix problems that other people cannot solve using 100 nested for-loops. Without Jens, this thesis and many other things would not have been possible.

Second, I want to thank Roderich Moessner for evaluating this thesis and for supporting me throughout my time at MPI PKS. He manages the institute in the most pleasant way, resulting in the excellent scientific environment at PKS. He further enabled me to visit a large number of schools and conferences, which were essential for my scientific development. I also want to thank Carsten Timm for evaluating this thesis.

This work is largely the result of numerous scientific collaborations. Probably the most important and most productive collaboration was together with Adolfo G. Grushin. I benefited substantially from his huge insight into various fields of physics and his skill to think outside the box. Roni Ilan helped me to understand a phletora of condensed-matter phenomena and she inspired big parts of this thesis work, thanks to her creativity and her great skill to pursue a goal until it is reached. Thanks to the support of Jens H. Bardarson, Roderich Moessner, and Joel Moore, I was able to visit both Adolfo and Roni at the University of California, Berkeley, in August 2016. Roni Ilan further supported me to pay another visit to Tel Aviv University in September 2017, which was funded by MPI PKS and TAU. Another big fraction of this thesis was carried out together with Jun Won Rhim. I want to thank him for illuminating discussions that resulted in a lot of ideas, including some unfinished work. I genuinely hope that these collaborations will continue in the future.

My insight into topological condensed matter physics was driven forward at various schools and conferences. Most notably, the Boulder summer school 2016 helped to significantly increase my knowledge about topology and inspired some of the projects presented here. It was the starting point for the fruitful collaboration with Björn Sbierski and Flore K. Kunst that was intensified at another conference in Stockholm. Moreover, I am sincerely grateful to Hubert Scherrer-Paulus and the entire IT crowd at MPI PKS. Careful proof reading of this thesis was done, among others, by André Holzbecher, Niels Schroeter, Talía L. M. Lezama, and Robert-Jan Slager.

Life at PKS wouldn't have been as enjoyable and inspiring without Cécile, Izaak, Matthias, Omar, Robert-Jan, Ruben, Talía, Younes, and many others. The best possible base in Dresden was my WG, Joachim, Joel, Johanna, Stephan, and Zarah. The skiing team A (including those who sneaked in), our nightmarish theater group, especially Amina, and all countless boulder fellows made the time in Dresden a memorable experience that I do not want to miss. My entire PhD wouldn't have been possible without the constant love and support by my parents and my sister. Thank you!

List of Publications

1. Jan Behrends, Flore K. Kunst, Björn Sbierski, "Transversal magnetotransport in Weyl semimetals: Exact numerical approach", *Phys. Rev. B* **97**, 064203 (2018).

2. Jan Behrends, Jun-Won Rhim, Shang Liu, Adolfo G. Grushin, Jens H. Bardarson, "Nodal-line semimetals from Weyl superlattices", *Phys. Rev. B* **96**, 245101 (2017).

3. Jan Behrends, Jens H Bardarson, "Strongly angle-dependent magnetoresistance in Weyl semimetals with long-range disorder", *Phys. Rev. B* **96**, 060201 (2017).

4. Jun-Won Rhim, Jan Behrends, Jens H Bardarson, "Bulk-boundary correspondence from the intercellular Zak phase", *Phys. Rev. B* **95**, 035421 (2017).

5. Jan Behrends, Adolfo G Grushin, Teemu Ojanen, Jens H Bardarson, "Visualizing the chiral anomaly in Dirac and Weyl semimetals with photoemission spectroscopy", *Phys. Rev. B* **93**, 075114 (2016).

6. Suoqing Ji, Robert T Fisher, Petros Tzeferacos, George Jordan, Dongwook Lee, Pascal Cremer, Jan Behrends, "The Post-Merger Magnetized Evolution of White Dwarf Binaries: The Double-Degenerate Channel of Sub-Chandrasekhar Type Ia Supernovae and the Formation of Magnetized White Dwarfs", *Astrophys. J* **773**, 136 (2013).

7. Yoong Ahm Kim, Kazunori Fujisawa, Hiroyuki Muramatsu, Takuya Hayashi, Morinobu Endo, Toshihiko Fujimori, Katsumi Kaneko, Mauricio Terrones, Jan Behrends, Axel Eckmann, Cinzia Casiraghi, Kostya S Novoselov, Riichiro Saito, Mildred S Dresselhaus, "Raman spectroscopy of boron-doped single-layer graphene", *ACS nano* **6**, 6293–6300 (2012).

Publications 1–5 resulted from the work presented in this thesis. In addition, the results presented in Secs. 3.5, 4.3 and 6 are currently being prepared for separate publications.

Versicherung

Diese Arbeit wurde am Max-Planck-Institut für Physik komplexer Systeme in Dresden unter der wissenschaftlichen Betreuung von Prof. Dr. Jens H. Bardarson durchgeführt.

Hiermit versichere ich, dass ich die vorliegende Arbeit ohne unzulässige Hilfe Dritter und ohne Benutzung anderer als der angegebenen Hilfsmittel angefertigt habe; die aus fremden Quellen direkt oder indirekt übernommenen Gedanken sind als solche kenntlich gemacht. Die Arbeit wurde bisher weder im Inland noch im Ausland in gleicher oder ähnlicher Form einer anderen Prüfungsbehörde vorgelegt.

Darüber hinaus erkenne ich die Promotionsordnung des Bereichs Mathematik und Naturwissenschaften der Technischen Universität Dresden vom 23. Februar 2011 an.

Jan Behrends

Dresden, 13.07.2018